British Geological Survey
NATURAL ENVIRONMENT RESEARCH COUNCIL

Mineralogy, petrography and stable isotope study of methane-derived authigenic carbonate (MDAC) from the Croker Carbonate Slab, CEND 23/25 Survey. Part 2

Land, Soil and Coast Programme

Commissioned Report CR/16/164

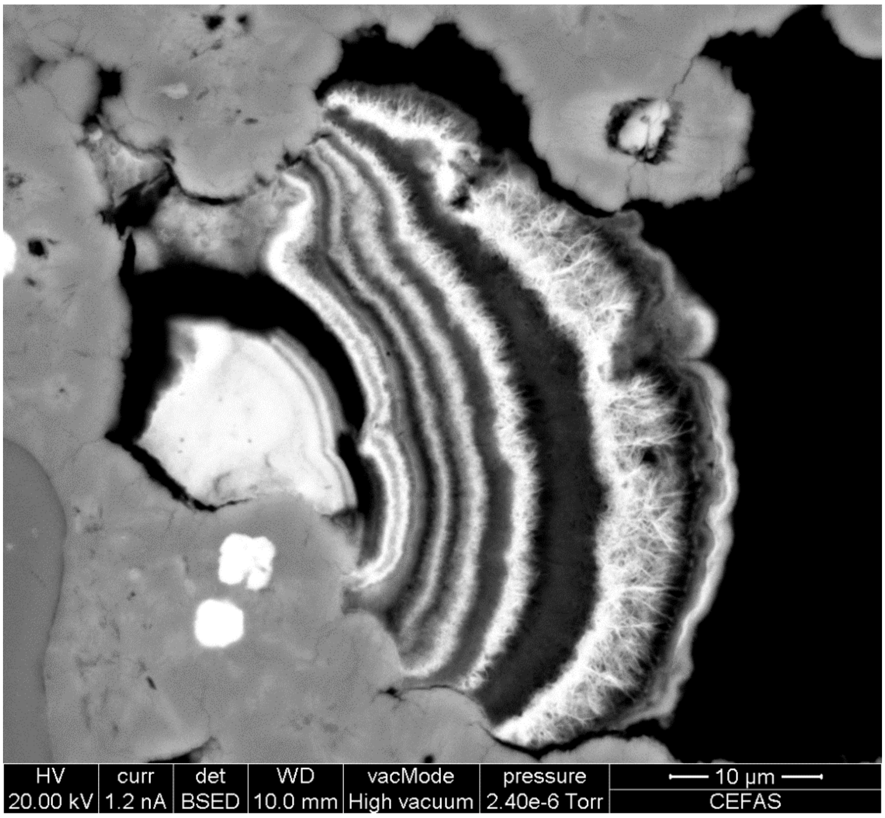

BRITISH GEOLOGICAL SURVEY

LAND, SOIL AND COAST PROGRAMME

COMMISSIONED REPORT CR/16/164

The National Grid and other Ordnance Survey data © Crown Copyright and database rights 2016. Ordnance Survey Licence No. 100021290 EUL.

Keywords

Methane derived authigenic carbonate, MDAC, calcite, magnesian calcite, aragonite, dolomite, Irish Sea, Croker, XRD, petrography, BSEM, EDXA, stable isotopes.

National Grid Reference

Not applicable

Map

Not applicable

Front cover

BSEM image of a Mn-rich colloform precipitate from sample GT025.

Bibliographical reference

FIELD, L.P., MILODOWSKI, A.E., WAGNER, D., SLOANE, H., LENG, M.J., AND MARRIOTT, A.L.. 2016. Mineralogy, petrography and stable isotope study of methane-derived authigenic carbonate (MDAC) from the Croker Carbonate Slab, CEND 23/25 Survey. Part 2. *British Geological Survey Commissioned Report*, CR/16/164. 149pp.

Copyright in materials derived from the British Geological Survey's work is owned by the Natural Environment Research Council (NERC) and/or the authority that commissioned the work. You may not copy or adapt this publication without first obtaining permission. Contact the BGS Intellectual Property Rights Section, British Geological Survey, Keyworth, e-mail ipr@bgs.ac.uk. You may quote extracts of a reasonable length without prior permission, provided a full acknowledgement is given of the source of the extract.

© NERC 2016. All rights reserved

Mineralogy, petrography and stable isotope study of methane-derived authigenic carbonate (MDAC) from the Croker Carbonate Slab, CEND 23/25 Survey. Part 2

L.P. Field, A.E. Milodowski, D. Wagner, H. Sloane, M.J. Leng and A.L. Marriott.

Keyworth, Nottingham British Geological Survey 2016

BRITISH GEOLOGICAL SURVEY

The full range of our publications is available from BGS shops at Nottingham, Edinburgh, London and Cardiff (Welsh publications only) see contact details below or shop online at www.geologyshop.com

The London Information Office also maintains a reference collection of BGS publications, including maps, for consultation.

We publish an annual catalogue of our maps and other publications; this catalogue is available online or from any of the BGS shops.

The British Geological Survey carries out the geological survey of Great Britain and Northern Ireland (the latter as an agency service for the government of Northern Ireland), and of the surrounding continental shelf, as well as basic research projects. It also undertakes programmes of technical aid in geology in developing countries.

The British Geological Survey is a component body of the Natural Environment Research Council.

British Geological Survey offices

BGS Central Enquiries Desk

Tel 0115 936 3143 Fax 0115 936 3276

email enquiries@bgs.ac.uk

Environmental Science Centre, Keyworth, Nottingham NG12 5GG

Tel 0115 936 3241 Fax 0115 936 3488
email sales@bgs.ac.uk

The Lyell Centre, Research Avenue South, Edinburgh EH14 4AP

Tel 0131 667 1000 Fax 0131 668 2683
email scotsales@bgs.ac.uk

Natural History Museum, Cromwell Road, London SW7 5BD

Tel 020 7589 4090 Fax 020 7584 8270
Tel 020 7942 5344/45 email bgslondon@bgs.ac.uk

Columbus House, Greenmeadow Springs, Tongwynlais, Cardiff CF15 7NE

Tel 029 2052 1962 Fax 029 2052 1963

Maclean Building, Crowmarsh Gifford, Wallingford OX10 8BB

Tel 01491 838800 Fax 01491 692345

Geological Survey of Northern Ireland, Department of Enterprise, Trade & Investment, Dundonald House, Upper Newtownards Road, Ballymiscaw, Belfast, BT4 3SB

Tel 028 9038 8462 Fax 028 9038 8461

www.bgs.ac.uk/gsni/

Parent Body

Natural Environment Research Council, Polaris House, North Star Avenue, Swindon SN2 1EU

Tel 01793 411500 Fax 01793 411501
www.nerc.ac.uk

Website www.bgs.ac.uk
Shop online at www.geologyshop.com

Foreword

This report is the second part of the 2-part published product of a study by the British Geological Survey (BGS) commissioned by the Centre for Environment, Fisheries and Aquaculture Science (Cefas) on behalf of the Joint Nature Conservation Committee (JNCC), to undertake petrographic, X-ray diffraction analysis and carbon and oxygen stable isotope compositions of samples of carbonate-cemented sediment recovered from the Croker Carbonate Slabs (Candidate Special Area of Conservation / Site of Community Importance (cSAC/SCI)) of the mid Irish Sea. Cefas recovered a suite of 30 samples as part of a multidisciplinary survey (Cefas cruise CEND 23/15). The objective of this study was to characterise the mineralogy and determine the origin of carbonate-cemented sediment, and in particular, to confirm whether the samples are methane-derived authigenic carbonates (MDAC). This report presents the analyses on all samples including the four samples identified by Cefas as a priority for investigation, which were reported on in BGS report number CR/16/156.

This work was carried out under Cefas purchase orders 20034409 and 20035669: contract reference MPM023-15. The specific objectives of the BGS study were as follows:

1. To undertake whole-sample X-ray diffraction analysis to determine the bulk mineralogy of 30 samples of potential MDAC collected by Cefas, and to confirm the nature of any carbonate cements;
2. To undertake detailed petrographic analysis of 30 polished thin sections prepared each of the potential MDAC samples, by scanning electron microscopy (backscattered electron imaging) with energy-dispersive X-ray microanalysis to characterise the composition of any carbonate cements, after initial optical observation of the thin sections in transmitted light by optical petrographic microscopy;
3. To undertake carbon ($\delta^{13}C$) and oxygen ($\delta^{18}O$) stable isotope analyses of the different carbonate mineral components in each of the potential MDAC samples to establish the origin of the cement.

Due to the size of this report, for convenience, it has been split into two parts:

- Part 1: Introduction, X-ray diffraction and petrology (samples GT004 to GT0071);
- Part 2: Petrology (samples GT0076 to GT150), oxygen and carbon stable isotope analysis of carbonate cements and other carbonate components, discussion and conclusions.

Acknowledgements

Mr John Fletcher (BGS, Thin Section Laboratory) is gratefully acknowledged for preparing the polished thin sections and blocks from the MDAC samples.

Contents

FIGURES

PLATES

TABLES

Summary

Refer to Part 1.

1 Introduction

The British Geological Survey (BGS) was contracted by the Centre for Environment, Fisheries and Aquaculture Science (Cefas), to undertake a mineralogical and petrological study of thirty samples of diagenetic, carbonate-cemented sediment samples recovered by Cefas from the seabed as part of a multidisciplinary survey (CEND 23/15) to Croker Carbonate Slabs cSAC/SCI (Figure 1, Part 1) between 24th October and 6th November 2015. These carbonate-cemented sediments are considered to potentially represent Methane-Derived Authigenic Carbonate (MDAC).

This volume (Part 2) is the second part of a two-volume report that presents the mineralogical and petrological observations (including, petrographic, X-ray diffraction (XRD) and carbon ($\delta^{13}C$) and oxygen ($\delta^{18}O$) stable isotope analyses) on the carbonate-cemented sediment samples, and discusses these findings in regard to whether the carbonate cements and associated mineralisation can be interpreted to have an MDAC origin. Part 2 includes the petrographic analysis for samples GT076 to GT150 and the results from carbon and oxygen stable isotope analyses of the carbonate cements. For the list of samples and methodologies, please refer to the first volume (Part 1) of the report

2 Petrology (Part 2)

2.1 SAMPLE GT076

Sample GT076 comprised three light buff coloured, angular, tabular clasts (<160 mm diameter) of carbonate-cemented sandstone (Plate 1). Some minor orange-brown iron-oxyhydroxide stains the surfaces of the clasts. Evidence of bioturbation and minor boring by marine organisms is present. Some encrustations by bryozoa are also present on the surfaces of the clasts (Plate 2).

Plate 1. Photograph of sample GT076. Grey scale bar divisions = 10 mm.

Plate 2. Optical photomicrograph of an encrusting bryozoan present on the surface of sample GT076.

The detrital mineralogy is similar to that described in the previous samples (see Part 1 of the report), being dominated by quartz, with subordinate feldspar. The sample is close-packed and reasonably well sorted (Plate 3), with angular to sub-rounded sand grains (<250 µm). The fabric is grain supported with simple point grain contacts. There is no evidence of any compactional deformation, indicating cementation occurred before any significant depth of burial. Patchy orange-brown colouration defines the poorer-sorted, matrix-rich areas in thin section (Plate 3), and is due to finely disseminated iron oxyhydroxides in the matrix and on grain surfaces. This heterogeneous distribution of matrix is quite typical of bioturbated sediments. There is some limited secondary porosity where unstable detrital grains and bioclastic debris have dissolved out (Plate 4). Cementation in this sample is heterogeneous in distribution, occurring in discontinuous and irregular patches rather than in in discrete laminae (Plate 3). This heterogeneity may reflect the bioturbation of the sediment, which may have locally controlled the transport of the mineralising fluids through the sediment. The main cement comprises micritic high magnesian-calcite cement occurring as globular aggregates within the intergranular matrix of the sandstone (Plate 5). Vestiges of a possible microcellular fabric were observed but it is not as well developed as in some of the other samples (e.g. GT004, GT071). Aragonite cement is also present as a minor cement, occurring as discrete acicular needles of aragonite in open pores (Plate 6). The aragonite is relatively late and has grown on top of the earlier micritic magnesian calcite. XRD analyses indicate that aragonite makes up 5.5 wt. % of the sample (see Volume 1: Table 2). Aragonite is more abundant than in sample GT050, although not to the extent that it forms a well-developed aragonite cement such as that observed in sample GT012.

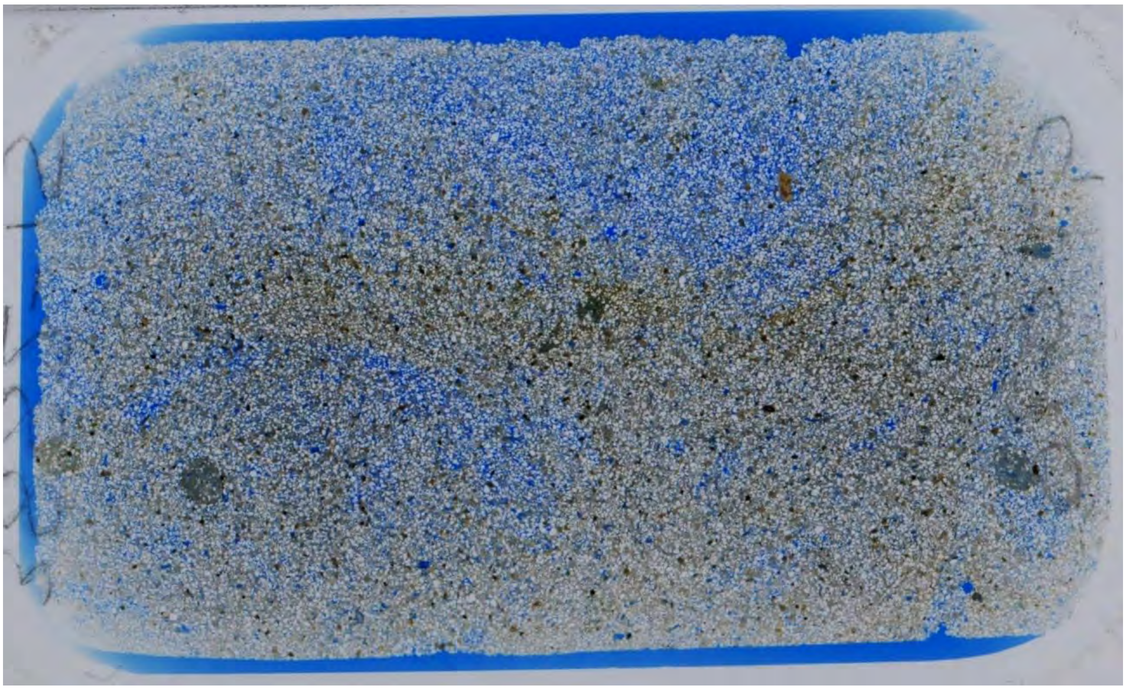

Plate 3. Scanned image of the thin section prepared from one of the clasts in sample GT076. It shows fine sandstone with a heterogeneous distribution of porosity (blue resin-impregnated regions) and muddy micritic matrix (brown areas). Field of view = 48 mm wide.

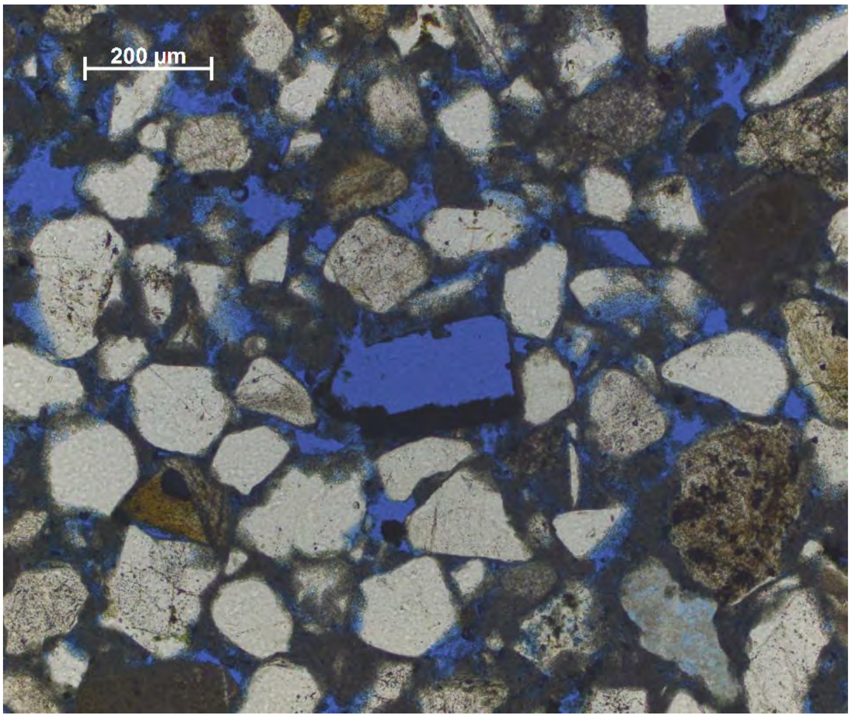

Plate 4. Transmitted light photomicrograph (plain polarised light) showing the angular to sub-rounded grains and some secondary grain dissolution porosity (large blue-resin filled pore in centre of image). The micritic matrix cement appears dark brown and semi-opaque in transmitted light. Sample GT076.

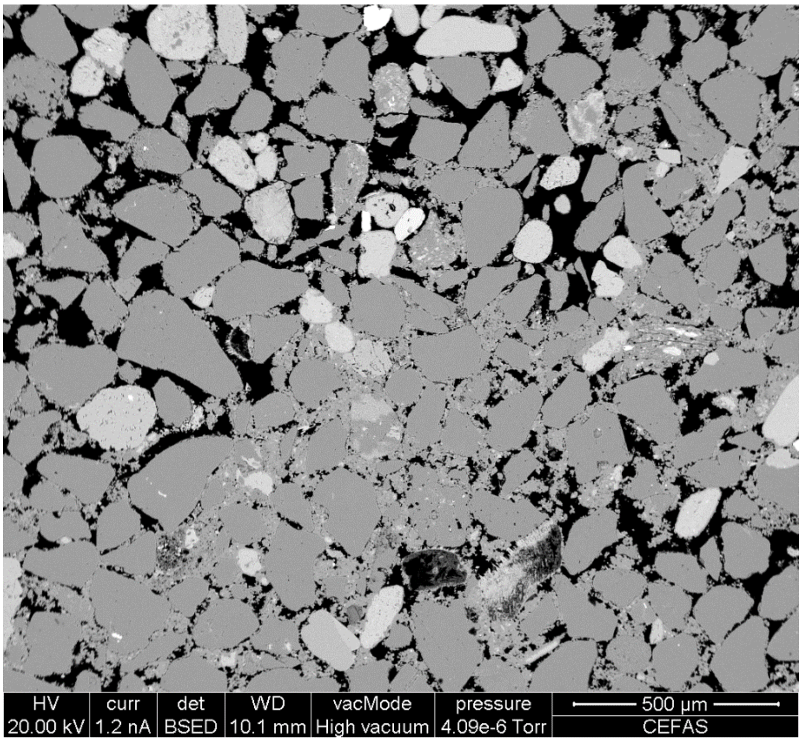

Plate 5. BSEM image showing the patchy nature of the micritic cementation. Sample GT076.

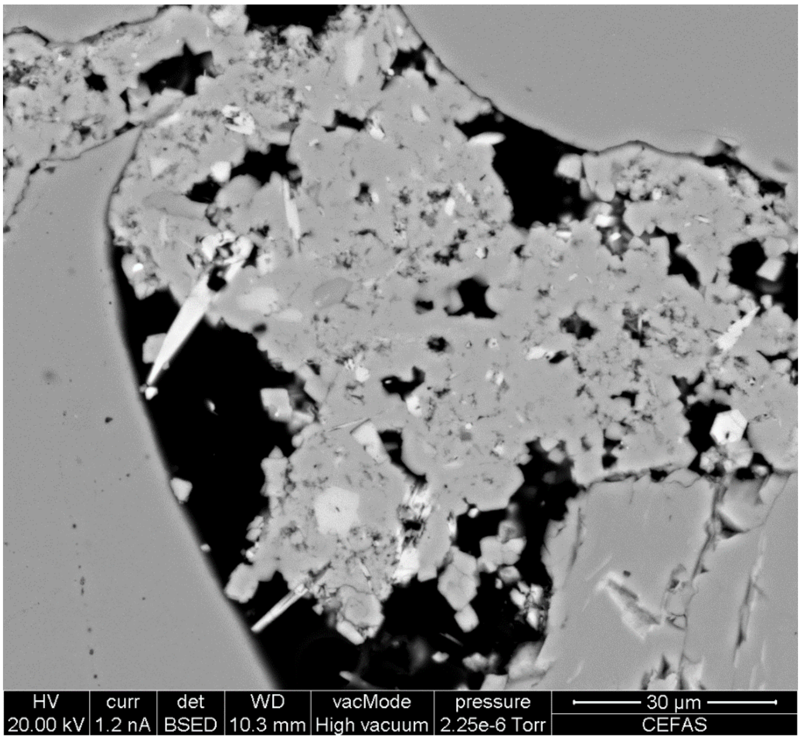

Plate 6. BSEM image detailing the micritic high magnesian-calcite cement (dull grey). Longitudinal and euhedral cross-sections of fine-grained acicular aragonite (white) can be seen intergrown within the micritic calcite cement. Sample GT076.

ED-EPMA major element compositional data for the carbonate cements and some example shell fragments in sample GT143 are given in Table 1. Their compositional variation, expressed in terms of molar proportions of CaO_3-$MgCO_3$ and $SrCO_3$, is summarised in Figure 1. The micritic magnesian calcite cements contain between 35 and 44 mole % $MgCO_3$ in solid solution (i.e. the structural formula of the calcite can be represented as $Ca_{0.36-0.65}Mg_{0.44-0.35}CO_3$). The ED-EPMA data is consistent with the bulk XRD analysis, which indicates the presence of very high magnesian-calcite of similar composition, as a major component of the rock (see Volume 1: Table 2). As such, these cements are also similar to the high magnesian-calcite cement found in many the other samples (see Volume 1: Section 4, and other samples described below).

The aragonite cement is slightly strontium-bearing, with up to 1 mole % $SrCO_3$ in solid-solution (i.e. the structural formula (i.e. the structural formula of the aragonite can be represented as $Ca_{0.99-1.00}Sr_{0.01-0.00}CO_3$). Significant magnesium (up to 11 mole % $MgCO_3$) was detected in many of the ED-EPMA from the acicular aragonite (Figure 1 and Table 1). However, these data most probably represent mixed analyses, resulting from the inclusion of magnesian calcite in the analyses, due to the very fine-nature of the aragonite and its intimate intergrowth with the micritic calcite (see Plate 6), resulting in mixed analysis.

The shell fragment analysed appears to be aragonite and contains up to 2 mole % Sr.

The sequence of sedimentary and post-depositional diagenetic events recorded from sample GT076 can be summarised as follows:

1. Deposition of fine-grained sandy sediment.
2. Syndepositional bioturbation.
3. Precipitation of micritic high magnesian-calcite under shallow burial depth, causing lithification.
4. Limited precipitation of later acicular aragonite cement.
5. Some later microscopic boring of the lithified sandstone sediment by marine micro-organisms.

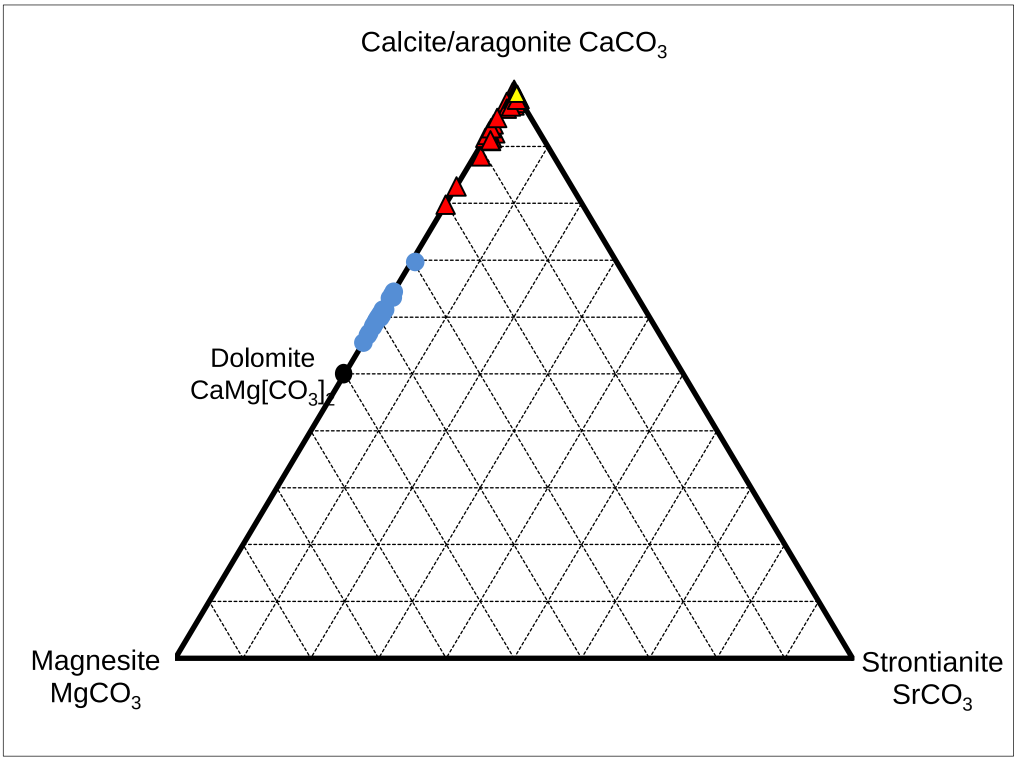

Figure 1. $CaCO_3$-$MgCO_3$-$SrCO_3$ molar ratio plot illustrating the compositions of the micritic high magnesian-calcite cement (solid blue circles) and shell fragments (yellow triangles) from sample GT076.

Table 1. Electron microprobe analyses of carbonate cements in sample GT076

		Weight % oxide (normalised)							Ionic ratio [normalised to 3 [O]						COMMENTS
SAMPLE	No	MgO	CaO	MnO	FeO	SrO	CO_2 (calc)	*Total wt%	Mg^{2+}	Ca^{2+}	Mn^{2+}	Fe^{2+}	Sr^{2+}	CO_3^{2-}	
GT076	1	0.00	55.27	0.00	0.00	0.96	43.77	100	0.00	0.99	0.00	0.00	0.01	1.00	aragonite
GT076	2	0.00	54.81	0.00	0.00	1.53	43.66	100	0.00	0.99	0.00	0.00	0.01	1.00	aragonite
GT076	3	0.00	54.82	0.00	0.00	1.53	43.66	100	0.00	0.99	0.00	0.00	0.01	1.00	aragonite
GT076	4	0.00	54.70	0.00	0.00	1.67	43.63	100	0.00	0.98	0.00	0.00	0.02	1.00	aragonite
GT076	5	0.14	54.87	0.00	0.00	1.25	43.74	100	0.00	0.98	0.00	0.00	0.01	1.00	aragonite
GT076	6	0.00	54.98	0.00	0.00	1.32	43.70	100	0.00	0.99	0.00	0.00	0.01	1.00	aragonite
GT076	7	0.00	55.56	0.00	0.00	0.59	43.85	100	0.00	0.99	0.00	0.00	0.01	1.00	shell
GT076	8	0.00	55.62	0.00	0.00	0.52	43.86	100	0.00	0.99	0.00	0.00	0.01	1.00	shell
GT076	9	0.00	55.42	0.00	0.00	0.77	43.81	100	0.00	0.99	0.00	0.00	0.01	1.00	shell
GT076	10	0.00	56.04	0.00	0.00	0.00	43.96	100	0.00	1.00	0.00	0.00	0.00	1.00	aragonite
GT076	11	0.17	54.47	0.00	1.51	0.00	43.85	100	0.00	0.97	0.00	0.02	0.00	1.00	aragonite
GT076	12	0.00	55.76	0.00	0.00	0.34	43.90	100	0.00	1.00	0.00	0.00	0.00	1.00	aragonite
GT076	13	0.53	54.20	0.00	0.00	1.52	43.75	100	0.01	0.97	0.00	0.00	0.01	1.00	aragonite in micrite
GT076	14	0.88	55.01	0.00	0.00	0.00	44.12	100	0.02	0.98	0.00	0.00	0.00	1.00	aragonite in micrite
GT076	15	0.25	55.02	0.00	0.00	0.90	43.83	100	0.01	0.98	0.00	0.00	0.01	1.00	aragonite in micrite
GT076	16	2.68	52.01	0.00	0.00	1.10	44.20	100	0.07	0.92	0.00	0.00	0.01	1.00	aragonite in micrite
GT076	17	3.04	51.65	0.00	0.00	1.03	44.28	100	0.08	0.92	0.00	0.00	0.01	1.00	aragonite in micrite
GT076	18	2.98	52.54	0.00	0.00	0.00	44.48	100	0.07	0.93	0.00	0.00	0.00	1.00	aragonite in micrite
GT076	19	4.39	50.09	0.00	0.00	1.00	44.52	100	0.11	0.88	0.00	0.00	0.01	1.00	aragonite in micrite
GT076	20	2.47	53.14	0.00	0.00	0.00	44.39	100	0.06	0.94	0.00	0.00	0.00	1.00	aragonite in micrite
GT076	21	8.34	45.86	0.00	0.43	0.00	45.36	100	0.20	0.79	0.00	0.01	0.00	1.00	aragonite in micrite
GT076	22	3.43	51.69	0.00	0.36	0.00	44.52	100	0.08	0.91	0.00	0.00	0.00	1.00	aragonite encased in micrite
GT076	23	3.12	52.22	0.00	0.18	0.00	44.48	100	0.08	0.92	0.00	0.00	0.00	1.00	aragonite encased in micrite
GT076	24	3.23	52.24	0.00	0.00	0.00	44.52	100	0.08	0.92	0.00	0.00	0.00	1.00	aragonite encased in micrite
GT076	25	3.21	51.36	0.00	0.00	1.14	44.29	100	0.08	0.91	0.00	0.00	0.01	1.00	aragonite encased in micrite
GT076	26	1.10	54.03	0.00	0.24	0.62	44.01	100	0.03	0.96	0.00	0.00	0.01	1.00	aragonite encased in micrite
GT076	27	0.00	55.18	0.00	0.00	1.08	43.75	100	0.00	0.99	0.00	0.00	0.01	1.00	aragonite encased in micrite
GT076	28	0.24	55.11	0.00	0.00	0.80	43.85	100	0.01	0.99	0.00	0.00	0.01	1.00	aragonite encased in micrite
GT076	29	0.37	54.75	0.00	0.27	0.76	43.85	100	0.01	0.98	0.00	0.00	0.01	1.00	aragonite encased in micrite
GT076	30	0.00	55.03	0.00	0.32	0.90	43.75	100	0.00	0.99	0.00	0.00	0.01	1.00	aragonite encased in micrite
GT076	31	0.36	54.46	0.00	0.00	1.44	43.74	100	0.01	0.98	0.00	0.00	0.01	1.00	aragonite encased in micrite
GT076	32	2.75	52.57	0.00	0.26	0.00	44.41	100	0.07	0.93	0.00	0.00	0.00	1.00	aragonite encased in micrite

		Weight % oxide (normalised)							Ionic ratio [normalised to 3 [O]						COMMENTS
SAMPLE	No	MgO	CaO	MnO	FeO	SrO	CO_2 (calc)	*Total wt%	Mg^{2+}	Ca^{2+}	Mn^{2+}	Fe^{2+}	Sr^{2+}	CO_3^{2-}	
GT076	33	2.01	53.43	0.00	0.28	0.00	44.28	100	0.05	0.95	0.00	0.00	0.00	1.00	aragonite encased in micrite
GT076	34	0.16	55.03	0.00	0.00	1.03	43.79	100	0.00	0.99	0.00	0.00	0.01	1.00	aragonite encased in micrite
GT076	35	3.17	50.85	0.00	0.72	1.02	44.24	100	0.08	0.90	0.00	0.01	0.01	1.00	aragonite encased in micrite
GT076	36	0.75	53.58	0.00	0.82	1.05	43.80	100	0.02	0.96	0.00	0.01	0.01	1.00	aragonite encased in micrite
GT076	37	0.17	54.53	0.00	0.25	1.34	43.70	100	0.00	0.98	0.00	0.00	0.01	1.00	aragonite encased in micrite
GT076	38	7.03	47.79	0.00	0.00	0.00	45.17	100	0.17	0.83	0.00	0.00	0.00	1.00	aragonite in micrite
GT076	39	17.98	34.97	0.00	0.00	0.00	47.06	100	0.42	0.58	0.00	0.00	0.00	1.00	micrite
GT076	40	12.35	40.27	0.00	0.93	0.57	45.88	100	0.29	0.69	0.00	0.01	0.01	1.00	micrite
GT076	41	17.38	35.16	0.00	0.56	0.00	46.90	100	0.40	0.59	0.00	0.01	0.00	1.00	micrite
GT076	42	17.25	35.55	0.00	0.29	0.00	46.90	100	0.40	0.59	0.00	0.00	0.00	1.00	micrite
GT076	43	17.67	34.73	0.00	0.66	0.00	46.94	100	0.41	0.58	0.00	0.01	0.00	1.00	micrite
GT076	44	17.44	35.60	0.00	0.00	0.00	46.96	100	0.41	0.59	0.00	0.00	0.00	1.00	micrite
GT076	45	16.95	35.51	0.00	0.42	0.34	46.77	100	0.40	0.60	0.00	0.01	0.00	1.00	micrite
GT076	46	15.58	37.44	0.00	0.37	0.00	46.61	100	0.36	0.63	0.00	0.00	0.00	1.00	micrite
GT076	47	15.35	37.49	0.00	0.29	0.36	46.50	100	0.36	0.63	0.00	0.00	0.00	1.00	micrite
GT076	48	16.30	35.93	0.00	1.11	0.00	46.66	100	0.38	0.60	0.00	0.01	0.00	1.00	micrite
GT076	49	16.44	36.52	0.00	0.00	0.32	46.73	100	0.38	0.61	0.00	0.00	0.00	1.00	micrite
GT076	50	16.86	36.02	0.00	0.00	0.32	46.80	100	0.39	0.60	0.00	0.00	0.00	1.00	micrite
GT076	51	16.84	36.30	0.00	0.00	0.00	46.86	100	0.39	0.61	0.00	0.00	0.00	1.00	micrite
GT076	52	17.57	35.44	0.00	0.00	0.00	46.99	100	0.41	0.59	0.00	0.00	0.00	1.00	micrite
GT076	53	17.44	35.37	0.00	0.24	0.00	46.94	100	0.41	0.59	0.00	0.00	0.00	1.00	micrite
GT076	54	16.87	36.06	0.00	0.23	0.00	46.84	100	0.39	0.60	0.00	0.00	0.00	1.00	micrite
GT076	55	17.12	35.82	0.00	0.17	0.00	46.89	100	0.40	0.60	0.00	0.00	0.00	1.00	micrite
GT076	56	17.25	35.08	0.00	0.81	0.00	46.85	100	0.40	0.59	0.00	0.01	0.00	1.00	micrite
GT076	57	17.53	35.49	0.00	0.00	0.00	46.98	100	0.41	0.59	0.00	0.00	0.00	1.00	micrite
GT076	58	18.67	34.15	0.00	0.00	0.00	47.18	100	0.43	0.57	0.00	0.00	0.00	1.00	micrite
GT076	59	18.40	34.23	0.00	0.27	0.00	47.10	100	0.43	0.57	0.00	0.00	0.00	1.00	micrite
GT076	60	17.32	35.41	0.00	0.35	0.00	46.91	100	0.40	0.59	0.00	0.00	0.00	1.00	micrite
GT076	61	17.65	35.20	0.00	0.17	0.00	46.98	100	0.41	0.59	0.00	0.00	0.00	1.00	micrite
GT076	62	17.21	35.41	0.00	0.51	0.00	46.88	100	0.40	0.59	0.00	0.01	0.00	1.00	micrite
GT076	63	17.39	35.38	0.00	0.30	0.00	46.93	100	0.40	0.59	0.00	0.00	0.00	1.00	micrite
GT076	64	15.37	38.02	0.00	0.00	0.00	46.61	100	0.36	0.64	0.00	0.00	0.00	1.00	micrite
GT076	65	17.28	35.79	0.00	0.00	0.00	46.94	100	0.40	0.60	0.00	0.00	0.00	1.00	micrite
GT076	66	17.41	35.63	0.00	0.00	0.00	46.96	100	0.40	0.60	0.00	0.00	0.00	1.00	micrite

		Weight % oxide (normalised)							Ionic ratio [normalised to 3 [O]						COMMENTS
SAMPLE	No	MgO	CaO	MnO	FeO	SrO	CO_2 (calc)	*Total wt%	Mg^{2+}	Ca^{2+}	Mn^{2+}	Fe^{2+}	Sr^{2+}	CO_3^{2-}	
GT076	67	17.29	35.78	0.00	0.00	0.00	46.94	100	0.40	0.60	0.00	0.00	0.00	1.00	micrite
GT076	68	17.05	36.05	0.00	0.00	0.00	46.90	100	0.40	0.60	0.00	0.00	0.00	1.00	micrite
GT076	69	15.11	38.13	0.00	0.22	0.00	46.54	100	0.35	0.64	0.00	0.00	0.00	1.00	micrite
GT076	70	19.27	33.45	0.00	0.00	0.00	47.28	100	0.44	0.56	0.00	0.00	0.00	1.00	micrite

**Note: Some analytical totals were low (<90%) because of the microporous nature of the cements. Therefore, all data were normalised to 100%*

2.2 SAMPLE GT104

This sample comprises ten angular to sub-angular tabular clasts of grey-buff sandstone (Plate 7). The sandstone also includes lenses of coarse detrital bioclastic material. Patches of orange to brown, and black patchy surface colouration is present from iron-oxyhydroxide staining. Some of this staining penetrates deep into these clasts. Encrustations of bryozoan and calcareous serpulid worm casings are present on the surface.

Plate 7. Photograph of the clasts which make up sample GT104. These show evidence of bioturbation, and have a patchy orange to brown colouration from iron oxyhydroxide staining. Grey scale bar divisions = 10 mm.

The polished thin section prepared through one of the clasts from sample GT104 is shown in Plate 8. Two different sediment types can be seen in the image: (i) a lower layer of reasonably well-sorted fine to medium grained (<300 µm) sandstone, with sub-angular to sub-rounded grains dominated by detrital quartz; (ii) an upper layer of poorly-sorted shelly sandstone varying from fine-grained silt to coarser sand (up to 600 µm) with abundant coarse bioclastic debris, including bivalve shells (Plate 8 and Plate 9).

The sample is cemented by two generations of carbonate cements (Plate 10):

- An early, fine-grained micritic high- magnesian-calcite, which forms a matrix comprised of globular aggregates of the micrite, and;
- A later fibrous cement comprising masses of acicular crystals of aragonite (<100 µm), which has nucleated on top of the micrite, and has grown into the intergranular pore spaces.

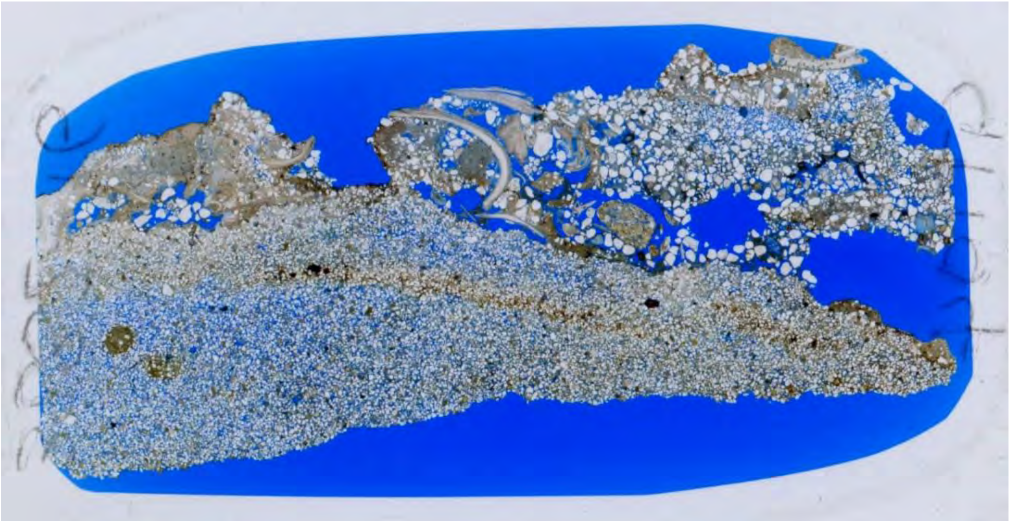

Plate 8. Scanned image of polished thin section prepared from sample GT104. There are two layers: at the base of the image is a reasonably well-sorted, fine to medium-grained sandstone; above this is a coarser, poorly sorted shelly sandstone containing abundant bioclastic debris including bivalve shells. Field of view = 48 mm wide.

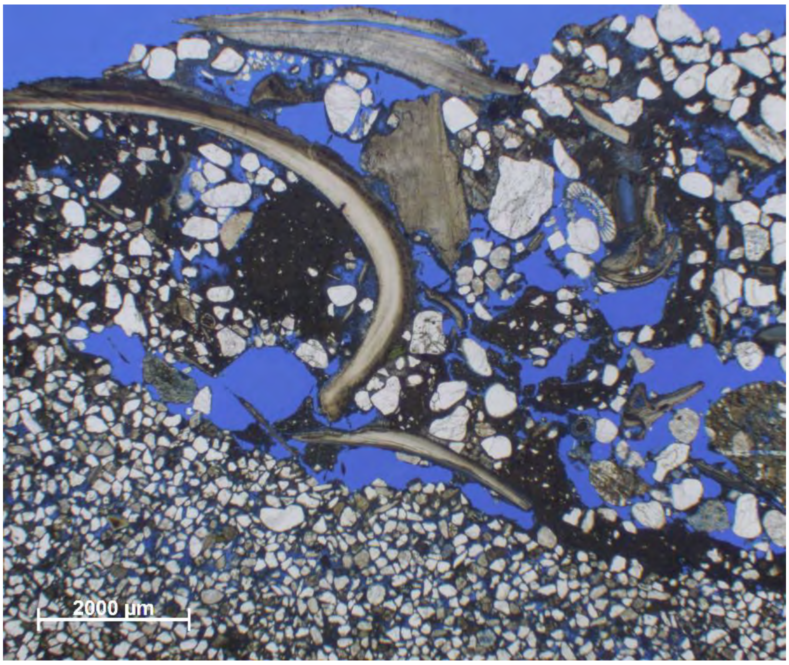

Plate 9. Transmitted light image (plain polarised light) showing the contrast between the lower, more uniform fine sandstone layer and the upper, coarse shelly sandstone layer in sample GT104.

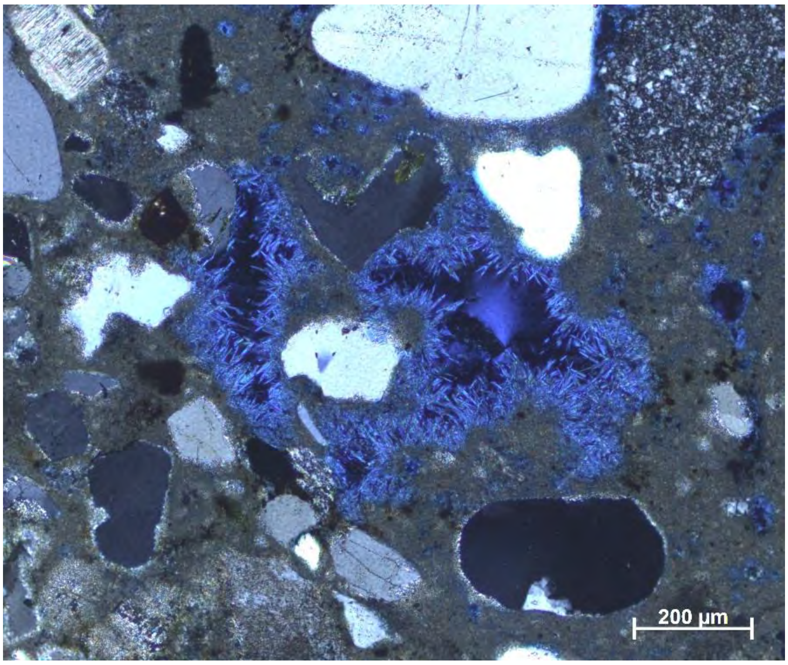

Plate 10. Transmitted light image (cross polarised light) showing the micritic high magnesian-calcite cement and the later, pore-filling and pore-lining fibrous acicular aragonite cement which lines the walls of open intergranular pores GT104.

The more porous areas of the sandstone (indicated by the areas impregnated by blue epoxy-resin in thin section (Plate 8)) are dominated by fibrous aragonite. The more tightly-cemented laminae (Plate 8) are predominantly cemented by micritic high magnesian-calcite. Bulk XRD analysis indicates that aragonite is the dominant carbonate mineral in this sample, forming 35.1 wt. % of the rock (see Volume 1, Table 2). However, given the abundance of shelly detritus, some of the aragonite determined by XRD may also be contributed by the molluscan shell fragments as well as being present as pore-filing aragonite cement.

Within some areas of micrite, spherical voids, or clusters of spherical voids, are present, trapped along the interface between the later aragonite cement and the earlier micrite, or detrital grain or shell surfaces (Plate 11). These cavities do not appear to result from mineral dissolution. Instead, they appear to form a discrete layer on the surface of the mollusc shell. Possibly, these might represent a former layer of microbial biofilm that might have been a site for the nucleation of the carbonate precipitation.

High resolution BSEM shows that boring by marine organisms is extensive in this sample, affecting both the bioclastic debris and penetrating into the pore-filling micritic calcite and aragonite cements (Plate 12).

There is a thin (<50 µm) coating of a colloform, iron and manganese oxyhydroxide crust on the outer edges of the sample (Plate 13). These crusts are discussed in more detail in Section 2.16.

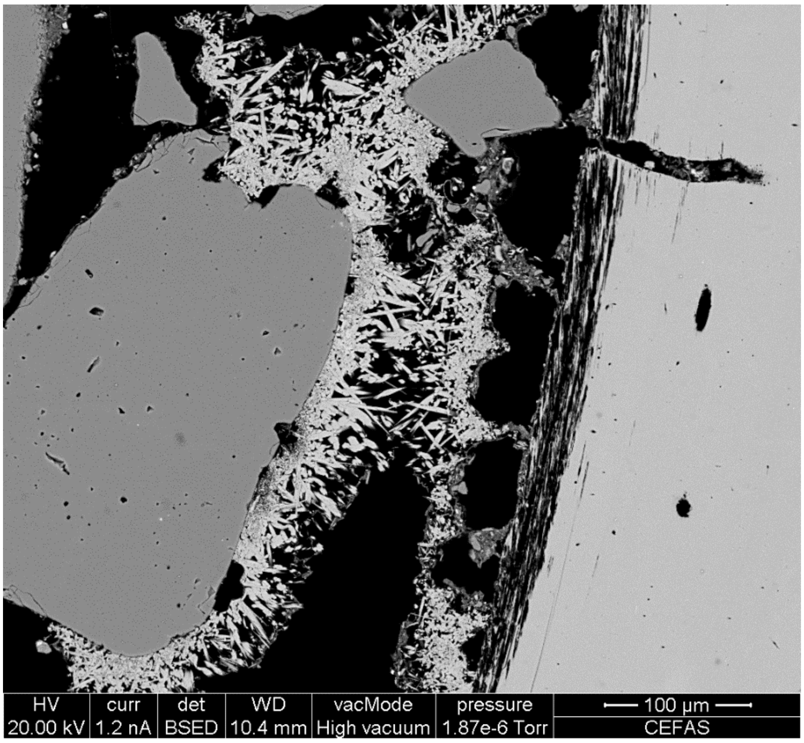

Plate 11. BSEM image showing evidence of a boring (seen as dark channel) penetrating the surface of a mollusc shell (right hand side of image). Acicular aragonite cement (light grey) coats the surfaces of detrital quartz grains, and can also be seen enclosing a series of voids (dark) along the surface of the mollusc shell. GT104.

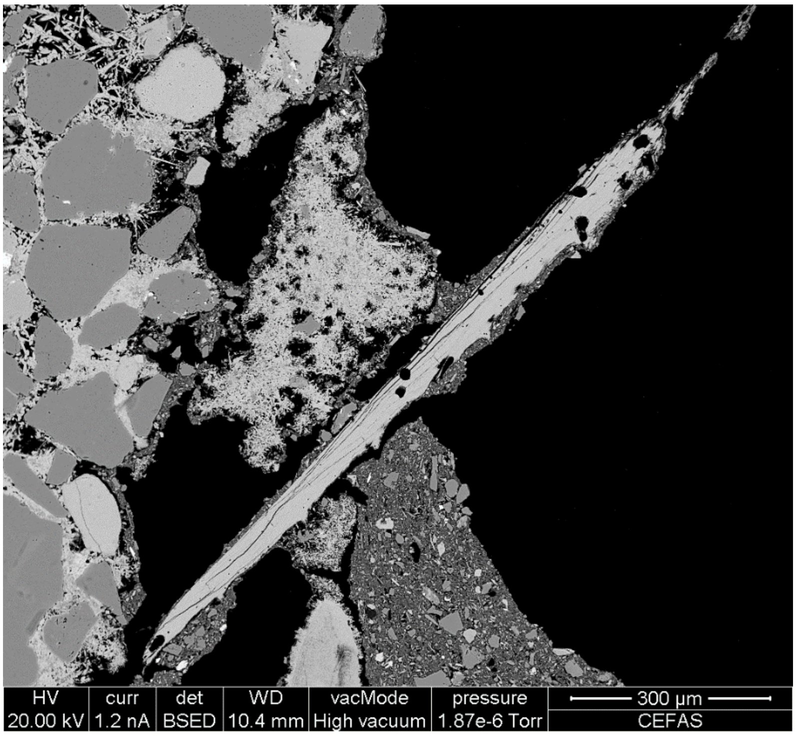

Plate 12. BSEM image showing extensive boring by marine micro-organisms. Both bioclastic debris and the aragonite cement has been exploited by borings. GT104

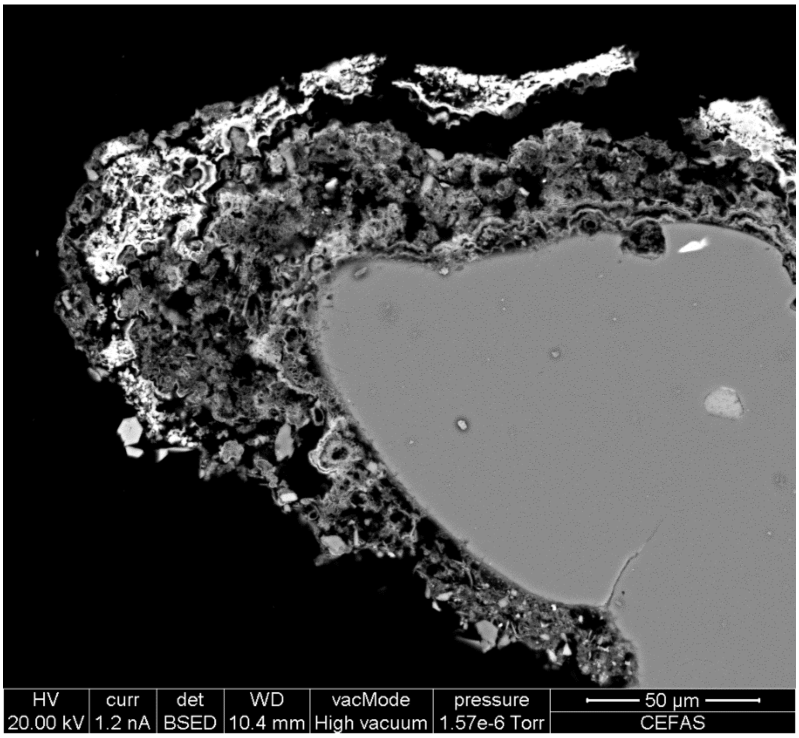

Plate 13. BSEM image of the thin iron and manganese oxyhydroxide-rich colloform crust on the outer edge of the sample. GT104

ED-EPMA major element compositional data for the cements and some example shell fragments in sample GT104 are given in Table 2. Their compositional variation, expressed in terms of molar proportions of CaO_3-$MgCO_3$ and $SrCO_3$, is summarised in Figure 2. The micritic high magnesian-calcite cements have a range in composition between 10 and 48 mole % $MgCO_3$ in solid solution (i.e. the structural formula of the calcite can be represented as $Ca_{0.52-0.90}Mg_{0.48-0.10}CO_3$). This is less magnesian than many of the other samples from the Croker Carbonate Slabs analysed in this study.

The acicular aragonite is mildly strontium bearing, with up to 2 mole % $SrCO_3$ in solid-solution (i.e. the structural formula (i.e. the structural formula of the aragonite can be represented as $Ca_{0.98-1.00}Sr_{0.02-0.00}CO_3$).

The sequence of sedimentary and post-depositional diagenetic events recorded from sample GT104 can be summarised as follows:

1. Deposition of initial, fine-grained sand.
2. Syndepositional bioturbation.
3. Precipitation of micritic high magnesian-calcite under shallow burial depth, causing lithification.
4. Accumulation of coarser, poorly-sorted shelly sand and silt.
5. Precipitation of late pore-filling and pore-lining acicular aragonite cement causing further lithification.
6. Oxidative alteration of the sediment, and formation of a thin, colloform iron and manganese oxyhydroxide-rich crusts.
7. Later boring of the lithified sandstone by marine micro-organisms and encrustation by bryozoan and calcareous serpulid worm casings.

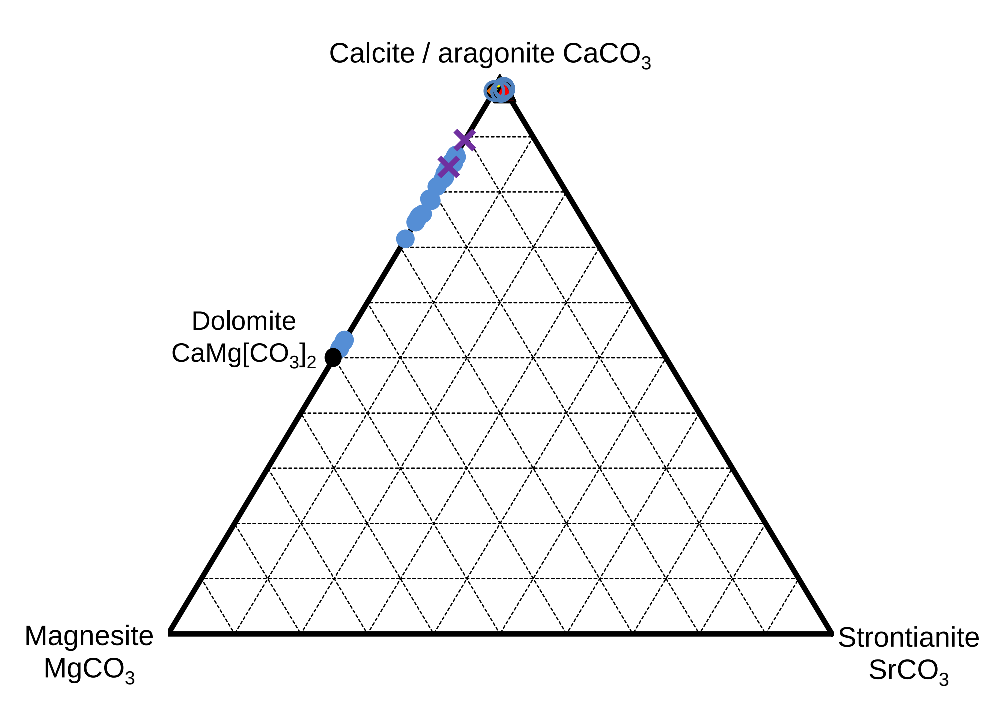

Figure 2. $CaCO_3$-$MgCO_3$-$SrCO_3$ molar ratio plot illustrating the compositions of the aragonite (red triangles), the micritic high magnesian-calcite (solid blue circles) microsparite (open blue circles) cements, micritic cement cores within shell cavities (purple crosses), and calcareous shell fragments (yellow triangles) from sample GT104.

Table 2. Electron microprobe analyses of cements and bioclastic debris from sample GT104.

		Weight % oxide (normalised)							Ionic ratio [normalised to 3 [O]]						COMMENTS
SAMPLE	No	MgO	CaO	MnO	FeO	SrO	CO_2 (calc)	*Total wt.%	Mg^{2+}	Ca^{2+}	Mn^{2+}	Fe^{2+}	Sr^{2+}	CO_3^{2-}	
GT104	1	0.00	54.87	0.00	0.00	1.47	43.67	100	0.00	0.99	0.00	0.00	0.01	1.00	aragonite
GT104	2	0.00	54.78	0.00	0.00	1.57	43.65	100	0.00	0.98	0.00	0.00	0.02	1.00	aragonite
GT104	3	0.00	54.90	0.00	0.00	1.42	43.68	100	0.00	0.99	0.00	0.00	0.01	1.00	aragonite
GT104	4	0.00	54.82	0.00	0.00	1.52	43.66	100	0.00	0.99	0.00	0.00	0.01	1.00	aragonite
GT104	5	0.00	54.70	0.00	0.20	1.45	43.65	100	0.00	0.98	0.00	0.00	0.01	1.00	aragonite
GT104	6	0.20	54.34	0.00	0.21	1.60	43.66	100	0.00	0.98	0.00	0.00	0.02	1.00	aragonite
GT104	7	0.00	53.80	0.00	1.33	1.30	43.58	100	0.00	0.97	0.00	0.02	0.01	1.00	aragonite
GT104	8	0.00	54.92	0.00	0.00	1.40	43.68	100	0.00	0.99	0.00	0.00	0.01	1.00	aragonite
GT104	9	0.00	54.91	0.00	0.00	1.40	43.68	100	0.00	0.99	0.00	0.00	0.01	1.00	aragonite
GT104	10	0.00	54.75	0.00	0.00	1.61	43.64	100	0.00	0.98	0.00	0.00	0.02	1.00	aragonite
GT104	11	0.00	54.69	0.00	0.00	1.69	43.62	100	0.00	0.98	0.00	0.00	0.02	1.00	aragonite
GT104	12	4.27	50.29	0.00	0.82	0.00	44.62	100	0.10	0.88	0.00	0.01	0.00	1.00	micritic core
GT104	13	6.26	47.77	0.39	0.64	0.00	44.94	100	0.15	0.83	0.01	0.01	0.00	1.00	micritic core
GT104	14	0.22	55.78	0.00	0.00	0.00	44.00	100	0.01	0.99	0.00	0.00	0.00	1.00	shell
GT104	15	0.16	55.84	0.00	0.00	0.00	43.99	100	0.00	1.00	0.00	0.00	0.00	1.00	shell
GT104	16	0.00	56.04	0.00	0.00	0.00	43.96	100	0.00	1.00	0.00	0.00	0.00	1.00	shell
GT104	17	0.00	54.68	0.16	0.00	1.52	43.64	100	0.00	0.98	0.00	0.00	0.01	1.00	acicular aragonite cement
GT104	18	0.00	54.57	0.00	0.17	1.64	43.62	100	0.00	0.98	0.00	0.00	0.02	1.00	acicular aragonite cement
GT104	19	0.00	54.74	0.00	0.00	1.62	43.64	100	0.00	0.98	0.00	0.00	0.02	1.00	acicular aragonite cement
GT104	20	0.00	54.88	0.00	0.00	1.44	43.67	100	0.00	0.99	0.00	0.00	0.01	1.00	acicular aragonite cement
GT104	21	0.00	54.64	0.00	0.33	1.37	43.66	100	0.00	0.98	0.00	0.00	0.01	1.00	acicular aragonite cement
GT104	22	0.00	54.77	0.00	0.19	1.36	43.67	100	0.00	0.98	0.00	0.00	0.01	1.00	acicular aragonite cement
GT104	23	0.00	54.50	0.00	0.00	1.93	43.58	100	0.00	0.98	0.00	0.00	0.02	1.00	acicular aragonite cement
GT104	24	0.00	54.97	0.00	0.00	1.34	43.70	100	0.00	0.99	0.00	0.00	0.01	1.00	acicular aragonite cement
GT104	25	0.00	54.75	0.00	0.00	1.61	43.64	100	0.00	0.98	0.00	0.00	0.02	1.00	acicular aragonite cement
GT104	26	0.00	54.94	0.00	0.00	1.37	43.69	100	0.00	0.99	0.00	0.00	0.01	1.00	acicular aragonite cement
GT104	27	0.00	54.96	0.00	0.00	1.35	43.69	100	0.00	0.99	0.00	0.00	0.01	1.00	acicular aragonite cement
GT104	28	5.92	48.55	0.37	0.24	0.00	44.93	100	0.14	0.85	0.01	0.00	0.00	1.00	micritic rim around shell cavities
GT104	29	5.41	48.84	0.35	0.35	0.28	44.77	100	0.13	0.86	0.00	0.00	0.00	1.00	micritic rim around shell cavities
GT104	30	11.35	39.73	0.26	3.05	0.00	45.60	100	0.27	0.68	0.00	0.04	0.00	1.00	micritic rim around shell cavities
GT104	31	7.83	46.37	0.28	0.27	0.00	45.26	100	0.19	0.80	0.00	0.00	0.00	1.00	micritic rim around shell cavities
GT104	32	5.54	49.10	0.25	0.24	0.00	44.87	100	0.13	0.86	0.00	0.00	0.00	1.00	micritic rim around shell cavities

		Weight % oxide (normalised)							Ionic ratio [normalised to 3 [O]						COMMENTS
SAMPLE	No	MgO	CaO	MnO	FeO	SrO	CO_2 (calc)	*Total wt.%	Mg^{2+}	Ca^{2+}	Mn^{2+}	Fe^{2+}	Sr^{2+}	CO_3^{2-}	
GT104	33	9.44	40.98	0.00	4.41	0.00	45.16	100	0.23	0.71	0.00	0.06	0.00	1.00	micritic rim around shell cavities
GT104	34	5.77	47.69	0.22	1.14	0.44	44.74	100	0.14	0.84	0.00	0.02	0.00	1.00	micritic rim around shell cavities
GT104	35	8.29	42.78	0.19	3.34	0.43	44.96	100	0.20	0.75	0.00	0.05	0.00	1.00	micritic rim around shell cavities
GT104	36	9.91	40.41	0.29	4.14	0.00	45.24	100	0.24	0.70	0.00	0.06	0.00	1.00	micritic rim around shell cavities
GT104	37	7.02	47.54	0.00	0.00	0.34	45.10	100	0.17	0.83	0.00	0.00	0.00	1.00	micritic rim around shell cavities
GT104	38	5.41	49.13	0.38	0.25	0.00	44.84	100	0.13	0.86	0.01	0.00	0.00	1.00	micritic rim around shell cavities
GT104	39	6.84	47.72	0.33	0.00	0.00	45.11	100	0.17	0.83	0.00	0.00	0.00	1.00	micritic rim around shell cavities
GT104	40	7.18	47.19	0.24	0.00	0.26	45.12	100	0.17	0.82	0.00	0.00	0.00	1.00	micritic rim around shell cavities
GT104	41	6.49	47.99	0.21	0.27	0.00	45.04	100	0.16	0.84	0.00	0.00	0.00	1.00	micritic rim around shell cavities
GT104	42	9.83	44.01	0.26	0.00	0.33	45.56	100	0.24	0.76	0.00	0.00	0.00	1.00	micritic rim around shell cavities
GT104	43	7.73	46.22	0.25	0.59	0.00	45.21	100	0.19	0.80	0.00	0.01	0.00	1.00	micritic rim around shell cavities
GT104	44	10.24	43.58	0.31	0.20	0.00	45.68	100	0.24	0.75	0.00	0.00	0.00	1.00	micritic rim around shell cavities
GT104	45	8.80	45.47	0.28	0.00	0.00	45.45	100	0.21	0.78	0.00	0.00	0.00	1.00	micritic rim around shell cavities
GT104	46	20.72	31.03	0.29	0.51	0.00	47.45	100	0.48	0.51	0.00	0.01	0.00	1.00	micritic rim around shell cavities
GT104	47	20.91	31.09	0.28	0.21	0.00	47.52	100	0.48	0.51	0.00	0.00	0.00	1.00	micritic rim around shell cavities
GT104	48	20.34	31.76	0.29	0.20	0.00	47.42	100	0.47	0.53	0.00	0.00	0.00	1.00	micritic rim around shell cavities
GT104	49	20.01	31.67	0.54	0.47	0.00	47.31	100	0.46	0.53	0.01	0.01	0.00	1.00	micritic rim around shell cavities
GT104	50	0.66	54.81	0.00	0.50	0.00	44.03	100	0.02	0.98	0.00	0.01	0.00	1.00	microsparite
GT104	51	0.00	55.06	0.00	0.00	1.23	43.72	100	0.00	0.99	0.00	0.00	0.01	1.00	microsparite
GT104	52	0.00	55.09	0.00	0.00	1.18	43.73	100	0.00	0.99	0.00	0.00	0.01	1.00	microsparite
GT104	53	0.00	54.96	0.00	0.00	1.34	43.69	100	0.00	0.99	0.00	0.00	0.01	1.00	microsparite
GT104	54	0.00	55.02	0.00	0.00	1.28	43.71	100	0.00	0.99	0.00	0.00	0.01	1.00	microsparite
GT104	55	0.00	54.92	0.00	0.00	1.39	43.68	100	0.00	0.99	0.00	0.00	0.01	1.00	microsparite
GT104	56	0.00	55.09	0.00	0.00	1.18	43.73	100	0.00	0.99	0.00	0.00	0.01	1.00	microsparite
GT104	57	0.00	55.03	0.00	0.00	1.26	43.71	100	0.00	0.99	0.00	0.00	0.01	1.00	microsparite
GT104	58	0.00	54.98	0.00	0.00	1.32	43.70	100	0.00	0.99	0.00	0.00	0.01	1.00	microsparite
GT104	59	0.00	54.97	0.00	0.00	1.33	43.70	100	0.00	0.99	0.00	0.00	0.01	1.00	microsparite
GT104	60	0.00	55.14	0.00	0.00	1.12	43.74	100	0.00	0.99	0.00	0.00	0.01	1.00	microsparite
GT104	61	0.30	54.49	0.00	0.34	1.10	43.76	100	0.01	0.98	0.00	0.00	0.01	1.00	microsparite

**Note: Some analytical totals were low (<90%) because of the microporous nature of the cements. Therefore, all data were normalised to 100%*

2.3 SAMPLE GT106

This sample comprises one large angular roughly-tabular clast (<130 mm), and two smaller fragments of carbonate-cemented sandstone (Plate 14). The smaller clasts are pale grey in colour, whereas the larger clast has a dense orange-brown-black coating due to heavy staining and impregnation by iron oxyhydroxide. A white calcareous coating is also present on some parts of the surface (Plate 15). The sample has been bioturbated and is significantly bored by marine micro-organisms.

Plate 14. Photograph of sample GT106 showing orange-brown and black staining by iron oxyhydroxide. White calcareous encrustations are also present. Grey scale bar divisions = 10 mm.

The polished thin section prepared from sample GT106 is shown in Plate 16. The sample comprises two lithotypes:

- The main bulk of the clast comprises a reasonably well-sorted, close-packed carbonate-cemented sandstone, and;
- A highly porous and vuggy or vesicular calcareous crust overlying the sandstone

The sandstone is medium-grained (<300 µm) and dominated by detrital quartz. The detrital grains are, angular to sub-rounded, and matrix supported. The thin section clearly displays patchy orange-brown staining from finely disseminated iron-oxyhydroxide within the cements and around grain surfaces. This staining is developed in the sandstone immediately beneath the calcareous crust layer, penetrating the matrix to a depth of 3 mm (Plate 16). Iron oxyhydroxide staining also permeates deeper in the sandstone forming irregular patches that appear to delineate diffuse 'burrows-like' feature. This suggests that burrows provide more permeable pathways for porewater movement and diffusion of oxygen through the sediment.

XRD analysis (Volume 1: Table 2) shows that aragonite is the dominant cement, forming 59.5 wt. % of the sandstone, with only very minor high magnesian calcite (0.5 wt. %). Cementation in the sandstone is patchy; with areas that are well-cemented with little intergranular porosity and areas which are highly porous and only weakly cemented (Plate 16). High resolution BSEM shows that the more porous areas are dominated by sand containing an intergranular micritic matrix composed of very high magnesian-calcite cement. The micrite typically occurs in globular aggregates (Plate 17 and is microporous. It contains numerous fine (<5 µm) spheroids of iron oxide, which are probably pseudomorphs after pyrite. Some acicular aragonite is present in the intergranular pore spaces, and this has nucleated on the micrite. The well cemented areas are aragonite-dominated. These also contain early globular high magnesian-calcite micrite, but the remaining intergranular pore space is almost entirely filled by the acicular aragonite (Plate 17).

Plate 15. Optical micrograph of sample GT106 showing a portion of the vuggy or vesicular aragonite-rich calcareous crust that has formed on the surface of the sample.

The calcareous crust has a variable texture. Some parts are very densely cemented by fibrous aragonite (Plate 15 and Plate 18), other areas are more friable and porous with large vuggy or vesicular cavities (Plate 16 and Plate 17). Detailed observation shows that the more massive aragonite cement contains relict inclusions of globular or micro-nodular aggregates of micritic high magnesian calcite (Plate 19). The aragonite cement high magnesian calcite micrite aggregates are overprinted and partially replaced by the aragonite. The denser areas comprise numerous sprays, or fans, of acicular needles up to 1500 µm in length (Plate 15). Parts of the denser crust displayed a very faint mottling but no chemical difference were detected by ED-EPMA analyses (cf. Table 3: dark and light aragonite).

More porous aragonitic cemented areas sometimes preserve a fabric comprising of small (1-2 µm diameter), spherical to ovoid cavities enclosed within the intergrown aragonite-magnesian calcite cement (Plate 19). These features are similar in size to bacterial cells (e.g. Konhauser, 2007) and very closely resemble fossilised and mineralised bacterial cells described from experimental studies and other environments in the literature (c.f. Martill and Wilby, 1994; Wilby and Whyte, 1995). Consequently, they may possibly represent preserved bacterial cells around which the aragonite and magnesian calcite cements have nucleated. Similar features were also observed in sample GT112: (see Volume 1: Section 4.7). Plate 20 illustrates a portion of the calcareous crust which displays the abundant development of enigmatic microscopic channels and tube-like features. The origin of these features is unclear. Some of these microscopic structures may represent borings by microorganisms and can be seen cutting across the interfaces between carbonate cement and bioclasts. However, many of these features comprise ‘strings’ or ‘chains’ of cavities (Plate 20), separated by discrete nodes. Their size and shape closely resembles that of chains of bacilli-shaped bacterial cells (Konhauser, 1970), some of which appear to have been preserved in the process of mitosis (i.e. cell-division).

The sample has been heavily bioturbated. Sediment-filled burrows are evident giving the rock a characteristic ‘mottled’ appearance. These appear to pre-date lithification of the sandstone and may have influenced subsequent cement distribution. In addition, there is evidence for the activity of boring organisms. Microscopic borings were observed to penetrate both detrital bioclasts and the aragonite cement crust, and therefore clearly post-date lithification.

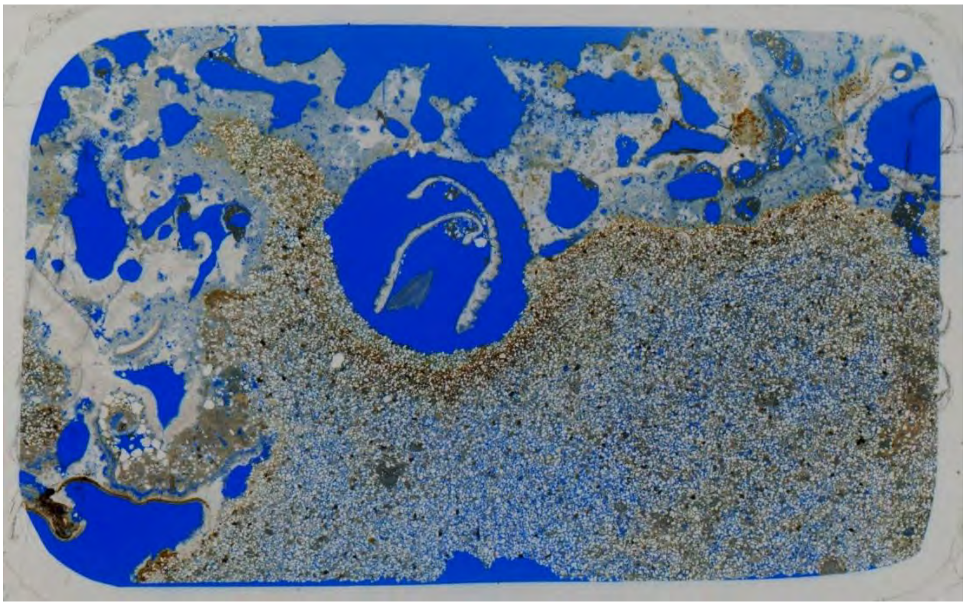

Plate 16. Scanned image of thin section prepared from sample GT106. This shows relatively uniform carbonate-cemented sandstone with intergranular porosity, overlain by a vuggy or vesicular carbonate crust. Field of view = 48 mm wide.

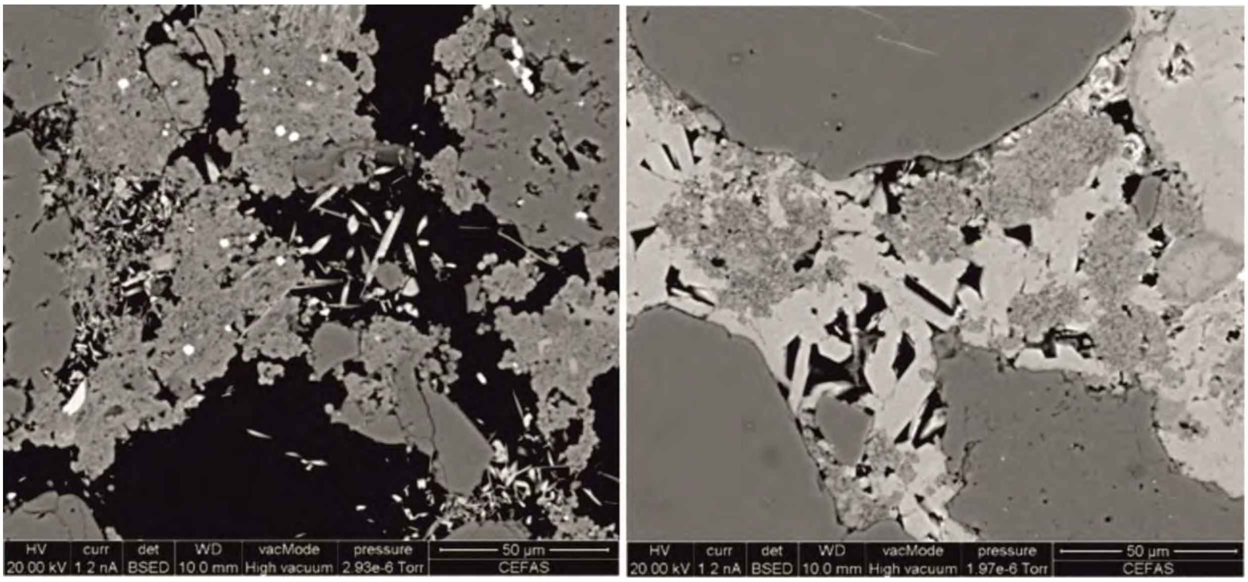

Plate 17. BSEM images from sample GT106 showing the variation in cement. Left: porous high magnesian-calcite micrite-dominated matrix (dull grey) with traces of acicular aragonite resting on the micrite aggregate surfaces within the residual porosity. Note the very fine, spherical particles of iron oxyhydroxide (white) dispersed within the micrite – these are probably pseudomorphs after framboidal pyrite. Right: low porosity, aragonite-dominated area with small clots of micritic, high magnesian-calcite enclosed within a later

dense aragonite cement. Note the traces of early micrite rim coating a detrital calcite grain in the upper right corner of the image.

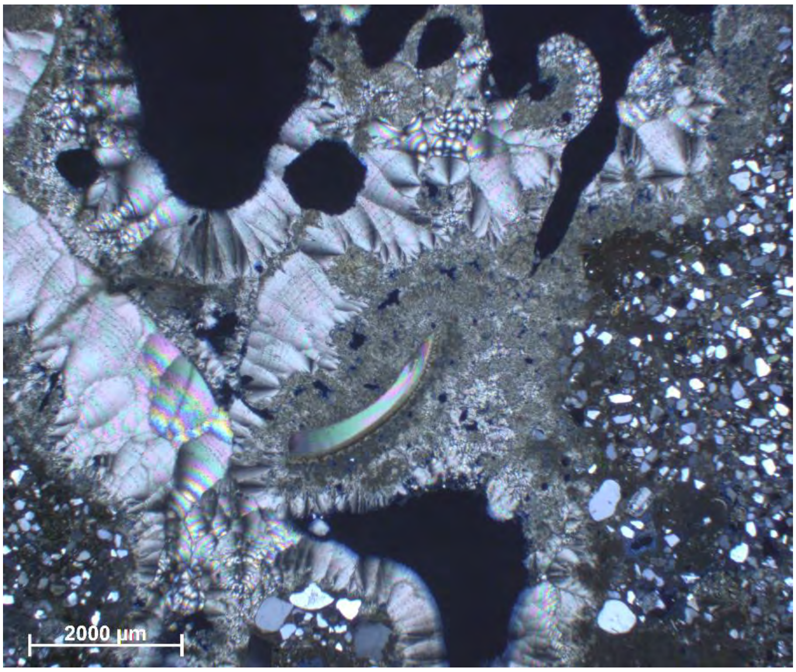

Plate 18. Transmitted light photomicrograph (cross-polarised light) showing the dense fibrous aragonite cement filling vuggy cavities in the calcareous crust. Sample GT106.

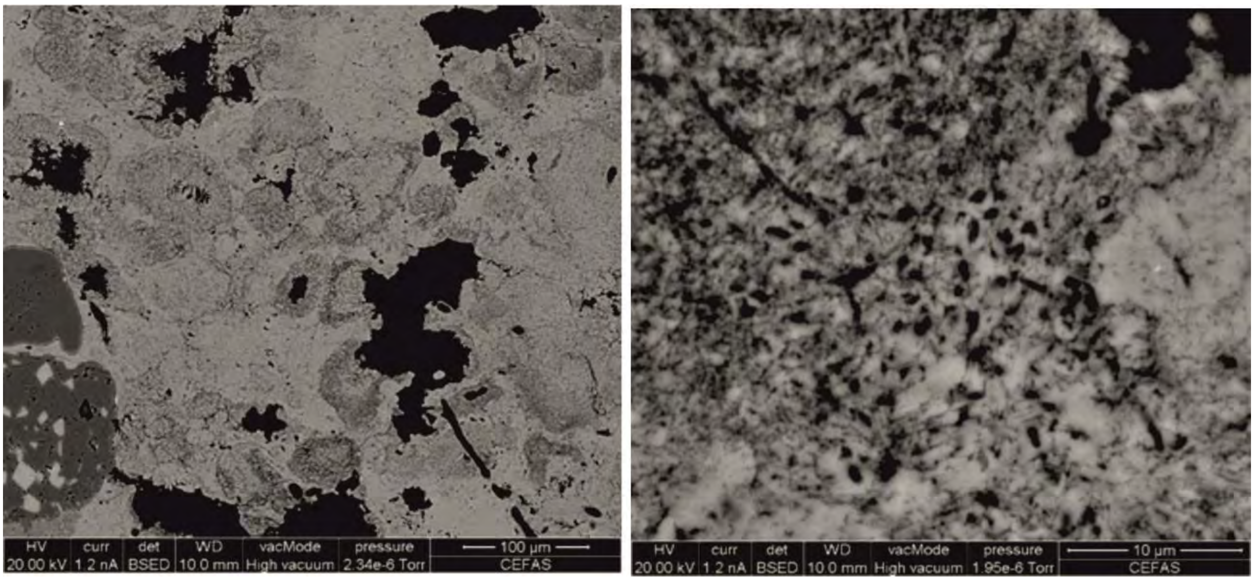

Plate 19. BSEM images of the calcareous crust. Left: porous vuggy calcareous crust, showing globular or nodular aggregates of micritic high magnesian calcite (dull grey) enclosed within and partially replaced and overprinted by later massive aragonite cement (light grey). Right: detail of one of the more porous patches of aragonite-high magnesian-calcite cement showing preservation of microcellular texture comprising small sub-spherical to ovoid cavities (black) encased within micritic magnesian-calcite (dull grey) that is partially-replaced by aragonite (light grey).

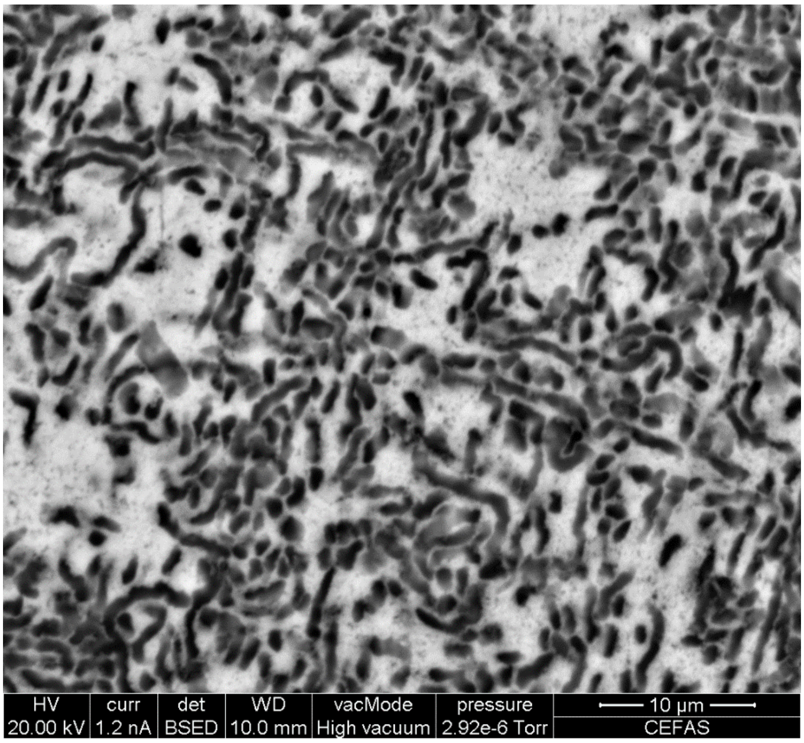

Plate 20. BSEM image showing enigmatic microorganism structures preserved within the aragonitic calcareous crust in sample GT106.

ED-EPMA major element compositional data for the cements in sample GT106 are given in Table 3. Their compositional variation, expressed in terms of molar proportions of CaO_3-$MgCO_3$ and $SrCO_3$, is summarised in Figure 3 and Figure 4. Although XRD analysis indicates that the micritic calcite is very highly magnesium-substituted (Volume 1: Table 2), ED-EPMA indicates the micritic calcite cements are to be generally less magnesian than the micrite found in many of the other samples, containing between 16 and 25 mole % $MgCO_3$ in solid solution (i.e. the structural formula of the calcite can be represented as $Ca_{0.75-0.84}Mg_{0.25-0.16}CO_3$) and similar to sample GT012. However, these data should be regarded cautiously since the micrite is closely intergrown with aragonite, and consequently the ED-EPMA may represent analyses of mixtures of high magnesian calcite and aragonite.

The acicular aragonite is strontium bearing, with up to 1 mole % $SrCO_3$ in solid-solution (i.e. the structural formula (i.e. the structural formula of the aragonite can be represented as $Ca_{0.99-1.00}Sr_{0.01-0.00}CO_3$). This is similar to the aragonite observed in other samples.

The sequence of sedimentary and post-depositional diagenetic events recorded from sample GT106 can be summarised as follows:

1. Deposition of initial, medium-grained sandy sediment.
2. Syndepositional bioturbation of the unlithified sediment by burrowing organisms.
3. Precipitation of micritic high-magnesian calcite causing lithification.
4. Precipitation of framboidal pyrite within the micrite, indicating reducing early diagenetic porewater conditions during magnesian calcite precipitation.
5. Precipitation of late acicular aragonite cement causing further lithification and development of a thick calcareous crust, probably associated with microbial activity.
6. Oxidation of pyrite to iron oxyhydroxide.
7. Extensive post-lithification boring by marine micro-organisms.

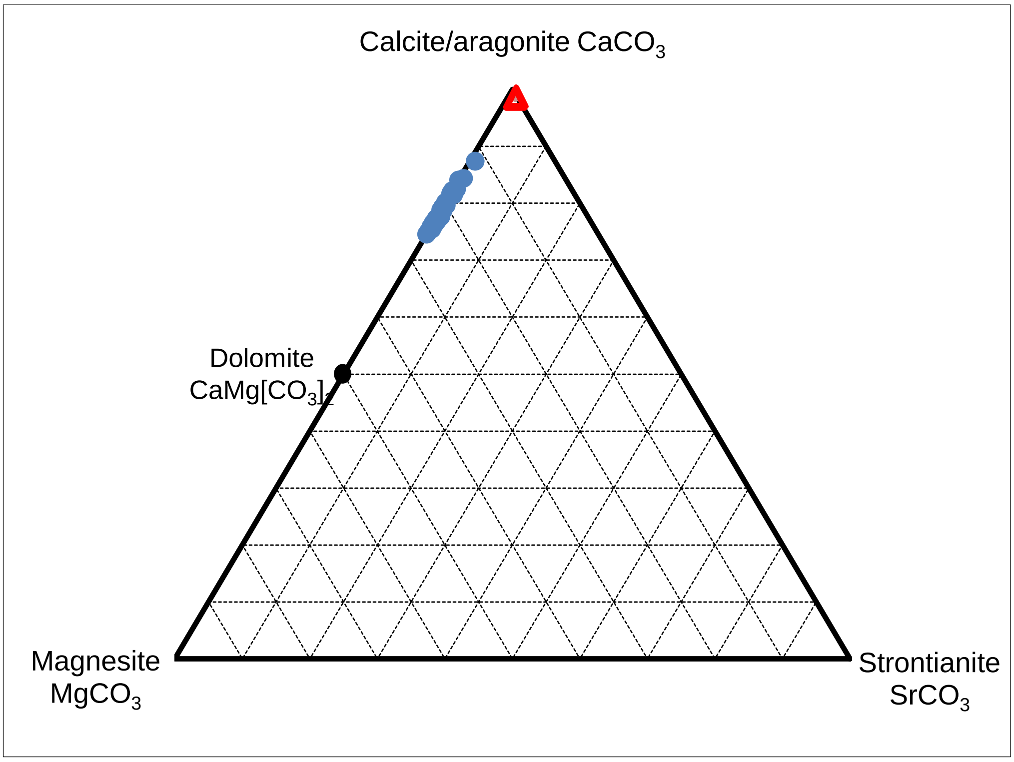

Figure 3. $CaCO_3$-$MgCO_3$-$SrCO_3$ molar ratio plot illustrating the high-magnesian micritic cement (solid blue circles) and the microcellular micrite within the calcareous crust from sample GT106.

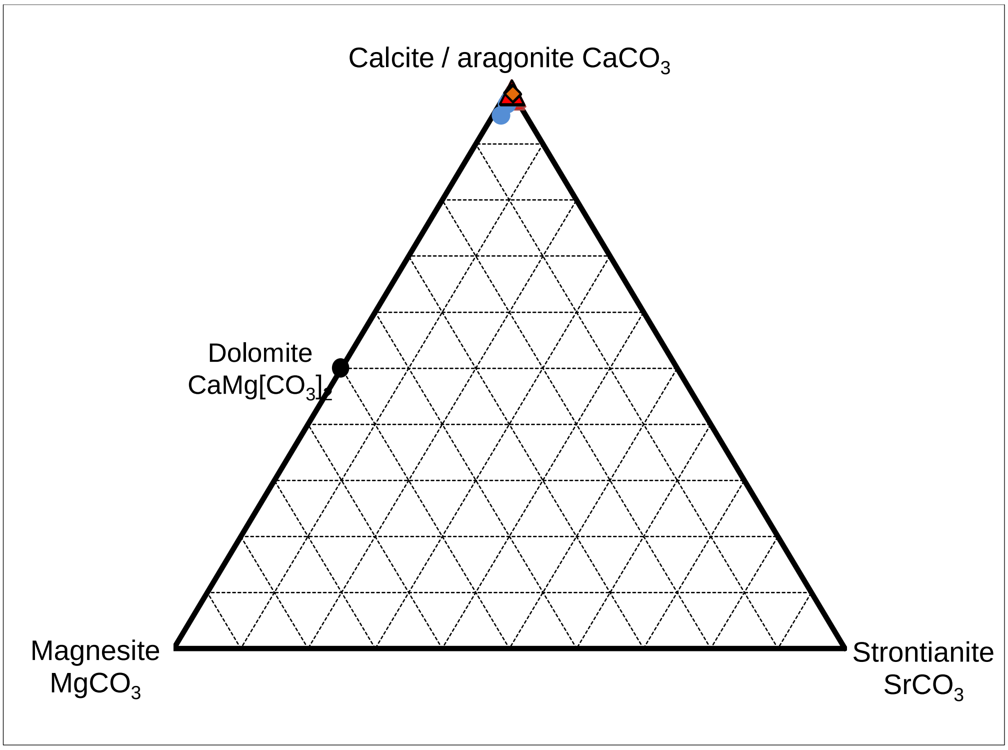

Figure 4. $CaCO_3$-$MgCO_3$-$SrCO_3$ molar ratio plot illustrating the calcite and aragonite analyses from sample GT106. Acicular aragonite cement (red triangles), light micrite (blue circles), light aragonite (open red triangles) and dark aragonite (orange diamonds).

Table 3. Electron microprobe analysis from the carbonate cements and calcareous crust from sample GT106

		Weight % oxide (normalised)							Ionic ratio [normalised to 3 [O]						COMMENTS
SAMPLE	No	MgO	CaO	MnO	FeO	SrO	CO_2 (calc)	*Total wt.%	Mg^{2+}	Ca^{2+}	Mn^{2+}	Fe^{2+}	Sr^{2+}	CO_3^{2-}	
GT106	1	10.05	43.98	0.00	0.31	0.00	45.66	100	0.24	0.76	0.00	0.00	0.00	1.00	micrite
GT106	2	9.77	44.35	0.00	0.27	0.00	45.62	100	0.23	0.76	0.00	0.00	0.00	1.00	micrite
GT106	3	7.48	46.84	0.00	0.48	0.00	45.21	100	0.18	0.81	0.00	0.01	0.00	1.00	micrite
GT106	4	8.24	46.38	0.00	0.00	0.00	45.38	100	0.20	0.80	0.00	0.00	0.00	1.00	micrite
GT106	5	9.40	44.81	0.00	0.23	0.00	45.56	100	0.23	0.77	0.00	0.00	0.00	1.00	micrite
GT106	6	6.53	48.02	0.00	0.40	0.00	45.05	100	0.16	0.84	0.00	0.01	0.00	1.00	micrite
GT106	7	8.74	45.79	0.00	0.00	0.00	45.47	100	0.21	0.79	0.00	0.00	0.00	1.00	micrite
GT106	8	10.46	42.68	0.57	0.64	0.00	45.65	100	0.25	0.73	0.01	0.01	0.00	1.00	micrite
GT106	9	8.58	45.68	0.00	0.33	0.00	45.41	100	0.21	0.79	0.00	0.00	0.00	1.00	micrite
GT106	10	8.45	45.85	0.00	0.32	0.00	45.39	100	0.20	0.79	0.00	0.00	0.00	1.00	micrite
GT106	11	8.79	45.53	0.22	0.00	0.00	45.46	100	0.21	0.79	0.00	0.00	0.00	1.00	micrite
GT106	12	7.29	46.99	0.34	0.22	0.00	45.17	100	0.18	0.82	0.00	0.00	0.00	1.00	micrite
GT106	13	8.56	45.81	0.00	0.21	0.00	45.42	100	0.21	0.79	0.00	0.00	0.00	1.00	micrite
GT106	14	8.22	45.81	0.30	0.00	0.40	45.27	100	0.20	0.79	0.00	0.00	0.00	1.00	micrite
GT106	15	10.50	43.15	0.20	0.44	0.00	45.71	100	0.25	0.74	0.00	0.01	0.00	1.00	micrite
GT106	16	10.20	42.65	0.58	1.00	0.00	45.57	100	0.24	0.73	0.01	0.01	0.00	1.00	micrite
GT106	17	7.28	45.26	1.53	0.95	0.00	44.98	100	0.18	0.79	0.02	0.01	0.00	1.00	micrite
GT106	18	0.00	55.14	0.00	0.00	1.13	43.74	100	0.00	0.99	0.00	0.00	0.01	1.00	acicular aragonite
GT106	19	0.15	54.74	0.00	0.00	1.40	43.71	100	0.00	0.98	0.00	0.00	0.01	1.00	acicular aragonite
GT106	20	0.00	55.22	0.00	0.00	1.02	43.76	100	0.00	0.99	0.00	0.00	0.01	1.00	acicular aragonite
GT106	21	0.00	55.09	0.00	0.00	1.18	43.73	100	0.00	0.99	0.00	0.00	0.01	1.00	acicular aragonite
GT106	22	0.00	55.44	0.00	0.00	0.74	43.82	100	0.00	0.99	0.00	0.00	0.01	1.00	acicular aragonite
GT106	23	0.00	55.16	0.00	0.00	1.09	43.74	100	0.00	0.99	0.00	0.00	0.01	1.00	acicular aragonite
GT106	24	0.00	55.09	0.00	0.00	1.18	43.73	100	0.00	0.99	0.00	0.00	0.01	1.00	acicular aragonite
GT106	25	0.00	55.10	0.00	0.00	1.17	43.73	100	0.00	0.99	0.00	0.00	0.01	1.00	acicular aragonite
GT106	26	0.00	55.02	0.00	0.00	1.27	43.71	100	0.00	0.99	0.00	0.00	0.01	1.00	acicular aragonite
GT106	27	0.00	55.01	0.00	0.00	1.28	43.71	100	0.00	0.99	0.00	0.00	0.01	1.00	acicular aragonite
GT106	28	0.00	55.41	0.00	0.00	0.78	43.81	100	0.00	0.99	0.00	0.00	0.01	1.00	acicular aragonite
GT106	29	0.00	55.29	0.00	0.00	0.93	43.78	100	0.00	0.99	0.00	0.00	0.01	1.00	light aragonite
GT106	30	0.00	55.34	0.00	0.00	0.87	43.79	100	0.00	0.99	0.00	0.00	0.01	1.00	light aragonite
GT106	31	0.00	55.30	0.00	0.00	0.92	43.78	100	0.00	0.99	0.00	0.00	0.01	1.00	light aragonite
GT106	32	0.00	55.27	0.00	0.00	0.95	43.77	100	0.00	0.99	0.00	0.00	0.01	1.00	light aragonite

		Weight % oxide (normalised)							Ionic ratio [normalised to 3 [O]						COMMENTS
SAMPLE	No	MgO	CaO	MnO	FeO	SrO	CO_2 (calc)	*Total wt.%	Mg^{2+}	Ca^{2+}	Mn^{2+}	Fe^{2+}	Sr^{2+}	CO_3^{2-}	
GT106	33	0.00	55.37	0.00	0.00	0.83	43.80	100	0.00	0.99	0.00	0.00	0.01	1.00	light aragonite
GT106	34	0.00	55.40	0.00	0.00	0.80	43.80	100	0.00	0.99	0.00	0.00	0.01	1.00	light aragonite
GT106	35	0.00	55.40	0.00	0.00	0.79	43.80	100	0.00	0.99	0.00	0.00	0.01	1.00	light aragonite
GT106	36	0.00	55.32	0.00	0.00	0.89	43.79	100	0.00	0.99	0.00	0.00	0.01	1.00	light aragonite
GT106	37	0.00	55.38	0.00	0.00	0.81	43.80	100	0.00	0.99	0.00	0.00	0.01	1.00	light aragonite
GT106	38	0.00	55.22	0.00	0.00	1.03	43.76	100	0.00	0.99	0.00	0.00	0.01	1.00	light aragonite
GT106	39	0.00	55.38	0.00	0.00	0.82	43.80	100	0.00	0.99	0.00	0.00	0.01	1.00	light aragonite
GT106	40	0.00	55.18	0.00	0.00	1.08	43.75	100	0.00	0.99	0.00	0.00	0.01	1.00	dark aragonite
GT106	41	0.00	55.34	0.00	0.00	0.88	43.79	100	0.00	0.99	0.00	0.00	0.01	1.00	dark aragonite
GT106	42	0.00	55.20	0.00	0.00	1.04	43.75	100	0.00	0.99	0.00	0.00	0.01	1.00	dark aragonite
GT106	43	0.00	55.09	0.00	0.00	1.19	43.72	100	0.00	0.99	0.00	0.00	0.01	1.00	dark aragonite
GT106	44	0.00	55.16	0.00	0.00	1.09	43.74	100	0.00	0.99	0.00	0.00	0.01	1.00	dark aragonite
GT106	45	0.00	55.09	0.00	0.00	1.18	43.73	100	0.00	0.99	0.00	0.00	0.01	1.00	dark aragonite
GT106	46	0.00	55.15	0.00	0.00	1.11	43.74	100	0.00	0.99	0.00	0.00	0.01	1.00	dark aragonite
GT106	47	0.00	55.15	0.00	0.00	1.10	43.74	100	0.00	0.99	0.00	0.00	0.01	1.00	dark aragonite
GT106	48	0.00	55.30	0.00	0.00	0.92	43.78	100	0.00	0.99	0.00	0.00	0.01	1.00	dark aragonite
GT106	49	0.00	55.15	0.00	0.00	1.11	43.74	100	0.00	0.99	0.00	0.00	0.01	1.00	dark aragonite
GT106	50	0.00	55.02	0.00	0.00	1.28	43.71	100	0.00	0.99	0.00	0.00	0.01	1.00	microcellular micrite
GT106	51	0.00	54.92	0.00	0.00	1.40	43.68	100	0.00	0.99	0.00	0.00	0.01	1.00	microcellular micrite
GT106	52	0.00	55.03	0.00	0.00	1.26	43.71	100	0.00	0.99	0.00	0.00	0.01	1.00	microcellular micrite
GT106	53	0.00	55.05	0.00	0.00	1.23	43.72	100	0.00	0.99	0.00	0.00	0.01	1.00	microcellular micrite
GT106	54	0.00	55.06	0.00	0.00	1.22	43.72	100	0.00	0.99	0.00	0.00	0.01	1.00	microcellular micrite
GT106	55	0.00	55.08	0.00	0.00	1.20	43.72	100	0.00	0.99	0.00	0.00	0.01	1.00	microcellular micrite
GT106	56	0.00	54.70	0.00	0.39	1.23	43.68	100	0.00	0.98	0.00	0.01	0.01	1.00	microcellular micrite
GT106	57	0.00	55.05	0.00	0.00	1.23	43.72	100	0.00	0.99	0.00	0.00	0.01	1.00	microcellular micrite
GT106	58	0.00	54.90	0.00	0.00	1.42	43.68	100	0.00	0.99	0.00	0.00	0.01	1.00	microcellular micrite
GT106	59	0.00	54.94	0.00	0.00	1.37	43.69	100	0.00	0.99	0.00	0.00	0.01	1.00	microcellular micrite
GT106	60	0.15	54.94	0.00	0.00	1.15	43.76	100	0.00	0.99	0.00	0.00	0.01	1.00	microcellular micrite
GT106	61	0.16	54.64	0.00	0.17	1.32	43.71	100	0.00	0.98	0.00	0.00	0.01	1.00	microcellular micrite
GT106	62	6.05	47.41	0.00	1.12	0.65	44.77	100	0.15	0.83	0.00	0.02	0.01	1.00	dark micrite in clot
GT106	63	7.31	46.38	0.00	0.66	0.61	45.04	100	0.18	0.81	0.00	0.01	0.01	1.00	dark micrite in clot
GT106	64	9.24	43.57	0.00	1.43	0.42	45.33	100	0.22	0.75	0.00	0.02	0.00	1.00	dark micrite in clot
GT106	65	6.56	44.33	0.25	3.76	0.50	44.61	100	0.16	0.78	0.00	0.05	0.00	1.00	dark micrite in clot
GT106	66	7.15	45.03	0.00	2.41	0.56	44.85	100	0.17	0.79	0.00	0.03	0.01	1.00	dark micrite in clot

		Weight % oxide (normalised)							Ionic ratio [normalised to 3 [O]						COMMENTS
SAMPLE	No	MgO	CaO	MnO	FeO	SrO	CO_2 (calc)	*Total wt.%	Mg^{2+}	Ca^{2+}	Mn^{2+}	Fe^{2+}	Sr^{2+}	CO_3^{2-}	
GT106	67	4.79	49.45	0.18	0.18	0.81	44.59	100	0.12	0.87	0.00	0.00	0.01	1.00	dark micrite in clot
GT106	68	8.30	41.20	0.43	4.70	0.59	44.78	100	0.20	0.72	0.01	0.06	0.01	1.00	dark micrite in clot
GT106	69	8.35	43.81	0.18	2.19	0.38	45.10	100	0.20	0.76	0.00	0.03	0.00	1.00	dark micrite in clot
GT106	70	9.59	43.39	0.00	1.24	0.35	45.42	100	0.23	0.75	0.00	0.02	0.00	1.00	dark micrite in clot
GT106	71	9.71	42.21	0.00	2.35	0.42	45.32	100	0.23	0.73	0.00	0.03	0.00	1.00	dark micrite in clot
GT106	72	4.65	47.99	0.18	1.94	0.84	44.39	100	0.11	0.85	0.00	0.03	0.01	1.00	dark micrite in clot
GT106	73	0.72	54.29	0.00	0.00	1.13	43.86	100	0.02	0.97	0.00	0.00	0.01	1.00	light micrite around clot
GT106	74	1.39	50.20	0.00	3.61	1.18	43.62	100	0.03	0.90	0.00	0.05	0.01	1.00	light micrite around clot
GT106	75	0.31	54.44	0.00	0.28	1.23	43.74	100	0.01	0.98	0.00	0.00	0.01	1.00	light micrite around clot

**Note: Some analytical totals were low (<90%) because of the microporous nature of the cements. Therefore, all data were normalised to 100%*

2.4 SAMPLE GT108

This sample comprises two large, tabular clasts (<170 mm): one is angular, the other sub-angular (Plate 21). They are a grey-buff sandstone, with some orange-brown, iron-oxyhydroxide staining evident on their surfaces. A broken edge on the smaller, angular clast, which exposes the interior of the clast shows that this staining is present in bands within the clast, probably related to the original depositional structure. The sample is a well-sorted, medium-grained sandstone. White calcareous bryozoan and serpulid worm encrustations are present on the clast surfaces (Plate 21).

Plate 21. Photograph of sample GT108. This comprises two large, flat, angular to sub-rounded buff coloured clasts. Grey scale bar divisions = 10 mm.

The thin section prepared from sample GT108 is shown in Plate 22. The sample shows a horizontal laminated fabric highlighted by iron-oxyhydroxide staining. The lamination is non-planar but 'pinches-and-swells', resembling symmetrical ripple lamination (Plate 22). Optical microscopy observations show that the iron-oxyhydroxides are both finely disseminated and present as diffuse and dendritic 'polka-dot-like' clots (Plate 23). Spheroidal pyrite grains (<10 µm) were also observed within the intergranular clays and carbonate cements indicating that porewaters in the sediment were reducing during carbonate precipitation. The pyrite is now partially oxidised to iron oxyhydroxide, which is probably the cause of the iron oxyhydroxide staining within the sandstone and on clast surface. This suggests that the sandstone was exposed to late-stage weathering and oxidation on the seabed.

The sandstone is reasonably well sorted, and has a close-packed grain framework, Detrital grains are angular to sub-angular, medium-grained (<300 µm) and dominated by quartz, with subordinate rounded, detrital glauconite ('glauconie' *sensu lato*) and rare bioclastic debris. Some secondary, oversized pore spaces have developed through the dissolution of unstable detrital framework grains (cf. Schmidt and McDonald, 1979).

BSEM shows that there is a high proportion of detrital clay-rich matrix material in the intergranular pore spaces. Micritic high magnesian-calcite is also present, and has formed microporous, globular aggregates within the matrix. The micrite aggregates preserve a possible microcellular texture

(Plate 24) (cf. similar textures in samples GT004, GT112). Some coarser euhedral rhombs of calcite are observed as overgrowths on the outer edges of the micritic clots. XRD analysis (Volume 1: Table 2) identified very high magnesian-calcite as the dominant carbonate cement in this sample, with only minor amounts of aragonite, non-magnesian calcite and dolomite. Petrographic analysis found no evidence of aragonite and non-magnesian calcite cements. Therefore, these minerals may be present as within the bioclastic components. Although dolomite was detected by XRD analysis, it could not be differentiated by BSEM-EDXA from very high magnesian-calcite (see earlier discussion in Volume 1 Section 3).

Within the cement, rounded pelloids can be discerned, which may represent faecal pellets in origin (Plate 25).

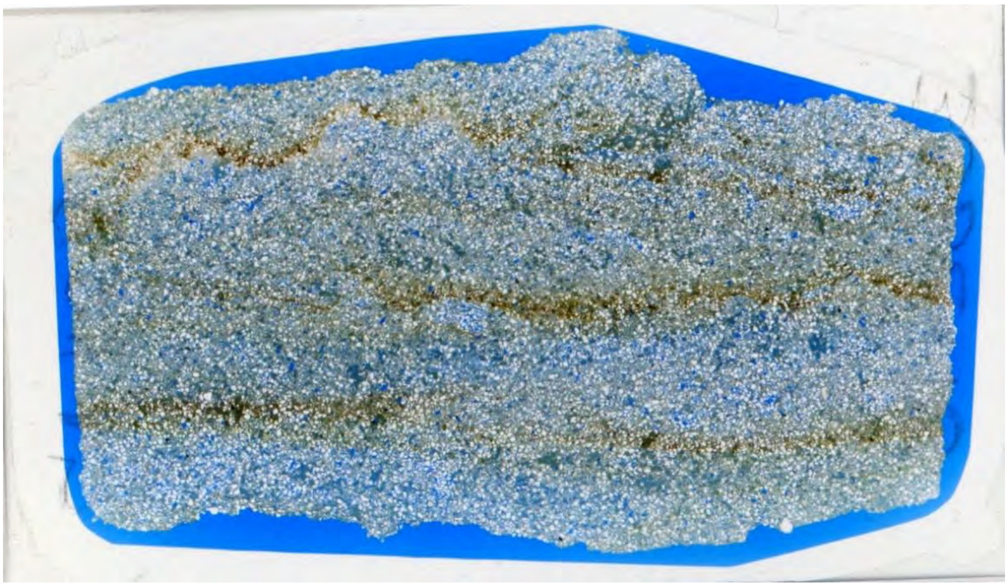

Plate 22. Scanned image of thin section from sample GT108, showing the horizontal laminated fabric. Field of view = 48 mm wide.

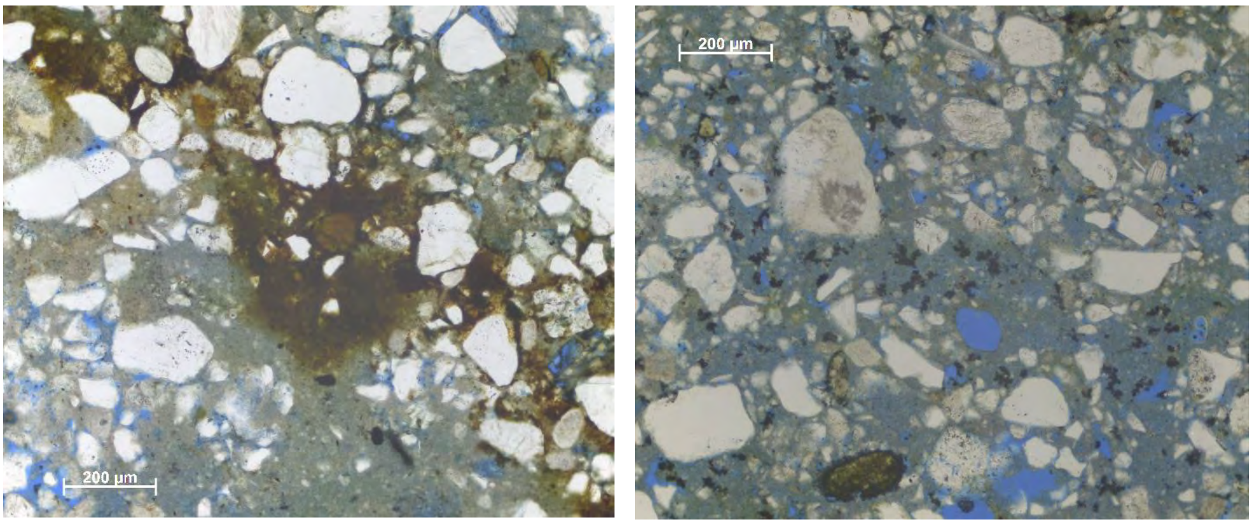

Plate 23. Transmitted light photomicrographs (plain polarised light) showing the variation in staining by iron oxyhydroxides within the sample. GT108

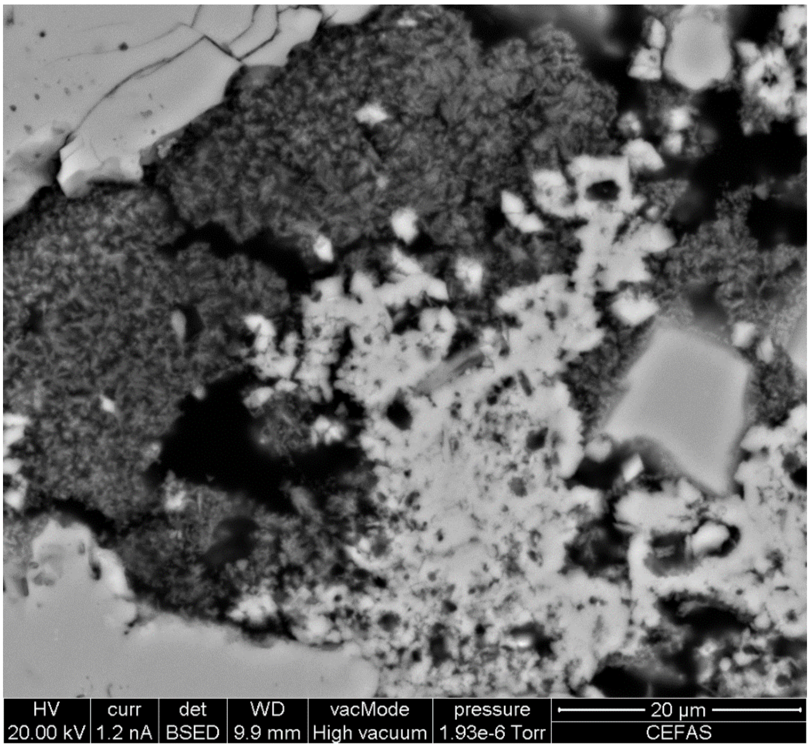

Plate 24. BSEM image showing the high clay content within the sample. The micrite clot preserves traces of a potential microcellular texture. Some euhedral rhombic overgrowths of calcite have developed around the margins of the micrite clot. GT108.

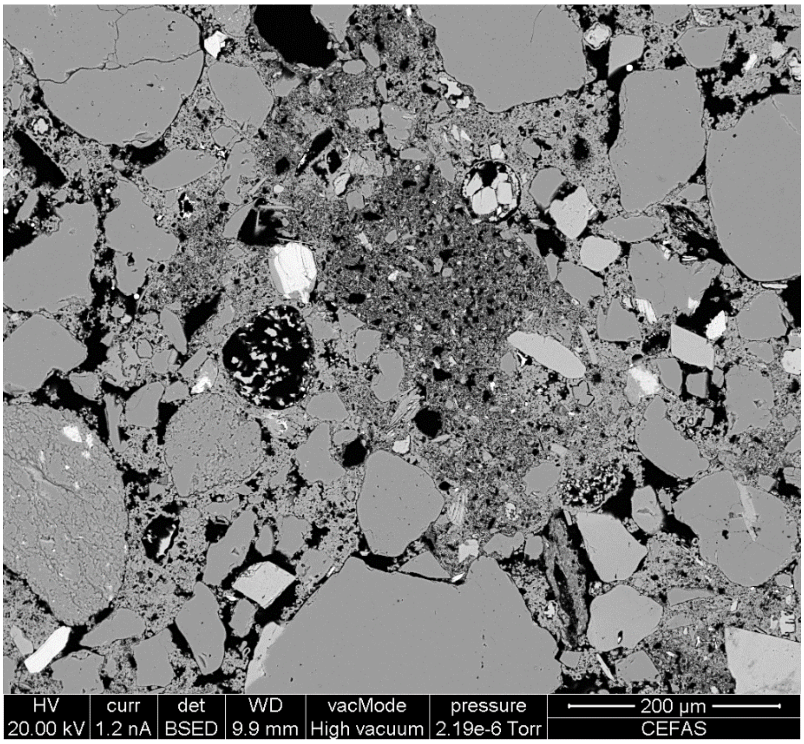

Plate 25. BSEM image of a large rounded clay-rich micrite pellet within the sample. This is probably a detrital faecal pellet. GT108.

ED-EPMA analysis of the carbonate cements are presented in Table 4 and are summarised in Figure 5. The micritic magnesian calcite cements contain between 34 and 41 mole % $MgCO_3$ in solid solution (i.e. the structural formula of the calcite can be represented as $Ca_{0.59-0.66}Mg_{0.41-}$

$_{0.34}CO_3$). This is consistent with the predominant very high magnesian-calcite identified by XRD analysis (Volume 1: Table 2).

The sequence of sedimentary and post-depositional diagenetic events recorded from sample GT108 can be summarised as follows:

1. Deposition of medium-grained sand with fine-grained, intergranular clay and silt.
2. Precipitation of micritic high-magnesian calcite under shallow burial depth, causing lithification.
3. Precipitation of pyrite coeval with micrite formation [2], under anoxic porewater conditions.
4. Oxidation of some framboidal pyrite and precipitation of fine secondary iron oxyhydroxide within the micrite matrix and around detrital grain boundaries.
5. Colonisation by bryozoans, and calcareous serpulid worm encrustations on the lithified surface of the clast.

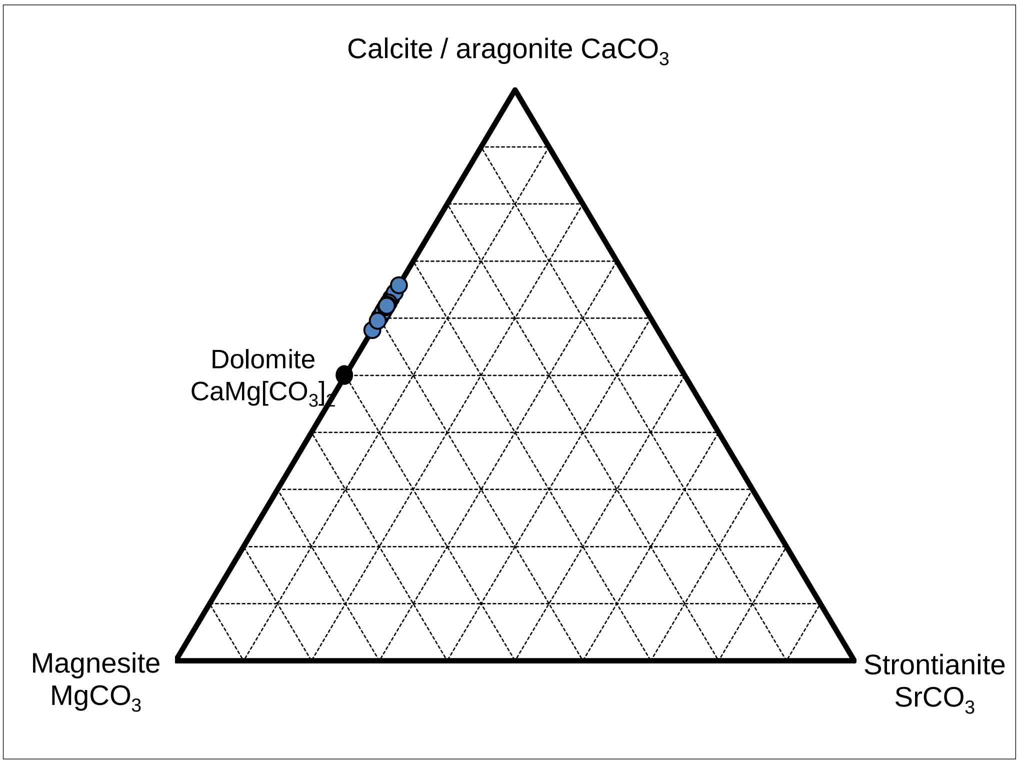

Figure 5. $CaCO_3$-$MgCO_3$-$SrCO_3$ molar ratio plot illustrating the composition of the micritic high-magnesian calcite cement (solid blue circles) from sample GT108.

Table 4. Electron microprobe analyses for the carbonate cements in sample GT108

		Weight % oxide (normalised)							Ionic ratio [normalised to 3 [O]						COMMENTS
SAMPLE	No	MgO	CaO	MnO	FeO	SrO	CO_2 (calc)	*Total wt.%	Mg^{2+}	Ca^{2+}	Mn^{2+}	Fe^{2+}	Sr^{2+}	CO_3^{2-}	
GT108	1	17.77	34.05	0.00	1.28	0.00	46.90	100	0.41	0.57	0.00	0.02	0.00	1.00	microcellular micrite
GT108	2	17.07	35.85	0.00	0.20	0.00	46.88	100	0.40	0.60	0.00	0.00	0.00	1.00	microcellular micrite
GT108	3	16.13	36.81	0.00	0.35	0.00	46.71	100	0.38	0.62	0.00	0.00	0.00	1.00	microcellular micrite
GT108	4	15.80	37.07	0.00	0.49	0.00	46.64	100	0.37	0.62	0.00	0.01	0.00	1.00	microcellular micrite
GT108	5	16.89	35.58	0.00	0.73	0.00	46.80	100	0.39	0.60	0.00	0.01	0.00	1.00	microcellular micrite
GT108	6	16.96	35.89	0.00	0.29	0.00	46.85	100	0.40	0.60	0.00	0.00	0.00	1.00	microcellular micrite
GT108	7	16.48	36.72	0.00	0.00	0.00	46.80	100	0.38	0.62	0.00	0.00	0.00	1.00	microcellular micrite
GT108	8	17.12	35.97	0.00	0.00	0.00	46.91	100	0.40	0.60	0.00	0.00	0.00	1.00	microcellular micrite
GT108	9	16.64	36.04	0.00	0.54	0.00	46.78	100	0.39	0.60	0.00	0.01	0.00	1.00	microcellular micrite
GT108	10	16.54	36.26	0.00	0.43	0.00	46.77	100	0.39	0.61	0.00	0.01	0.00	1.00	micrite
GT108	11	16.10	36.60	0.00	0.63	0.00	46.67	100	0.38	0.62	0.00	0.01	0.00	1.00	micrite
GT108	12	16.38	36.36	0.00	0.53	0.00	46.73	100	0.38	0.61	0.00	0.01	0.00	1.00	micrite
GT108	13	15.42	37.38	0.00	0.65	0.00	46.55	100	0.36	0.63	0.00	0.01	0.00	1.00	micrite
GT108	14	16.51	36.01	0.00	0.75	0.00	46.73	100	0.39	0.60	0.00	0.01	0.00	1.00	micrite
GT108	15	17.33	35.49	0.00	0.26	0.00	46.92	100	0.40	0.59	0.00	0.00	0.00	1.00	micrite
GT108	16	15.09	38.14	0.00	0.23	0.00	46.54	100	0.35	0.64	0.00	0.00	0.00	1.00	micrite
GT108	17	14.51	38.84	0.00	0.21	0.00	46.44	100	0.34	0.66	0.00	0.00	0.00	1.00	micrite
GT108	18	15.95	37.35	0.00	0.00	0.00	46.71	100	0.37	0.63	0.00	0.00	0.00	1.00	micrite
GT108	19	16.16	36.90	0.00	0.22	0.00	46.72	100	0.38	0.62	0.00	0.00	0.00	1.00	micrite
GT108	20	16.21	36.78	0.00	0.28	0.00	46.73	100	0.38	0.62	0.00	0.00	0.00	1.00	micrite
GT108	21	16.05	36.98	0.00	0.27	0.00	46.70	100	0.38	0.62	0.00	0.00	0.00	1.00	micrite
GT108	22	16.06	36.81	0.00	0.45	0.00	46.68	100	0.38	0.62	0.00	0.01	0.00	1.00	micrite

**Note: Some analytical totals were low (<90%) because of the microporous nature of the cements. Therefore, all data were normalised to 100%*

2.5 SAMPLE GT110

This sample comprises one small irregular clast about 60 mm in diameter (Plate 26). This is a light buff coloured, medium to coarse grained sandstone. A discontinuous, fine-grained micritic crust is present on one the surface. Bulk XRD analysis shows that aragonite is the principal carbonate mineral present (26.6 wt. %), with only very minor calcite and trace dolomite (Volume 1: Table 2).

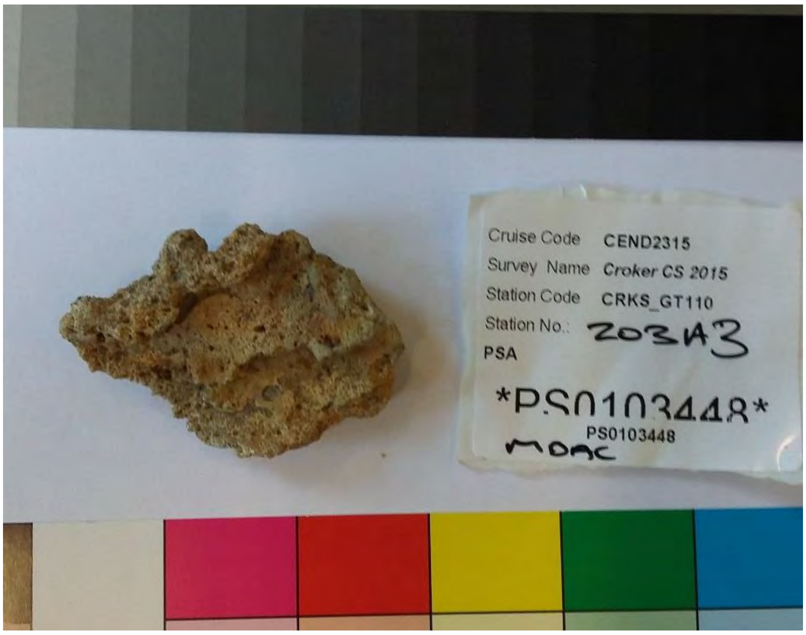

Plate 26. Photograph of sample GT110: a single buff coloured clast (<60 mm). Grey scale bar divisions = 10 mm.

The thin section prepared from sample GT110 is shown in Plate 27 and samples a vertical profile through the fine-grained crust and the sandstone substrate. The sandstone is coarse-grained (<800 µm), comprising sub-angular to sub-rounded detrital quartz with minor feldspar. It is moderately-sorted and has a patchy fine-grained muddy or clay-rich matrix. A fine grained micritic carbonate crust is discontinuous across the sandstone, varying between 0 to 300 µm thick, and comprises dense micrite with rare, diffuse, microsparite patches (Plate 28) A thin seam or vein of vuggy aragonite mineralisation, 400 to 500 µm thick, separates the micrite crust from the sandstone beneath (Plate 28). This has a complex texture, consisting of alternating bands of dirty micrite and clear fibrous or acicular aragonite. The basal part of the vein or seam immediately adjacent to the sandstone is vuggy, with cavities up to 8 mm long, lined by radiating sheaves of coarse acicular aragonite crystals. These aragonite crystals are often nucleated on top of earlier sub-spherical 'clots' of micritic carbonate (Plate 28). Micritic carbonate and coarser aragonite cement are also present in the underlying sandstone. The micrite forms thin 'dirt fringes' coating the sand grain surfaces, and as dirty pelloidal or spheroidal aggregates within the intergranular porosity (Plate 29 and Plate 30). This micrite fringe contains finely-disseminated pyrite, which indicates that the porewaters were reducing during micrite precipitation. Fibrous acicular aragonite has also nucleated on top of the micrite fringe, to partially fill the pore space (Plate 29 and Plate 30). The micritic carbonate must also be largely aragonite since XRD analysis demonstrates that aragonite is the principal carbonate mineral in this sample.

BSEM observations occasionally show the preservation of microscopic spherical voids, about 1 to 2 µm in size, encased within aragonite and micrite (Plate 31). This is similar to features described from some of the other samples) and may be of microbial origin (cf. GT004, GT108 and GT112).

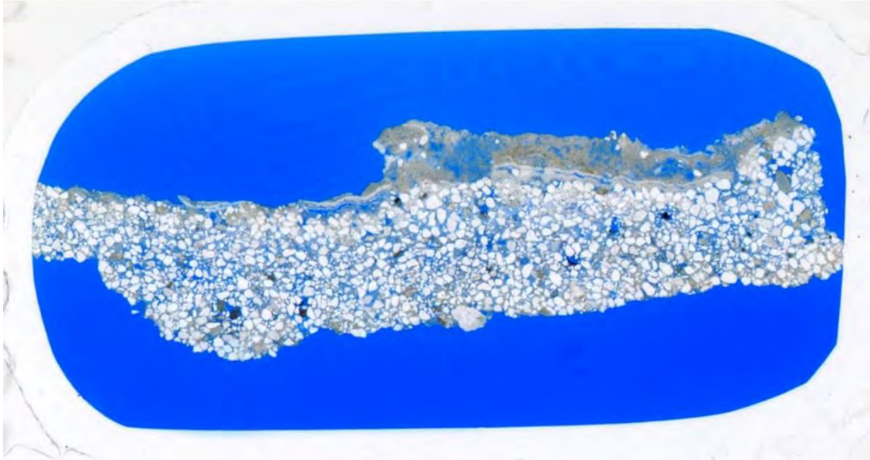

Plate 27. Scanned image of the thin section prepared from sample GT110. A calcareous / muddy crust is present on one edge of the sample. Field of view = 48 mm wide.

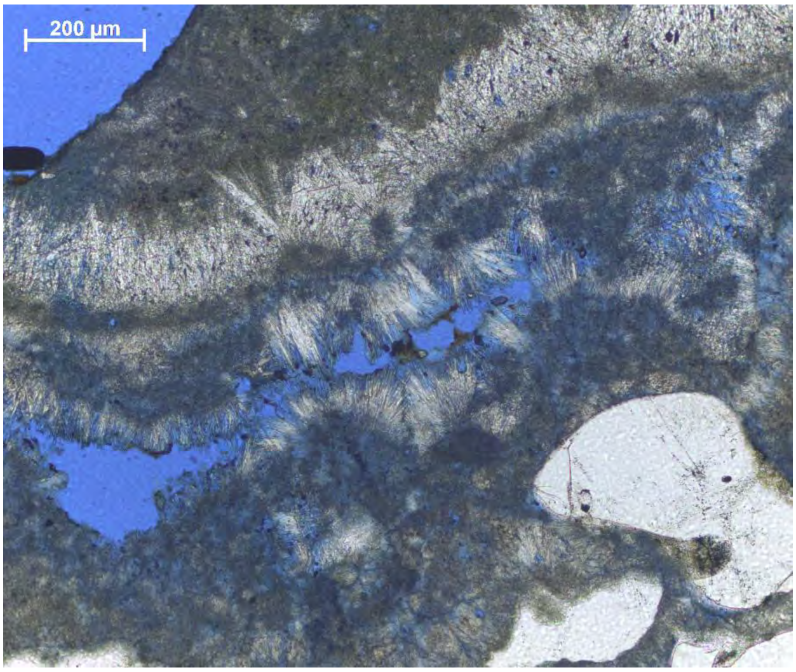

Plate 28. Transmitted light photomicrograph (plain polarised light) showing the dense micritic crust coating the sandstone substrate. Small, diffuse microsparite (clear) patches can be seen within the micrite layering Layers of acicular aragonite have nucleated on, and been coated with, layers of fine-grained silt indicating periodic influxes of silty material, halting calcareous growth. Sample GT110.

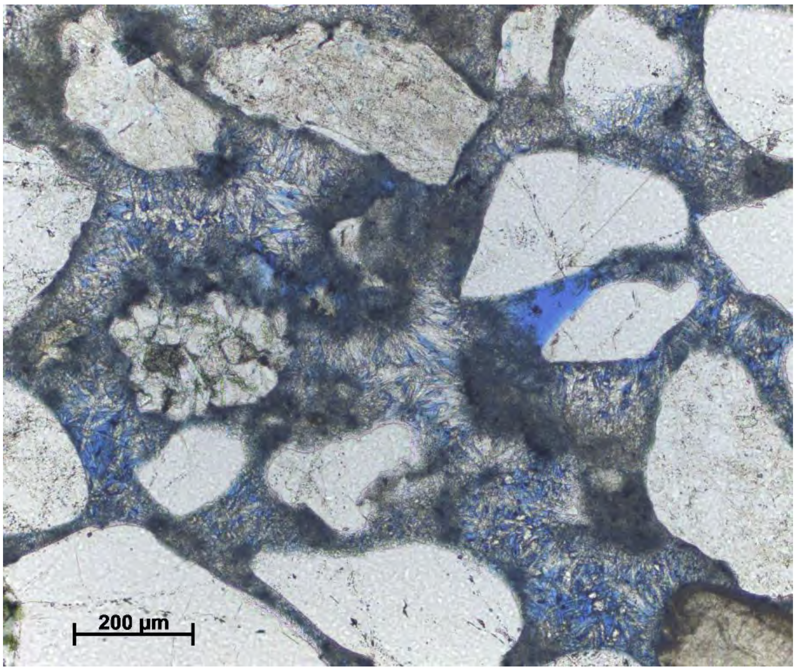

Plate 29. Transmitted light photomicrograph (plain polarised light) showing intergranular pores lined by dirty micritic carbonate fringes and pelloidal aggregates of dirty micrite. Fibrous acicular aragonite has nucleated on top of the micrite fringe, to fill the pore space. Sample GT110

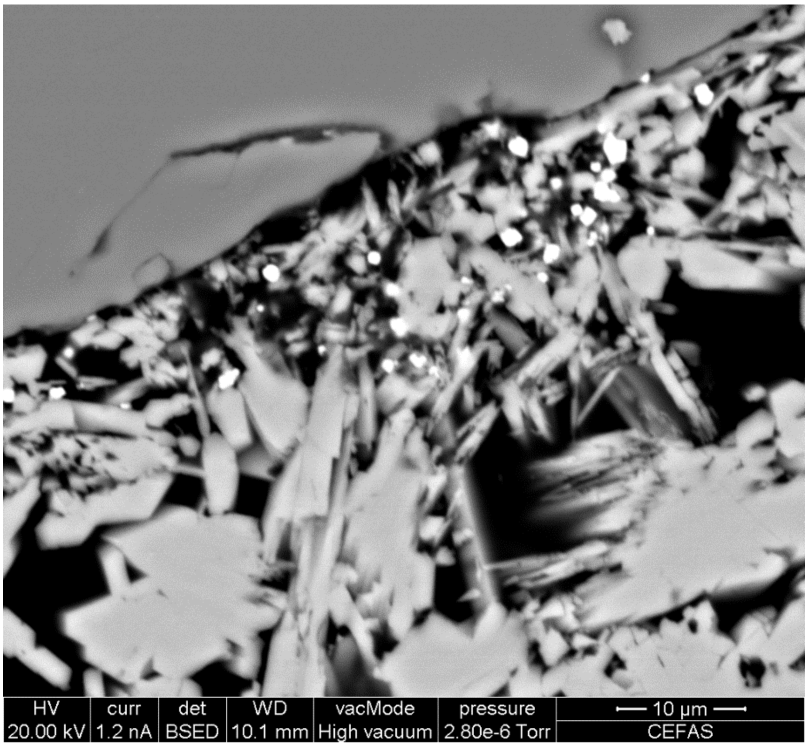

Plate 30. BSEM image showing a layer of clay-rich micrite, with disseminated very fine pyrite crystals (white), coating the surface of a detrital quartz grain. Coarser acicular aragonite crystals have nucleated on the earlier grain coating micrite fringe and have grown into to the pore space. Sample GT110

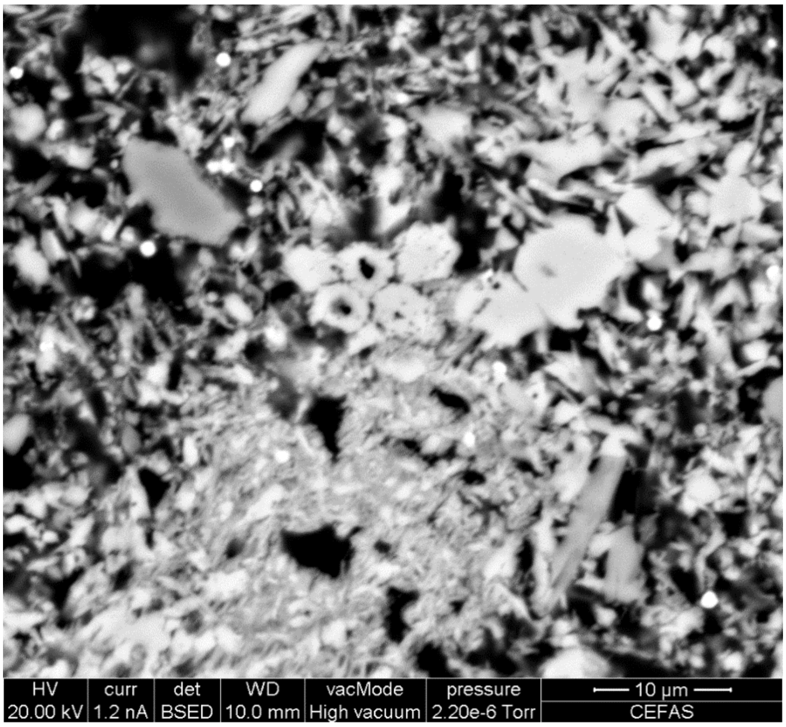

Plate 31. Detail of the micritic cement showing nucleation of aragonite around 1 µm cavities spaces and may represent preserved microbial texture. Clay minerals and numerous pyrite crystals are present within the micrite. Sample GT110

ED-EPMA major element compositional data for the micrite and acicular aragonite cements are given in Table 5. Their compositional variation, expressed in terms of molar proportions of CaO_3-$MgCO_3$ and $SrCO_3$, is summarised in Figure 6.

Both the micritic aragonite and coarser acicular aragonite cements are strontium bearing, with 1 mole % $SrCO_3$ in solid-solution (Figure 6) (i.e. the structural formula (i.e. the structural formula of the aragonite can be represented as $Ca_{0.99-1.00}Sr_{0.01-0.00}CO_3$).

No magnesian calcite cement was identified by SEM or ED-EPMA in this sample.

The sequence of sedimentary and post-depositional diagenetic events recorded from sample GT110 can be summarised as follows:

1. Deposition of a coarse sandstone.
2. Precipitation of microspheroidal or pelloidal aragonite micrite, incorporating fine silt and clay minerals. This formed both within the intergranular porosity of the sand and as a carbonate coating on the surface of the sandy sediment.
3. Precipitation of pyrite in close association, and coeval with the micritic aragonite [2]. This indicates that the micrite precipitated under reducing conditions.
4. Precipitation of a later acicular aragonite cement, lithifying the sample.

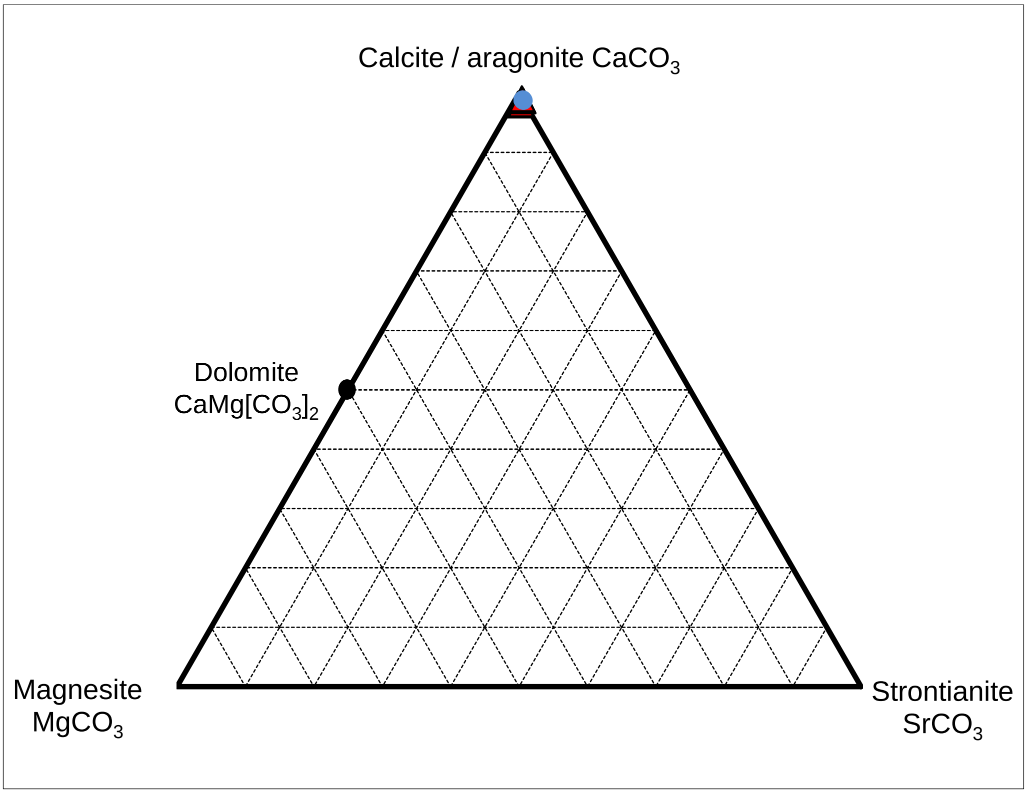

Figure 6. $CaCO_3$-$MgCO_3$-$SrCO_3$ molar ratio plot illustrating the compositions of the micritic cement (solid blue circles) and acicular aragonite (red triangles) from sample GT110.

Table 5. Electron microprobe analyses for the carbonate cements in sample GT110.

		Weight % oxide (normalised)							Ionic ratio [normalised to 3 [O]						COMMENTS
SAMPLE	No	MgO	CaO	MnO	FeO	SrO	CO_2 (calc)	*Total wt.%	Mg^{2+}	Ca^{2+}	Mn^{2+}	Fe^{2+}	Sr^{2+}	CO_3^{2-}	
GT110	1	0.00	55.12	0.00	0.00	1.15	43.73	100	0.00	0.99	0.00	0.00	0.01	1.00	acicular aragonite
GT110	2	0.00	54.98	0.00	0.00	1.32	43.70	100	0.00	0.99	0.00	0.00	0.01	1.00	acicular aragonite
GT110	3	0.00	55.23	0.00	0.00	1.01	43.76	100	0.00	0.99	0.00	0.00	0.01	1.00	acicular aragonite
GT110	4	0.00	55.11	0.00	0.00	1.17	43.73	100	0.00	0.99	0.00	0.00	0.01	1.00	acicular aragonite
GT110	5	0.00	55.04	0.00	0.00	1.24	43.71	100	0.00	0.99	0.00	0.00	0.01	1.00	acicular aragonite
GT110	6	0.00	54.93	0.00	0.00	1.38	43.69	100	0.00	0.99	0.00	0.00	0.01	1.00	acicular aragonite
GT110	7	0.00	55.00	0.00	0.00	1.29	43.70	100	0.00	0.99	0.00	0.00	0.01	1.00	acicular aragonite
GT110	8	0.00	55.10	0.00	0.00	1.17	43.73	100	0.00	0.99	0.00	0.00	0.01	1.00	acicular aragonite
GT110	9	0.00	55.08	0.00	0.00	1.19	43.72	100	0.00	0.99	0.00	0.00	0.01	1.00	acicular aragonite
GT110	10	0.00	55.00	0.00	0.00	1.29	43.70	100	0.00	0.99	0.00	0.00	0.01	1.00	acicular aragonite
GT110	11	0.00	55.05	0.00	0.00	1.23	43.72	100	0.00	0.99	0.00	0.00	0.01	1.00	acicular aragonite
GT110	12	0.00	54.99	0.00	0.00	1.31	43.70	100	0.00	0.99	0.00	0.00	0.01	1.00	acicular aragonite
GT110	13	0.00	55.11	0.00	0.00	1.16	43.73	100	0.00	0.99	0.00	0.00	0.01	1.00	acicular aragonite
GT110	14	0.00	55.01	0.00	0.00	1.29	43.71	100	0.00	0.99	0.00	0.00	0.01	1.00	acicular aragonite
GT110	15	0.00	55.05	0.00	0.00	1.23	43.72	100	0.00	0.99	0.00	0.00	0.01	1.00	acicular aragonite
GT110	16	0.00	55.02	0.00	0.00	1.27	43.71	100	0.00	0.99	0.00	0.00	0.01	1.00	acicular aragonite
GT110	17	0.22	54.81	0.00	0.00	1.22	43.76	100	0.01	0.98	0.00	0.00	0.01	1.00	acicular aragonite
GT110	18	0.45	54.37	0.00	0.33	1.05	43.80	100	0.01	0.97	0.00	0.00	0.01	1.00	acicular aragonite
GT110	19	0.24	54.70	0.00	0.00	1.32	43.74	100	0.01	0.98	0.00	0.00	0.01	1.00	acicular aragonite
GT110	20	0.00	55.04	0.00	0.00	1.25	43.71	100	0.00	0.99	0.00	0.00	0.01	1.00	acicular aragonite
GT110	21	0.00	55.17	0.00	0.00	1.08	43.75	100	0.00	0.99	0.00	0.00	0.01	1.00	acicular aragonite
GT110	22	0.00	55.37	0.00	0.00	0.83	43.80	100	0.00	0.99	0.00	0.00	0.01	1.00	acicular aragonite
GT110	23	0.00	55.34	0.00	0.00	0.87	43.79	100	0.00	0.99	0.00	0.00	0.01	1.00	acicular aragonite
GT110	24	0.00	54.97	0.00	0.00	1.33	43.70	100	0.00	0.99	0.00	0.00	0.01	1.00	acicular aragonite
GT110	25	0.00	55.05	0.00	0.00	1.23	43.72	100	0.00	0.99	0.00	0.00	0.01	1.00	acicular aragonite
GT110	26	0.00	54.92	0.00	0.00	1.40	43.68	100	0.00	0.99	0.00	0.00	0.01	1.00	acicular aragonite
GT110	27	0.00	55.28	0.00	0.00	0.94	43.77	100	0.00	0.99	0.00	0.00	0.01	1.00	acicular aragonite
GT110	28	0.00	55.17	0.00	0.00	1.09	43.75	100	0.00	0.99	0.00	0.00	0.01	1.00	acicular aragonite
GT110	29	0.00	55.25	0.00	0.00	0.98	43.77	100	0.00	0.99	0.00	0.00	0.01	1.00	acicular aragonite
GT110	30	0.00	55.06	0.00	0.00	1.22	43.72	100	0.00	0.99	0.00	0.00	0.01	1.00	acicular aragonite
GT110	31	0.00	54.85	0.00	0.00	1.48	43.67	100	0.00	0.99	0.00	0.00	0.01	1.00	acicular aragonite
GT110	32	0.00	55.06	0.00	0.00	1.22	43.72	100	0.00	0.99	0.00	0.00	0.01	1.00	acicular aragonite

		Weight % oxide (normalised)							Ionic ratio [normalised to 3 [O]						COMMENTS
SAMPLE	No	MgO	CaO	MnO	FeO	SrO	CO_2 (calc)	*Total wt.%	Mg^{2+}	Ca^{2+}	Mn^{2+}	Fe^{2+}	Sr^{2+}	CO_3^{2-}	
GT110	33	0.00	55.17	0.00	0.00	1.09	43.75	100	0.00	0.99	0.00	0.00	0.01	1.00	acicular aragonite
GT110	34	0.00	55.02	0.00	0.00	1.27	43.71	100	0.00	0.99	0.00	0.00	0.01	1.00	acicular aragonite
GT110	35	0.00	55.17	0.00	0.00	1.08	43.75	100	0.00	0.99	0.00	0.00	0.01	1.00	acicular aragonite
GT110	36	0.00	55.09	0.00	0.00	1.19	43.72	100	0.00	0.99	0.00	0.00	0.01	1.00	micrite
GT110	37	0.00	55.08	0.00	0.00	1.20	43.72	100	0.00	0.99	0.00	0.00	0.01	1.00	micrite
GT110	38	0.00	54.98	0.00	0.00	1.32	43.70	100	0.00	0.99	0.00	0.00	0.01	1.00	micrite
GT110	39	0.00	55.10	0.00	0.00	1.17	43.73	100	0.00	0.99	0.00	0.00	0.01	1.00	micrite
GT110	40	0.00	55.12	0.00	0.00	1.14	43.73	100	0.00	0.99	0.00	0.00	0.01	1.00	micrite

**Note: Some analytical totals were low (<90%) because of the microporous nature of the cements. Therefore, all data were normalised to 100%*

2.6 SAMPLE GT112

Sample GT112 comprised a single clast, approximately 150 mm diameter and comprises a light grey siltstone to fine-medium sandstone. It has a brownish outer surface indicating some iron oxidation has occurred. The rock is intensely bioturbated: several large, open burrow-like channels (up to 15 mm diameter) penetrate deeply from the surface of the rock (Plate 32). Numerous shelly fragments have been incorporated into the sample by cementation and encrustation on the sandstone surface, and the lithified sandstone surface is also encrusted by some pale, white-cream bryozoa (Plate 33).

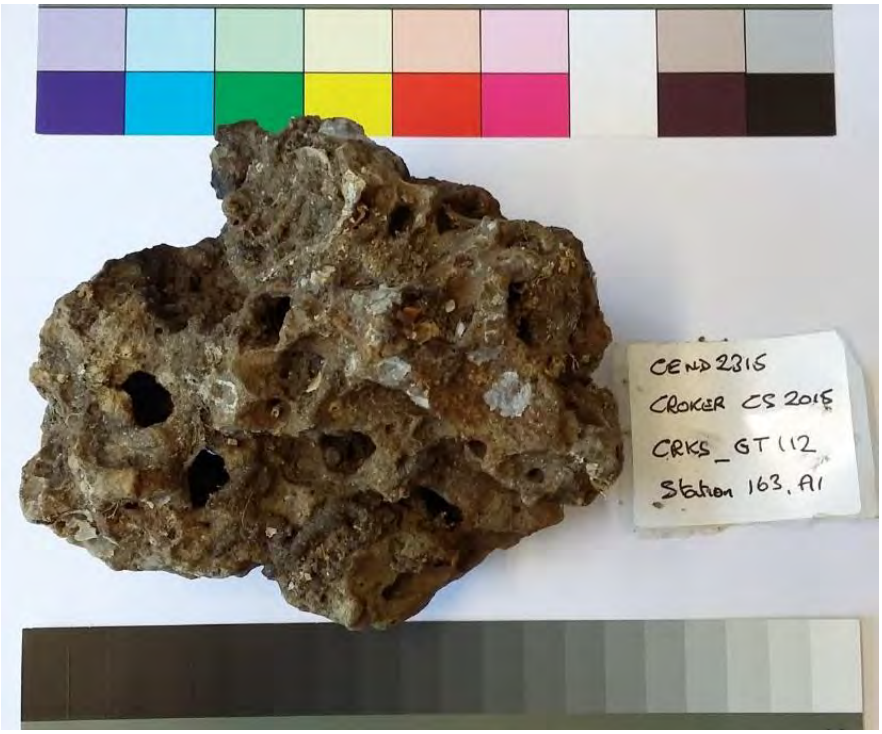

Plate 32. Photograph showing sample GT112. The sample has been heavily bored and encrusting bryozoans can be seen on the surface. Numerous shell fragments are also visible. Grey scale bar divisions = 10 mm.

The polished thin section prepared through a fragment of GT112 is shown in Plate 34. The sample has a patchy brown colouration where the micritic carbonate cement in the sandstone matrix, and detrital grain surfaces, have been stained by brown iron oxyhydroxides, particularly around the largest burrow in the centre of the section.

The sandstone is dominantly fine- to medium-grained, with angular to subordinate sub-angular grains. It has an un-compacted, grain-supported fabric, with simple point contacts between the detrital grains. The detrital mineralogy is dominated by quartz sand, with subordinate carbonate grains, lithic fragments, and feldspar. Some chloritized detrital silicate grains are also present.

The matrix of the sandstone is micritic, comprising high-magnesian calcite. The micrite occurs in spherical aggregates of microcrystals within the matrix. The distribution of the micrite cement is heterogeneous: some areas preserving an open, highly porous fabric, whilst other areas are tightly-cemented with brown-coloured micritic cement (Plate 35). The sandstone immediately surrounding the burrow structures has been preferentially cemented, and is highlighted by the subsequent iron oxyhydroxide staining (Plate 34). This suggests that the burrows have provided preferential pathways for the carbonate-mineralising pore fluids. Some minor fine grained iron oxide was noted to be disseminated in the micrite but no fresh pyrite was observed. Some of these burrow channels have been partially infilled, often with coarser-grained (up to 1 mm grain size), winnowed sand and shelly debris (Plate 34). BSEM observations show that the micritic high-magnesian calcite is typically microporous, and made up of spherical to microboytryoidal aggregates up to 50 µm diameter (e.g. Plate 36). Subidiomorphic to idiomorphic rhombic calcite crystals (microsparite cement) have developed as overgrowths around the microporous, micrite aggregates. BSEM observations also show that the microsparite cement also encloses minute spherical cavities (<2 µm diameter), around which the microspar calcite crystals appear to have nucleated (Plate 37). These cavities are similar in size and form to those described earlier from some of the other samples, and may potentially represent preserved relicts of bacterial cells Denser subidiomorphic to idiomorphic rhombic calcite crystals form crystal fringes around detrital grains and line intergranular pore space. This may be due to recrystallization and coarsening-up of the micritic cement.

The bryozoan surfaces have not been subjected to any secondary recrystallisation or mineralisation, which suggests colonisation most likely occurred after precipitation of MDAC had ended. The bryozoan comprises a magnesian calcite core and a non-magnesian calcite outer layer.

Plate 33. Optical micrograph showing the detail of one of the encrusting bryozoans on the surface of sample GT112.

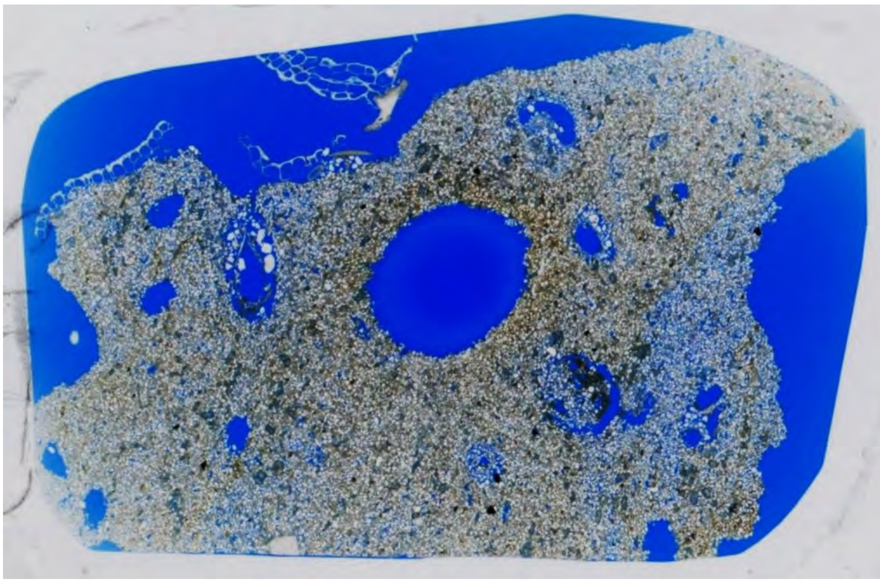

Plate 34 Scan of sample GT112 polished thin section. Numerous cross sections through burrows and borings are visible, as are the encrusting bryozoans (upper surface in this image). Field of view = 48 mm wide.

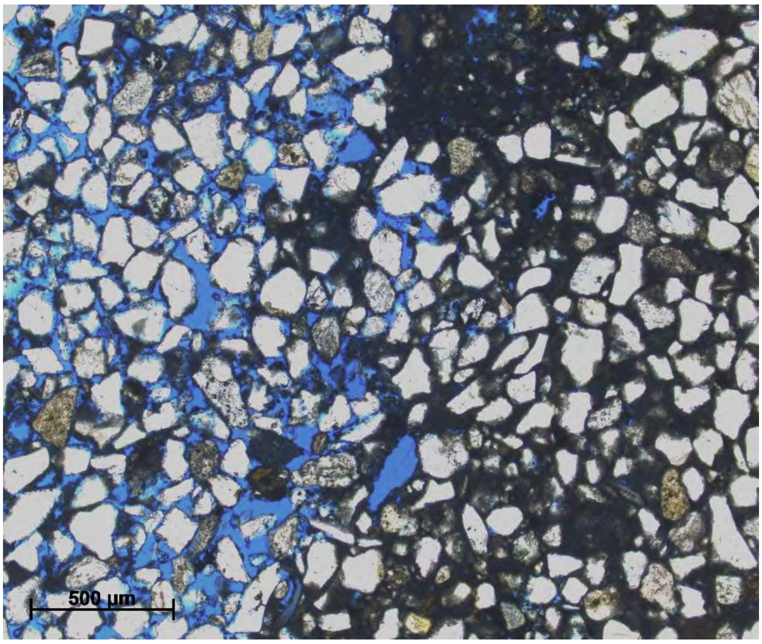

Plate 35. Transmitted light photomicrograph (plain polarised light) showing the contrast between a densely cemented area, and a more porous, weakly cemented area. The micritic cement has a dark-brown colouration. The sample is un-compacted and grain-supported, where the angular to sub-angular grains have simple point contacts. At the top of this image is a cross-section through a burrow which has been infilled with clay-rich, micritic cement and lined around the edge with outwardly-aligned grains. Occasional secondary pore spaces are present (e.g. lower centre of image within the cemented portion) where grains or shelly fragments have been dissolved out. Sample GT112.

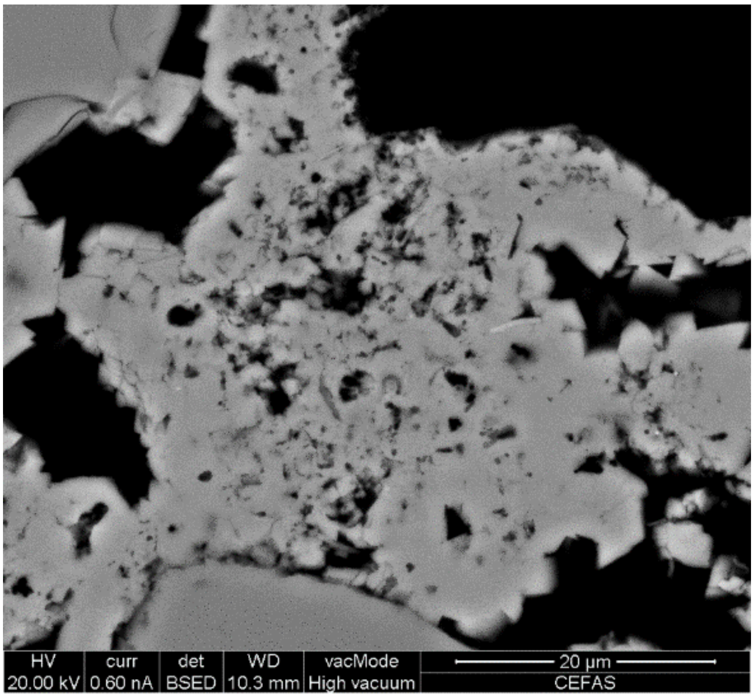

Plate 36. BSEM photomicrograph showing the detail of the micritic high-magnesian calcite cement. The calcite preserves a well-developed cellular micro-fabric that represents mineralised bacterial cells. The cement is coarser and less porous around the edges of the pore space compared to the centre. Some clay fines have been incorporated within the cement. Sample GT112.

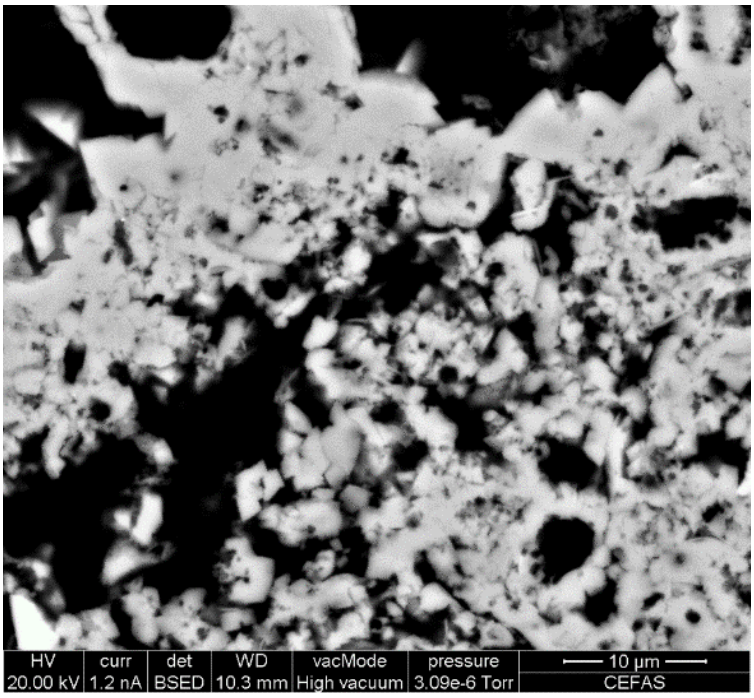

Plate 37. A higher magnification BSED photomicrograph of the micrite. Rhombic crystals of calcite can be seen, together with spheroidal voids. It is possible that the larger voids may originally have been trapped gas bubbles. Wisps of clay material can be seen between the crystals. Coarser crystals are present around the edge of the pore space. Sample GT112.

ED-EPMA analysis of the carbonate cements are presented in Table 6 and are summarised in Figure 7. The micritic magnesian calcite cements contain between 36 and 43 mole % $MgCO_3$ in solid solution (i.e. the structural formula of the calcite can be represented as $Ca_{0.57-0.64}Mg_{0.43-0.36}CO_3$). This composition is consistent with the bulk XRD analysis (Volume 1: Table 2), which shows that the bulk of the carbonate cement is a very high magnesian-calcite.

The bryozoan encrustation is composed of a magnesian calcite core with between 9 and 11 mole % $MgCO_3$. This is surrounded by a non-magnesian-calcite outer coating. A small amount of strontium was detected in both types of calcite forming the bryozoan skeleton.

The sequence of sedimentary and post-depositional diagenetic events recorded from sample GT112 can be summarised as follows:

1. Deposition of fine sand and silt sediment.
2. Syndepositional bioturbation
3. Precipitation of micritic high-magnesian calcite under shallow burial, causing lithification.
4. Erosion and abrasion of the sample. Boring of the clast surfaces by marine biota, and minor oxidation within the micritic matrix and around some grains.
5. Colonisation by bryozoans on the lithified surface of the clast.

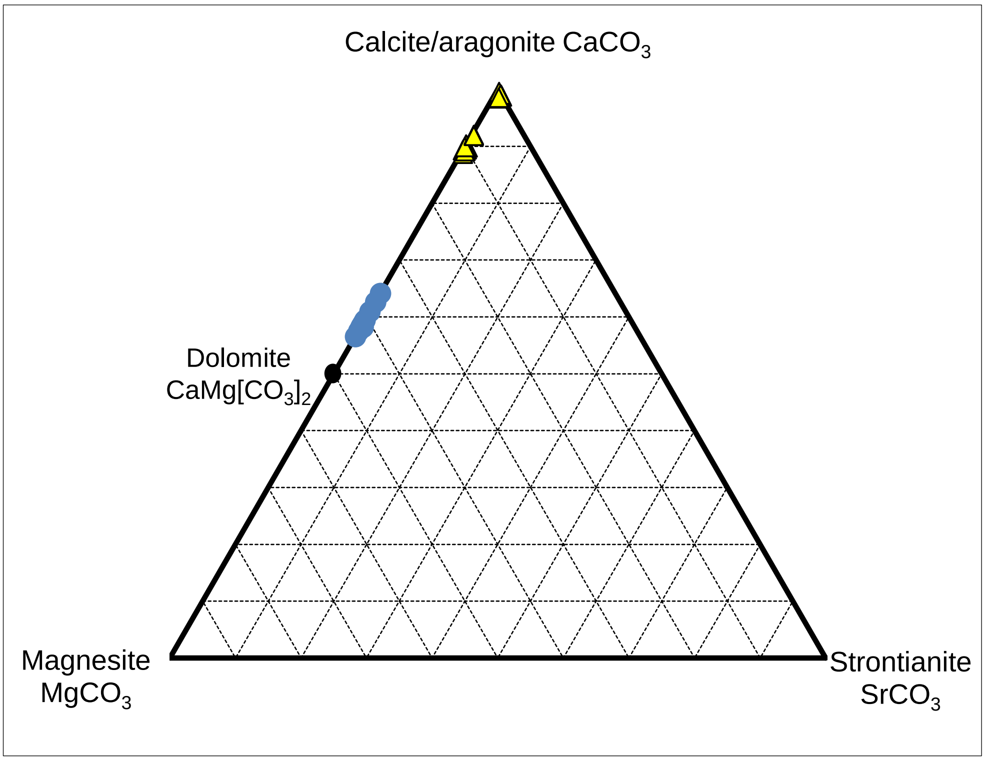

Figure 7. $CaCO_3$-$MgCO_3$-$SrCO_3$ molar ratio plot illustrating the compositions of the surface-encrusting bryozoan (yellow triangles) and the micritic high-magnesian calcite cement (solid blue circles) from sample GT112.

Table 6. Electron microprobe analyses of encrusting bryozoan and carbonate cements in sample GT112

		Weight % oxide (normalised)							Ionic ratio [normalised to 3 [O]						COMMENTS
SAMPLE	No	MgO	CaO	MnO	FeO	SrO	CO_2 (calc)	*Total wt.%	Mg^{2+}	Ca^{2+}	Mn^{2+}	Fe^{2+}	Sr^{2+}	CO_3^{2-}	
GT112	1	4.27	50.72	0.00	0.00	0.39	44.62	100	0.10	0.89	0.00	0.00	0.00	1.00	Bryozoan core
GT112	2	3.94	51.41	0.00	0.00	0.00	44.64	100	0.10	0.90	0.00	0.00	0.00	1.00	Bryozoan core
GT112	3	3.95	51.03	0.00	0.00	0.47	44.55	100	0.10	0.90	0.00	0.00	0.00	1.00	Bryozoan core
GT112	4	4.08	50.84	0.00	0.00	0.51	44.56	100	0.10	0.90	0.00	0.00	0.00	1.00	Bryozoan core
GT112	5	4.25	51.06	0.00	0.00	0.00	44.70	100	0.10	0.90	0.00	0.00	0.00	1.00	Bryozoan core
GT112	6	3.48	51.65	0.00	0.00	0.38	44.49	100	0.09	0.91	0.00	0.00	0.00	1.00	Bryozoan core
GT112	12	4.21	50.71	0.00	0.00	0.49	44.59	100	0.10	0.89	0.00	0.00	0.00	1.00	Bryozoan core
GT112	13	4.38	50.90	0.00	0.00	0.00	44.72	100	0.11	0.89	0.00	0.00	0.00	1.00	Bryozoan core
GT112	14	4.49	50.49	0.00	0.00	0.36	44.66	100	0.11	0.89	0.00	0.00	0.00	1.00	Bryozoan core
GT112	15	4.27	50.71	0.00	0.00	0.40	44.62	100	0.10	0.89	0.00	0.00	0.00	1.00	Bryozoan core
GT112	16	4.14	51.19	0.00	0.00	0.00	44.68	100	0.10	0.90	0.00	0.00	0.00	1.00	Bryozoan core
GT112	7	0.00	55.04	0.00	0.00	1.24	43.71	100	0.00	0.99	0.00	0.00	0.01	1.00	bryozoan
GT112	8	0.00	55.33	0.00	0.00	0.89	43.79	100	0.00	0.99	0.00	0.00	0.01	1.00	bryozoan
GT112	9	0.00	55.17	0.00	0.00	1.08	43.75	100	0.00	0.99	0.00	0.00	0.01	1.00	bryozoan
GT112	10	0.00	55.08	0.00	0.00	1.20	43.72	100	0.00	0.99	0.00	0.00	0.01	1.00	bryozoan
GT112	11	0.00	55.09	0.00	0.00	1.19	43.73	100	0.00	0.99	0.00	0.00	0.01	1.00	bryozoan
GT112	17	0.00	55.28	0.00	0.00	0.94	43.77	100	0.00	0.99	0.00	0.00	0.01	1.00	bryozoan
GT112	18	0.24	54.95	0.00	0.00	1.00	43.80	100	0.01	0.98	0.00	0.00	0.01	1.00	bryozoan
GT112	19	0.00	55.25	0.00	0.00	0.98	43.77	100	0.00	0.99	0.00	0.00	0.01	1.00	bryozoan
GT112	20	0.00	55.32	0.00	0.00	0.90	43.78	100	0.00	0.99	0.00	0.00	0.01	1.00	bryozoan
GT112	21	0.23	55.07	0.00	0.00	0.87	43.83	100	0.01	0.99	0.00	0.00	0.01	1.00	bryozoan
GT112	22	3.11	52.10	0.00	0.00	0.36	44.43	100	0.08	0.92	0.00	0.00	0.00	1.00	bryozoan
GT112	23	3.15	52.01	0.00	0.00	0.42	44.42	100	0.08	0.92	0.00	0.00	0.00	1.00	bryozoan
GT112	24	17.98	34.97	0.00	0.00	0.00	47.06	100	0.42	0.58	0.00	0.00	0.00	1.00	micrite
GT112	25	17.67	35.33	0.00	0.00	0.00	47.00	100	0.41	0.59	0.00	0.00	0.00	1.00	micrite
GT112	26	17.78	35.20	0.00	0.00	0.00	47.02	100	0.41	0.59	0.00	0.00	0.00	1.00	micrite
GT112	27	17.88	35.08	0.00	0.00	0.00	47.04	100	0.41	0.59	0.00	0.00	0.00	1.00	micrite
GT112	28	18.08	34.85	0.00	0.00	0.00	47.07	100	0.42	0.58	0.00	0.00	0.00	1.00	micrite
GT112	29	15.30	38.10	0.00	0.00	0.00	46.60	100	0.36	0.64	0.00	0.00	0.00	1.00	micrite
GT112	30	17.91	35.04	0.00	0.00	0.00	47.05	100	0.42	0.58	0.00	0.00	0.00	1.00	micrite
GT112	31	17.70	34.79	0.00	0.56	0.00	46.95	100	0.41	0.58	0.00	0.01	0.00	1.00	micrite
GT112	32	18.78	34.03	0.00	0.00	0.00	47.19	100	0.43	0.57	0.00	0.00	0.00	1.00	micrite

		Weight % oxide (normalised)							Ionic ratio [normalised to 3 [O]						COMMENTS
SAMPLE	No	MgO	CaO	MnO	FeO	SrO	CO_2 (calc)	*Total wt.%	Mg^{2+}	Ca^{2+}	Mn^{2+}	Fe^{2+}	Sr^{2+}	CO_3^{2-}	
GT112	33	15.98	37.31	0.00	0.00	0.00	46.71	100	0.37	0.63	0.00	0.00	0.00	1.00	micrite
GT112	34	18.16	34.22	0.00	0.59	0.00	47.03	100	0.42	0.57	0.00	0.01	0.00	1.00	micrite
GT112	35	17.87	34.84	0.00	0.28	0.00	47.01	100	0.41	0.58	0.00	0.00	0.00	1.00	micrite
GT112	36	17.43	35.61	0.00	0.00	0.00	46.96	100	0.41	0.59	0.00	0.00	0.00	1.00	micrite
GT112	37	16.83	34.13	0.00	2.41	0.00	46.63	100	0.39	0.57	0.00	0.03	0.00	1.00	micrite
GT112	38	18.06	34.87	0.00	0.00	0.00	47.07	100	0.42	0.58	0.00	0.00	0.00	1.00	micrite
GT112	39	17.59	35.03	0.00	0.43	0.00	46.95	100	0.41	0.59	0.00	0.01	0.00	1.00	micrite
GT112	40	17.71	35.28	0.00	0.00	0.00	47.01	100	0.41	0.59	0.00	0.00	0.00	1.00	micrite
GT112	41	17.84	34.85	0.00	0.00	0.35	46.96	100	0.41	0.58	0.00	0.00	0.00	1.00	micrite
GT112	42	17.93	35.02	0.00	0.00	0.00	47.05	100	0.42	0.58	0.00	0.00	0.00	1.00	micrite
GT112	43	16.67	36.20	0.00	0.32	0.00	46.80	100	0.39	0.61	0.00	0.00	0.00	1.00	micrite
GT112	44	17.95	35.00	0.00	0.00	0.00	47.05	100	0.42	0.58	0.00	0.00	0.00	1.00	micrite
GT112	45	17.81	34.91	0.00	0.27	0.00	47.00	100	0.41	0.58	0.00	0.00	0.00	1.00	micrite

**Note: Some analytical totals were low (<90%) because of the microporous nature of the cements. Therefore, all data were normalised to 100%*

2.7 SAMPLE GT116

This sample consisted of five roughly tabular fragments of grey, coarse-grained, well-cemented muddy sandstone, containing numerous fragments of detrital bioclastic debris (Plate 38).

Plate 38. Photograph of the grey, sub-angular clasts which comprise sample GT116. Grey scale bar divisions = 10 mm.

A scanned image of the thin section prepared from one of the clasts from sample GT116 is shown in Plate 39. The rock comprises a medium- to coarse grained sandstone with abundant bioclastic debris. It has a grain-supported fabric with intergranular clay and silt (Plate 40). The sample is dominated by sub-angular to rounded detrital quartz grains (grain size up to 1300 µm). Areas of dark brown, fine-grained, silty material seen in some parts of the thin section are possibly infilled burrows.

Bulk rock XRD analysis (Volume 1: Table 2) identified aragonite as the major carbonate mineral present, forming 37.6 wt. % of the rock. Only minor to trace amounts of calcite and dolomite were identified by XRD. BSEM shows that this aragonite cement is largely fibrous to acicular and extensively fills the intergranular porosity of the sandstone (Plate 41 and Plate 42). The fibrous aragonite appears to have nucleated around initial pelloidal or spherical aggregates of micritic aragonite (Plate 41). Many bioclastic fragments also have acicular fringes of aragonite, and in some cases appear to have been preferential sites for coarse fibrous aragonite nucleation. Some shells contain a fine-grained micritic carbonate within their skeletal cavities. Some shells also show evidence of being extensively bored by marine micro-organisms, possibly prior to deposition and lithification. No evidence was noted of the aragonite cement having been affected by boring in this sample.

Fine framboidal pyrite is present within the silty matrix material (Plate 43) indicating porewater conditions in the sediment were anoxic during early diagenesis.

Plate 39. Scanned image of the thin section prepared from sample GT116. Field of view = 48 mm wide.

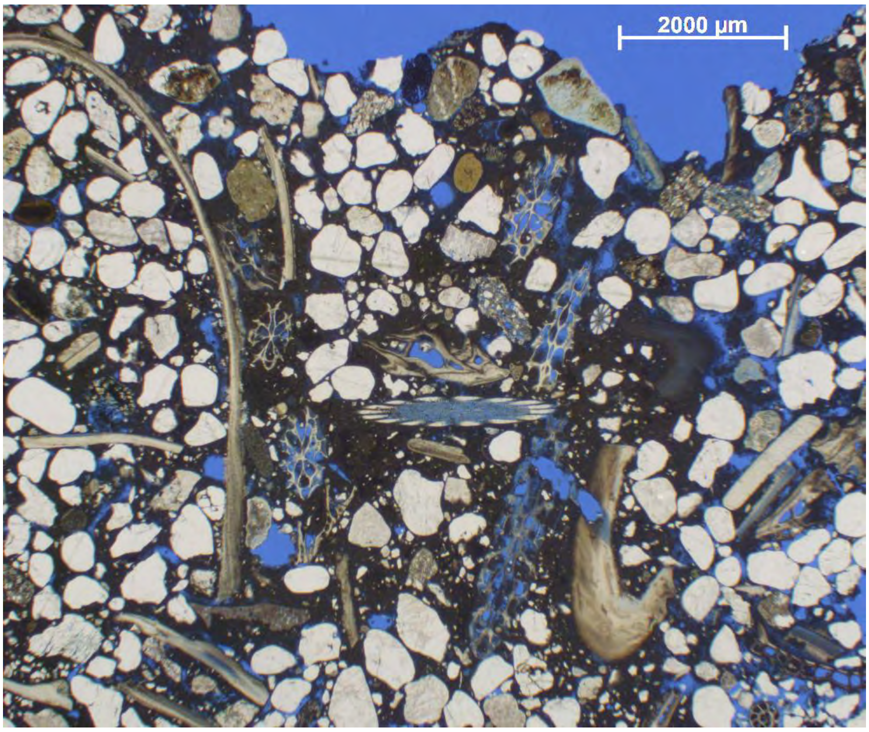

Plate 40. Transmitted light photograph (plain polarised light) showing the medium to coarse grain-supported sandstone fabric, and high matrix and bioclastic content. Sample GT116.

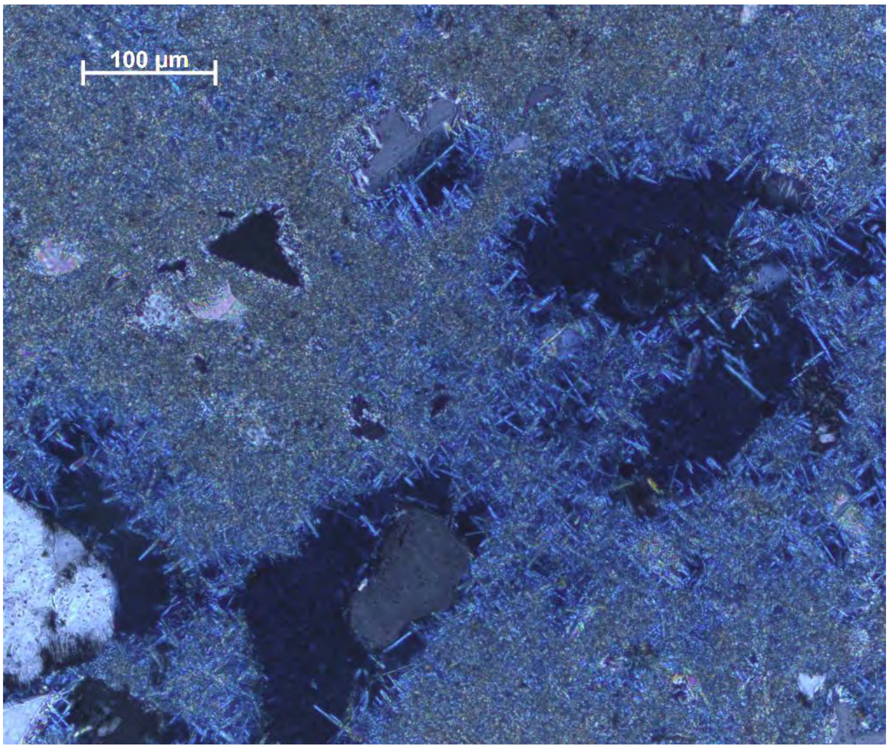

Plate 41. Transmitted light photomicrograph (cross polarised light) showing extensive pore-filling acicular aragonite cement nucleating around diffuse micritic aragonite pelloidal aggregates. Sample GT116.

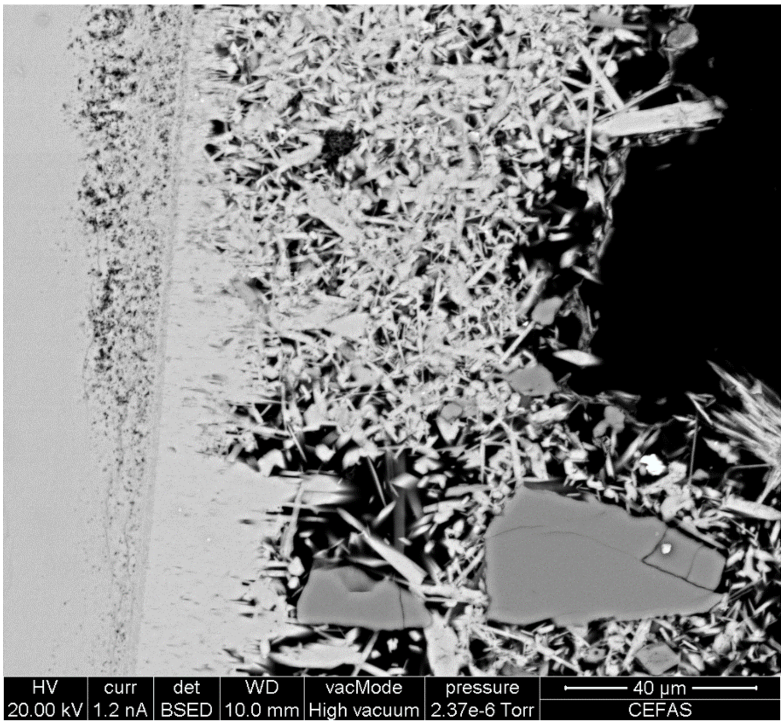

Plate 42. BSEM image showing the acicular nature of the aragonite cement. Sample GT116.

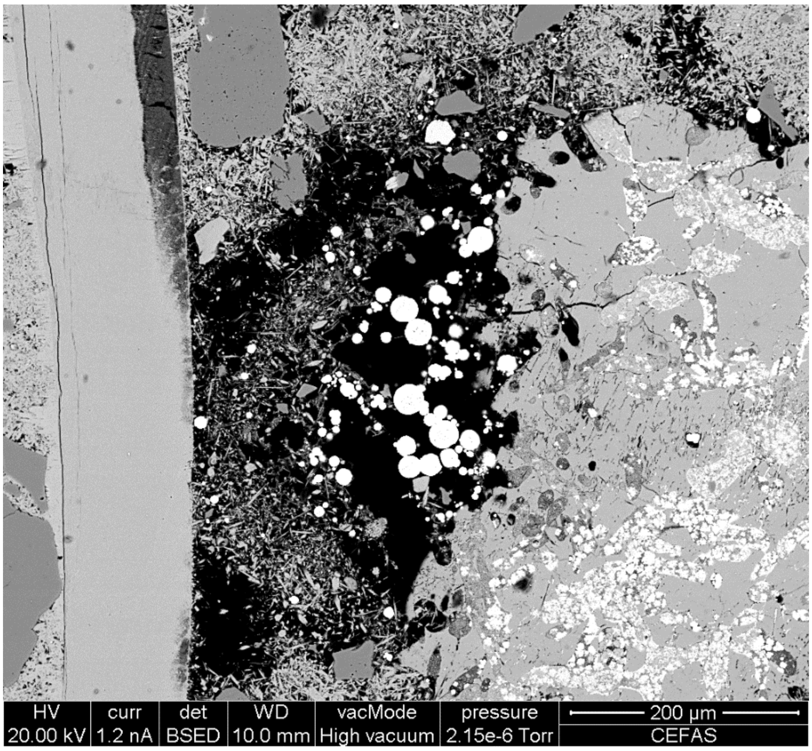

Plate 43. BSEM image showing framboidal pyrite. Note the extensive boring by marine micro-organisms of the bioclastic fragment in the right of the image. Sample GT116.

ED-EPMA major element compositional data for the acicular aragonite cement, and an example shell are given in Table 7. Their compositional variation, expressed in terms of molar proportions of CaO_3-$MgCO_3$ and $SrCO_3$, is summarised in Figure 8.

The acicular cement is strontium bearing, with up to 2 mole % $SrCO_3$ in solid-solution (Figure 8) (i.e. the structural formula of the aragonite can be represented as $Ca_{0.98-1.00}Sr_{0.02-0.00}CO_3$). An example of shell debris that was analysed contained calcite (light areas) as well as high magnesian-calcite (dark areas), and was low in strontium, which was detected in only two analyses. The high magnesian-calcite part of the shell contained 12 mole % $MgCO_3$. The micrite filling shell cavities was more magnesium-rich, and contained between 16 and 18 mole % $MgCO_3$ in solid solution (i.e. the structural formula of the calcite can be represented as $Ca_{0.82-0.84}Mg_{0.18-0.16}CO_3$).

The sequence of sedimentary and post-depositional diagenetic events recorded from sample GT116 can be summarised as follows:

1. Deposition of a moderately sorted medium to coarse sand and silt, along with abundant bioclastic debris.
2. Syndepositional bioturbation.
3. Formation of pyrite under reducing porewater conditions.
4. Precipitation of an acicular aragonite cement and lithification of the sediment.

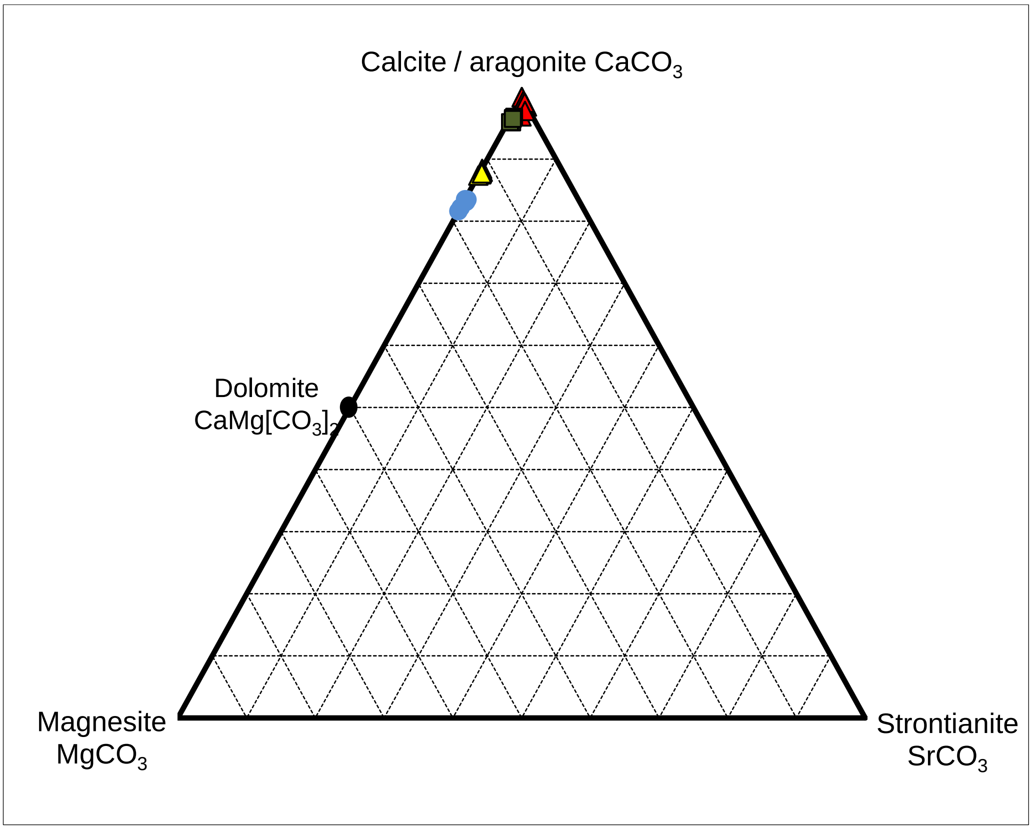

Figure 8. $CaCO_3$-$MgCO_3$-$SrCO_3$ molar ratio plot illustrating the compositions of micritic high-magnesian calcite cement (solid blue circles) located within shell cavities, acicular aragonite cement (red triangles), and dark shell material (yellow triangles), light shell material (green squares) from sample GT116.

Table 7. Electron microprobe analyses from carbonate cements and an example shell fragment from sample GT116

		Weight % oxide (normalised)							Ionic ratio [normalised to 3 [O]						COMMENTS
SAMPLE	No	MgO	CaO	MnO	FeO	SrO	CO_2 (calc)	*Total wt.%	Mg^{2+}	Ca^{2+}	Mn^{2+}	Fe^{2+}	Sr^{2+}	CO_3^{2-}	
GT116	1	0.00	56.04	0.00	0.00	0.00	43.96	100	0.00	1.00	0.00	0.00	0.00	1.00	aragonite cement
GT116	2	0.00	56.04	0.00	0.00	0.00	43.96	100	0.00	1.00	0.00	0.00	0.00	1.00	aragonite cement
GT116	3	0.00	56.04	0.00	0.00	0.00	43.96	100	0.00	1.00	0.00	0.00	0.00	1.00	aragonite cement
GT116	4	0.00	56.04	0.00	0.00	0.00	43.96	100	0.00	1.00	0.00	0.00	0.00	1.00	aragonite cement
GT116	5	0.00	56.04	0.00	0.00	0.00	43.96	100	0.00	1.00	0.00	0.00	0.00	1.00	aragonite cement
GT116	6	0.00	54.79	0.00	0.00	1.55	43.65	100	0.00	0.98	0.00	0.00	0.02	1.00	aragonite cement
GT116	7	0.00	55.08	0.00	0.00	1.20	43.72	100	0.00	0.99	0.00	0.00	0.01	1.00	aragonite cement
GT116	8	0.00	55.01	0.00	0.00	1.29	43.71	100	0.00	0.99	0.00	0.00	0.01	1.00	aragonite cement
GT116	9	0.00	55.03	0.00	0.00	1.26	43.71	100	0.00	0.99	0.00	0.00	0.01	1.00	aragonite cement
GT116	10	0.00	54.92	0.00	0.00	1.40	43.68	100	0.00	0.99	0.00	0.00	0.01	1.00	aragonite cement
GT116	11	0.00	55.18	0.00	0.00	1.08	43.75	100	0.00	0.99	0.00	0.00	0.01	1.00	aragonite cement
GT116	12	0.00	54.92	0.00	0.25	1.12	43.72	100	0.00	0.99	0.00	0.00	0.01	1.00	aragonite cement
GT116	13	0.26	54.53	0.00	0.28	1.17	43.75	100	0.01	0.98	0.00	0.00	0.01	1.00	aragonite cement
GT116	14	0.00	54.97	0.00	0.00	1.33	43.70	100	0.00	0.99	0.00	0.00	0.01	1.00	aragonite cement
GT116	15	0.00	55.59	0.00	0.00	0.56	43.85	100	0.00	0.99	0.00	0.00	0.01	1.00	aragonite cement
GT116	16	0.26	54.49	0.00	0.41	1.08	43.75	100	0.01	0.98	0.00	0.01	0.01	1.00	aragonite cement
GT116	17	0.21	54.72	0.00	0.23	1.08	43.76	100	0.01	0.98	0.00	0.00	0.01	1.00	aragonite cement
GT116	18	0.00	55.25	0.00	0.00	0.99	43.77	100	0.00	0.99	0.00	0.00	0.01	1.00	aragonite cement
GT116	19	0.30	53.65	0.00	1.15	1.24	43.66	100	0.01	0.96	0.00	0.02	0.01	1.00	aragonite cement
GT116	20	0.61	52.77	0.00	1.47	1.54	43.62	100	0.02	0.95	0.00	0.02	0.01	1.00	aragonite cement
GT116	21	0.00	54.99	0.00	0.39	0.87	43.75	100	0.00	0.99	0.00	0.01	0.01	1.00	aragonite cement
GT116	22	0.25	52.99	0.00	1.64	1.58	43.53	100	0.01	0.96	0.00	0.02	0.02	1.00	aragonite cement
GT116	23	4.97	49.96	0.00	0.00	0.32	44.75	100	0.12	0.88	0.00	0.00	0.00	1.00	darker outer rim of shell
GT116	24	5.12	49.42	0.00	0.68	0.00	44.78	100	0.12	0.87	0.00	0.01	0.00	1.00	darker outer rim of shell
GT116	25	4.72	50.50	0.00	0.00	0.00	44.78	100	0.12	0.88	0.00	0.00	0.00	1.00	darker outer rim of shell
GT116	26	4.77	50.14	0.00	0.00	0.38	44.71	100	0.12	0.88	0.00	0.00	0.00	1.00	darker outer rim of shell
GT116	27	4.89	50.04	0.00	0.00	0.33	44.74	100	0.12	0.88	0.00	0.00	0.00	1.00	darker outer rim of shell
GT116	28	1.07	54.39	0.00	0.00	0.50	44.05	100	0.03	0.97	0.00	0.00	0.00	1.00	lighter inner part of shell
GT116	29	1.37	53.37	0.00	0.59	0.66	44.01	100	0.03	0.95	0.00	0.01	0.01	1.00	lighter inner part of shell
GT116	30	1.51	54.01	0.00	0.00	0.33	44.16	100	0.04	0.96	0.00	0.00	0.00	1.00	lighter inner part of shell
GT116	31	1.20	54.31	0.00	0.00	0.41	44.09	100	0.03	0.97	0.00	0.00	0.00	1.00	lighter inner part of shell
GT116	32	1.23	54.21	0.00	0.00	0.48	44.08	100	0.03	0.96	0.00	0.00	0.00	1.00	lighter inner part of shell

		Weight % oxide (normalised)							Ionic ratio [normalised to 3 [O]						COMMENTS
SAMPLE	No	MgO	CaO	MnO	FeO	SrO	CO_2 (calc)	*Total wt.%	Mg^{2+}	Ca^{2+}	Mn^{2+}	Fe^{2+}	Sr^{2+}	CO_3^{2-}	
GT116	33	7.36	47.41	0.00	0.00	0.00	45.23	100	0.18	0.82	0.00	0.00	0.00	1.00	micritic infill of shell
GT116	34	6.78	47.54	0.00	0.25	0.40	45.03	100	0.16	0.83	0.00	0.00	0.00	1.00	micritic infill of shell
GT116	35	6.77	47.87	0.00	0.26	0.00	45.10	100	0.16	0.83	0.00	0.00	0.00	1.00	micritic infill of shell
GT116	36	6.65	47.94	0.00	0.00	0.37	45.03	100	0.16	0.84	0.00	0.00	0.00	1.00	micritic infill of shell
GT116	37	7.62	47.11	0.00	0.00	0.00	45.27	100	0.18	0.82	0.00	0.00	0.00	1.00	micritic infill of shell

**Note: Some analytical totals were low (<90%) because of the microporous nature of the cements. Therefore, all data were normalised to 100%*

2.8 SAMPLE GT117

This sample comprises two sub-angular tabular clasts (up to 80 mm) of dark grey, well-cemented, medium-grained sandstone. One clast has been oxidised and its surface is strongly stained by orange-brown iron-oxyhydroxide (Plate 44). Some bryozoan and calcareous serpulid worm encrustations are present.

Plate 44. Photograph of sample GT117. Grey scale bar divisions = 10 mm.

A scanned image of the thin section prepared from one of the GT117 clasts is shown in Plate 45. This shows the sample to be reasonably well sorted, with a brown coloured cement, that is particularly dark along one edge of the sample (top edge in the image). This colouration is due to iron-oxyhydroxide staining which permeates into the frock from the iron-stained surface. The sandstone is medium-grained (up to 400 μm), and composed predominantly of angular to sub-rounded detrital quartz. The sample is largely matrix-supported, although there are some detrital framework grains with simple point grain-contacts. Some of the quartz grains are 'organised' into well-defined structures that are circular in section (Plate 46). These enigmatic features are most probably agglutinated foraminifera present within the sediment. Rare fragments of calcareous bioclastic debris, comparable in grain size to the detrital quartz, are present. Some limited secondary porosity is present where unstable calcareous bioclastic fragments have dissolved out (Plate 46). The mottled appearance of the rock in thin section suggests that the sediment has been bioturbated prior to lithification.

Bulk XRD analysis identified the presence of major high magnesian-calcite and subordinate aragonite, BSEM petrographic observations show that the matrix of the rock is micritic magnesian-calcite. It occurs as microporous globular aggregates surrounded by blocky rims of coarser euhedral calcite microspar rhombs (Plate 47), which may result from recrystallisation and coarsening-up of the cement (as also seen in other samples, e.g. GT004 and GT112). No discrete aragonite could be recognised from the petrographic observations. However, fine inclusions of more calcic, lower magnesium calcite inclusions were seen within the high magnesian calcite micrite aggregates.

This sample is particularly iron-rich and the micritic cement abundant disseminated fine spherical iron oxyhydroxide grains (Plate 48), some of which may be pseudomorphs after framboidal pyrite. This imparts the brown colouration to the cement seen in thin section. Some intergranular pore spaces (particularly close to the edge of the sample) have been infilled with major amounts of secondary iron oxyhydroxide, and now forms a localised cement. The pore-filling iron oxyhydroxide displays irregular tensional fractures, which are probably a result of dehydration (i.e. desiccation fractures), and indicate that it was originally very hydrous and possibly a poorly-crystalline gel-like phase. Similar secondary iron oxyhydroxide alteration / cement was also observed in samples GT025, GT126 and GT129 and is discussed further in section 2.16 (Volume 2) of this report.

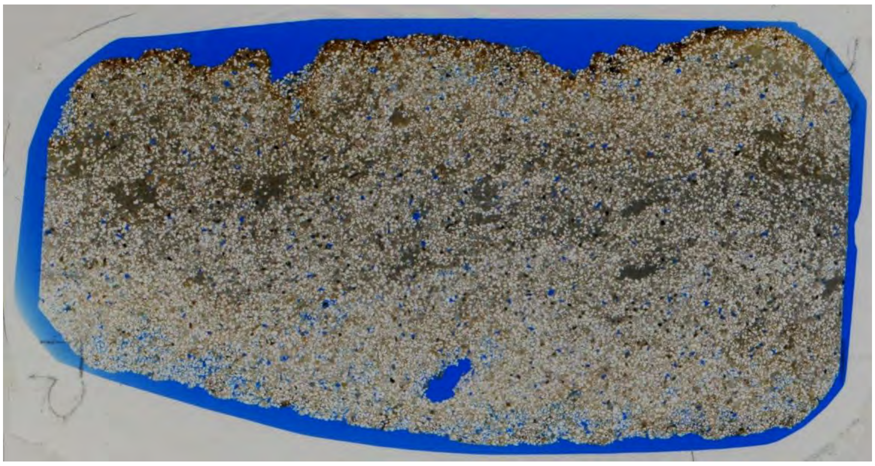

Plate 45. Scanned image of thin section prepared from sample GT117. Field of view = 48 mm wide.

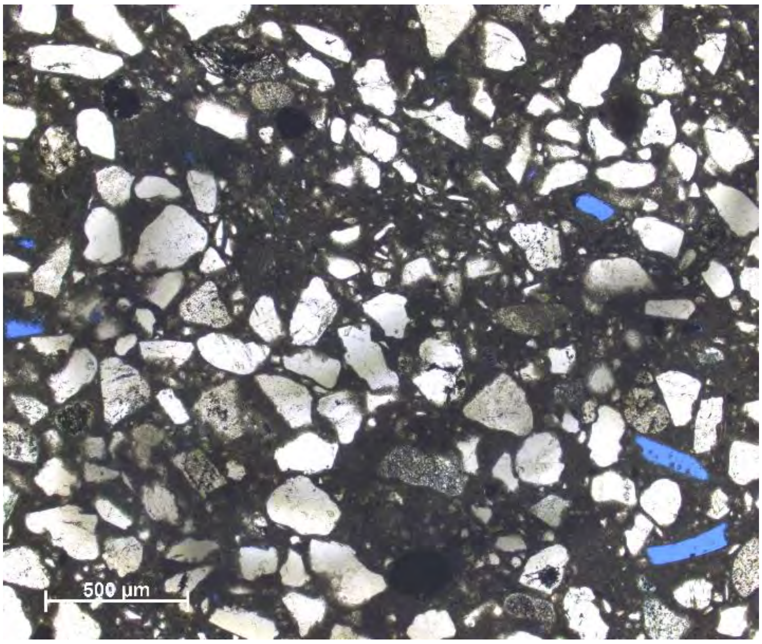

Plate 46. Transmitted light photomicrograph (plain polarised light) showing the dark brown, muddy matrix. Note the ring-like organisation of detrital quartz grains: these probably represent cross-sections through agglutinated foraminifera. Secondary porosity (blue dyed pores) is also present where unstable bioclastic grains have dissolved. GT117

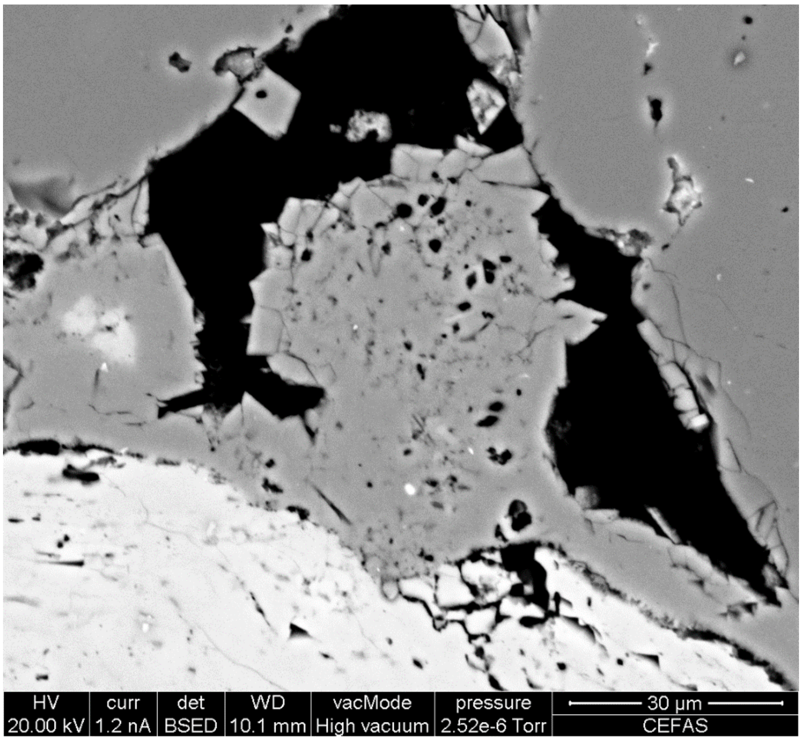

Plate 47. BSEM image of micrite in sample GT117. The micrite aggregate is typically microporous, with small cavities in the core, and a rim of blocky, euhedral magnesian-calcite rhomb overgrowths into open pore space.

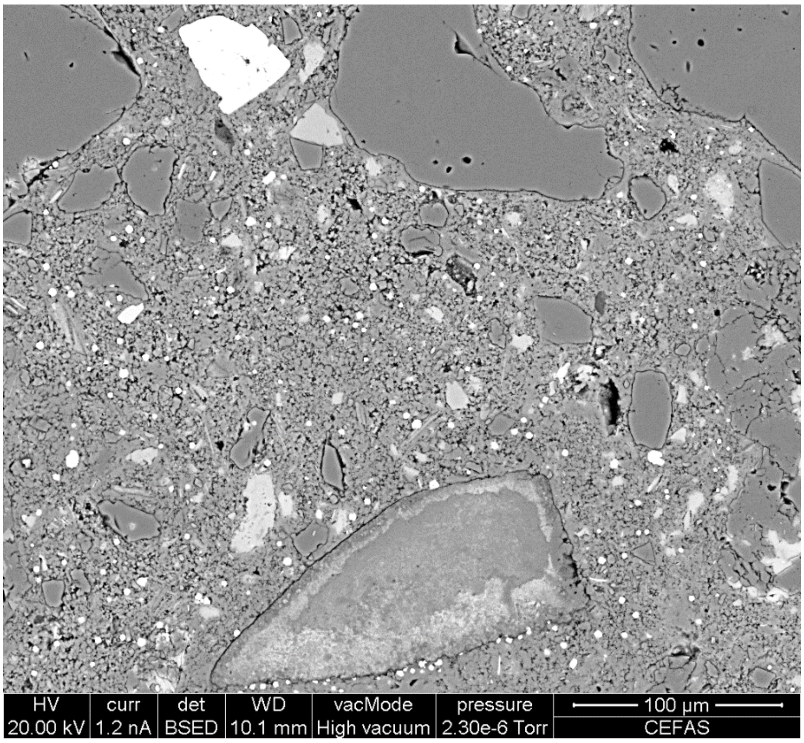

Plate 48. BSEM image showing a well-cemented, matrix supported area from sample GT117. Fine iron oxyhydroxide (white particles) is disseminated throughout the cement. Sample GT117.

ED-EPMA analysis of the carbonate cements are presented in Table 8 and are summarised in Figure 9. The micritic magnesian calcite cements contain between 40 and 43 mole % $MgCO_3$ in solid solution within the crystal lattice (i.e. the structural formula of the calcite can be represented as $Ca_{0.57-0.60}Mg_{0.43-0.40}CO_3$). The calcite inclusions within the micritic magnesian-calcite are more calcic with a lower Mg content (3 – 39 mole % $MgCO_3$). Acicular fringes around some shells also contains 9 – 12 mole % $MgCO_3$, and therefore appear to be calcite rather than aragonite.

The sequence of sedimentary and post-depositional diagenetic events recorded from sample GT117 can be summarised as follows:

1. Deposition of medium-grained sand and silty sediment.
2. Syndepositional bioturbation.
3. Precipitation of micritic high-magnesian calcite within the sediment, causing lithification.
4. Pyrite formation under reducing porewater conditions in close association, and coeval with micritic high-magnesian calcite [2].
5. Oxidation of pyrite within the micrite cement and precipitation of fine secondary iron oxyhydroxide.
6. Colonisation of the rock by bryozoans, and calcareous serpulid worm tubes on the lithified surface of the sediment.

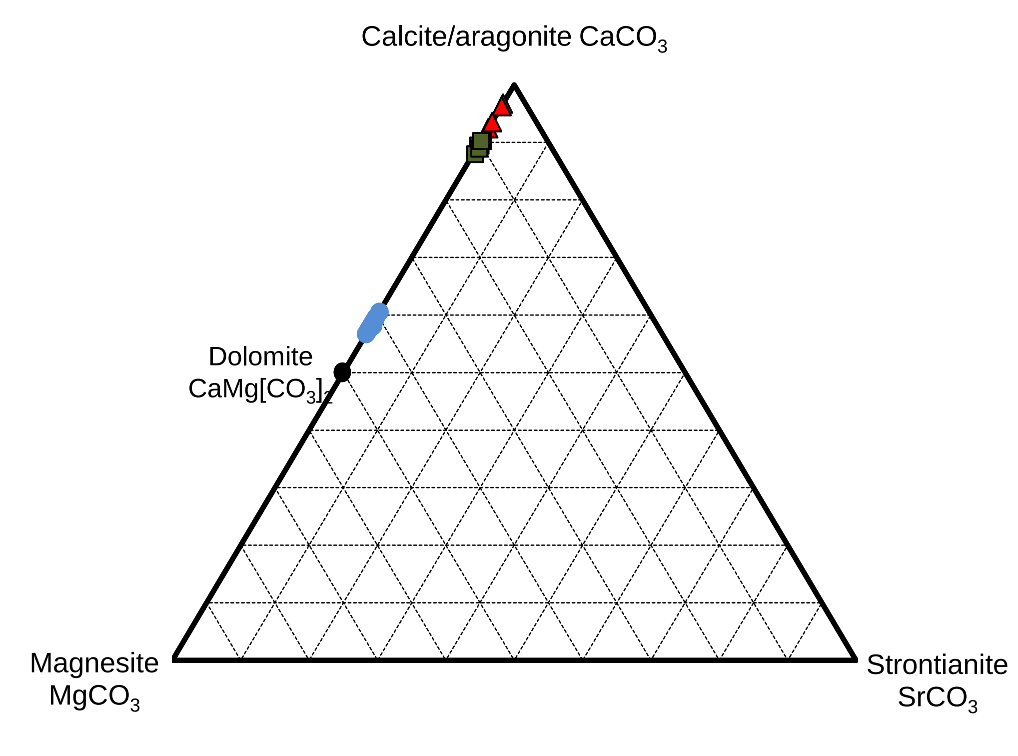

Figure 9. $CaCO_3$-$MgCO_3$-$SrCO_3$ molar ratio plot illustrating the compositions of the micritic cement and blocky microsparite (blue circles), light inclusions within the micrite (red triangles) and acicular fringe around bioclastic fragments (green squares) from sample GT117.

Table 8. Electron microprobe analyses of the carbonate cements and acicular fringes in sample GT117

		Weight % oxide (normalised)							Ionic ratio [normalised to 3 [O]						COMMENTS
SAMPLE	No	MgO	CaO	MnO	FeO	SrO	CO_2 (calc)	*Total wt.%	Mg^{2+}	Ca^{2+}	Mn^{2+}	Fe^{2+}	Sr^{2+}	CO_3^{2-}	
GT117	1	18.05	34.88	0.00	0.00	0.00	47.07	100	0.42	0.58	0.00	0.00	0.00	1.00	blocky microsparite
GT117	2	17.59	35.42	0.00	0.00	0.00	46.99	100	0.41	0.59	0.00	0.00	0.00	1.00	blocky microsparite
GT117	3	17.66	35.34	0.00	0.00	0.00	47.00	100	0.41	0.59	0.00	0.00	0.00	1.00	blocky microsparite
GT117	4	17.91	34.84	0.22	0.00	0.00	47.03	100	0.42	0.58	0.00	0.00	0.00	1.00	blocky microsparite
GT117	5	17.66	35.34	0.00	0.00	0.00	47.00	100	0.41	0.59	0.00	0.00	0.00	1.00	blocky microsparite
GT117	6	17.83	35.14	0.00	0.00	0.00	47.03	100	0.41	0.59	0.00	0.00	0.00	1.00	blocky microsparite
GT117	7	17.50	35.53	0.00	0.00	0.00	46.97	100	0.41	0.59	0.00	0.00	0.00	1.00	blocky microsparite
GT117	8	18.36	34.32	0.00	0.22	0.00	47.10	100	0.43	0.57	0.00	0.00	0.00	1.00	blocky microsparite
GT117	9	18.33	34.55	0.00	0.00	0.00	47.12	100	0.42	0.58	0.00	0.00	0.00	1.00	blocky microsparite
GT117	10	17.71	35.28	0.00	0.00	0.00	47.01	100	0.41	0.59	0.00	0.00	0.00	1.00	blocky microsparite
GT117	11	18.06	34.87	0.00	0.00	0.00	47.07	100	0.42	0.58	0.00	0.00	0.00	1.00	blocky microsparite
GT117	12	18.46	34.02	0.00	0.42	0.00	47.10	100	0.43	0.57	0.00	0.01	0.00	1.00	blocky microsparite
GT117	13	17.24	35.38	0.00	0.49	0.00	46.88	100	0.40	0.59	0.00	0.01	0.00	1.00	blocky microsparite
GT117	14	17.51	35.29	0.00	0.25	0.00	46.95	100	0.41	0.59	0.00	0.00	0.00	1.00	blocky microsparite
GT117	15	17.96	34.10	0.00	0.98	0.00	46.96	100	0.42	0.57	0.00	0.01	0.00	1.00	blocky microsparite
GT117	16	17.93	35.02	0.00	0.00	0.00	47.05	100	0.42	0.58	0.00	0.00	0.00	1.00	blocky microsparite
GT117	17	17.88	35.08	0.00	0.00	0.00	47.04	100	0.41	0.59	0.00	0.00	0.00	1.00	blocky microsparite
GT117	18	18.12	34.10	0.00	0.76	0.00	47.01	100	0.42	0.57	0.00	0.01	0.00	1.00	micrite
GT117	19	17.77	34.58	0.15	0.24	0.34	46.92	100	0.41	0.58	0.00	0.00	0.00	1.00	micrite
GT117	20	17.82	33.46	0.00	1.87	0.00	46.85	100	0.42	0.56	0.00	0.02	0.00	1.00	micrite
GT117	21	17.96	32.71	0.00	2.52	0.00	46.81	100	0.42	0.55	0.00	0.03	0.00	1.00	micrite
GT117	22	18.09	34.62	0.00	0.24	0.00	47.05	100	0.42	0.58	0.00	0.00	0.00	1.00	micrite
GT117	23	17.71	34.88	0.00	0.44	0.00	46.97	100	0.41	0.58	0.00	0.01	0.00	1.00	micrite
GT117	24	17.61	34.62	0.00	0.86	0.00	46.91	100	0.41	0.58	0.00	0.01	0.00	1.00	micrite
GT117	25	17.58	35.03	0.17	0.28	0.00	46.95	100	0.41	0.59	0.00	0.00	0.00	1.00	micrite
GT117	26	17.63	33.65	0.31	1.59	0.00	46.82	100	0.41	0.56	0.00	0.02	0.00	1.00	micrite
GT117	27	17.90	34.76	0.00	0.33	0.00	47.01	100	0.42	0.58	0.00	0.00	0.00	1.00	micrite
GT117	28	17.85	34.67	0.22	0.26	0.00	46.99	100	0.41	0.58	0.00	0.00	0.00	1.00	micrite
GT117	29	1.28	52.81	0.00	1.91	0.00	44.00	100	0.03	0.94	0.00	0.03	0.00	1.00	light micrite inclusion
GT117	30	1.47	53.73	0.00	0.64	0.00	44.16	100	0.04	0.95	0.00	0.01	0.00	1.00	light micrite inclusion
GT117	31	2.99	51.02	0.00	1.67	0.00	44.32	100	0.07	0.90	0.00	0.02	0.00	1.00	light micrite inclusion
GT117	32	16.61	35.48	0.00	1.21	0.00	46.70	100	0.39	0.60	0.00	0.02	0.00	1.00	light micrite inclusion

		Weight % oxide (normalised)							Ionic ratio [normalised to 3 [O]						COMMENTS
SAMPLE	No	MgO	CaO	MnO	FeO	SrO	CO_2 (calc)	*Total wt.%	Mg^{2+}	Ca^{2+}	Mn^{2+}	Fe^{2+}	Sr^{2+}	CO_3^{2-}	
GT117	33	2.55	51.58	0.00	1.62	0.00	44.25	100	0.06	0.91	0.00	0.02	0.00	1.00	light micrite inclusion
GT117	34	4.30	50.81	0.00	0.20	0.00	44.68	100	0.11	0.89	0.00	0.00	0.00	1.00	microporous acicular fringe of shell
GT117	35	4.12	50.14	0.00	0.84	0.39	44.51	100	0.10	0.88	0.00	0.01	0.00	1.00	microporous acicular fringe of shell
GT117	36	4.77	49.89	0.00	0.32	0.32	44.69	100	0.12	0.88	0.00	0.00	0.00	1.00	microporous acicular fringe of shell
GT117	37	4.30	50.12	0.00	0.54	0.48	44.56	100	0.11	0.88	0.00	0.01	0.00	1.00	microporous acicular fringe of shell
GT117	38	3.83	51.04	0.00	0.24	0.37	44.53	100	0.09	0.90	0.00	0.00	0.00	1.00	microporous acicular fringe of shell
GT117	39	3.95	51.08	0.00	0.36	0.00	44.61	100	0.10	0.90	0.00	0.00	0.00	1.00	microporous acicular fringe of shell

**Note: Some analytical totals were low (<90%) because of the microporous nature of the cements. Therefore, all data were normalised to 100%*

2.9 SAMPLE GT120

Sample GT120 comprised three clasts from approximately 20 mm to 70 mm diameter. These clasts are sub-tabular: no more than 30 mm thick, with rough, irregular surfaces (Plate 49). The clasts are light buff colour, medium- to coarse-grained shelly sandstone, which contains a high proportion of coarse bioclastic detritus (grains up to 1200 µm, bioclastic fragments up to 30 mm).

Plate 49. Photograph showing sample GT120. Numerous fragments of calcareous bioclastic detritus have been incorporated into this coarse-grained sandstone. Some evidence of burrowing / borings on the surfaces. Grey scale bar divisions = 10 mm.

The polished thin section prepared through one of the GT120 clasts is shown in Plate 50. The coarse calcareous bioclastic fragments are clearly visible and are strongly aligned parallel to bedding. Some of the shelly fragments display evidence of boring by marine organisms. In some cases, these borings also cut the adjacent carbonate cement, which demonstrates that at least some of the boring occurred after lithification.

Detrital grains are dominantly quartz with minor lithic fragments, plagioclase and K-feldspars. The bioclastic detritus is dominated by bivalve shells and foraminiferal tests. A high proportion of quartz grains are moderately well-rounded and probably derived from wind-blown aeolian sands. The sandstone contains abundant pelloidal grains composed of micritic carbonate (Plate 51). These pelloids have a similar grain (up to 600 µm) size to the quartz sand, are very well rounded, contain inclusions of detrital silt-grade quartz and bioclastic calcite, often singly or in ‘bunch-of-grape-like’ clusters (Plate 51), and are interpreted as faecal pellets. Some micrite pelloids are ferruginous and stained brown by finely-disseminated iron oxyhydroxide. BSEM observations reveal the preservation of a microporous and microcellular or framboidal fabric within the micritic carbonate matrix of some of these pelloidal grains (Plate 52). This fabric may be of microbial origin. The sandstone also contains a patchily-distributed dark, clay-rich matrix dominated by very fine angular quartz silt and clay minerals (this can be seen in pat in Plate 53).

Petrographic observations show that aragonite occurs as coarse acicular prismatic crystals up to 500 µm long, forming an intergranular cement (Plate 51 to Plate 53). Often the aragonite forms ‘sheaf-like’ crystal aggregates, or radiating ‘sprays’ of needles. Some of these sprays have bands of more porous material imparting a colloform texture. This banded or colloform fabric is probably a result of oscillatory periods of growth followed by hiatus. The aragonite cement has nucleated on most pore surfaces to form fibrous isopachous fringes. It is particularly well-developed as isopachous fringes and as pore-filling cement, where it has nucleated around the micritic and clay-rich pelloidal grains (Plate 51 and Plate 52) and calcareous shell fragments (Plate 51). Micrite is also present as grain-coating films, preserved beneath later fibrous aragonite. Since bulk XRD analysis (Volume 1: Table 2) shows that aragonite is the major carbonate mineral present, with minor calcite, the early micrite films and micritic pelloids must also be composed largely of aragonite rather than calcite. The shell detritus will be largely responsible for contributing the calcite identified by XRD.

In some areas of the sandstone, a thin film of clay has been deposited on top of the aragonite needles (Plate 53). This film forms a meniscus lining the residual pores and may represent infiltrated clay deposited as a meniscus along a gas/water interface of trapped gas bubbles in the sediment.

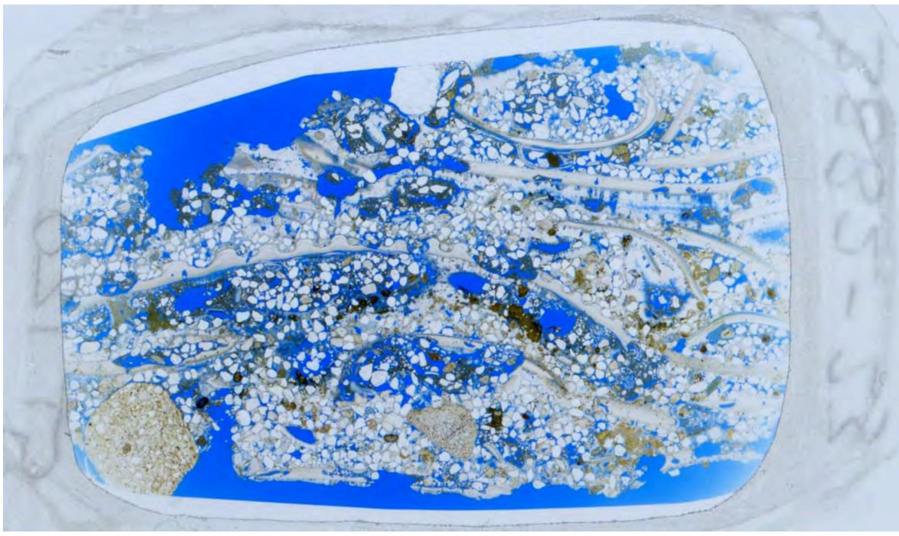

Plate 50. Scan of sample GT120 polished thin section. This sample has a high proportion of shelly material incorporated within it. Some spherical voids indicate bioturbation (cross-sectioned burrows and borings). Cementation is patchy, with areas of tight cementation, and areas of high porosity. Field of view = 48 mm wide.

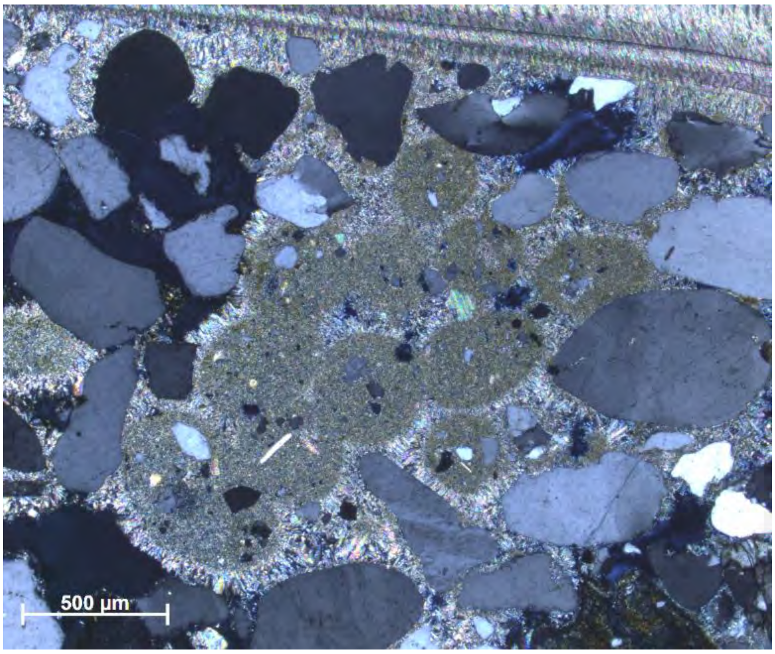

Plate 51. Transmitted light photomicrograph (crossed polarised light) showing a cluster of well-rounded rounded micritic pelloidal grains containing detrital silt-grade silicate minerals. The micrite pelloids are rimmed with acicular aragonite. At the top of the image is a bivalve shell which also has an isopachous rim of acicular aragonite. Sample GT120.

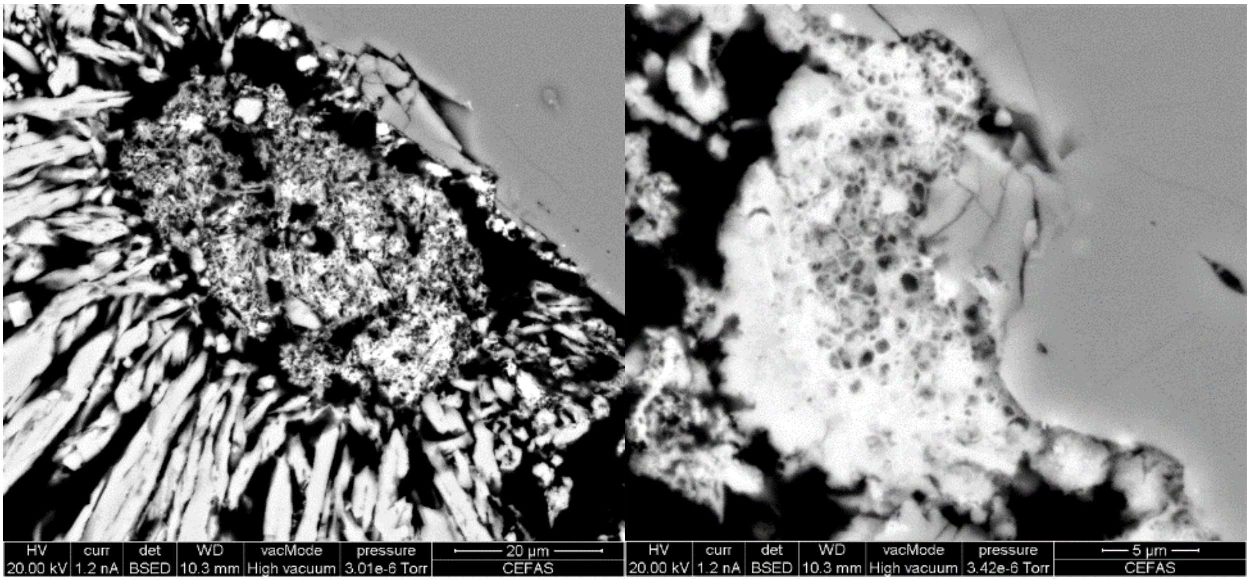

Plate 52. BSEM images of the ferruginous clay-micrite pellets on which fibrous aragonite has nucleated. Left: aragonite needles are clearly growing outward from the pellet. Right: detail of a ferruginous micritic carbonate pelloid, which has a porous microcellular texture of possible microbial origin. Sample GT120.

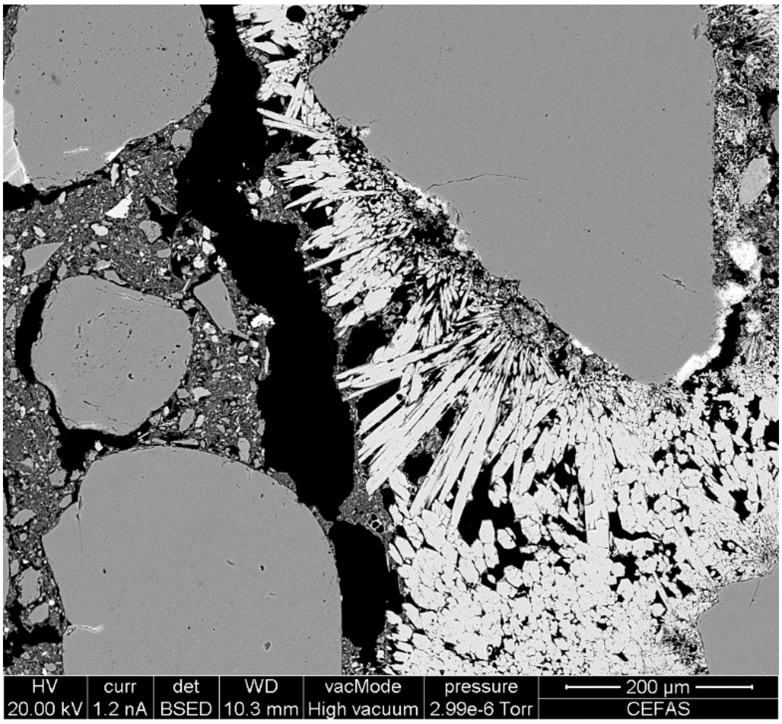

Plate 53. BSEM image of acicular aragonite that has nucleated on a ferruginous, micritic coating around a quartz grain, and has grown into the open intergranular pores. The ends of the needles towards the centre of the image are coated with a thin film of clay. Cross-sections of the needles in the lower-right of the image have an orthorhombic form, typical of aragonite. Sample GT120.

ED-EPMA major element compositional data for the aragonite cements and examples of shelly fragments are given in Figure 10. Their compositional variation, expressed in terms of molar proportions of CaO_3-$MgCO_3$ and $SrCO_3$, is summarised in Table 9.

The aragonite is strontium bearing, with <2 mole % $SrCO_3$ in solid-solution (Figure 10) (i.e. the structural formula (i.e. the structural formula of the aragonite can be represented as $Ca_{0.98\text{-}1.00}Sr_{0.02\text{-}0.00}CO_3$).

No magnesian calcite cement was identified by XRD, petrographic analysis or ED-EPMA in this sample.

The sequence of sedimentary and post-depositional diagenetic events recorded from sample GT120 can be summarised as follows:

1. Deposition of coarse sandy sediment, faecal pellets and shelly debris.
2. Precipitation of micritic aragonite
3. Precipitation of later acicular aragonite cement and sediment lithification. Evidence suggests aragonite crystal growth may have been locally terminated by the presence of gas-filled pores in the sediment.
4. Colonisation of lithified sandstone surfaces by boring organisms. This may indicate that the precipitation of MDAC had ceased prior to the colonisation.

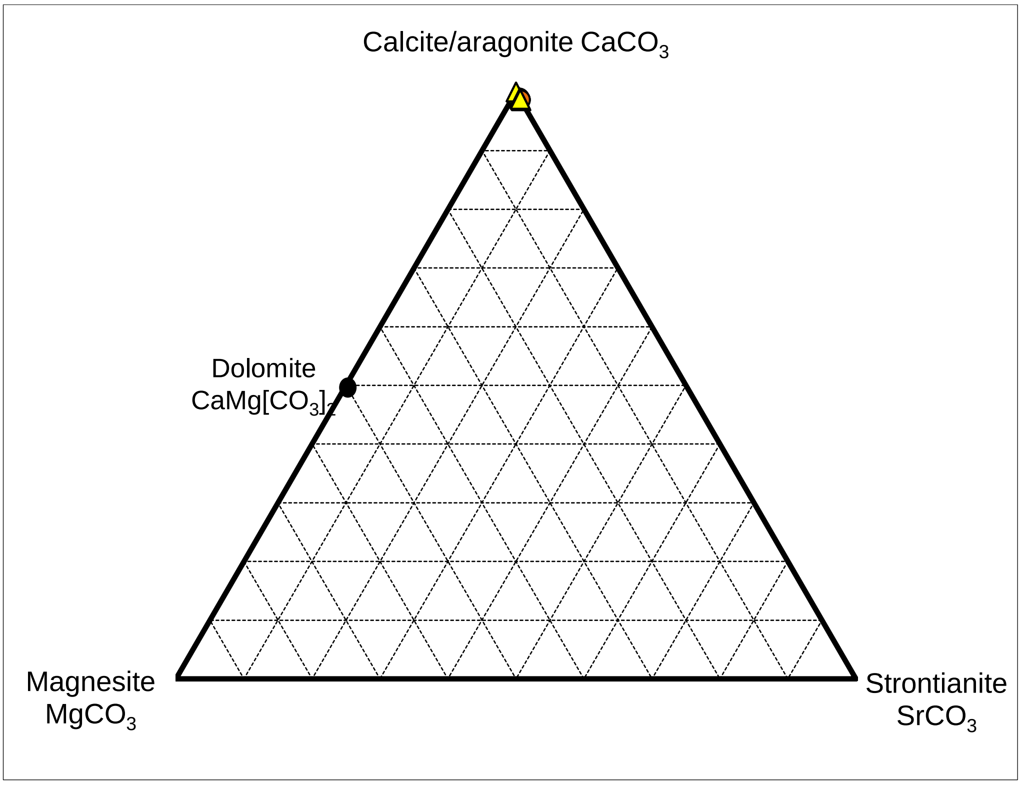

Figure 10. $CaCO_3$-$MgCO_3$-$SrCO_3$ molar ratio plot illustrating the compositions of the different carbonate components in sample GT120 (pore-filling acicular aragonite cement, isopachous aragonite fringe cement, a bivalve shell and shelly fragment).

Table 9. Electron microprobe analyses of shelly fragments and aragonite cements in sample GT120

		Weight % oxide (normalised)							Ionic ratio [normalised to 3 [O]						COMMENTS
SAMPLE	No	MgO	CaO	MnO	FeO	SrO	CO_2 (calc)	*Total wt.%	Mg^{2+}	Ca^{2+}	Mn^{2+}	Fe^{2+}	Sr^{2+}	CO_3^{2-}	
GT120	1	0.00	56.04	0.00	0.00	0.00	43.96	100	0.00	1.00	0.00	0.00	0.00	1.00	bivalve shell
GT120	2	0.00	56.04	0.00	0.00	0.00	43.96	100	0.00	1.00	0.00	0.00	0.00	1.00	bivalve shell
GT120	3	0.00	56.04	0.00	0.00	0.00	43.96	100	0.00	1.00	0.00	0.00	0.00	1.00	bivalve shell
GT120	4	0.00	56.04	0.00	0.00	0.00	43.96	100	0.00	1.00	0.00	0.00	0.00	1.00	bivalve shell
GT120	5	0.00	56.04	0.00	0.00	0.00	43.96	100	0.00	1.00	0.00	0.00	0.00	1.00	bivalve shell
GT120	6	0.00	56.04	0.00	0.00	0.00	43.96	100	0.00	1.00	0.00	0.00	0.00	1.00	bivalve shell
GT120	7	0.00	56.04	0.00	0.00	0.00	43.96	100	0.00	1.00	0.00	0.00	0.00	1.00	bivalve shell
GT120	8	0.00	56.04	0.00	0.00	0.00	43.96	100	0.00	1.00	0.00	0.00	0.00	1.00	bivalve shell
GT120	9	0.00	56.04	0.00	0.00	0.00	43.96	100	0.00	1.00	0.00	0.00	0.00	1.00	bivalve shell
GT120	10	0.00	55.76	0.00	0.00	0.34	43.90	100	0.00	1.00	0.00	0.00	0.00	1.00	bivalve shell
GT120	11	0.00	55.81	0.00	0.25	0.00	43.94	100	0.00	1.00	0.00	0.00	0.00	1.00	shell fragment
GT120	12	0.00	56.04	0.00	0.00	0.00	43.96	100	0.00	1.00	0.00	0.00	0.00	1.00	shell fragment
GT120	13	0.00	55.17	0.00	0.00	1.08	43.75	100	0.00	0.99	0.00	0.00	0.01	1.00	shell fragment
GT120	14	0.00	55.03	0.00	0.00	1.25	43.71	100	0.00	0.99	0.00	0.00	0.01	1.00	shell fragment
GT120	15	0.00	55.19	0.00	0.00	1.06	43.75	100	0.00	0.99	0.00	0.00	0.01	1.00	shell fragment
GT120	16	0.00	55.01	0.00	0.00	1.28	43.71	100	0.00	0.99	0.00	0.00	0.01	1.00	shell fragment
GT120	17	0.00	54.96	0.00	0.00	1.35	43.69	100	0.00	0.99	0.00	0.00	0.01	1.00	aragonite fringe
GT120	18	0.00	55.01	0.00	0.00	1.29	43.70	100	0.00	0.99	0.00	0.00	0.01	1.00	aragonite fringe
GT120	19	0.00	55.03	0.00	0.00	1.26	43.71	100	0.00	0.99	0.00	0.00	0.01	1.00	aragonite fringe
GT120	20	0.00	54.98	0.00	0.00	1.32	43.70	100	0.00	0.99	0.00	0.00	0.01	1.00	aragonite fringe
GT120	21	0.00	55.12	0.00	0.00	1.15	43.73	100	0.00	0.99	0.00	0.00	0.01	1.00	aragonite fringe
GT120	22	0.00	54.93	0.00	0.00	1.39	43.68	100	0.00	0.99	0.00	0.00	0.01	1.00	aragonite fringe
GT120	23	0.00	55.24	0.00	0.00	0.99	43.76	100	0.00	0.99	0.00	0.00	0.01	1.00	aragonite fringe
GT120	24	0.00	55.17	0.00	0.00	1.08	43.75	100	0.00	0.99	0.00	0.00	0.01	1.00	aragonite fringe
GT120	25	0.00	55.18	0.00	0.00	1.08	43.75	100	0.00	0.99	0.00	0.00	0.01	1.00	aragonite fringe
GT120	26	0.00	54.97	0.00	0.00	1.34	43.70	100	0.00	0.99	0.00	0.00	0.01	1.00	aragonite fringe
GT120	27	0.00	54.94	0.00	0.00	1.37	43.69	100	0.00	0.99	0.00	0.00	0.01	1.00	acicular aragonite cement
GT120	28	0.00	55.45	0.00	0.00	0.74	43.82	100	0.00	0.99	0.00	0.00	0.01	1.00	acicular aragonite cement
GT120	29	0.00	55.20	0.00	0.00	1.05	43.75	100	0.00	0.99	0.00	0.00	0.01	1.00	acicular aragonite cement
GT120	30	0.00	54.99	0.00	0.00	1.31	43.70	100	0.00	0.99	0.00	0.00	0.01	1.00	acicular aragonite cement
GT120	31	0.00	55.04	0.00	0.00	1.24	43.71	100	0.00	0.99	0.00	0.00	0.01	1.00	acicular aragonite cement
GT120	32	0.00	55.19	0.00	0.00	1.06	43.75	100	0.00	0.99	0.00	0.00	0.01	1.00	acicular aragonite cement

		Weight % oxide (normalised)							Ionic ratio [normalised to 3 [O]						COMMENTS
SAMPLE	No	MgO	CaO	MnO	FeO	SrO	CO_2 (calc)	*Total wt.%	Mg^{2+}	Ca^{2+}	Mn^{2+}	Fe^{2+}	Sr^{2+}	CO_3^{2-}	
GT120	33	0.00	55.32	0.00	0.00	0.89	43.79	100	0.00	0.99	0.00	0.00	0.01	1.00	acicular aragonite cement
GT120	34	0.00	55.09	0.00	0.00	1.19	43.73	100	0.00	0.99	0.00	0.00	0.01	1.00	acicular aragonite cement
GT120	35	0.00	55.36	0.00	0.00	0.85	43.79	100	0.00	0.99	0.00	0.00	0.01	1.00	acicular aragonite cement
GT120	36	0.00	55.29	0.00	0.00	0.94	43.78	100	0.00	0.99	0.00	0.00	0.01	1.00	acicular aragonite cement
GT120	37	0.00	55.00	0.00	0.00	1.29	43.70	100	0.00	0.99	0.00	0.00	0.01	1.00	acicular aragonite cement
GT120	38	0.00	54.97	0.00	0.00	1.34	43.69	100	0.00	0.99	0.00	0.00	0.01	1.00	acicular aragonite cement
GT120	39	0.00	55.05	0.00	0.00	1.23	43.72	100	0.00	0.99	0.00	0.00	0.01	1.00	acicular aragonite cement
GT120	40	0.00	54.80	0.00	0.00	1.55	43.65	100	0.00	0.98	0.00	0.00	0.02	1.00	acicular aragonite cement
GT120	41	0.00	54.89	0.00	0.00	1.43	43.68	100	0.00	0.99	0.00	0.00	0.01	1.00	acicular aragonite cement
GT120	42	0.00	54.86	0.00	0.00	1.47	43.67	100	0.00	0.99	0.00	0.00	0.01	1.00	acicular aragonite cement
GT120	43	0.00	55.13	0.00	0.00	1.13	43.74	100	0.00	0.99	0.00	0.00	0.01	1.00	acicular aragonite cement
GT120	44	0.00	54.97	0.00	0.00	1.34	43.70	100	0.00	0.99	0.00	0.00	0.01	1.00	acicular aragonite cement

**Note: Some analytical totals were low (<90%) because of the microporous nature of the cements. Therefore, all data were normalised to 100%*

2.10 SAMPLE GT121

This sample comprises one main (<140 mm), and two subordinate, irregular shaped clasts (<70 mm) of buff coloured, medium grained sandstone (Plate 54). The sample is heavily bioturbated with large burrows infilled with coarse sand grains and silt, along with some bioclastic debris. Bryozoan and calcareous serpulid worm encrustations are observed on the surface. Some evidence of borings by marine micro-biota is present. The surfaces of the clasts patchily-stained by orange-brown iron-oxyhydroxides.

Plate 54. Photograph of sample GT121. Grey scale bar divisions = 10 mm.

The thin section produced from one of the clasts comprising sample GT121 is shown in Plate 55. The rock comprises largely medium grained, well-sorted sandstone dominated by quartz, with sub-angular to sub-rounded grains (up to 400 µm). It has a grain-supported fabric with grains in simple point contact. However, the thin section also includes a profile section through a large vertical burrow, which has been infilled with winnowed, coarse grained sand (grain size up to 800 µm), fine silt and some bioclastic debris. Carbonate cementation is patchy, producing a mottled appearance in thin section, with large areas displaying high intergranular porosity with some oversized framework grain dissolution pores (Plate 56), and areas that are tightly carbonate cemented (Plate 57). In thin section, buff-coloured carbonate cement can be seen to be concentrated in the sandstone immediately adjacent to the walls of the large vertical burrow (Plate 55). This implies that the burrow channel has influenced the transport of diagenetic porewaters and the precipitation of carbonate cement.

XRD analysis (Volume 1: Table 2) identified aragonite as the major carbonate mineral present (24.8 wt. % of the rock), with minor calcite and high magnesian-calcite. Two discrete carbonate cements can be differentiated from the petrographic observations: (i) early magnesian calcite micrite partially crystallised to blockier microsparite, and; (ii) later acicular pore-filling aragonite (Plate 57). The aragonite has nucleated on top of pre-existing micrite surfaces (where present e.g.

Plate 58). BSEM shows the micrite to be compositionally-zoned (e.g. Plate 59). Variations in the brightness of the BSEM image reflects variations in the magnesium content corresponding to the compositional variation summarised in Figure 12 and Table 10. The very darkest areas are close to dolomite end member composition. Some of these areas may possibly represent inclusions of relict reworked earlier MDAC material.

Some areas of the cement show a distinctive, microporous texture. Some of the microporosity appears to be microscopic channels that were possibly created by boring microorganisms. In other cases, the carbonate cement appears to preserve a microcellular texture that may represent a microbial fabric (Plate 60). Similar textures have been observed seen within the micrite in other samples (e.g. GT004, GT112).

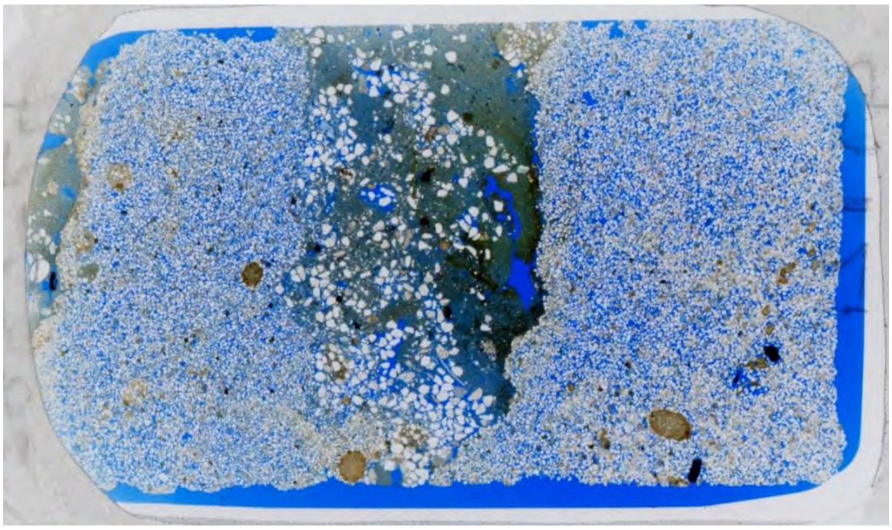

Plate 55. Scanned image of the thin section prepared from sample GT121. Note the large burrow in the centre of the section which has subsequently been infilled with coarser, winnowed sand, and fine-grained silt which contrast to the rest of the sample. Field of view = 48 mm wide.

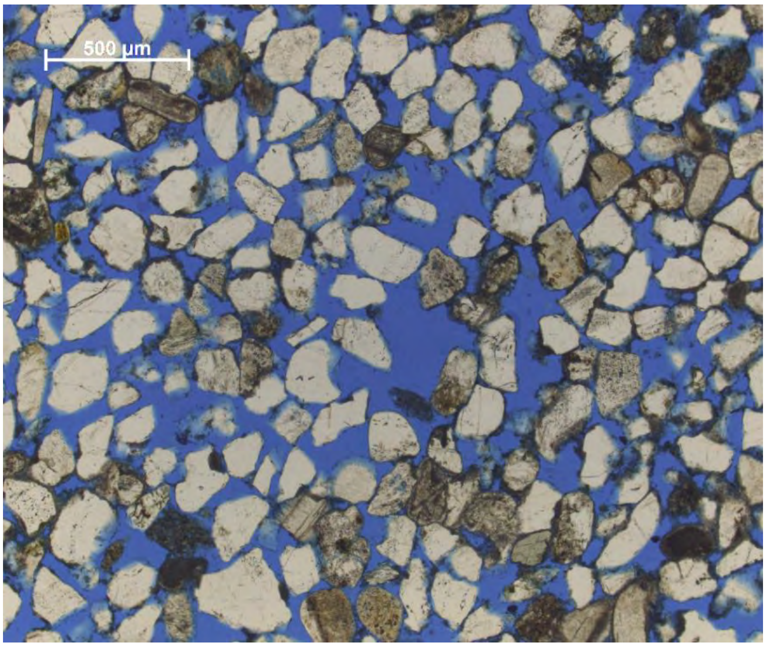

Plate 56. Optical photomicrograph showing an area of high porosity with oversized pore spaces, probably caused by dissolution and removal of the original cement. GT121.

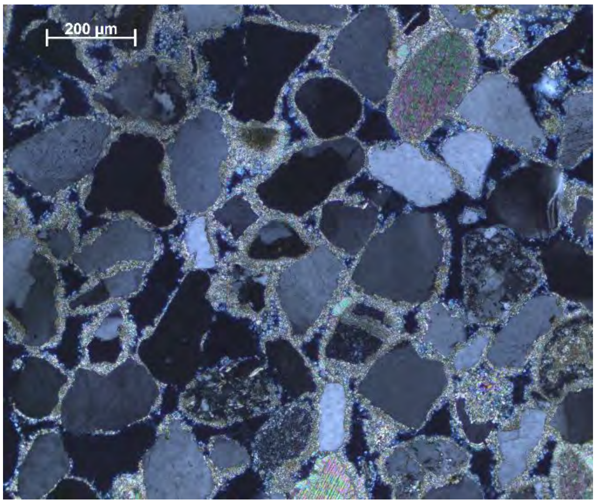

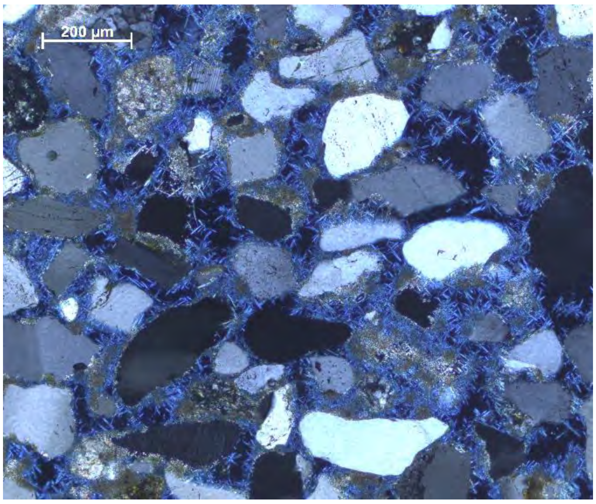

Plate 57. Transmitted light photomicrographs (cross polarised light) showing two contrasting cements: left, birefringent grain-coating micrite and microsparite fringes; right, pore-filling acicular aragonite. GT121.

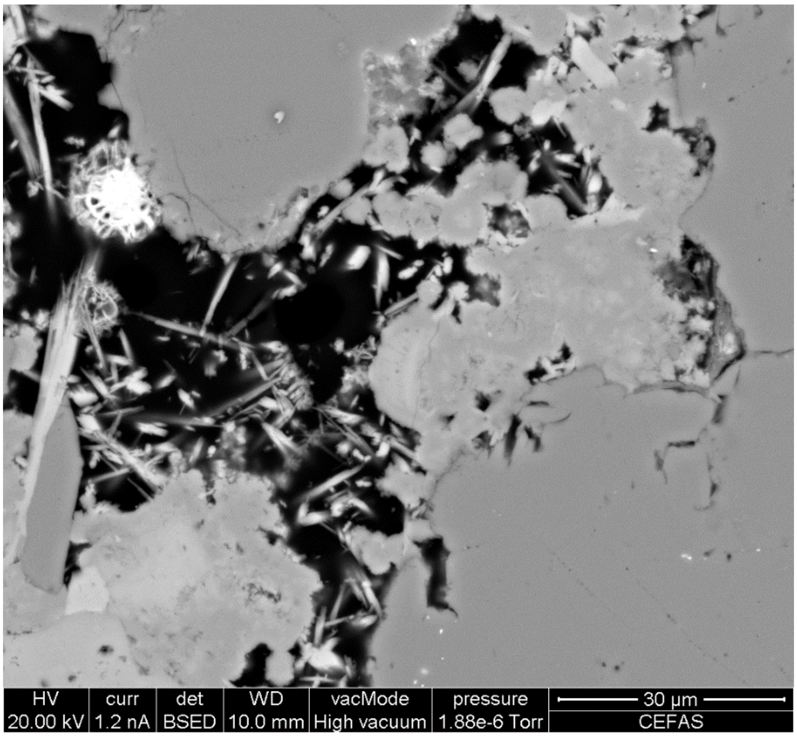

Plate 58. BSEM image of the cements in sample GT121. This image shows early, microspherulitic or globular grain-coating micrite (showing a slight greyscale variation indicating a compositional change) and later pore-filling acicular aragonite resting on the micrite surfaces.

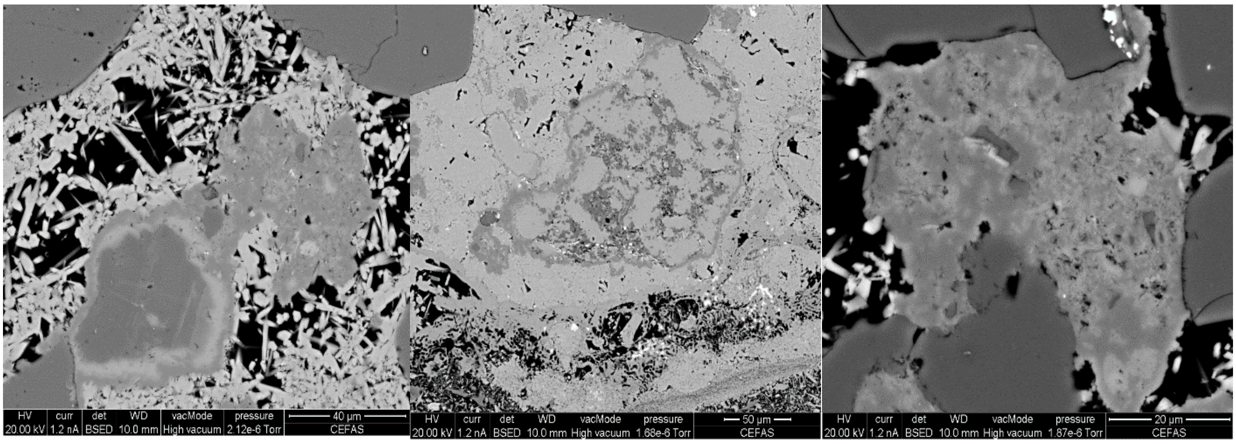

Plate 59. BSEM images showing compositional zoning within the micritic cement. The darker areas are very high in magnesium, and are close to dolomite end-member compositions. These may comprise relicts of reworked earlier MDAC-derived material. GT121.

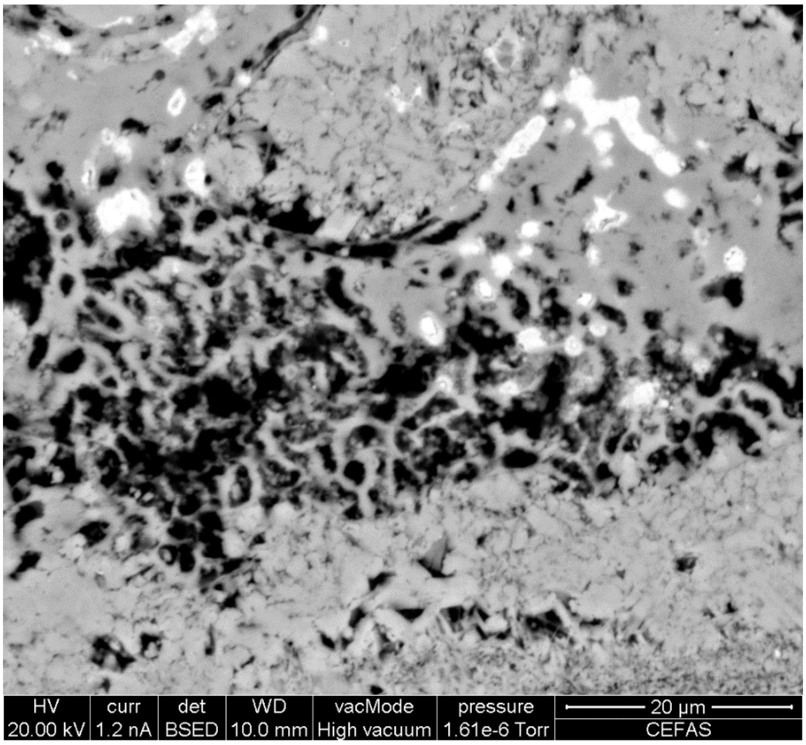

Plate 60. BSEM image showing some micrite cement with distinctive microcellular texture, and some disseminated secondary iron oxyhydroxide. The texture may represent the preservation of a carbonate-mineralised microbial fabric. Sample GT121.

ED-EPMA major element compositional data for the cements in sample GT121 are given in Table 10. Their compositional variation, expressed in terms of molar proportions of CaO_3-$MgCO_3$ and $SrCO_3$, is summarised in Figure 11 and Figure 12. The micritic magnesian calcite cements show a large range in compositions, containing between 0 and 35 mole % $MgCO_3$ in solid solution (i.e. the structural formula of the calcite can be represented as $Ca_{0.65\text{-}1.00}Mg_{0.35\text{-}0.00}CO_3$). This range may in part be due to mixed analyses resulting from the patchy nature of the zoned micrite, and/or inclusion of intimately mixed aragonite within the micritic calcite analyses. The darkest areas within the patchy and zoned micrite as shown in Plate 59, are close to dolomite end-member composition (up to 49 mole % $MgCO_3$), and may be relict earlier MDAC.

The acicular aragonite is strontium bearing, with 1 mole % $SrCO_3$ in solid-solution (i.e. the structural formula (i.e. the structural formula of the aragonite can be represented as $Ca_{0.99\text{-}1.00}Sr_{0.01\text{-}0.00}CO_3$). This is similar to aragonite found in other samples.

The sequence of sedimentary and post-depositional diagenetic events recorded from sample GT121 can be summarised as follows:

1. Deposition of initial, medium-grained sandy sediment.
2. Bioturbation by burrowing marine biota. These burrows provided channels into the sediment that appear to have locally influenced the subsequent transport of carbonate-mineralising fluids.
3. Initial cementation by micritic magnesian calcite.
4. Precipitation of later acicular aragonite cement causing further lithification and development of a calcareous crust.
5. Oxidation and precipitation of secondary iron-manganese oxyhydroxide-rich cement and coatings.
6. Encrustation of surfaces by bryozoan and calcareous worm / serpulid casings.

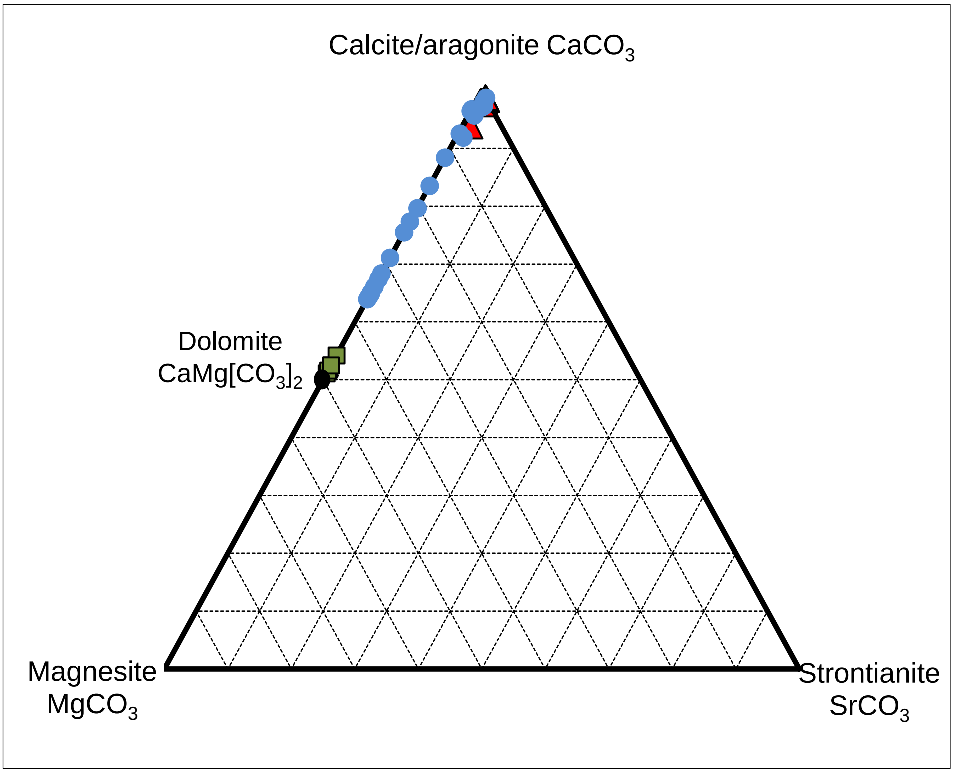

Figure 11. $CaCO_3$-$MgCO_3$-$SrCO_3$ molar ratio plot illustrating the compositions of the high-magnesian micrite (blue circles), relict dolomite / high magnesian-calcite grain (green squares), and the acicular aragonite cement (red open circles). Sample GT121.

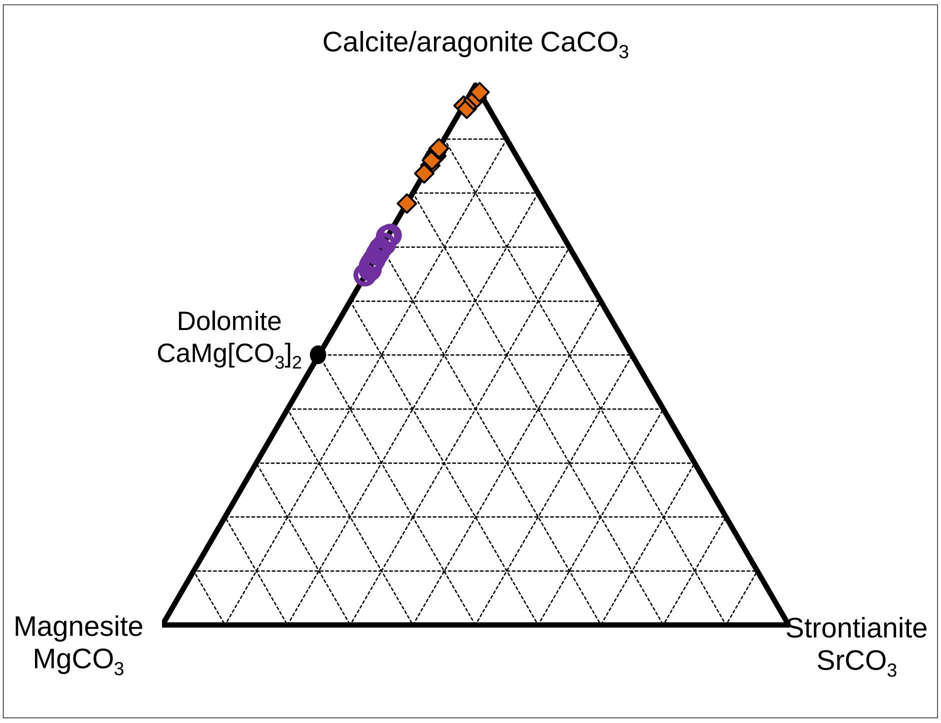

Figure 12. $CaCO_3$-$MgCO_3$-$SrCO_3$ molar ratio plot illustrating the compositions of the high-magnesian dark micrite rims (purple open circles), high magnesian-calcite light micrite rims (orange diamonds). Sample GT121.

Table 10. Electron microprobe analyses of carbonate cements and grains within sample GT121

		Weight % oxide (normalised)							Ionic ratio [normalised to 3 [O]						COMMENTS
SAMPLE	No	MgO	CaO	MnO	FeO	SrO	CO_2 (calc)	*Total wt.%	Mg^{2+}	Ca^{2+}	Mn^{2+}	Fe^{2+}	Sr^{2+}	CO_3^{2-}	
GT121	1	1.55	54.22	0.00	0.00	0.00	44.23	100	0.04	0.96	0.00	0.00	0.00	1.00	light rim of micrite (outer)
GT121	2	1.43	52.70	0.00	1.12	0.82	43.94	100	0.04	0.94	0.00	0.02	0.01	1.00	light rim of micrite (outer)
GT121	3	0.69	54.33	0.00	0.00	1.12	43.86	100	0.02	0.97	0.00	0.00	0.01	1.00	light rim of micrite (outer)
GT121	4	0.38	54.60	0.00	0.00	1.23	43.78	100	0.01	0.98	0.00	0.00	0.01	1.00	light rim of micrite (outer)
GT121	5	0.39	54.44	0.00	0.00	1.42	43.75	100	0.01	0.98	0.00	0.00	0.01	1.00	light rim of micrite (outer)
GT121	6	0.00	54.96	0.00	0.00	1.35	43.69	100	0.00	0.99	0.00	0.00	0.01	1.00	light rim of micrite (outer)
GT121	7	5.09	49.65	0.46	0.00	0.00	44.80	100	0.12	0.87	0.01	0.00	0.00	1.00	light rim of micrite (inner)
GT121	8	5.22	49.16	0.55	0.00	0.32	44.75	100	0.13	0.86	0.01	0.00	0.00	1.00	light rim of micrite (inner)
GT121	9	5.97	48.29	0.60	0.00	0.25	44.89	100	0.15	0.84	0.01	0.00	0.00	1.00	light rim of micrite (inner)
GT121	10	5.32	49.08	0.54	0.00	0.29	44.77	100	0.13	0.86	0.01	0.00	0.00	1.00	light rim of micrite (inner)
GT121	11	5.40	49.24	0.51	0.00	0.00	44.85	100	0.13	0.86	0.01	0.00	0.00	1.00	light rim of micrite (inner)
GT121	12	5.27	49.47	0.43	0.00	0.00	44.83	100	0.13	0.87	0.01	0.00	0.00	1.00	light rim of micrite (inner)
GT121	13	9.04	44.72	0.55	0.24	0.00	45.44	100	0.22	0.77	0.01	0.00	0.00	1.00	light micrite rim around dolomite /Mg Ca grain
GT121	14	5.56	49.06	0.29	0.22	0.00	44.87	100	0.14	0.86	0.00	0.00	0.00	1.00	light micrite rim around dolomite /Mg Ca grain
GT121	15	5.67	48.64	0.62	0.21	0.00	44.86	100	0.14	0.85	0.01	0.00	0.00	1.00	light micrite rim around dolomite /Mg Ca grain
GT121	16	6.72	47.84	0.35	0.00	0.00	45.09	100	0.16	0.83	0.00	0.00	0.00	1.00	light micrite rim around dolomite /Mg Ca grain
GT121	17	4.74	48.97	0.99	0.67	0.00	44.63	100	0.12	0.86	0.01	0.01	0.00	1.00	light micrite rim around dolomite /Mg Ca grain
GT121	18	4.74	49.77	0.54	0.24	0.00	44.71	100	0.12	0.87	0.01	0.00	0.00	1.00	light micrite rim around dolomite /Mg Ca grain
GT121	19	14.12	39.01	0.00	0.52	0.00	46.34	100	0.33	0.66	0.00	0.01	0.00	1.00	dark outer micrite rim /micrite clot
GT121	20	15.02	38.43	0.00	0.00	0.00	46.55	100	0.35	0.65	0.00	0.00	0.00	1.00	dark outer micrite rim /micrite clot
GT121	21	11.80	42.03	0.20	0.00	0.00	45.98	100	0.28	0.72	0.00	0.00	0.00	1.00	dark outer micrite rim /micrite clot
GT121	22	11.58	42.20	0.00	0.00	0.33	45.89	100	0.28	0.72	0.00	0.00	0.00	1.00	dark outer micrite rim /micrite clot
GT121	23	14.33	38.64	0.20	0.18	0.33	46.33	100	0.34	0.65	0.00	0.00	0.00	1.00	dark outer micrite rim /micrite clot
GT121	24	14.00	39.44	0.00	0.20	0.00	46.35	100	0.33	0.67	0.00	0.00	0.00	1.00	dark outer micrite rim /micrite clot
GT121	25	13.27	40.48	0.00	0.00	0.00	46.25	100	0.31	0.69	0.00	0.00	0.00	1.00	dark rim of micrite (mid)
GT121	26	12.82	41.00	0.00	0.00	0.00	46.17	100	0.30	0.70	0.00	0.00	0.00	1.00	dark rim of micrite (mid)
GT121	27	13.75	39.92	0.00	0.00	0.00	46.33	100	0.32	0.68	0.00	0.00	0.00	1.00	dark rim of micrite (mid)
GT121	28	14.06	39.56	0.00	0.00	0.00	46.38	100	0.33	0.67	0.00	0.00	0.00	1.00	dark rim of micrite (mid)
GT121	29	13.07	40.71	0.00	0.00	0.00	46.21	100	0.31	0.69	0.00	0.00	0.00	1.00	dark rim of micrite (mid)
GT121	30	12.34	41.35	0.00	0.00	0.29	46.03	100	0.29	0.70	0.00	0.00	0.00	1.00	dark rim of micrite (mid)
GT121	31	21.05	31.37	0.00	0.00	0.00	47.58	100	0.48	0.52	0.00	0.00	0.00	1.00	dolomite/Mg Ca grain
GT121	32	20.87	31.58	0.00	0.00	0.00	47.55	100	0.48	0.52	0.00	0.00	0.00	1.00	dolomite/Mg Ca grain

		Weight % oxide (normalised)							Ionic ratio [normalised to 3 [O]						COMMENTS
SAMPLE	No	MgO	CaO	MnO	FeO	SrO	CO_2 (calc)	*Total wt.%	Mg^{2+}	Ca^{2+}	Mn^{2+}	Fe^{2+}	Sr^{2+}	CO_3^{2-}	
GT121	33	21.04	31.37	0.00	0.00	0.00	47.58	100	0.48	0.52	0.00	0.00	0.00	1.00	dolomite/Mg Ca grain
GT121	34	20.92	31.51	0.00	0.00	0.00	47.56	100	0.48	0.52	0.00	0.00	0.00	1.00	dolomite/Mg Ca grain
GT121	35	21.03	31.39	0.00	0.00	0.00	47.58	100	0.48	0.52	0.00	0.00	0.00	1.00	dolomite/Mg Ca grain
GT121	36	20.25	31.13	0.79	0.50	0.00	47.33	100	0.47	0.52	0.01	0.01	0.00	1.00	dolomite/Mg Ca grain
GT121	37	21.21	30.83	0.38	0.00	0.00	47.58	100	0.49	0.51	0.00	0.00	0.00	1.00	dolomite/Mg Ca grain
GT121	38	20.59	30.59	0.50	0.95	0.00	47.37	100	0.47	0.51	0.01	0.01	0.00	1.00	dolomite/Mg Ca grain
GT121	39	19.65	32.34	0.72	0.00	0.00	47.28	100	0.45	0.54	0.01	0.00	0.00	1.00	dolomite/Mg Ca grain
GT121	40	20.68	31.80	0.00	0.00	0.00	47.52	100	0.47	0.53	0.00	0.00	0.00	1.00	dolomite/Mg Ca grain
GT121	41	0.00	54.97	0.00	0.00	1.34	43.69	100	0.00	0.99	0.00	0.00	0.01	1.00	acicular cement
GT121	42	0.00	55.04	0.00	0.00	1.24	43.71	100	0.00	0.99	0.00	0.00	0.01	1.00	acicular cement
GT121	43	0.17	54.74	0.00	0.00	1.37	43.72	100	0.00	0.98	0.00	0.00	0.01	1.00	acicular cement
GT121	44	0.00	54.81	0.00	0.00	1.53	43.66	100	0.00	0.99	0.00	0.00	0.01	1.00	acicular cement
GT121	45	0.00	55.14	0.00	0.00	1.12	43.74	100	0.00	0.99	0.00	0.00	0.01	1.00	acicular cement
GT121	46	0.22	54.61	0.00	0.00	1.47	43.71	100	0.01	0.98	0.00	0.00	0.01	1.00	acicular cement
GT121	47	0.00	54.85	0.00	0.00	1.48	43.67	100	0.00	0.99	0.00	0.00	0.01	1.00	acicular cement
GT121	48	0.18	54.62	0.00	0.00	1.52	43.69	100	0.00	0.98	0.00	0.00	0.01	1.00	acicular cement
GT121	49	0.00	54.99	0.00	0.00	1.30	43.70	100	0.00	0.99	0.00	0.00	0.01	1.00	acicular cement
GT121	50	0.00	54.86	0.00	0.00	1.48	43.67	100	0.00	0.99	0.00	0.00	0.01	1.00	acicular cement
GT121	51	0.43	54.09	0.00	0.38	1.38	43.72	100	0.01	0.97	0.00	0.01	0.01	1.00	acicular cement
GT121	52	0.00	54.82	0.00	0.19	1.30	43.68	100	0.00	0.98	0.00	0.00	0.01	1.00	acicular cement
GT121	53	0.00	54.88	0.00	0.00	1.45	43.67	100	0.00	0.99	0.00	0.00	0.01	1.00	acicular cement
GT121	54	0.00	55.11	0.00	0.00	1.16	43.73	100	0.00	0.99	0.00	0.00	0.01	1.00	acicular cement
GT121	55	0.00	54.81	0.00	0.00	1.53	43.66	100	0.00	0.99	0.00	0.00	0.01	1.00	acicular cement
GT121	56	0.00	54.92	0.00	0.00	1.39	43.68	100	0.00	0.99	0.00	0.00	0.01	1.00	acicular cement
GT121	57	0.00	54.68	0.00	0.00	1.70	43.62	100	0.00	0.98	0.00	0.00	0.02	1.00	acicular cement
GT121	58	0.00	54.99	0.00	0.00	1.30	43.70	100	0.00	0.99	0.00	0.00	0.01	1.00	acicular cement
GT121	59	0.00	54.98	0.00	0.00	1.32	43.70	100	0.00	0.99	0.00	0.00	0.01	1.00	acicular cement
GT121	60	1.43	54.36	0.00	0.00	0.00	44.21	100	0.04	0.96	0.00	0.00	0.00	1.00	micrite clot
GT121	61	1.31	54.50	0.00	0.00	0.00	44.19	100	0.03	0.97	0.00	0.00	0.00	1.00	micrite clot
GT121	62	6.78	47.79	0.00	0.33	0.00	45.10	100	0.16	0.83	0.00	0.00	0.00	1.00	micrite clot
GT121	63	2.93	52.38	0.00	0.00	0.28	44.41	100	0.07	0.93	0.00	0.00	0.00	1.00	micrite clot
GT121	64	4.74	50.26	0.24	0.00	0.00	44.76	100	0.12	0.88	0.00	0.00	0.00	1.00	micrite clot
GT121	65	8.33	45.45	0.19	0.73	0.00	45.31	100	0.20	0.79	0.00	0.01	0.00	1.00	micrite clot
GT121	66	10.14	43.52	0.22	0.48	0.00	45.64	100	0.24	0.75	0.00	0.01	0.00	1.00	micrite clot

		Weight % oxide (normalised)							Ionic ratio [normalised to 3 [O]						COMMENTS
SAMPLE	No	MgO	CaO	MnO	FeO	SrO	CO_2 (calc)	*Total wt.%	Mg^{2+}	Ca^{2+}	Mn^{2+}	Fe^{2+}	Sr^{2+}	CO_3^{2-}	
GT121	67	13.23	39.80	0.37	0.44	0.00	46.16	100	0.31	0.68	0.00	0.01	0.00	1.00	micrite clot
GT121	68	13.82	39.84	0.00	0.00	0.00	46.34	100	0.33	0.67	0.00	0.00	0.00	1.00	micrite clot
GT121	69	14.93	38.53	0.00	0.00	0.00	46.53	100	0.35	0.65	0.00	0.00	0.00	1.00	micrite clot
GT121	70	14.95	37.50	0.00	1.12	0.00	46.43	100	0.35	0.63	0.00	0.01	0.00	1.00	micrite clot
GT121	71	14.29	38.81	0.00	0.52	0.00	46.37	100	0.34	0.66	0.00	0.01	0.00	1.00	micrite clot
GT121	72	15.40	37.98	0.00	0.00	0.00	46.61	100	0.36	0.64	0.00	0.00	0.00	1.00	micrite clot
GT121	73	14.83	38.08	0.00	0.63	0.00	46.46	100	0.35	0.64	0.00	0.01	0.00	1.00	micrite clot
GT121	74	14.76	38.10	0.00	0.71	0.00	46.43	100	0.35	0.64	0.00	0.01	0.00	1.00	micrite clot
GT121	75	15.03	38.11	0.00	0.35	0.00	46.52	100	0.35	0.64	0.00	0.00	0.00	1.00	micrite clot
GT121	76	12.14	41.50	0.00	0.34	0.00	46.02	100	0.29	0.71	0.00	0.00	0.00	1.00	micrite clot
GT121	77	0.28	53.47	0.00	1.38	1.24	43.63	100	0.01	0.96	0.00	0.02	0.01	1.00	micrite clot
GT121	78	1.35	53.41	0.00	0.28	0.98	43.97	100	0.03	0.95	0.00	0.00	0.01	1.00	micrite clot
GT121	79	2.83	51.79	0.00	0.00	1.16	44.22	100	0.07	0.92	0.00	0.00	0.01	1.00	micrite clot
GT121	80	0.59	54.02	0.00	0.19	1.44	43.76	100	0.01	0.97	0.00	0.00	0.01	1.00	micrite clot
GT121	81	0.00	55.01	0.00	0.00	1.29	43.70	100	0.00	0.99	0.00	0.00	0.01	1.00	micrite clot
GT121	82	0.43	54.18	0.00	0.00	1.69	43.70	100	0.01	0.97	0.00	0.00	0.02	1.00	micrite clot

**Note: Some analytical totals were low (<90%) because of the microporous nature of the cements. Therefore, all data were normalised to 100%*

2.11 SAMPLE GT123

This sample is a clast of dark grey, fine-grained sandstone weathered to a buff colour on the outer surface. The clast irregular shaped, thin, tabular sample which has a relatively smooth outer surface compared to GT112 and GT120. The surface of is patchily-stained by brown, iron oxyhydroxide that also stains the walls of burrows penetrating from this surface into the rock (Plate 61 and Plate 62). Numerous borings are present, some of which are infilled with muddy sediment and shell debris. The outer surface has been encrusted by several bryozoans, and calcareous serpulid worm (Plate 62).

.

Plate 61. Photograph of sample GT123. This is a thin, flattish sample, with a relative smooth surface compared to samples GT112 and GT120. This sample still shows evidence of boring/ burrowing by marine organisms, and has some bryozoan and serpulid worm encrustations. Grey scale bar divisions = 10 mm.

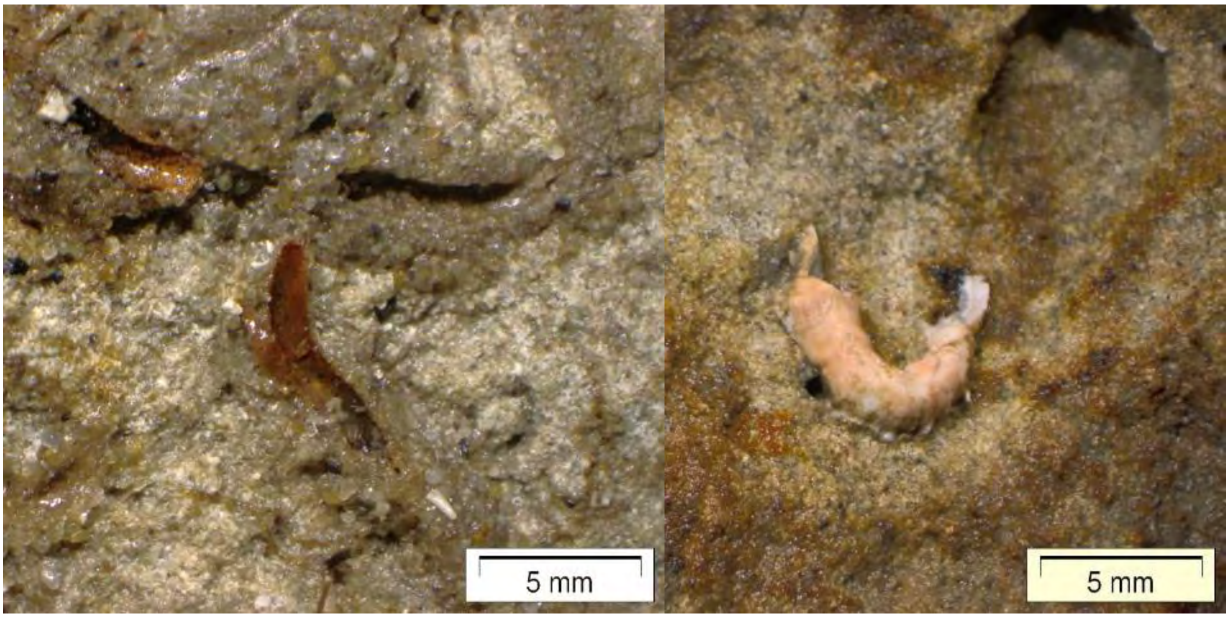

Plate 62. Optical micrographs of the surface of sample GT123 showing left: exposed burrows, the walls of which are stained by very finely-disseminated iron oxyhydroxide. Right: an example of a pinkish-coloured calcareous tube secreted by serpulid worms. The surface of the sample bears a patchy iron staining.

The polished thin section prepared from sample GT123 is shown in Plate 63. In thin section the sample is seen to be a fine-grained to very fine-grained sandstone, with a patchy carbonate cementation. It has been subject to burrowing, and a large sub-vertical burrow (12 mm in length), is intersected in the centre of the thin section. This has been infilled with a fine-grained, dark brown, muddy silt. Detrital grains are sub-angular to sub-rounded, and dominated by fine- to very fine-grained quartz. Several rounded, detrital glauconite ('glauconie' *sensu lato*) and calcium carbonate grains present (up to 300 μm in size). Some secondary framework grain dissolution porosity (cf. Schmidt and McDonald, 1979) has formed through the dissolution of unstable detrital grains and shelly fragments. The dissolution of bivalve shell fragments has produced distinctively curved mouldic cavities.

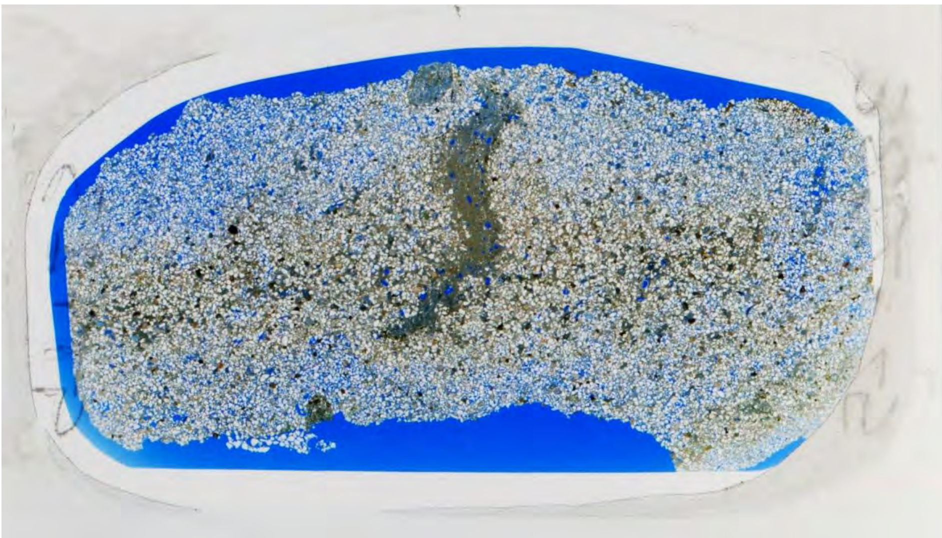

Plate 63. Scanned image of the thin section prepared from sample GT123. A subvertical mud-silt-infilled burrow cross-cuts the centre of the sample. Field of view = 48 mm wide.

Bulk XRD analysis has identified dolomite and highly magnesian-calcite as the major carbonate minerals present, with minor aragonite and non-magnesian calcite (Volume 1: Table 2). However, dolomite and high magnesian calcite could not be differentiated during petrographic analysis. The carbonate comprises intergranular micrite matrix material and grain-fringing microsparite. The carbonate is coarser around the rims of detrital grains, becoming finer and more microporous towards the centre of the intergranular regions (Plate 64). Irregular patches of microsparry carbonate also occur within the intergranular micrite (Plate 65). Some grains, particularly carbonate fragments, have been distinctively rimmed by a dense layer of calcite (Plate 66). Some of the micrite appears to comprise diffuse pelloidal aggregates, which have been squeezed and deformed after burial to form an intergranular ‘pseudomatrix’ (these are just discernible in Plate 64 and Plate 65). As such, much of the micrite was probably originally deposited as soft sand-sized pelloidal grains (probably faecal pellets in origin), rather than a true depositional fine-grained matrix sediment. This more readily explains the heterogeneous distribution of coarser microspar around detrital grain margins and in patches within the micritic carbonate. The microspar may therefore represent original grain-fringing / pore-lining cement that nucleated both on detrital quartz and on the micrite pelloids, within relatively clean open porosity. Subsequent, compaction of the soft faecal pelloids has resulted in the micritic pseudomatrix engulfing the microspar fringes. This is more consistent with the observation of microspar lining open pores in pellet / matrix-areas. The development of microsparite within the micrite pseudomatrix may also reflect coarsening of the micrite as a result of localised recrystallization, and its replacement by coarser calcite. Late-stage replacement and overprinting of the micrite by small patches of low- or non-magnesian calcite microspar has occurred (Plate 67). Relicts of the earlier micrite are found as inclusions within this later calcite.

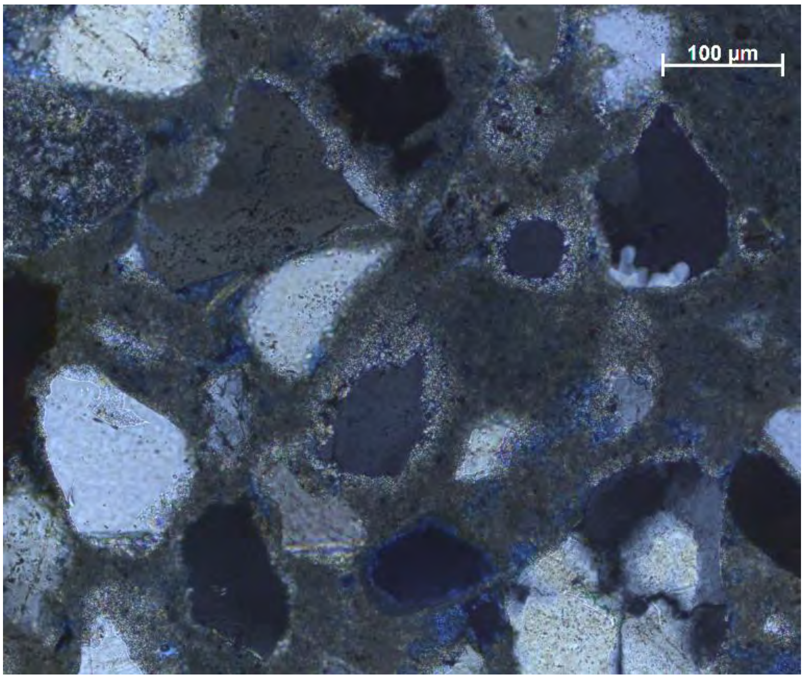

Plate 64. Transmitted light photomicrograph (crossed polarised light) showing halos of coarser cement around grains, and finer grained, micritic cement within the centre of the pore space. Sample GT123.

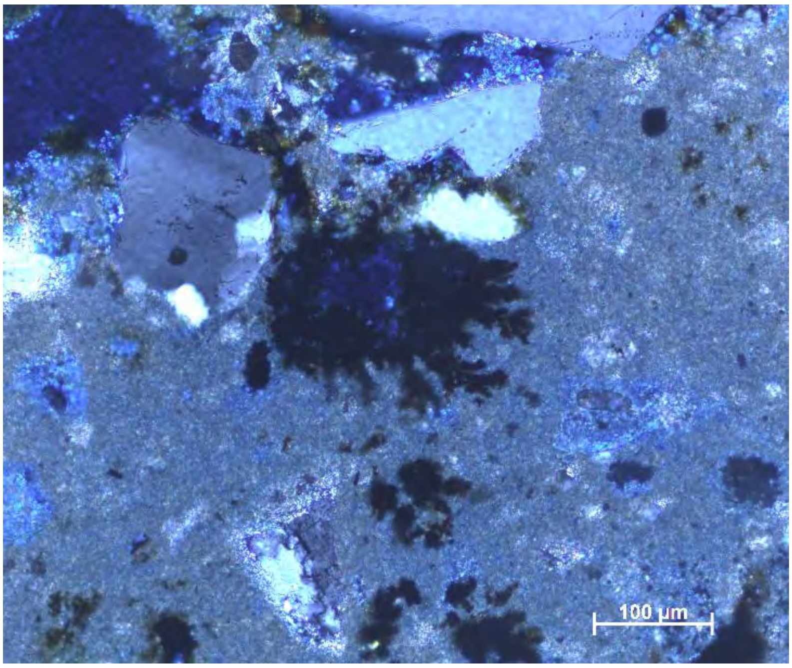

Plate 65. Transmitted light photomicrograph (crossed polarised light) showing patches of microsparry carbonate within intergranular micritic matrix carbonate. Late dendritic iron oxyhydroxide penetrate into the micrite matrix. Sample GT123.

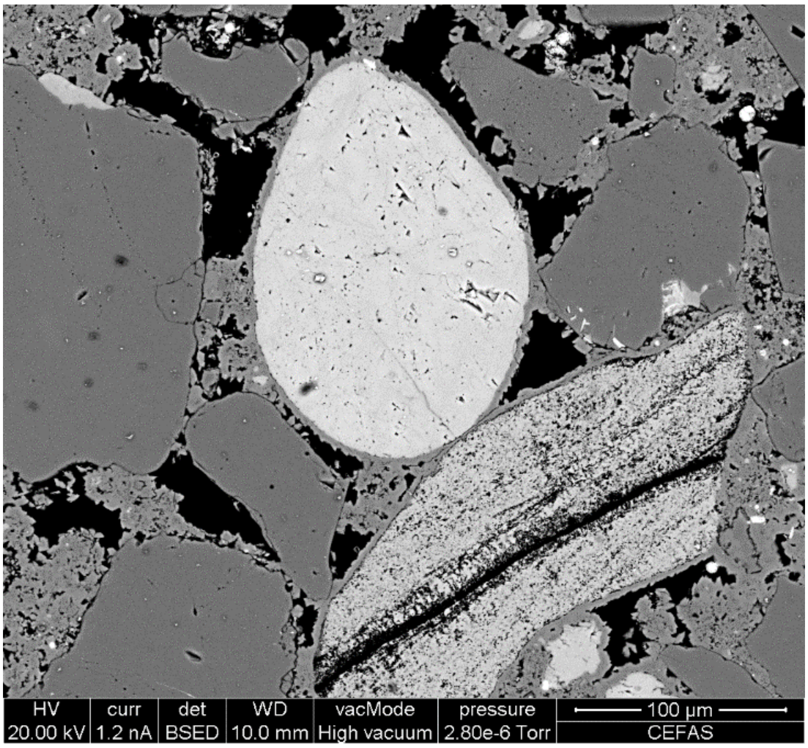

Plate 66. BSEM image of carbonate grains which are encased with rims of dense micrite. The pore filling micrite is microporous and forms globular clots. Sample GT123.

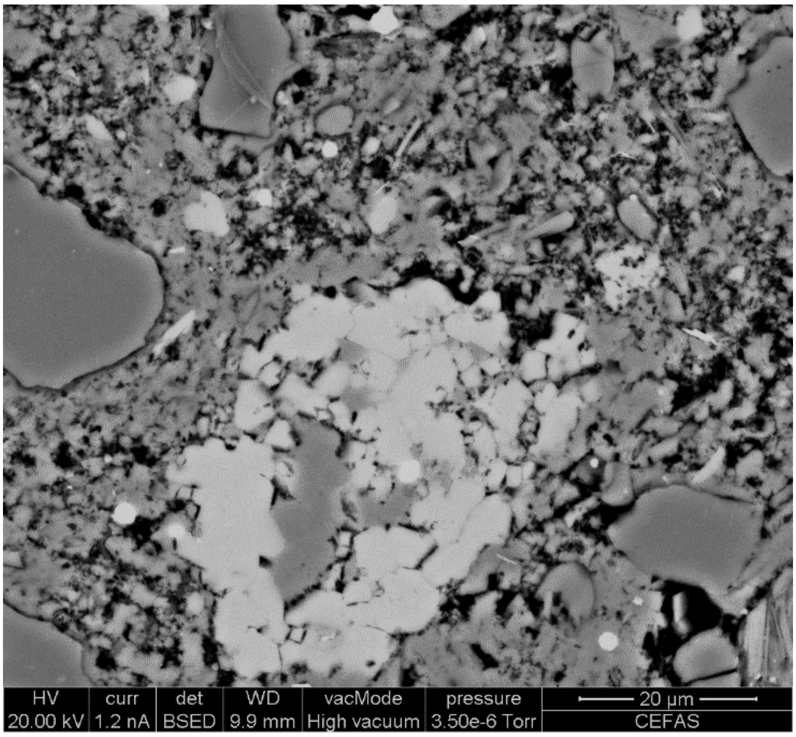

Plate 67. BSEM image showing the micrite cement in detail. The high-magnesian calcite cement (mid grey) is being replaced by interlocking subidiomorphic crystals of low- or non-magnesian microsparite cement. Sample GT123.

Optical observations show that fine iron oxyhydroxide is present as a minor component throughout the sample. It often displays a dendritic habit (Plate 65). BSEM imaging also shows that iron oxyhydroxide is finely- disseminated throughout the sample. The oxides are often present as fine-grained framboidal clusters, particularly within clay-rich pockets within the micrite, and therefore may be pseudomorphic after pyrite that was closely associated with the magnesian carbonate cement. This implies that the magnesian carbonate cements precipitated under reducing porewater conditions.

ED-EPMA major element compositional data for the calcite cements in sample GT123 are given in Figure 13. Their compositional variation, expressed in terms of molar proportions of CaO_3-$MgCO_3$ and $SrCO_3$, is summarised in Table 11. The micritic high-magnesian calcite cement and grain-fringing microsparry-calcite cement, are very similar in composition and contain between 31 and 44 mole % $MgCO_3$ (i.e. the structural formula of the calcite can be represented as $Ca_{0.56-0.69}Mg_{0.44-0.31}CO_3$). This is consistent with the presence of high magnesian-calcite detected by XRD. It is similar in composition to the micrite in sample GT112. ED-EPMA data for the later replacive rhombs of calcite indicate that the minor recrystallisation of the magnesian calcite micrite to coarser microsparry calcite, produced a relatively low magnesian calcite with less than 3 mole % $MgCO_3$ in solid solution. This is similar to observations made on carbonate cements in MDAC samples from the Braemar Pockmark Area (Milodowski et al., 2013).

Although XRD analysis definitively-identified the presence of significant dolomite in this sample (Volume 2: Table 2). This could not be differentiated in the petrographic observations from the fine high magnesian micritic matrix, described above as high magnesian calcite. However, it is possible that some of the ED-EPMA data for the micrite could correspond to 'excess-calcium dolomites' Unfortunately, it is likely that such dolomite and very highly-magnesium-substituted calcite is indistinguishable by BSEM (see detailed discussions in Volume 1: Section 3).

The sequence of sedimentary and post-depositional diagenetic events recorded from sample GT123 can be summarised as follows:

1. Deposition of fine sand and silt, including pelloidal grains of micritic high magnesian-calcite (probably of faecal origin)
2. Syndepositional bioturbation, and subsequent infilling of burrows with fine-grained mud and silts.
3. Precipitation of grain-fringing high-magnesian calcite microspar, probably accompanied by the precipitation of pyrite.
4. Partial recrystallisation and replacement of micritic high-magnesian calcite by coarser, high-magnesian calcite.
5. Partial recrystallisation and replacement of high-magnesian calcite by low- or non-magnesian calcite microspar cement.
6. Oxidation of pyrite and precipitation of secondary iron oxyhydroxide.

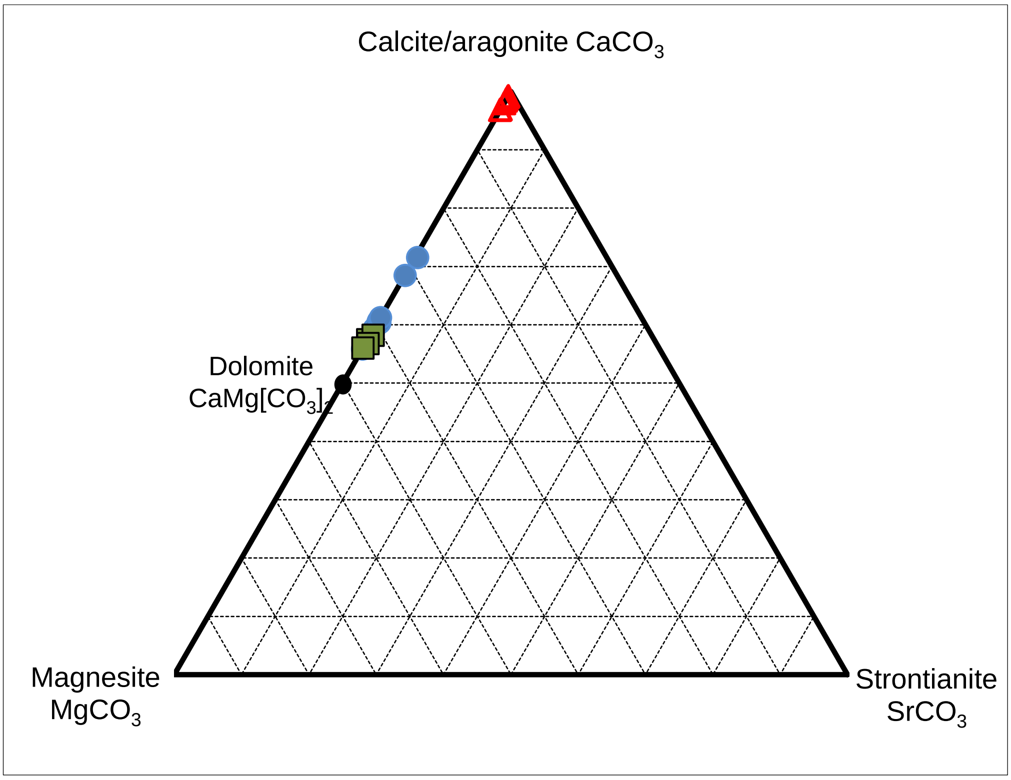

Figure 13. $CaCO_3$-$MgCO_3$-$SrCO_3$ molar ratio plot illustrating the compositions of the high-magnesian micrite (blue circles), high magnesian-calcite cores (green squares), and later, non-magnesian calcite cements replacing micrite (red open circles). Sample GT123.

Table 11. Electron microprobe analyses of micritic and calcic cements in sample GT123

		Weight % oxide (normalised)							Ionic ratio [normalised to 3 [O]						COMMENTS
SAMPLE	No	MgO	CaO	MnO	FeO	SrO	CO_2 (calc)	*Total wt.%	Mg^{2+}	Ca^{2+}	Mn^{2+}	Fe^{2+}	Sr^{2+}	CO_3^{2-}	
GT123	1	18.30	34.59	0.00	0.00	0.00	47.11	100	0.42	0.58	0.00	0.00	0.00	1.00	micrite
GT123	2	17.42	35.44	0.00	0.20	0.00	46.94	100	0.41	0.59	0.00	0.00	0.00	1.00	micrite
GT123	3	17.65	35.35	0.00	0.00	0.00	47.00	100	0.41	0.59	0.00	0.00	0.00	1.00	micrite
GT123	4	16.88	36.25	0.00	0.00	0.00	46.87	100	0.39	0.61	0.00	0.00	0.00	1.00	micrite
GT123	5	16.99	36.12	0.00	0.00	0.00	46.89	100	0.40	0.60	0.00	0.00	0.00	1.00	micrite
GT123	6	17.54	35.48	0.00	0.00	0.00	46.98	100	0.41	0.59	0.00	0.00	0.00	1.00	micrite
GT123	7	16.84	36.00	0.00	0.00	0.37	46.79	100	0.39	0.60	0.00	0.00	0.00	1.00	micrite
GT123	8	18.24	34.66	0.00	0.00	0.00	47.10	100	0.42	0.58	0.00	0.00	0.00	1.00	micrite
GT123	9	19.11	33.64	0.00	0.00	0.00	47.25	100	0.44	0.56	0.00	0.00	0.00	1.00	micrite
GT123	10	18.27	34.62	0.00	0.00	0.00	47.11	100	0.42	0.58	0.00	0.00	0.00	1.00	micrite
GT123	11	17.86	31.58	0.00	3.90	0.00	46.66	100	0.42	0.53	0.00	0.05	0.00	1.00	micrite
GT123	12	16.63	36.55	0.00	0.00	0.00	46.82	100	0.39	0.61	0.00	0.00	0.00	1.00	micrite
GT123	13	18.34	34.54	0.00	0.00	0.00	47.12	100	0.42	0.58	0.00	0.00	0.00	1.00	micrite
GT123	14	11.82	41.88	0.00	0.00	0.38	45.92	100	0.28	0.72	0.00	0.00	0.00	1.00	micrite
GT123	15	13.34	40.40	0.00	0.00	0.00	46.26	100	0.31	0.69	0.00	0.00	0.00	1.00	micrite
GT123	16	18.29	33.96	0.00	0.71	0.00	47.04	100	0.42	0.57	0.00	0.01	0.00	1.00	micrite
GT123	17	18.37	34.51	0.00	0.00	0.00	47.12	100	0.43	0.57	0.00	0.00	0.00	1.00	Mg calcite core
GT123	18	17.78	34.86	0.00	0.00	0.42	46.94	100	0.41	0.58	0.00	0.00	0.00	1.00	Mg calcite core
GT123	19	18.46	34.09	0.00	0.00	0.39	47.06	100	0.43	0.57	0.00	0.00	0.00	1.00	Mg calcite core
GT123	20	18.59	32.94	0.00	1.46	0.00	47.02	100	0.43	0.55	0.00	0.02	0.00	1.00	Mg calcite core
GT123	21	0.53	55.42	0.00	0.00	0.00	44.06	100	0.01	0.99	0.00	0.00	0.00	1.00	calcite rhombic cement
GT123	22	0.62	55.31	0.00	0.00	0.00	44.07	100	0.02	0.98	0.00	0.00	0.00	1.00	calcite rhombic cement
GT123	23	0.34	55.63	0.00	0.00	0.00	44.02	100	0.01	0.99	0.00	0.00	0.00	1.00	calcite rhombic cement
GT123	24	1.29	54.53	0.00	0.00	0.00	44.19	100	0.03	0.97	0.00	0.00	0.00	1.00	calcite rhombic cement
GT123	25	1.23	54.59	0.00	0.00	0.00	44.18	100	0.03	0.97	0.00	0.00	0.00	1.00	calcite rhombic cement
GT123	26	0.79	53.71	0.21	1.34	0.00	43.95	100	0.02	0.96	0.00	0.02	0.00	1.00	calcite rhombic cement
GT123	27	0.31	54.76	0.26	0.75	0.00	43.92	100	0.01	0.98	0.00	0.01	0.00	1.00	calcite rhombic cement
GT123	28	0.53	54.24	0.00	1.30	0.00	43.93	100	0.01	0.97	0.00	0.02	0.00	1.00	calcite rhombic cement
GT123	29	0.37	55.10	0.00	0.56	0.00	43.97	100	0.01	0.98	0.00	0.01	0.00	1.00	calcite rhombic cement

**Note: Some analytical totals were low (<90%) because of the microporous nature of the cements. Therefore, all data were normalised to 100%*

2.12 SAMPLE GT126

This sample was represented by three highly irregular shaped, heavily bioturbated clasts (<100 mm), similar in form to sample GT112 (Plate 68). These comprise a grey-buff coloured sandstone with patchy orange-brown/black iron-oxyhydroxide staining. Worm casts made of coarse-grained, cemented sand, and calcareous serpulid worm and bryozoan encrustations are present on the surface.

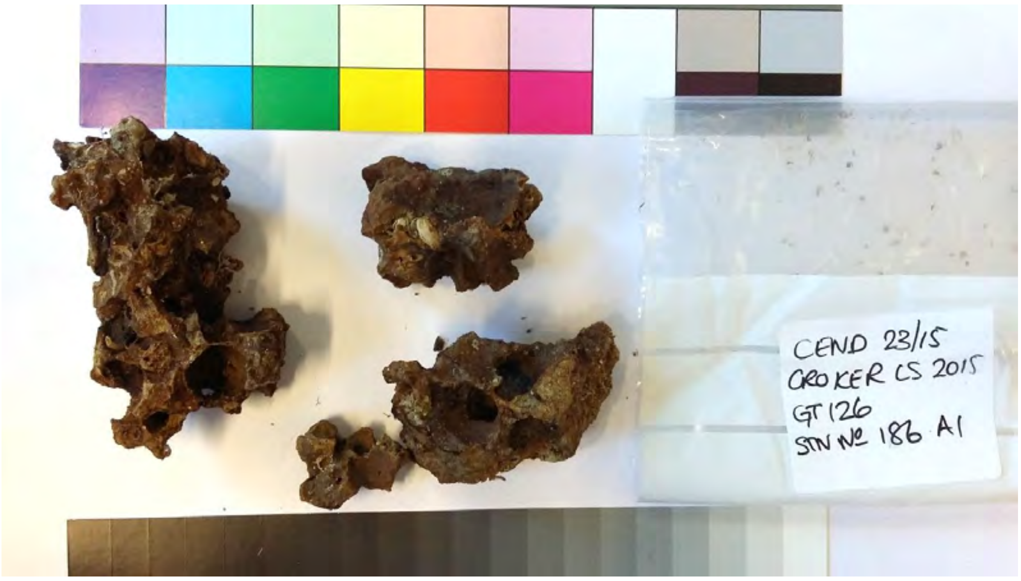

Plate 68. Photograph of the heavily bioturbated, irregular shaped clasts comprising sample GT126. Grey scale bar divisions = 10 mm.

The thin section prepared from one of the clasts is shown in Plate 69. The irregular morphology of the clast is clearly seen in the vertical thin section profile. Several burrow cross-sections are also present in the thin section. Patchy iron-oxyhydroxide staining is also visible, and is present throughout the sample and not just limited to the external surfaces of the clast. However, iron oxyhydroxide staining appears to be most strongly developed in the sandstone matrix immediately adjacent to the burrow walls, as well as around the periphery of the clast. This implies that the burrows provided preferential pathways into the rock for oxidative alteration to take place. The heterogeneous and patchy distribution of the colouration also hints at the sediment having been bioturbated.

The sandstone is reasonably well sorted, with a tightly packed and grain supported fabric. However, no compositional grain deformation is evident. The sand grains are angular to sub-angular, medium-grained (<400 µm) and dominated by detrital quartz. Numerous rounded, detrital glauconite ('glauconie' *sensu lato*) grains are also present. Secondary framework grain dissolution porosity (cf. Schmidt and McDonald, 1979) has formed where unstable detrital grains and bioclastic debris (e.g. bivalve shells) has been dissolved out (Plate 70). The rock is well cemented by patchy carbonate cement, which appears dark brown and semi-opaque in thin section due staining by iron oxyhydroxide.

XRD analysis shows that very high magnesian calcite is the main carbonate mineral present, with very minor non-magnesian calcite and traces of aragonite (Volume 1: Table2). BSEM indicates that the cement is a high-magnesian calcite, which is dominated by blocky rhombs of microsparite.

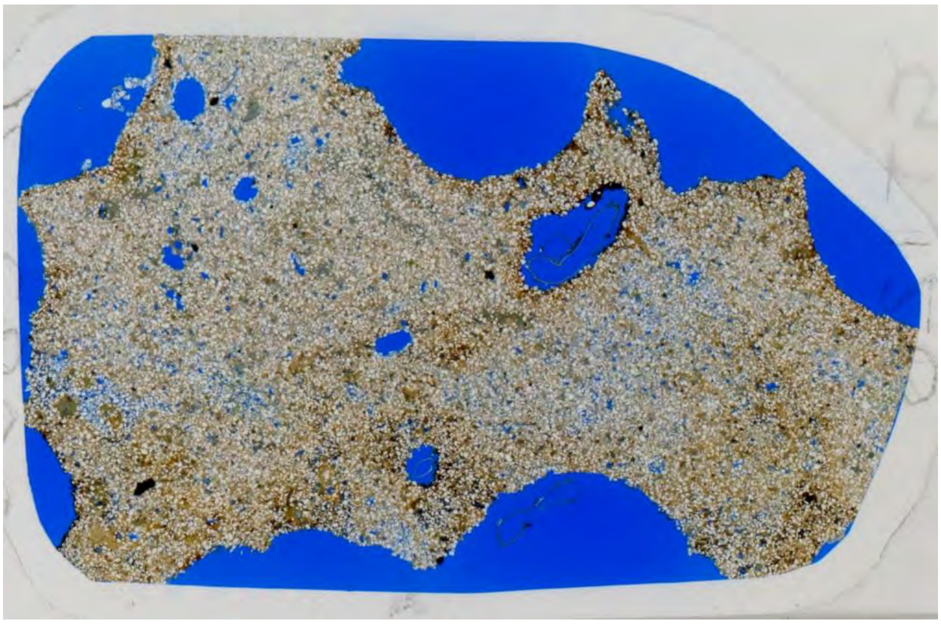

Plate 69. Scanned image of the thin section prepared from one of the clasts from sample GT126. It shows brown staining by iron oxyhydroxide around the clast margin, in the sandstone adjacent to burrows, and diffuse patches that define a probable bioturbated fabric. Field of view = 48 mm wide.

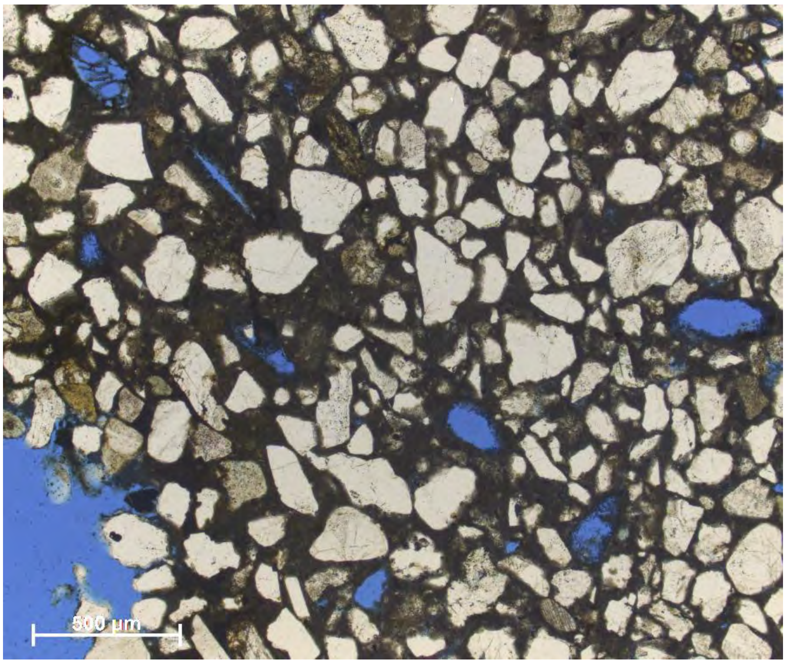

Plate 70. Transmitted light photomicrograph (plain polarised light) showing the well-cemented, and tightly packed grain fabric in sample GT126. Note the secondary framework grain dissolution porosity (blue dyed resin areas) where unstable bioclastic grains have been dissolved away.

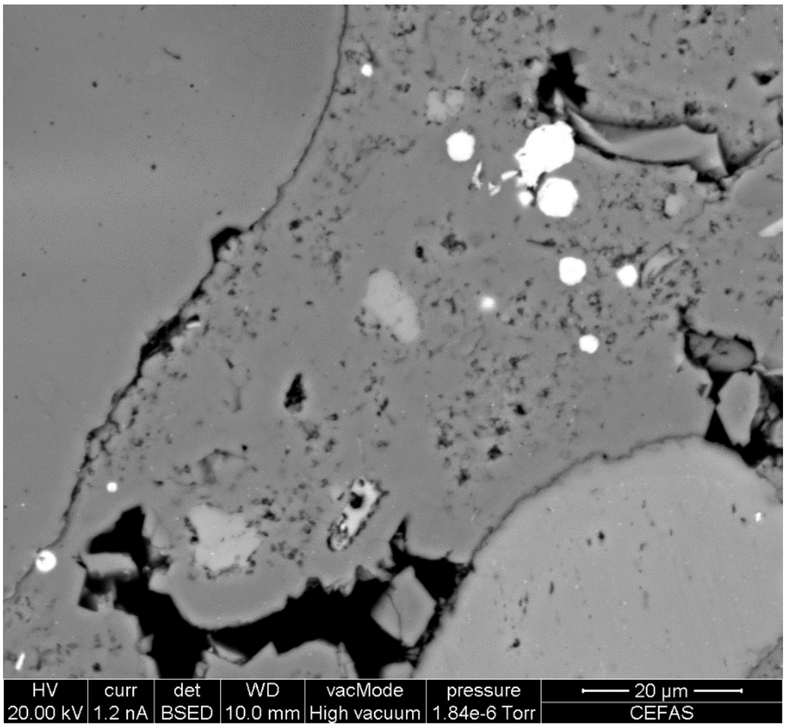

Plate 71. BSEM photomicrograph showing the detail of the micritic high-magnesian calcite cement. Here, the calcite preserves a well-developed cellular micro-fabric that represents mineralised bacterial cells. The cement is coarser (microsparite) and less porous around the edges of the pore space compared to the centre. Numerous Fe-oxides are present in the cement. GT126

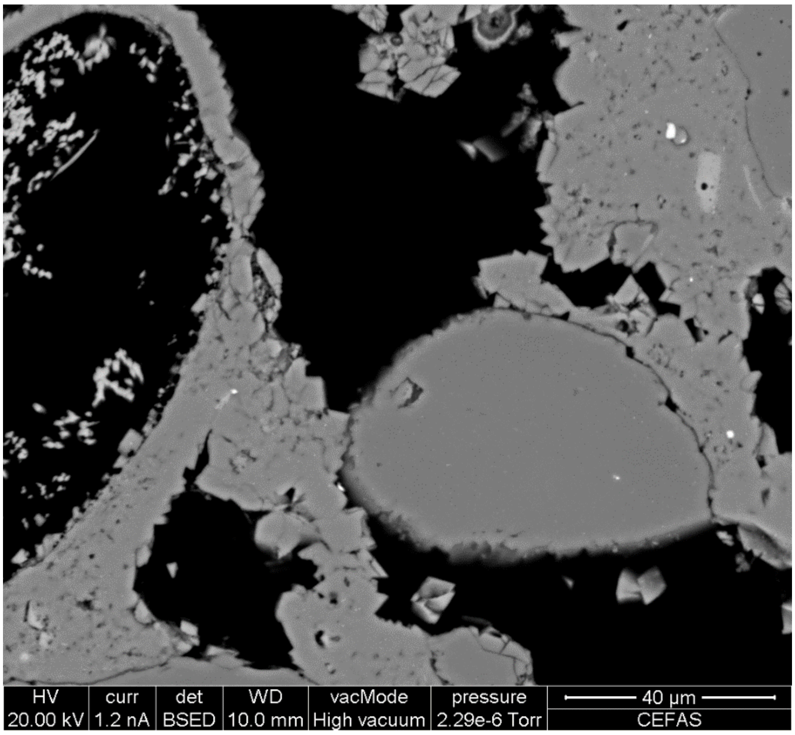

Plate 72. BSEM image showing the blocky microsparite cement. GT126

In places, cement is microporous, comprising relict spherical to microboytryoidal aggregates of micritic high magnesian-calcite that is largely recrystallised and overprinted by the microsparry calcite (Plate 71). Subidiomorphic to idiomorphic rhombic calcite crystals outline these microporous cores. The coarse subidiomorphic to idiomorphic rhombic calcite crystals line the open intergranular pores, occurring as grain-coating microsparite rims (Plate 72). The non-magnesian calcite detected by XRD is largely present as shell debris. Abundant framboidal Fe-oxides are present within the cement and may be pseudomorphs after pyrite.

This sample is also one of the four samples which contain colloform manganese oxyhydroxide precipitates and iron oxyhydroxide-rich cements. This is described in further detail in Section 2.16 of this volume.

ED-EPMA analysis of the carbonate cements are presented in Table 12 and are summarised in Figure 14. The magnesian calcite cements contain between 42 and 44 mole % $MgCO_3$ in solid solution (i.e. the structural formula of the calcite can be represented as $Ca_{0.56-0.58}Mg_{0.44-0.42}CO_3$). The lighter inclusions observed within the micrite by BSEM (Plate 71) have a significantly lower magnesium content, containing between 2 and 12 mole % $MgCO_3$ and may represent later microsparry calcite.

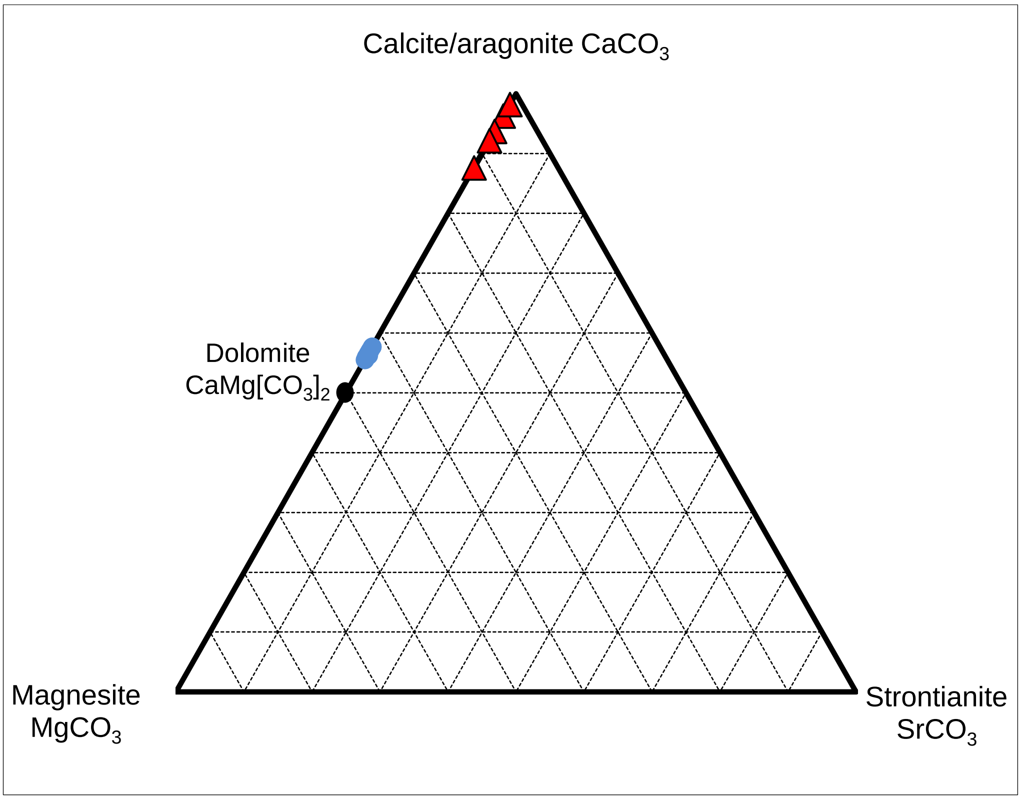

Figure 14. $CaCO_3$-$MgCO_3$-$SrCO_3$ molar ratio plot illustrating the compositions of the carbonate cements: blocky microsparite (blue circles), and lighter inclusions within the microsparite (red triangles). Sample GT126.

The sequence of sedimentary and post-depositional diagenetic events recorded from sample GT126 can be summarised as follows:

1. Deposition of medium-grained sandstone.
2. Syndepositional bioturbation
3. Precipitation of micritic high-magnesian calcite and lithification of the sediment. This was probably closely associated with the precipitation of early diagenetic framboidal pyrite.
4. Partial recrystallisation of micritic and replacement by microsparry high magnesian calcite

5. Oxidation of pyrite and precipitation of late-stage iron and manganese oxyhydroxide films and pore-fillings.
6. Colonisation by bryozoans, and calcareous serpulid worm tubes on the lithified surface of the sandstone / clast.

Table 12. Electron microprobe analyses of carbonate cements in GT126

		Weight % oxide (normalised)							Ionic ratio [normalised to 3 [O]						COMMENTS
SAMPLE	No	MgO	CaO	MnO	FeO	SrO	CO_2 (calc)	*Total wt.%	Mg^{2+}	Ca^{2+}	Mn^{2+}	Fe^{2+}	Sr^{2+}	CO_3^{2-}	
GT126	1	18.67	34.15	0.00	0.00	0.00	47.18	100	0.43	0.57	0.00	0.00	0.00	1.00	Microsparite/micrite
GT126	2	18.58	34.26	0.00	0.00	0.00	47.16	100	0.43	0.57	0.00	0.00	0.00	1.00	Microsparite/micrite
GT126	3	19.06	33.70	0.00	0.00	0.00	47.24	100	0.44	0.56	0.00	0.00	0.00	1.00	Microsparite/micrite
GT126	4	18.80	33.79	0.00	0.00	0.26	47.15	100	0.44	0.56	0.00	0.00	0.00	1.00	Microsparite/micrite
GT126	5	19.09	33.66	0.00	0.00	0.00	47.25	100	0.44	0.56	0.00	0.00	0.00	1.00	Microsparite/micrite
GT126	6	18.76	34.04	0.00	0.00	0.00	47.19	100	0.43	0.57	0.00	0.00	0.00	1.00	Microsparite/micrite
GT126	7	18.49	34.36	0.00	0.00	0.00	47.15	100	0.43	0.57	0.00	0.00	0.00	1.00	Microsparite/micrite
GT126	8	18.26	34.64	0.00	0.00	0.00	47.11	100	0.42	0.58	0.00	0.00	0.00	1.00	Microsparite/micrite
GT126	9	19.26	33.46	0.00	0.00	0.00	47.28	100	0.44	0.56	0.00	0.00	0.00	1.00	Microsparite/micrite
GT126	10	19.05	33.71	0.00	0.00	0.00	47.24	100	0.44	0.56	0.00	0.00	0.00	1.00	Microsparite/micrite
GT126	11	18.80	34.01	0.00	0.00	0.00	47.20	100	0.43	0.57	0.00	0.00	0.00	1.00	Microsparite/micrite
GT126	12	18.73	34.08	0.00	0.00	0.00	47.19	100	0.43	0.57	0.00	0.00	0.00	1.00	Microsparite/micrite
GT126	13	18.84	33.95	0.00	0.00	0.00	47.21	100	0.44	0.56	0.00	0.00	0.00	1.00	Microsparite/micrite
GT126	14	18.91	33.47	0.00	0.44	0.00	47.17	100	0.44	0.56	0.00	0.01	0.00	1.00	Microsparite/micrite
GT126	15	18.08	34.11	0.00	0.81	0.00	47.00	100	0.42	0.57	0.00	0.01	0.00	1.00	Microsparite/micrite
GT126	16	18.20	34.55	0.00	0.17	0.00	47.08	100	0.42	0.58	0.00	0.00	0.00	1.00	Microsparite/micrite
GT126	17	1.51	54.26	0.00	0.00	0.00	44.22	100	0.04	0.96	0.00	0.00	0.00	1.00	lighter microsparite inclusions
GT126	18	2.55	53.04	0.00	0.00	0.00	44.40	100	0.06	0.94	0.00	0.00	0.00	1.00	lighter microsparite inclusions
GT126	19	3.16	51.68	0.00	0.73	0.00	44.44	100	0.08	0.91	0.00	0.01	0.00	1.00	lighter microsparite inclusions
GT126	20	0.72	55.00	0.00	0.22	0.00	44.07	100	0.02	0.98	0.00	0.00	0.00	1.00	lighter microsparite inclusions
GT126	21	5.05	49.84	0.00	0.30	0.00	44.81	100	0.12	0.87	0.00	0.00	0.00	1.00	lighter microsparite inclusions

**Note: Some analytical totals were low (<90%) because of the microporous nature of the cements. Therefore, all data were normalised to 100%*

2.13 SAMPLE GT129

This sample comprises two angular, flat clasts of medium to coarse light grey sandstone (Plate 73). One of the clasts has patchy orange-brown iron-oxyhydroxide staining. However, the second sample has a dark orange to black coloured surface coating. This dark coating is a manganese oxyhydroxide-rich crust which has formed on the surface of the clast. The surfaces of both clasts are pock-marked and contain some borings by marine organisms.

Plate 73. Photograph of sample GT129. These two angular clasts are flat, and have very strong dark brown-black iron-oxyhydroxide staining. Grey scale bar divisions = 10 mm.

The thin section prepared from one of the clasts is shown in Plate 74. The patchy iron-oxyhydroxide staining is present throughout the sample, in a series of sub-parallel bands that may be picking out a weak primary bedding fabric. In thin section the rock is a reasonably well sorted predominantly medium grained sandstone (with grain size up to 650 μm). It has a close-packed grain framework composed mainly of sub-angular to sub-rounded detrital quartz sand. Secondary porosity has formed locally where unstable grains have been dissolved out. A dark brown micritic matrix or micrite cement is present and is nearly opaque in thin section (Plate 75), and the sample is generally well-cemented but contains patches of higher porosity rock. The edge of the sample has a thin black opaque rim (Plate 76), which is a manganese oxyhydroxide crust (this is described in more detail in Section 2.16 (Volume 2) of this report).

XRD analysis shows that high magnesian-calcite is the principal carbonate mineral forming 22.7 wt. % of the rock (Volume 1: Table 2). BSEM petrography shows that this occurs as intergranular ‘clots’ or ‘globular’ aggregates of micritic high magnesian-calcite, with coarser idiomorphic to sub-idiomorphic overgrowths high magnesian-calcite rhombs (Plate 77). The micrite aggregates are microporous and appear to preserve possible traces of a microcellular fabric that may be microbial in origin (Plate 77). Similar microcellular microfabrics are observed in some of the other samples (e.g. GT004, GT112). This early micrite is partially overprinted and replaced by the later microsparry calcite cement (Plate 77), and microsparry calcite cement also forms grain-coating fringes lining the open pores in cleaner parts of the sandstone.

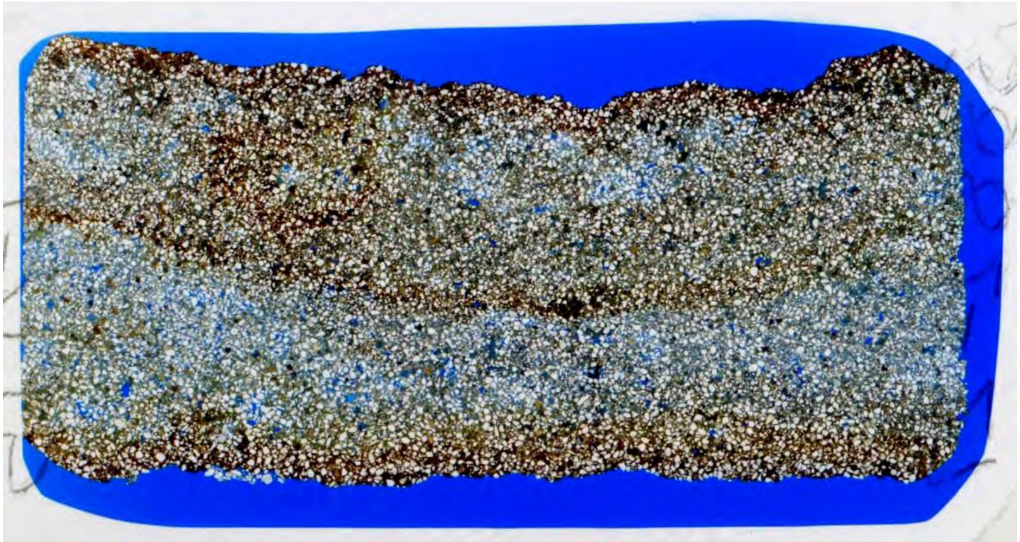

Plate 74. Scanned image of the thin section prepared from one of the clasts comprising sample GT129. The iron-oxyhydroxide staining is particularly strong. Field of view = 48 mm wide.

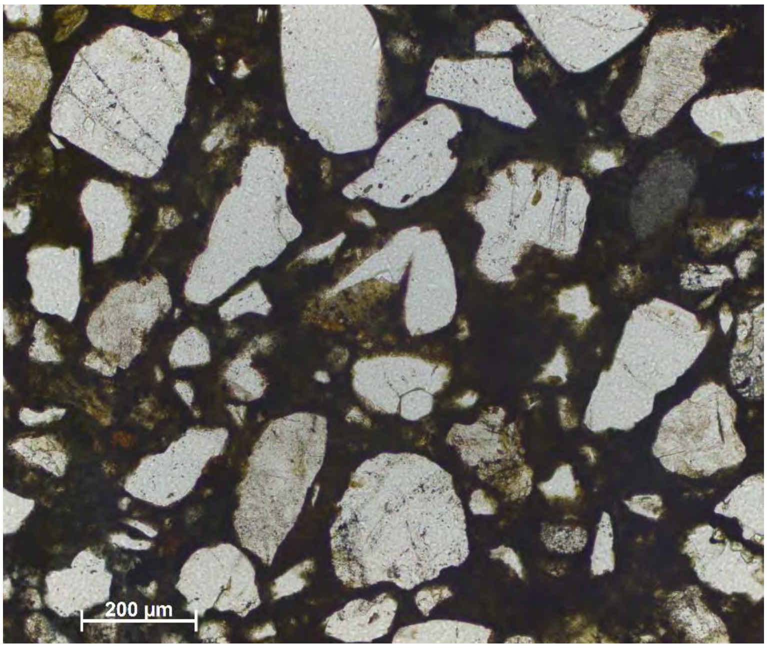

Plate 75. Transmitted light photomicrograph (plain polarised light) showing the dense, dark brown micrite cement. GT129.

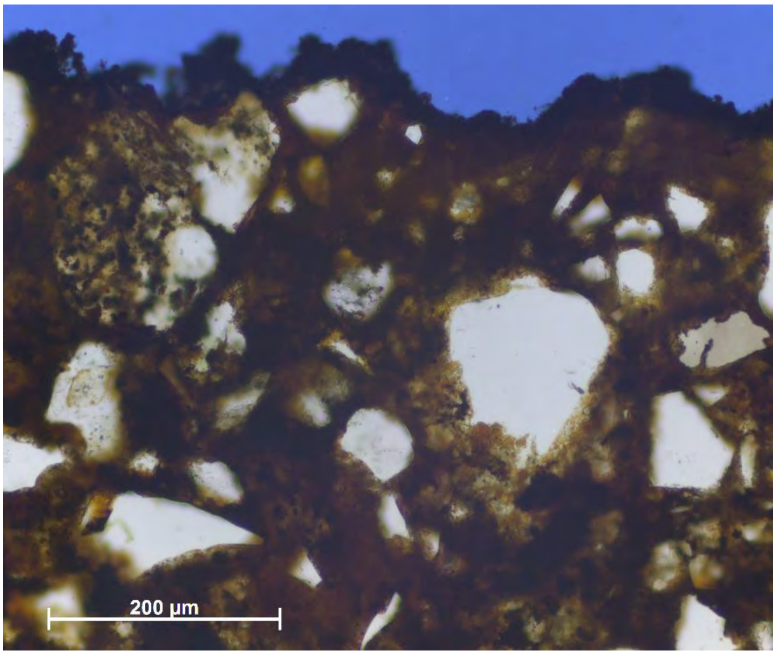

Plate 76. Transmitted light photomicrograph (plain polarised light) showing the dense, dark brown micrite cement, and thin black manganese oxyhydroxide crust on the outer edge of the sample. GT129.

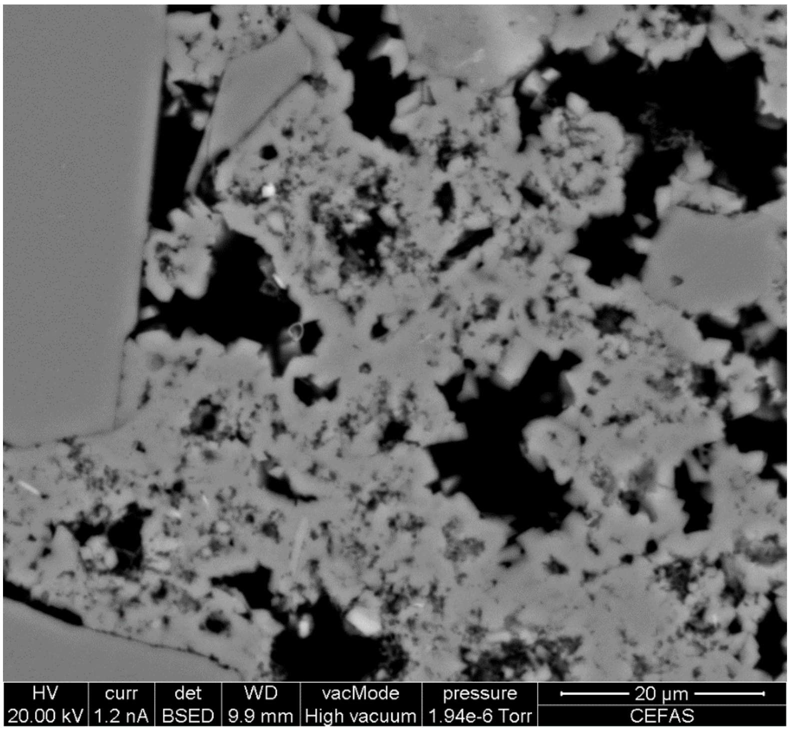

Plate 77. BSEM image showing the preservation of vestiges of a microcellular texture within micritic high magnesian-calcite aggregates. Coarser, idiomorphic to sub-idiomorphic high magnesian-calcite rhombs form overgrowths on the micrite aggregates and partially replace the micrite. GT129.

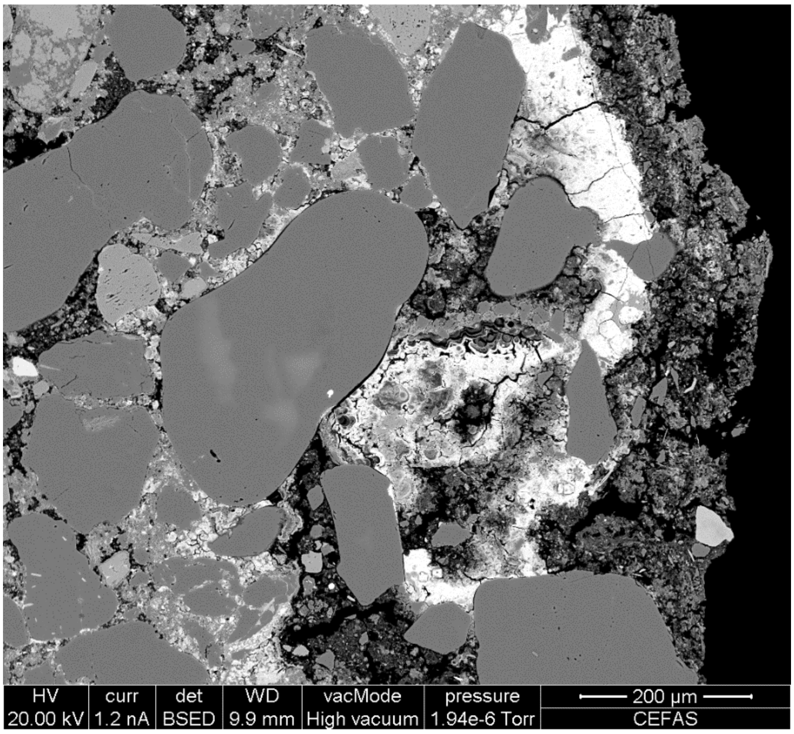

Plate 78. BSEM image of the Fe-rich cement (bright white) and manganese oxyhydroxide-rich crust (dark grey). The high-magnesium micritic cement can be seen on the left of the image (mid grey). GT129.

ED-EPMA analysis of the carbonate cements are presented in Table 13 and are summarised in Figure 17. The bulk of the magnesian calcite cements contain between 41 and 47 mole % $MgCO_3$ (i.e. the structural formula of the calcite can be represented as $Ca_{0.53-0.59}Mg_{0.47-0.41}CO_3$) This is similar to samples GT004 and GT112. However, two analyses returned a very low magnesium content (3 mole % $MgCO_3$), similar to both the late calcite found infilling cavities within iron oxyhydroxide cement (<1 mole % $MgCO_3$). Shell fragments contain <2 mole % $MgCO_3$. Analysis of one micritic grain indicated a dolomitic end-member composition with a near 1:1 Mg : Ca ratio.

The sequence of sedimentary and post-depositional diagenetic events recorded from sample GT129 can be summarised as follows:

1. Deposition of coarse-grained sandstone.
2. Syndepositional bioturbation.
3. Precipitation of micritic high-magnesian calcite and lithification of the sediment.
4. Partial recrystallisation and replacement of early-formed micrite by microsparry high magnesian-calcite.
5. Oxidation within the cement and precipitation of iron oxyhydroxide and colloform manganese oxyhydroxide crust.

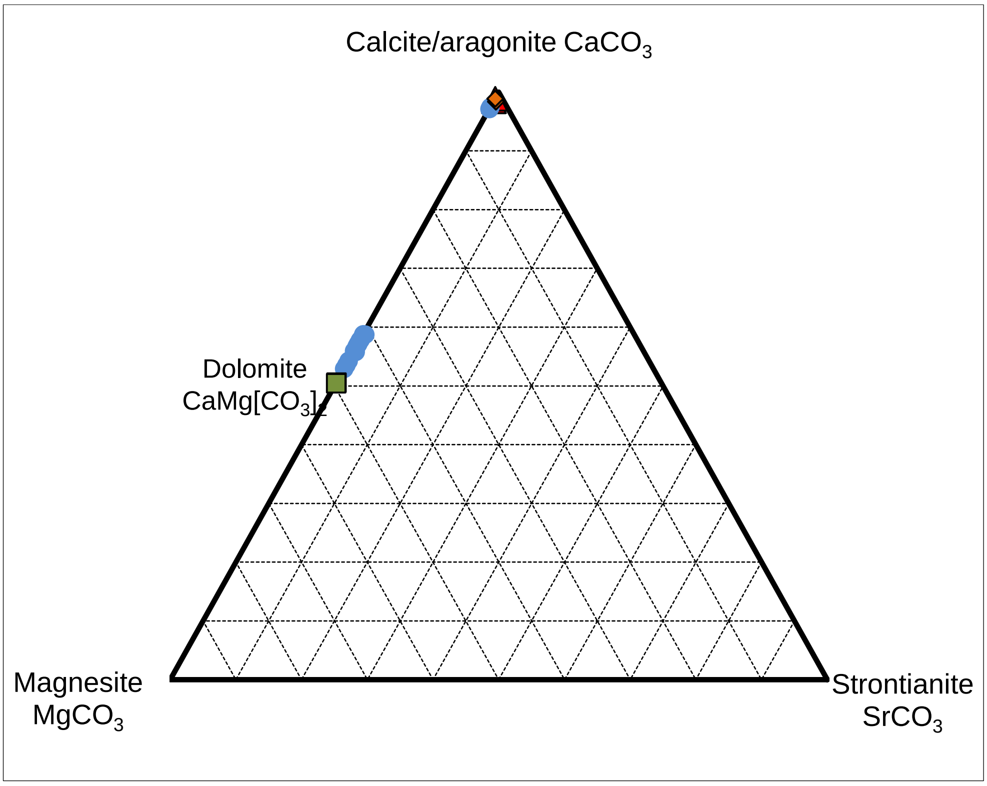

Figure 15. $CaCO_3$-$MgCO_3$-$SrCO_3$ molar ratio plot illustrating the compositions of the carbonate cements: blocky microsparite (blue circles), shell fragments (red triangles), calcite infill within the Fe-rich cement (orange diamonds), dolomite grain (green squares). Sample GT129.

Table 13. Electron microprobe analysis for the micrite cement and other components within sample GT129

		Weight % oxide (normalised)							Ionic ratio [normalised to 3 [O]						COMMENTS
SAMPLE	No	MgO	CaO	MnO	FeO	SrO	CO_2 (calc)	*Total wt.%	Mg^{2+}	Ca^{2+}	Mn^{2+}	Fe^{2+}	Sr^{2+}	CO_3^{2-}	
GT129	1	0.62	55.31	0.00	0.00	0.00	44.07	100	0.02	0.98	0.00	0.00	0.00	1.00	shell
GT129	2	0.61	55.32	0.00	0.00	0.00	44.07	100	0.02	0.98	0.00	0.00	0.00	1.00	shell
GT129	3	0.44	55.52	0.00	0.00	0.00	44.04	100	0.01	0.99	0.00	0.00	0.00	1.00	shell
GT129	4	18.48	34.38	0.00	0.00	0.00	47.14	100	0.43	0.57	0.00	0.00	0.00	1.00	micrite
GT129	5	17.62	35.13	0.00	0.00	0.32	46.93	100	0.41	0.59	0.00	0.00	0.00	1.00	micrite
GT129	6	17.83	35.14	0.00	0.00	0.00	47.03	100	0.41	0.59	0.00	0.00	0.00	1.00	micrite
GT129	7	18.26	34.64	0.00	0.00	0.00	47.11	100	0.42	0.58	0.00	0.00	0.00	1.00	micrite
GT129	8	18.15	34.47	0.00	0.33	0.00	47.05	100	0.42	0.57	0.00	0.00	0.00	1.00	micrite
GT129	9	19.78	32.68	0.00	0.19	0.00	47.35	100	0.46	0.54	0.00	0.00	0.00	1.00	micrite
GT129	10	18.45	34.26	0.00	0.18	0.00	47.12	100	0.43	0.57	0.00	0.00	0.00	1.00	micrite
GT129	11	19.07	33.69	0.00	0.00	0.00	47.24	100	0.44	0.56	0.00	0.00	0.00	1.00	micrite
GT129	12	1.02	54.84	0.00	0.00	0.00	44.14	100	0.03	0.97	0.00	0.00	0.00	1.00	micrite
GT129	13	1.16	54.67	0.00	0.00	0.00	44.16	100	0.03	0.97	0.00	0.00	0.00	1.00	micrite
GT129	14	17.75	35.23	0.00	0.00	0.00	47.02	100	0.41	0.59	0.00	0.00	0.00	1.00	micrite
GT129	15	18.51	34.16	0.00	0.21	0.00	47.13	100	0.43	0.57	0.00	0.00	0.00	1.00	micrite
GT129	16	18.90	33.42	0.00	0.20	0.36	47.12	100	0.44	0.56	0.00	0.00	0.00	1.00	micrite
GT129	17	18.09	34.57	0.00	0.30	0.00	47.05	100	0.42	0.58	0.00	0.00	0.00	1.00	micrite
GT129	18	18.14	34.77	0.00	0.00	0.00	47.09	100	0.42	0.58	0.00	0.00	0.00	1.00	micrite
GT129	19	20.48	32.03	0.00	0.00	0.00	47.49	100	0.47	0.53	0.00	0.00	0.00	1.00	micrite
GT129	20	18.70	34.12	0.00	0.00	0.00	47.18	100	0.43	0.57	0.00	0.00	0.00	1.00	micrite
GT129	21	20.11	32.30	0.00	0.18	0.00	47.41	100	0.46	0.53	0.00	0.00	0.00	1.00	micrite
GT129	22	0.50	54.08	0.23	0.96	0.37	43.86	100	0.01	0.97	0.00	0.01	0.00	1.00	calcite infill within Fe cement
GT129	23	0.43	54.65	0.19	0.79	0.00	43.95	100	0.01	0.98	0.00	0.01	0.00	1.00	calcite infill within Fe cement
GT129	24	21.13	30.08	0.52	0.80	0.00	47.47	100	0.49	0.50	0.01	0.01	0.00	1.00	dolomite/Mg Ca
GT129	25	21.20	30.07	0.56	0.68	0.00	47.49	100	0.49	0.50	0.01	0.01	0.00	1.00	dolomite/Mg Ca

**Note: Some analytical totals were low (<90%) because of the microporous nature of the cements. Therefore, all data were normalised to 100%*

2.14 SAMPLE GT141

This sample comprises three disparate sized (<120 mm), angular clasts of very pale, cream-coloured, coarse-grained sandstone (Plate 79). This sandstone has been heavily bioturbated. Numerous bryozoan and calcareous serpulid worm encrustations are visible on the clast surfaces.

Plate 79. Photograph of sample GT141 showing the irregular clasts. Grey scale bar divisions = 10 mm.

The scanned image of the thin section prepared from sample GT141 is shown in Plate 80 and shows thinly-interbedded or horizontally-laminated porous, moderately well-sorted, medium to coarse grained sandstone and less porous, poorly-sorted and moderately well-cemented, fine to medium grained sandstone, and coarse bioclastic shelly sandstone (Plate 80 and Plate 81). The lamination appears to be irregular and contorted, with lobed and flame-like structures, indicating synsedimentary disturbance. The convoluted upper surface is encrusted with a dense layer of white fibrous aragonite 1 to 2 mm thick (Plate 80 and Plate 81).

Aragonite was identified by XRD as the principal carbonate mineral, with only minor calcite. (Volume 1: Table 2). Petrographic analysis shows that this aragonite occurs within the sandstone as: (i) a structureless intergranular clay-rich, fine-grained micrite matrix; (ii) rounded micrite pelloids, which are probably faecal pellets (Plate 82); (iii) coarse fibrous or acicular, intergranular pore-filling and grain-coating aragonite (Plate 82 and Plate 83) and; (iv) as the dense fibrous aragonite crust coating the upper surface of the clast (Plate 80 and Plate 81). The micrite cement is seen to form an early coating with pores, where is often seen to be preferentially deposited on the underside of sand grains, to form 'pendant cements' or 'bearded grains' (Plate 83). This geopetal fabric is normally characteristic of cements formed in the subaerial or vadose zone sediments (e.g. Tucker, 2001). However, it seems highly unlikely that this is the case in these sediments from the Croker Carbonate Slabs area, in the central Irish Sea. A more plausible explanation is that this micrite cement fabric formed in 'gas-filled' porosity rather than water-saturated porosity. Under such conditions, the development of similar vadose-like cement fabrics might be expected to precipitate from porewater films draining under gravity through the unsaturated gas-filled porosity. Later, coarser acicular aragonite fringes have nucleated on the earlier micrite films and also line the intergranular porosity. The aragonite fringes vary in thickness from <1 μm to several tens of micrometres in thickness, and do not develop a geopetal fabric (Plate 83 and Plate 84). Therefore, the later aragonite is considered to have precipitated within water-saturated porosity rather than in gas-filled porosity, and most probably represents mineralisation after the loss of accumulated gas from the sediment.

The presence of synsedimentary soft-sediment disturbance (described above) with the development of 'flame-like' or 'flare-like' structures would be consistent with disturbance produced by gas-release from the underlying sediment. This, together with the formation geopetal 'bearded grain' micrite structures characteristic of cementation in unsaturated sediment, provide strong evidence for the sediment porosity being gas-filled during the precipitation of the early micritic high magnesian calcite.

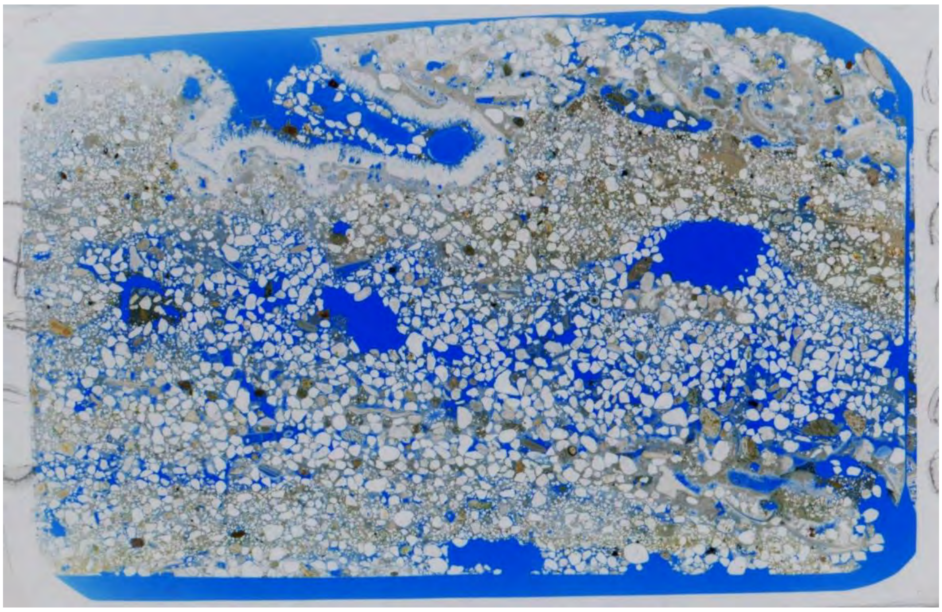

Plate 80. Scanned image of the thin section prepared from sample GT141. The section is broadly divided into four sub-horizontal bands. Note the calcareous band around the central embayment at the top of the image. Field of view = 48 mm wide.

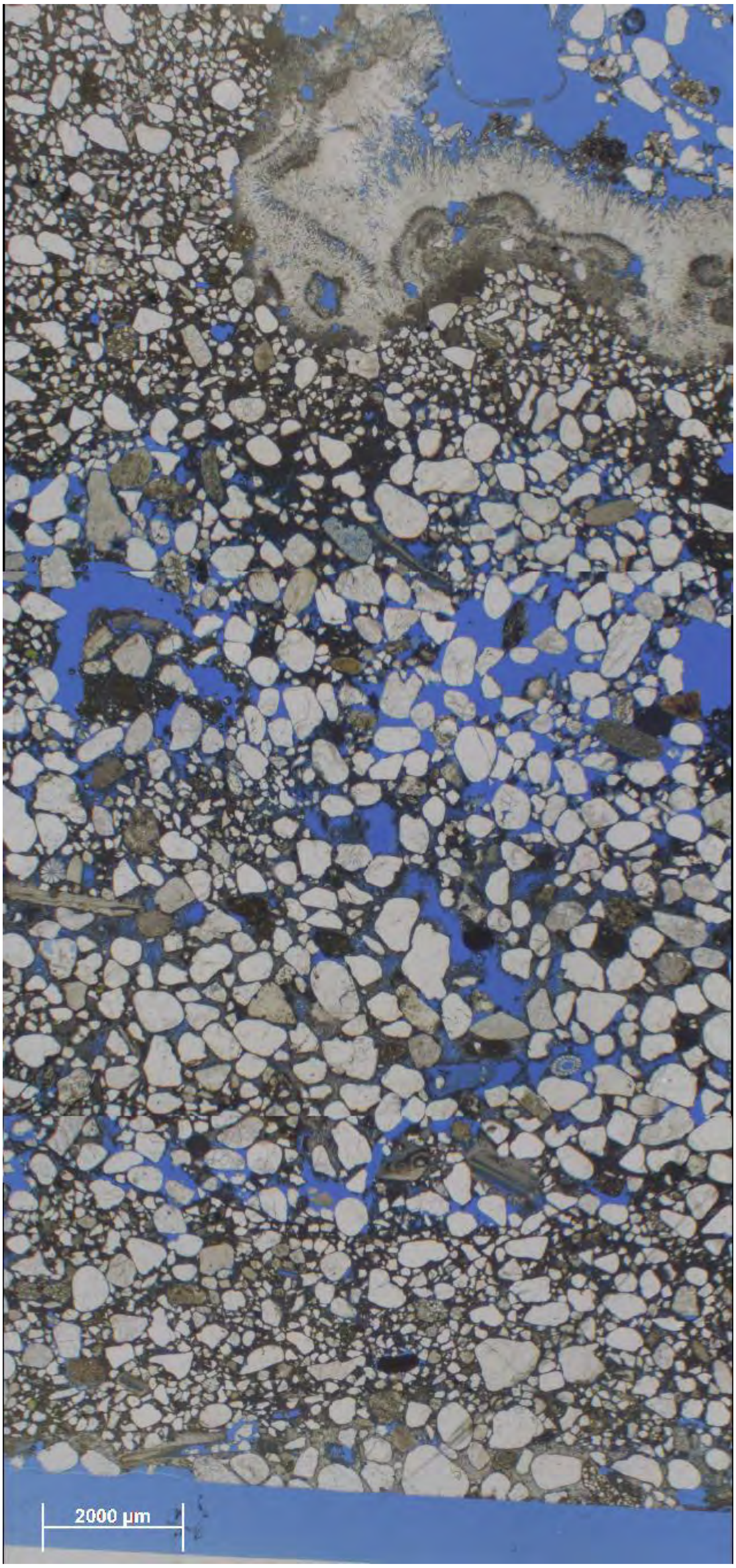

Plate 81. Transmitted light photomicrograph (plain polarised light) showing a panorama through the thin section. This details from the bottom to top: a well cemented layer, a more porous layer with oversized pores, a well cemented layer and the calcareous crust. The sample is rich in bioclastic debris. The sample is poorly-sorted, and grain size ranges from fine to coarse-grained sand. Sample GT141.

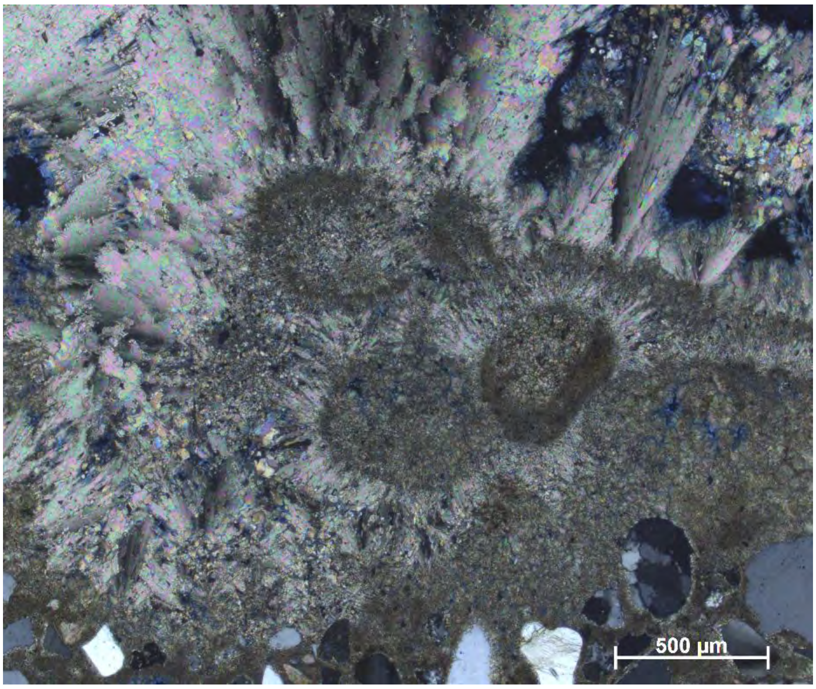

Plate 82. Transmitted light photomicrograph (cross polarised light) showing a pelloidal micrite fabric beneath the fibrous aragonite crust. The pelloids have been coated with a radial fringe of acicular aragonite. Sample GT141

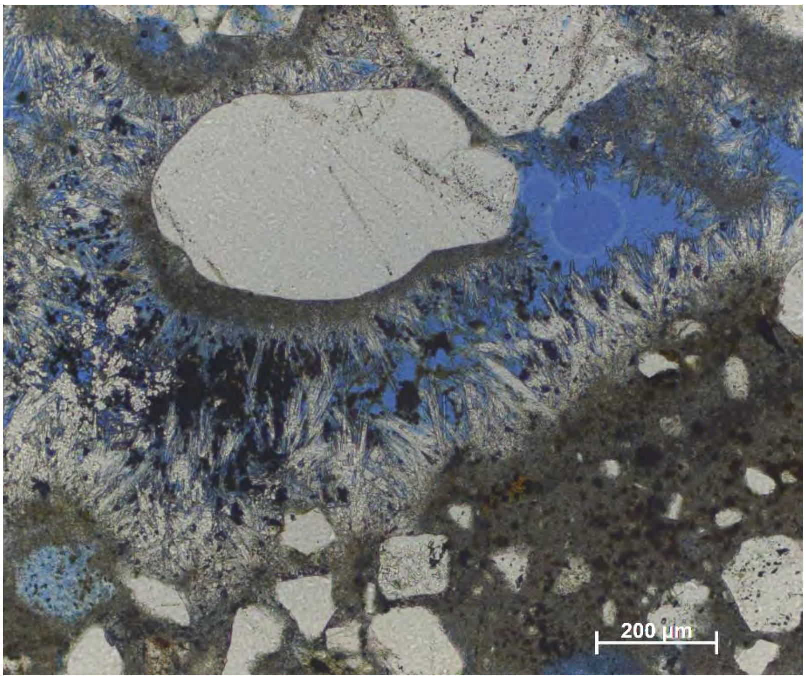

Plate 83. Transmitted light photomicrograph (plain polarised light) showing the asymmetric dark micritic aragonite cement fringes (or 'bearded' fringe) formed on the underside of quartz grains. Later, coarse acicular aragonite cement lines the pore walls. Sample GT141

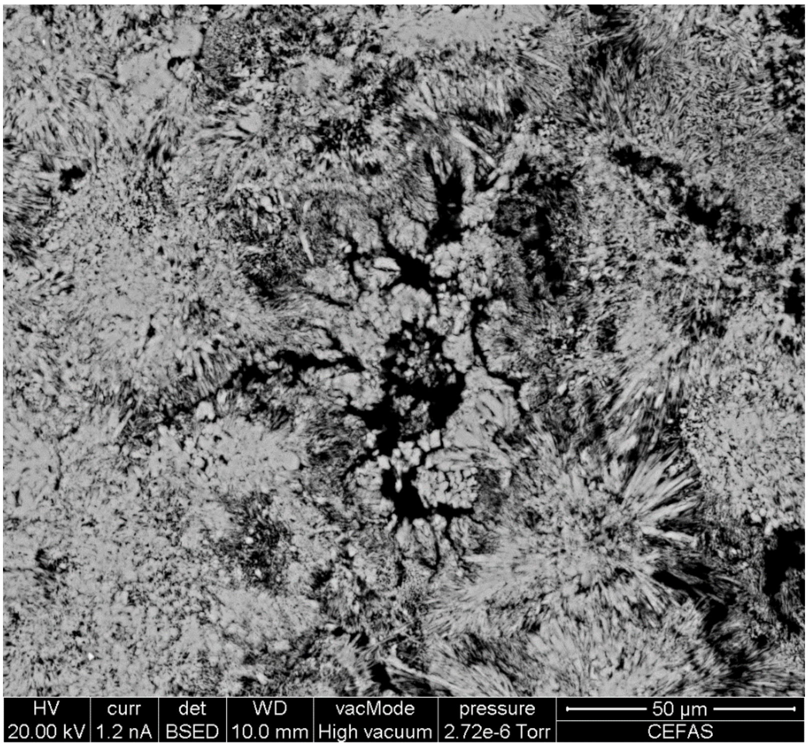

Plate 84. BSEM image of the calcareous crust showing the variability within the aragonite. Sample GT141

ED-EPMA major element compositional data for the aragonite cement in sample GT141 are given in Table 14. Their compositional variation, expressed in terms of molar proportions of CaO_3-$MgCO_3$ and $SrCO_3$, is summarised in Figure 16. The acicular aragonite is strontium bearing, with the highest values of strontium detected in these samples (up to 4 mole %: i.e. the structural formula of the aragonite can be represented as $Ca_{0.96\text{-}1.00}Sr_{0.04\text{-}0.00}CO_3$).

The sequence of sedimentary and post-depositional diagenetic events recorded from sample GT141 can be summarised as follows:

1. Deposition of intercalated medium to coarse and fine to medium sandy sediment, and coarse shelly sand and lesser amounts of fine muddy sediment.
2. Syndepositional bioturbation.
3. Accumulation of methane gas within sediment and precipitation of early micritic magnesian calcite in gas-saturated sediment, with synsedimentary disruption of the sedimentary fabric as a result of gas-release.
4. Displacement of methane gas from the sediment porosity and re-saturation with water.
5. Precipitation of pore-filling aragonite cement under water-saturated conditions, leading to sediment lithification.
6. Formation of an aragonite crust on the upper surface of the sample.
7. Exposure and colonisation and encrustation of the lithified sediment by bryozoan and calcareous serpulid worm tubes.

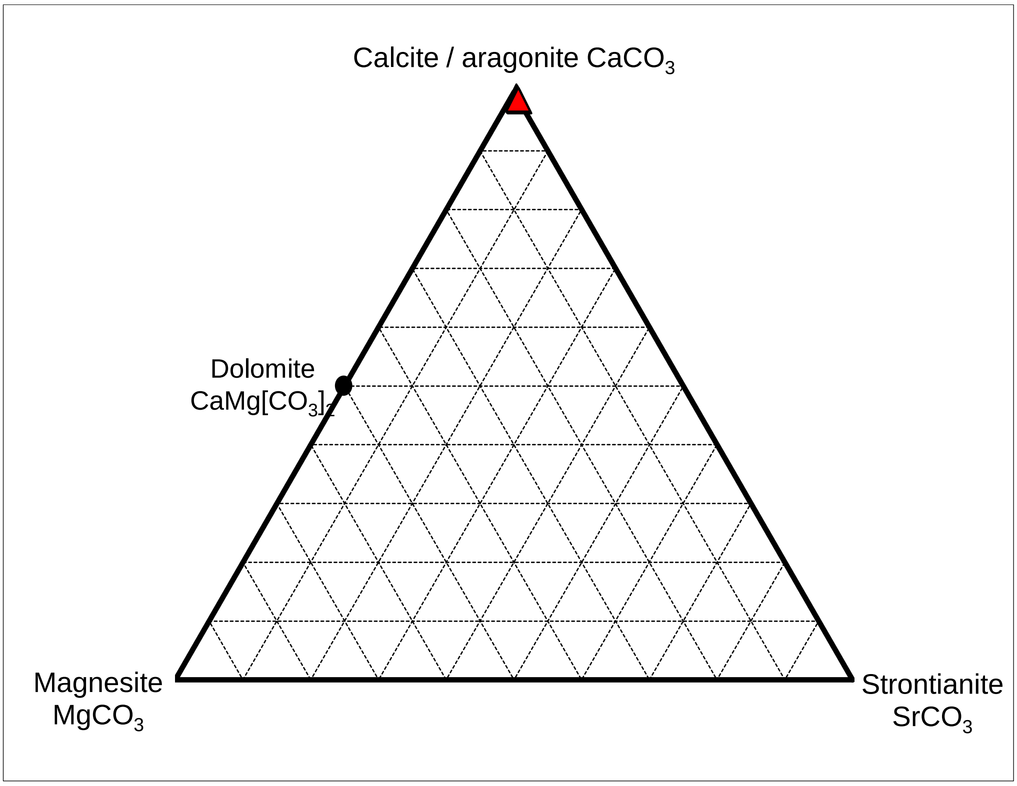

Figure 16. $CaCO_3$-$MgCO_3$-$SrCO_3$ molar ratio plot illustrating the compositions of the aragonite cement (red triangles). Sample GT141.

Table 14. Electron microprobe analyses of the aragonite cement in sample GT141

		Weight % oxide (normalised)							Ionic ratio [normalised to 3 [O]						COMMENTS
SAMPLE	No	MgO	CaO	MnO	FeO	SrO	CO_2 (calc)	*Total wt.%	Mg^{2+}	Ca^{2+}	Mn^{2+}	Fe^{2+}	Sr^{2+}	CO_3^{2-}	
GT141	1	0.00	54.76	0.00	0.00	1.59	43.64	100	0.00	1.25	0.00	0.00	0.04	1.00	aragonite cement
GT141	2	0.00	54.79	0.00	0.00	1.57	43.65	100	0.00	1.26	0.00	0.00	0.04	1.00	aragonite cement
GT141	3	0.00	54.83	0.00	0.00	1.51	43.66	100	0.00	1.26	0.00	0.00	0.03	1.00	aragonite cement
GT141	4	0.00	54.89	0.00	0.00	1.44	43.67	100	0.00	1.26	0.00	0.00	0.03	1.00	aragonite cement
GT141	5	0.00	54.83	0.00	0.00	1.52	43.66	100	0.00	1.26	0.00	0.00	0.03	1.00	aragonite cement
GT141	6	0.00	54.87	0.00	0.00	1.46	43.67	100	0.00	1.26	0.00	0.00	0.03	1.00	aragonite cement
GT141	7	0.00	54.93	0.00	0.00	1.39	43.69	100	0.00	1.26	0.00	0.00	0.03	1.00	aragonite cement
GT141	8	0.00	54.83	0.00	0.00	1.50	43.66	100	0.00	1.26	0.00	0.00	0.03	1.00	aragonite cement
GT141	9	0.00	54.78	0.00	0.00	1.57	43.65	100	0.00	1.26	0.00	0.00	0.04	1.00	aragonite cement
GT141	10	0.00	54.92	0.00	0.00	1.39	43.68	100	0.00	1.26	0.00	0.00	0.03	1.00	aragonite cement
GT141	11	0.00	55.05	0.00	0.00	1.23	43.72	100	0.00	1.26	0.00	0.00	0.03	1.00	aragonite cement
GT141	12	0.00	55.18	0.00	0.00	1.07	43.75	100	0.00	1.26	0.00	0.00	0.02	1.00	aragonite cement
GT141	13	0.00	55.07	0.00	0.00	1.20	43.72	100	0.00	1.26	0.00	0.00	0.03	1.00	aragonite cement
GT141	14	0.00	55.03	0.00	0.00	1.26	43.71	100	0.00	1.26	0.00	0.00	0.03	1.00	aragonite cement
GT141	15	0.00	55.00	0.00	0.00	1.30	43.70	100	0.00	1.26	0.00	0.00	0.03	1.00	aragonite cement
GT141	16	0.00	54.96	0.00	0.00	1.34	43.69	100	0.00	1.26	0.00	0.00	0.03	1.00	aragonite cement
GT141	17	0.00	55.08	0.00	0.00	1.20	43.72	100	0.00	1.26	0.00	0.00	0.03	1.00	aragonite cement
GT141	18	0.00	55.00	0.00	0.00	1.29	43.70	100	0.00	1.26	0.00	0.00	0.03	1.00	aragonite cement
GT141	19	0.00	55.04	0.00	0.00	1.25	43.71	100	0.00	1.26	0.00	0.00	0.03	1.00	aragonite cement
GT141	20	0.00	54.75	0.17	0.00	1.41	43.66	100	0.00	1.25	0.00	0.00	0.03	1.00	aragonite cement
GT141	21	0.00	54.97	0.00	0.00	1.34	43.69	100	0.00	1.26	0.00	0.00	0.03	1.00	aragonite cement
GT141	22	0.00	55.00	0.00	0.00	1.29	43.70	100	0.00	1.26	0.00	0.00	0.03	1.00	aragonite cement
GT141	23	0.00	55.37	0.00	0.00	0.83	43.80	100	0.00	1.26	0.00	0.00	0.02	1.00	aragonite cement
GT141	24	0.00	54.97	0.00	0.00	1.34	43.70	100	0.00	1.26	0.00	0.00	0.03	1.00	aragonite cement
GT141	25	0.00	55.29	0.00	0.00	0.93	43.78	100	0.00	1.26	0.00	0.00	0.02	1.00	aragonite cement
GT141	26	0.00	55.48	0.00	0.00	0.70	43.82	100	0.00	1.27	0.00	0.00	0.02	1.00	aragonite cement
GT141	27	0.00	55.30	0.00	0.00	0.92	43.78	100	0.00	1.26	0.00	0.00	0.02	1.00	aragonite cement
GT141	28	0.00	55.14	0.00	0.00	1.12	43.74	100	0.00	1.26	0.00	0.00	0.03	1.00	aragonite cement
GT141	29	0.00	55.18	0.00	0.00	1.07	43.75	100	0.00	1.26	0.00	0.00	0.02	1.00	aragonite cement
GT141	30	0.00	55.23	0.00	0.00	1.01	43.76	100	0.00	1.26	0.00	0.00	0.02	1.00	aragonite cement
GT141	31	0.00	55.14	0.00	0.00	1.12	43.74	100	0.00	1.26	0.00	0.00	0.03	1.00	aragonite cement
GT141	32	0.00	55.25	0.00	0.00	0.98	43.77	100	0.00	1.26	0.00	0.00	0.02	1.00	aragonite cement

		Weight % oxide (normalised)							Ionic ratio [normalised to 3 [O]						COMMENTS
SAMPLE	No	MgO	CaO	MnO	FeO	SrO	CO_2 (calc)	*Total wt.%	Mg^{2+}	Ca^{2+}	Mn^{2+}	Fe^{2+}	Sr^{2+}	CO_3^{2-}	
GT141	33	0.00	54.94	0.00	0.00	1.37	43.69	100	0.00	1.26	0.00	0.00	0.03	1.00	aragonite cement
GT141	34	0.00	54.85	0.00	0.00	1.48	43.67	100	0.00	1.26	0.00	0.00	0.03	1.00	aragonite cement
GT141	35	0.00	54.72	0.00	0.00	1.65	43.63	100	0.00	1.25	0.00	0.00	0.04	1.00	aragonite cement
GT141	36	0.00	54.98	0.00	0.00	1.32	43.70	100	0.00	1.26	0.00	0.00	0.03	1.00	aragonite cement
GT141	37	0.00	54.85	0.00	0.00	1.48	43.67	100	0.00	1.26	0.00	0.00	0.03	1.00	aragonite cement
GT141	38	0.00	54.87	0.00	0.00	1.46	43.67	100	0.00	1.26	0.00	0.00	0.03	1.00	aragonite cement
GT141	39	0.00	54.92	0.00	0.00	1.40	43.68	100	0.00	1.26	0.00	0.00	0.03	1.00	aragonite cement
GT141	40	0.00	54.91	0.00	0.00	1.41	43.68	100	0.00	1.26	0.00	0.00	0.03	1.00	aragonite cement
GT141	41	0.00	55.05	0.00	0.00	1.23	43.72	100	0.00	1.26	0.00	0.00	0.03	1.00	aragonite cement
GT141	42	0.00	55.01	0.00	0.00	1.28	43.71	100	0.00	1.26	0.00	0.00	0.03	1.00	aragonite cement

**Note: Some analytical totals were low (<90%) because of the microporous nature of the cements. Therefore, all data were normalised to 100%*

2.15 SAMPLE GT143

This sample comprises two clasts of mid-grey, coarse-grained sandstone, approximately 10 cm diameter (Plate 85). Both are tabular, irregular in shape, and no thicker than 4 cm. Their surfaces are rough, with evidence of numerous burrows, borings, serpulid worm encrustations (Plate 86), and minor encrustation by bryozoa. The burrow walls are cemented and more indurated than the surrounding sandstone. Consequently, the burrow walls have 'weathered' to form circular structures, which stand proud of the surface (Plate 85).

Plate 85 Photograph of sample GT143. The two clasts show evidence of numerous burrows and serpulid worm encrustations on the surface. Grey scale bar divisions = 10 mm.

The polished thin section prepared from sample GT143 is shown in Plate 87. The sandstone is medium grained in thin section (grains size up to 500 µm), and appears finer than initially noted in the hand specimen. This may be due to some variation within the clasts. The rock is patchily cemented (Plate 87), and this heterogeneous distribution of cementation and porosity may reflect bioturbation: as noted above, cementation is preferentially developed in the sand matrix immediately adjacent to burrow walls. Some of the intergranular pores are oversized relative to the detrital grain size (Plate 88), indicative of the dissolution of unstable grains.

XRD analysis indicates that high magnesian calcite comprises the bulk of the carbonate present, with non-magnesian calcite and aragonite representing only a minor component (Volume 1: Table 2). High magnesian calcite forms irregular, strongly cemented patches of sandstone, and comprises fine-grained, micrite which contain significant clay and silicate material. This contrasts with more porous areas where the acicular needles of aragonite line the surfaces of the open intergranular pore space (Plate 88). Some of the aragonite is coarse, with needles up to 200 µm long. The aragonite has preferentially nucleated on carbonate shell fragments, which bear fringes of coarse needles growing into the adjacent pores (Plate 89). Some patches of high-magnesian calcite appear to be corroded clasts that have been partially overprinted and replaced by the later aragonite (Plate 90). These are possibly relict fragments derived (eroded and reworked) from an earlier MDAC deposit. The clasts vary in magnesium content (as indicated by variation in grey level in BSEM images).

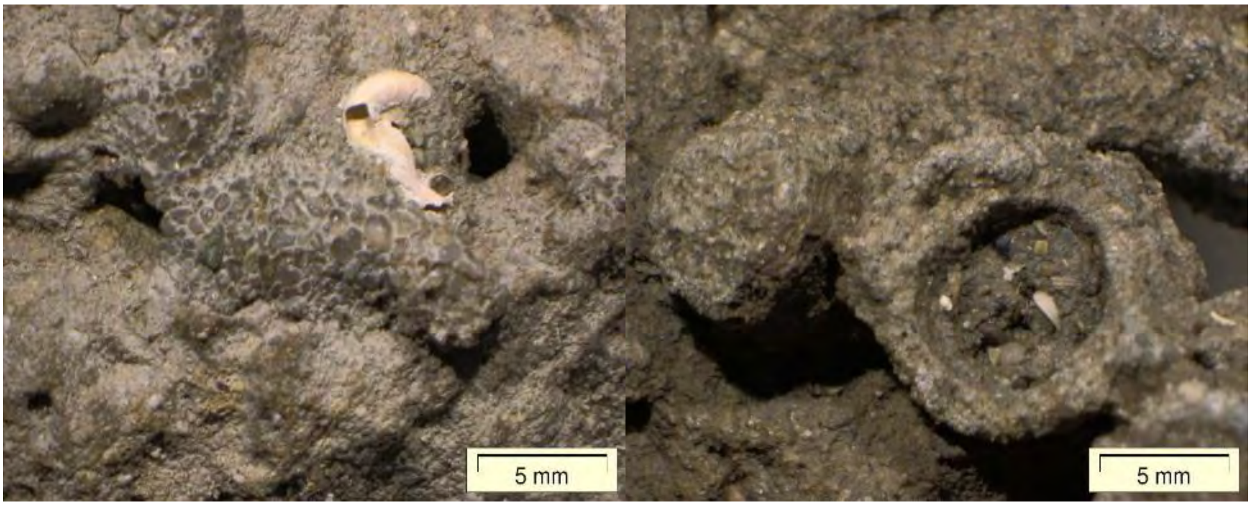

Plate 86. Photographs of the surface of GT143 showing left: coarse-grained sand (<1.5 mm) and serpulid worm encrustation, and right: cross sections through cemented and indurated burrow walls that have weathered or eroded to stand proud of the surfaces.

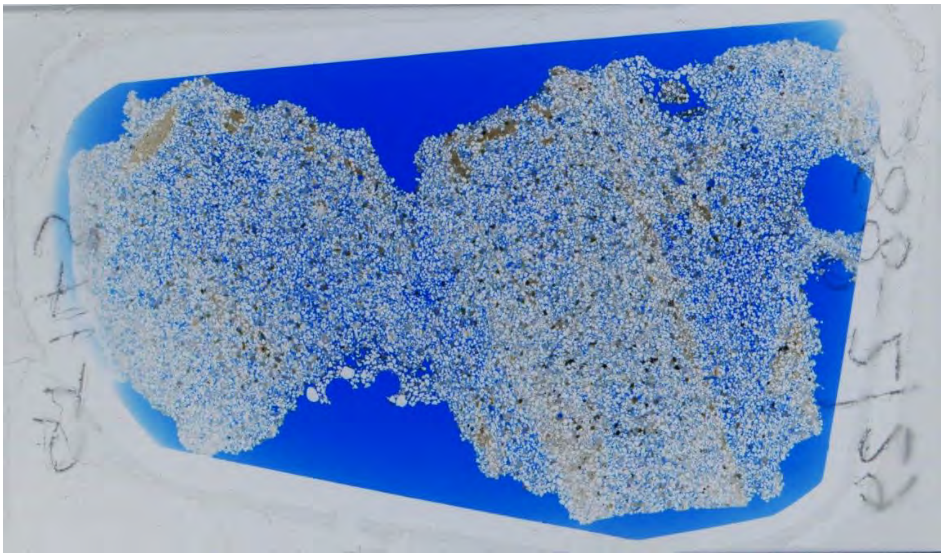

Plate 87. Scanned image of the polished thin section for sample GT143. Field of view = 48 mm wide.

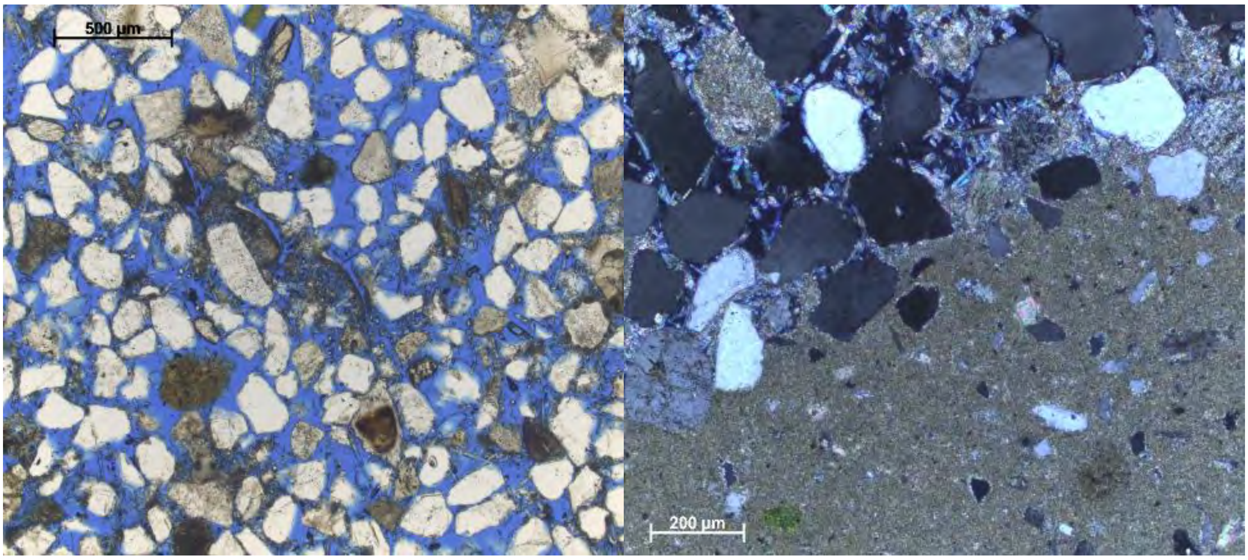

Plate 88. Transmitted light photomicrographs (Left: plain and right: polarised light). These show the variation in the degree of cementation and porosity within the sample. Left: porous sandstone with secondary oversized pore space formed by dissolved shell fragments (centre of image). Right: dense high magnesian-calcite micritic cement occurs as a nodular patch (seen in the lower right side of the image); acicular aragonite has grown into open intergranular pore space (seen in the upper left of the image). Sample GT143.

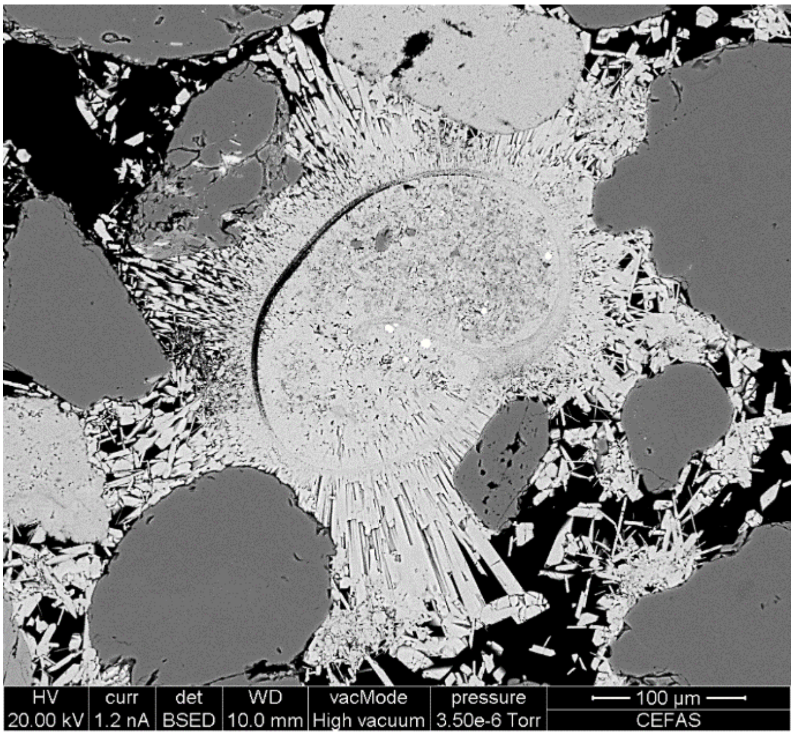

Plate 89. BSEM image of a carbonate shell onto which aragonite has preferentially nucleated as a radiating cement fringe filling the adjacent intergranular porosity. Sample GT143.

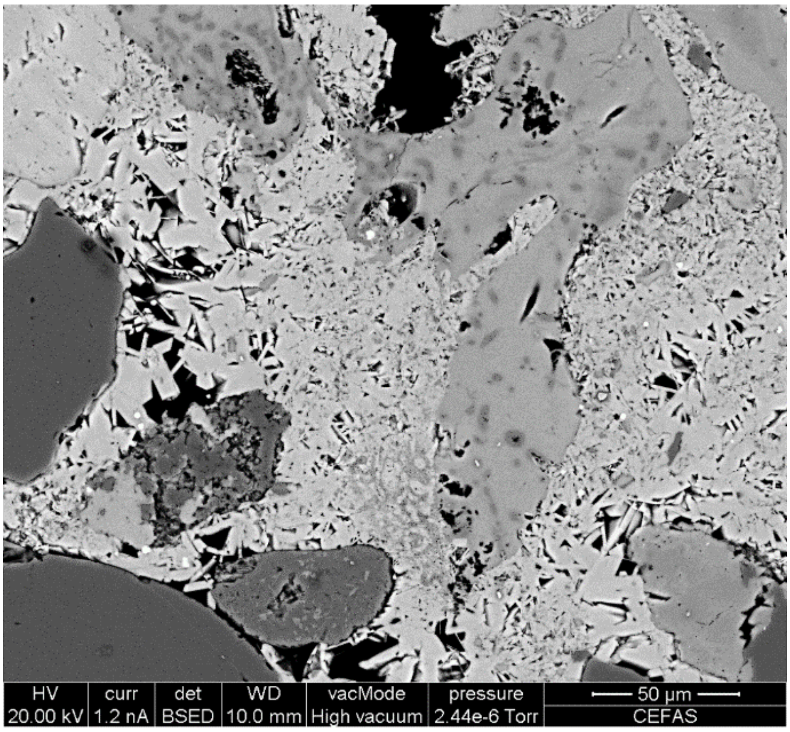

Plate 90. BSEM image showing probable relict MDAC clasts (mid grey) enclosed by fibrous aragonite cement. Note the patchy area (bottom centre) within the aragonite cement. This appears to be overprinting and replacement of relicts of earlier MDAC cement by the aragonite. Sample GT143.

ED-EPMA major element compositional data for the cements and some example shell fragments in sample GT143 are given in Figure 17. Their compositional variation, expressed in terms of molar proportions of CaO_3-$MgCO_3$ and $SrCO_3$, is summarised in Table 15. The acicular aragonite is strontium bearing, with up to 2 mole % $SrCO_3$ (i.e. the structural formula of the aragonite can be represented as $Ca_{0.98-1.00}Sr_{0.02-0.00}CO_3$)., and is identical to aragonite cement in sample GT120. The aragonite cement coating relict MDAC fragments was more variable in compositions with up to 9 mole % $MgCO_3$ (Figure 17, Table 15). This is probably due to the inclusion of remnants of magnesian-calcite in the ED-EPMA, resulting in mixed analysis. The relict MDAC itself, contains between 0 and 33 mole % $MgCO_3$ (i.e. the structural formula of the calcite can be represented as $Ca_{1.00-0.67}Mg_{0.00-0.33}CO_3$). This variation probably reflects mixed analysis with aragonite replacing the earlier MDAC. The shell fragment analysed appears to have been replaced by high-magnesian calcite but varies in composition, from 13 to 25 mole % $MgCO_3$.

The sequence of sedimentary and post-depositional diagenetic events recorded from sample GT143 can be summarised as follows:

1. Deposition of coarse sandy sediment, shelly debris and some silica-rich, fine grained micritic muds.
2. Partial cementation by high-magnesian calcite.
3. Dissolution of some detrital grains and shell fragments, and much of the original cement.
4. Precipitation of a replacive, aragonite cement which began to replace relict clasts of the magnesian calcite cement. Precipitation of acicular aragonite within larger intergranular pore spaces.
5. Syndepositional colonisation by boring marine organisms.

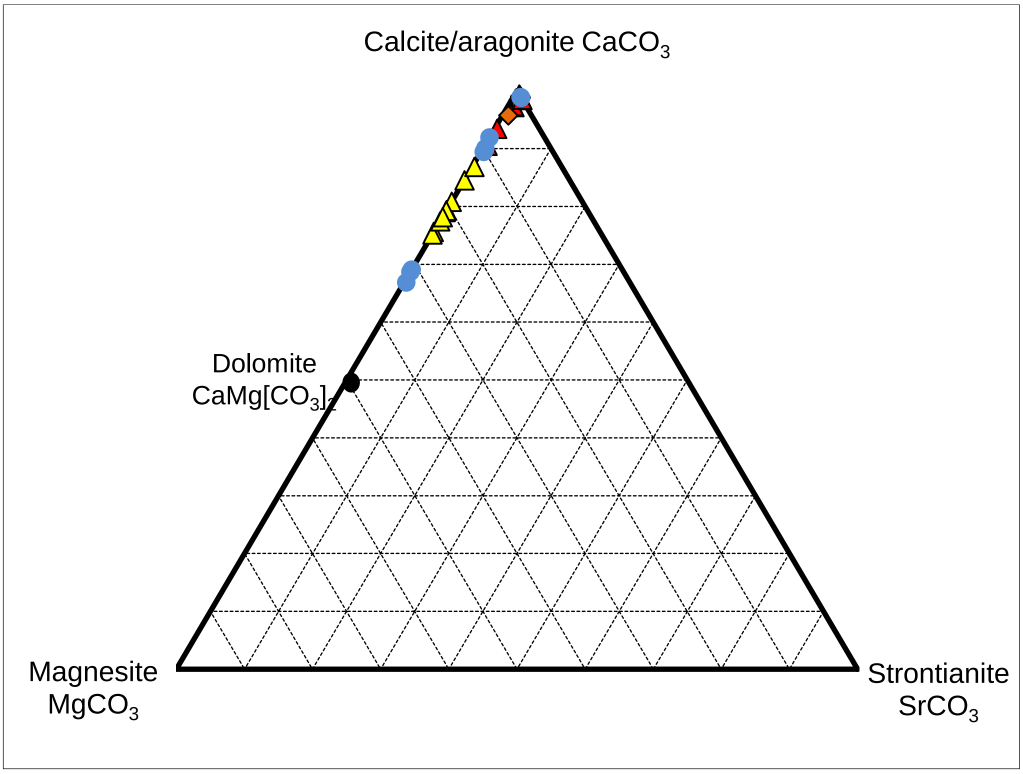

Figure 17. $CaCO_3$-$MgCO_3$-$SrCO_3$ molar ratio plot illustrating the compositions of the pore-filling aragonite cement (red triangles), aragonite replacing relict MDAC fragments (orange diamonds), shell fragments (yellow triangles), relict MDAC (blue circles). Sample GT143.

Table 15. Electron microprobe analyses of cements and shell fragments in sample GT143

		Weight % oxide (normalised)							Ionic ratio [normalised to 3 [O]						COMMENTS
SAMPLE	No	MgO	CaO	MnO	FeO	SrO	CO_2 (calc)	*Total wt.%	Mg^{2+}	Ca^{2+}	Mn^{2+}	Fe^{2+}	Sr^{2+}	CO_3^{2-}	
GT143	1	0.00	55.41	0.00	0.00	0.79	43.81	100	0.00	0.99	0.00	0.00	0.01	1.00	aragonite cement
GT143	2	0.00	55.18	0.00	0.00	1.07	43.75	100	0.00	0.99	0.00	0.00	0.01	1.00	aragonite cement
GT143	3	0.00	54.72	0.00	0.00	1.65	43.63	100	0.00	0.98	0.00	0.00	0.02	1.00	aragonite cement
GT143	4	0.21	55.02	0.00	0.00	0.96	43.81	100	0.01	0.99	0.00	0.00	0.01	1.00	aragonite cement
GT143	5	0.00	55.35	0.00	0.00	0.85	43.79	100	0.00	0.99	0.00	0.00	0.01	1.00	aragonite cement
GT143	6	0.00	55.21	0.00	0.00	1.03	43.76	100	0.00	0.99	0.00	0.00	0.01	1.00	aragonite cement
GT143	7	0.00	55.41	0.00	0.00	0.78	43.81	100	0.00	0.99	0.00	0.00	0.01	1.00	aragonite cement
GT143	8	0.00	55.46	0.00	0.00	0.72	43.82	100	0.00	0.99	0.00	0.00	0.01	1.00	aragonite cement
GT143	9	0.00	55.22	0.00	0.00	1.02	43.76	100	0.00	0.99	0.00	0.00	0.01	1.00	aragonite cement
GT143	10	0.71	54.10	0.00	0.26	1.09	43.84	100	0.02	0.97	0.00	0.00	0.01	1.00	aragonite cement
GT143	11	2.50	52.30	0.00	0.57	0.37	44.26	100	0.06	0.93	0.00	0.01	0.00	1.00	aragonite cement
GT143	12	3.69	51.36	0.00	0.00	0.45	44.51	100	0.09	0.91	0.00	0.00	0.00	1.00	aragonite cement
GT143	13	0.00	55.21	0.00	0.00	1.03	43.76	100	0.00	0.99	0.00	0.00	0.01	1.00	aragonite cement
GT143	14	0.00	55.41	0.00	0.00	0.78	43.81	100	0.00	0.99	0.00	0.00	0.01	1.00	aragonite cement
GT143	15	0.00	55.06	0.00	0.00	1.23	43.72	100	0.00	0.99	0.00	0.00	0.01	1.00	aragonite cement
GT143	16	0.72	54.50	0.00	0.00	0.87	43.91	100	0.02	0.97	0.00	0.00	0.01	1.00	aragonite cement
GT143	17	0.00	55.25	0.00	0.00	0.98	43.77	100	0.00	0.99	0.00	0.00	0.01	1.00	acicular aragonite cement
GT143	18	0.00	55.17	0.00	0.00	1.08	43.75	100	0.00	0.99	0.00	0.00	0.01	1.00	acicular aragonite cement
GT143	19	0.00	55.15	0.00	0.00	1.11	43.74	100	0.00	0.99	0.00	0.00	0.01	1.00	acicular aragonite cement
GT143	20	0.00	55.49	0.00	0.00	0.68	43.83	100	0.00	0.99	0.00	0.00	0.01	1.00	acicular aragonite cement
GT143	21	0.00	55.28	0.00	0.00	0.94	43.77	100	0.00	0.99	0.00	0.00	0.01	1.00	acicular aragonite cement
GT143	22	0.00	55.34	0.00	0.00	0.88	43.79	100	0.00	0.99	0.00	0.00	0.01	1.00	acicular aragonite cement
GT143	23	0.00	55.36	0.00	0.00	0.84	43.79	100	0.00	0.99	0.00	0.00	0.01	1.00	acicular aragonite cement
GT143	24	0.00	55.44	0.00	0.00	0.75	43.81	100	0.00	0.99	0.00	0.00	0.01	1.00	acicular aragonite cement
GT143	25	0.00	55.16	0.00	0.00	1.10	43.74	100	0.00	0.99	0.00	0.00	0.01	1.00	acicular aragonite cement
GT143	26	0.00	54.80	0.00	0.00	1.54	43.65	100	0.00	0.98	0.00	0.00	0.02	1.00	acicular aragonite cement
GT143	27	0.21	54.92	0.00	0.00	1.08	43.78	100	0.01	0.98	0.00	0.00	0.01	1.00	overprinting by aragonite
GT143	28	0.00	55.20	0.00	0.00	1.04	43.75	100	0.00	0.99	0.00	0.00	0.01	1.00	overprinting by aragonite
GT143	29	1.37	53.72	0.00	0.00	0.88	44.02	100	0.03	0.96	0.00	0.00	0.01	1.00	overprinting by aragonite
GT143	30	0.00	54.85	0.00	0.24	1.20	43.70	100	0.00	0.98	0.00	0.00	0.01	1.00	overprinting by aragonite
GT143	31	0.00	55.05	0.00	0.20	1.00	43.74	100	0.00	0.99	0.00	0.00	0.01	1.00	overprinting by aragonite
GT143	32	0.00	55.24	0.00	0.00	1.00	43.76	100	0.00	0.99	0.00	0.00	0.01	1.00	overprinting by aragonite

		Weight % oxide (normalised)							Ionic ratio [normalised to 3 [O]						COMMENTS
SAMPLE	No	MgO	CaO	MnO	FeO	SrO	CO_2 (calc)	*Total wt.%	Mg^{2+}	Ca^{2+}	Mn^{2+}	Fe^{2+}	Sr^{2+}	CO_3^{2-}	
GT143	33	4.16	50.84	0.00	0.00	0.40	44.60	100	0.10	0.89	0.00	0.00	0.00	1.00	Relict MDAC
GT143	34	3.29	52.18	0.00	0.00	0.00	44.53	100	0.08	0.92	0.00	0.00	0.00	1.00	Relict MDAC
GT143	35	3.93	51.15	0.00	0.00	0.36	44.57	100	0.10	0.90	0.00	0.00	0.00	1.00	Relict MDAC
GT143	36	13.10	40.69	0.00	0.00	0.00	46.22	100	0.31	0.69	0.00	0.00	0.00	1.00	Relict MDAC
GT143	37	13.92	39.45	0.00	0.00	0.34	46.29	100	0.33	0.67	0.00	0.00	0.00	1.00	Relict MDAC
GT143	38	13.26	40.49	0.00	0.00	0.00	46.25	100	0.31	0.69	0.00	0.00	0.00	1.00	Relict MDAC
GT143	39	0.00	55.03	0.00	0.00	1.25	43.71	100	0.00	0.99	0.00	0.00	0.01	1.00	Relict MDAC
GT143	40	0.00	55.15	0.00	0.00	1.11	43.74	100	0.00	0.99	0.00	0.00	0.01	1.00	Relict MDAC
GT143	41	6.38	48.56	0.00	0.00	0.00	45.06	100	0.15	0.85	0.00	0.00	0.00	1.00	shell fragment
GT143	42	5.28	49.58	0.00	0.00	0.34	44.80	100	0.13	0.87	0.00	0.00	0.00	1.00	shell fragment
GT143	43	8.59	45.97	0.00	0.00	0.00	45.44	100	0.21	0.79	0.00	0.00	0.00	1.00	shell fragment
GT143	44	7.96	46.70	0.00	0.00	0.00	45.33	100	0.19	0.81	0.00	0.00	0.00	1.00	shell fragment
GT143	45	8.69	45.63	0.00	0.24	0.00	45.44	100	0.21	0.79	0.00	0.00	0.00	1.00	shell fragment
GT143	46	10.22	44.06	0.00	0.00	0.00	45.72	100	0.24	0.76	0.00	0.00	0.00	1.00	shell fragment
GT143	47	8.63	45.93	0.00	0.00	0.00	45.45	100	0.21	0.79	0.00	0.00	0.00	1.00	shell fragment
GT143	48	10.41	43.84	0.00	0.00	0.00	45.75	100	0.25	0.75	0.00	0.00	0.00	1.00	shell fragment
GT143	49	9.42	45.00	0.00	0.00	0.00	45.58	100	0.23	0.77	0.00	0.00	0.00	1.00	shell fragment
GT143	50	9.11	45.36	0.00	0.00	0.00	45.53	100	0.22	0.78	0.00	0.00	0.00	1.00	shell fragment

**Note: Some analytical totals were low (<90%) because of the microporous nature of the cements. Therefore, all data were normalised to 100%*

2.16 SAMPLE GT150

This sample comprises a selection of sub-rounded clasts varying in colour from grey to mid-brown (Plate 91). These clasts are fine-grained, and some are clearly lithic clasts. No evidence of bioturbation or boring by marine organisms. Some calcareous bryozoan encrustations are present on the surfaces.

Plate 91. Photograph of sample GT150. This comprises a collection of angular to sub-rounded clasts, some of which are lithics. Some bryozoan encrustations are present on the surfaces. Grey scale bar divisions = 10 mm.

Two of the most promising clasts were selected for XRD and petrographic analysis. The thin section prepared from one of the clasts is shown in Plate 92. Although encrusted with bryozoa, this clast was found to be a fine grained metasedimentary rock. It has a fine-grained fabric with some coarse quartz grains (<1500 µm), and a healed fracture infilled with quartz. The fabric is a penetrative domainal cleavage comprising dark folia of fine-grained, well-aligned phyllosilicate minerals (micas and chlorite, formed through pressure-solution), anastomosing around stronger domains dominated by detrital quartz (Plate 93). The presence of quartz-phyllosilicate fringes or 'beards' of fibrous grains extending parallel to cleavage indicates this is a lithic of highly compacted rock of meta-sandstone origin (Vernon, 2004). No carbonate was identified within this thin section, indicating this clast is not an MDAC sample. This contrasts to the XRD results from a second clast, which was a fragment of dolomite-cemented sandstone with >24% dolomite (Volume 1, Table 2).

Plate 92. Scanned image of the thin section prepared from sample GT150. Field of view = 48 mm wide.

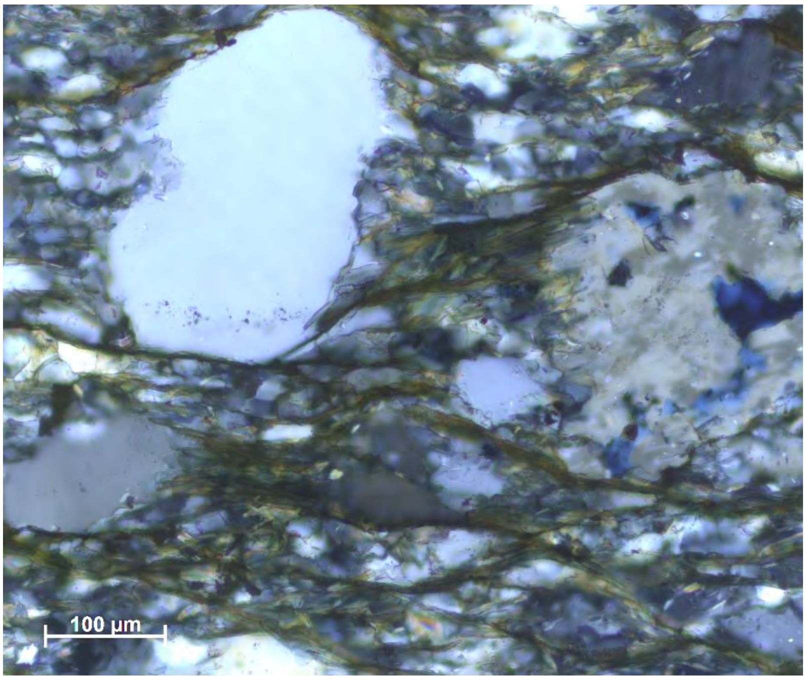

Plate 93. Transmitted light photomicrograph (cross polarised light) showing the penetrative domainal cleavage defined by folia of well-aligned micas and chlorite, and stronger domains of detrital fragments, mainly quartz. GT150

2.17 IRON AND MANGANESE OXYHYDROXIDE CEMENTS

In four samples, GT025, GT117, GT126 and GT129, significant amounts of pore filling iron oxyhydroxide cement (Plate 94, Plate 95), and colloform manganese oxyhydroxide precipitates and crusts were identified (Plate 94, Plate 96). Minor colloform iron-manganese oxyhydroxide crusts were also noted in GT104. In sample GT129, the iron-manganese oxyhydroxide-rich cement is present around the edge of the sample forming a 'weathered' rim. The manganese oxyhydroxide precipitate has formed a thin crust around the outer edge of the sample. In samples GT025, GT117 and GT126, the cements and colloform precipitates have infilled smaller pores in the rock. The iron-manganese oxyhydroxide cements probably precipitated as a very hydrous or gel-like material, and in thin section, these are now seen to be fractured, displaying a cracked or crazed texture that is probably (in part) due to dehydration and shrinkage during sample drying and thin section preparation. ED-EDXA analysis indicates that the secondary iron-manganese oxyhydroxide contains up to 2.7 wt. % phosphorous. The colloform manganese oxyhydroxide precipitates do not contain any phosphorous.

Manganese crusts and nodules are common within the oceans, although the majority of manganese nodules are associated with the deep ocean (>4,000 m) and crusts (>1000 m: Glasby, 2006). Ferromanganese concretions however, have been identified in shallow marine environments (e.g. Loch Fyne, 180-200 m: Calvert and Price, 1970) and in temperate-zone lakes, and these are faster growing by 3-4 orders of magnitude than their deep ocean equivalents (Glasby, 2006). In concretions and nodules from the Baltic, Mn and Fe precipitate initially as an unstable gel, but are ultimately incorporated as oxyhydroxides (Glasby, 2006). Chester and Jichells (2012) propose that ferromanganese encrustations can form via hydrogenous supply i.e. the elements necessary for growth can be taken directly from the overlying seawater without receiving input from sediment sources. Ferromanganese crusts have also been described in association with methane seep sites, where it is considered to be related to the alteration and oxidation of earlier-formed diagenetic pyrite (e.g. Merinero et al., 2008), similar to that seen in some these samples.

The EDXA analysis (Table 16) show that unlike many deep marine ferromanganese crusts and nodules, the samples here contain <1 wt. % elemental Co. Other elements which are often enriched e.g. Ni, Zn and V (e.g. Calvert and Price, 1970 and 1977, Chester and Jickells, 2012, Glasby, 2006), are also not detectable in these samples. Phosphorous concentrations up to 2.7 wt. % P are found in the Fe-rich cement, although it was not detectable in the colloform manganese oxyhydroxide precipitates and crust.

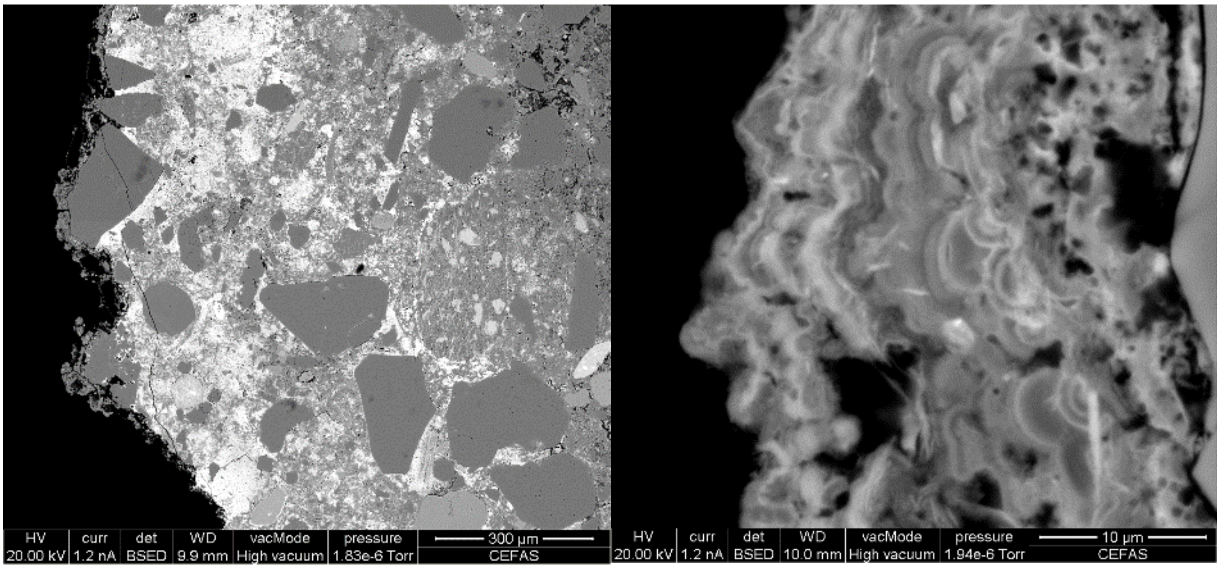

Plate 94. BSEM images showing the iron and manganese-rich oxyhydroxide cement and colloform manganese oxyhydroxide crust on sample GT129

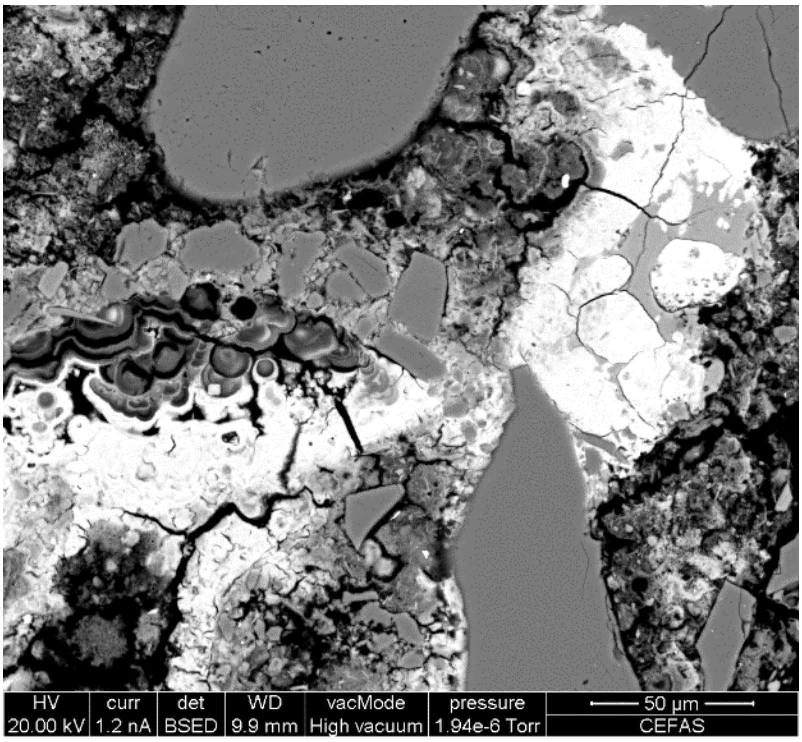

Plate 95. BSEM image of the gel-like iron-manganese oxyhydroxide cement in sample GT129. Colloform manganese oxyhydroxide precipitate is also present as an earlier-formed phase (centre, left side of image); calcite (mid-grey) has precipitated between this and the later (enclosing) iron-manganese oxyhydroxide cement (bright white: centre, right side of image). The irregularly 'cracked' texture of the iron-manganese oxyhydroxide, probably caused by dehydration of the sample.

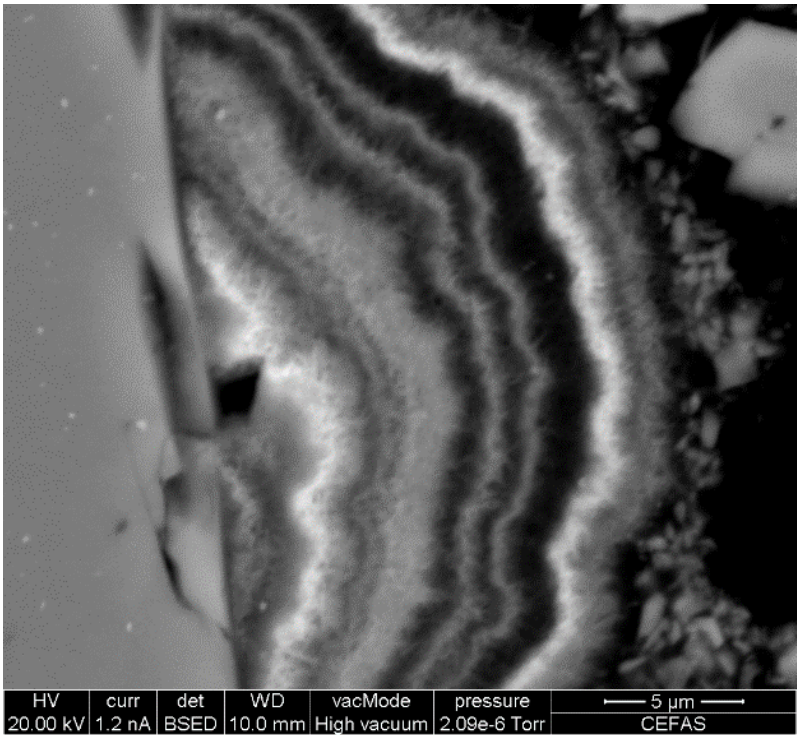

Plate 96. BSEM image from sample GT126 showing a colloform manganese oxyhydroxide-rich precipitate. ED-EPMA analyses of the bands are shown in Table 16.

Table 16. Electron microprobe analysis of the iron oxyhydroxide cements and colloform manganese oxyhydroxide precipitates

		Element (weight % normalised to 100 %)														COMMENTS
SAMPLE	No	Na	Mg	Al	Si	P	K	Ca	V	Mn	Fe	Co	Sr	O (calc)	*Total wt.%	
GT025	1	1.67	1.59	1.18	5.65	2.66	0.58	1.44	0.24	0.47	54.33	0.32	0.56	29.32	100	Fe-oxyhydroxide. cement
GT025	2	2.05	1.72	1.55	6.21	2.38	0.61	1.13	0.20	0.37	54.08	0.00	0.00	29.70	100	Fe-oxyhydroxide. cement
GT025	3	1.74	1.63	1.64	6.18	2.47	0.81	1.15	0.23	0.23	53.62	0.00	0.60	29.70	100	Fe-oxyhydroxide. cement
GT025	4	1.74	1.57	1.37	5.92	2.72	0.61	1.33	0.28	0.18	54.59	0.00	0.00	29.68	100	Fe-oxyhydroxide. cement
GT025	5	1.70	1.69	1.16	5.44	2.60	0.54	1.07	0.25	0.37	55.10	0.33	0.62	29.13	100	Fe-oxyhydroxide. cement
GT025	6	1.44	1.77	1.14	5.11	2.53	0.47	0.96	0.35	0.30	55.94	0.45	0.66	28.88	100	Fe-oxyhydroxide. cement
GT025	7	1.41	2.84	3.39	6.76	2.86	0.75	0.68	0.23	0.42	48.61	0.50	0.00	31.56	100	Fe-oxyhydroxide. cement
GT025	8	1.30	2.97	3.19	6.62	3.09	0.85	0.78	0.33	0.40	48.10	0.00	0.81	31.57	100	Fe-oxyhydroxide. cement
GT025	9	1.12	2.37	1.47	8.53	2.73	0.32	0.75	0.23	0.18	49.97	0.00	0.78	31.55	100	Fe-oxyhydroxide. cement
GT025	10	2.12	1.64	1.02	5.62	2.76	0.42	1.23	0.24	1.29	54.29	0.00	0.00	29.38	100	Fe-oxyhydroxide. cement
GT025	11	2.15	1.46	1.21	5.85	2.61	0.64	1.25	0.14	1.17	53.18	0.33	0.65	29.35	100	Fe-oxyhydroxide. cement
GT025	12	2.03	1.79	1.36	6.23	3.00	0.57	1.44	0.00	0.35	53.13	0.00	0.00	30.09	100	Fe-oxyhydroxide. cement
GT117	1	1.66	1.77	0.00	4.12	1.76	0.23	3.44	0.00	19.37	39.69	0.00	0.67	27.27	100	Fe-Mn oxyhydroxide. cement
GT117	2	1.82	2.03	0.37	4.90	1.67	0.26	2.88	0.00	13.72	44.40	0.00	0.00	27.96	100	Fe-Mn oxyhydroxide. cement
GT117	3	2.17	1.30	0.27	8.26	1.48	0.27	3.03	0.00	14.09	38.30	0.40	0.69	29.74	100	Fe-Mn oxyhydroxide. cement
GT117	4	1.80	1.46	0.60	5.83	2.00	0.28	2.95	0.14	4.88	50.67	0.00	0.65	28.74	100	Fe-Mn oxyhydroxide. cement
GT117	5	2.02	1.41	0.32	4.36	1.93	0.22	3.06	0.00	4.40	54.30	0.39	0.00	27.59	100	Fe-Mn oxyhydroxide. cement
GT126	1	2.31	2.04	0.38	3.67	1.79	0.36	2.80	0.23	0.17	58.95	0.00	0.00	27.29	100	Fe-oxyhydroxide. cement
GT126	2	2.03	2.43	1.11	4.29	1.90	0.60	2.28	0.28	4.35	52.20	0.33	0.00	28.20	100	Fe-oxyhydroxide. cement
GT126	3	2.26	2.31	0.42	4.07	1.71	0.48	3.95	0.19	5.59	51.35	0.00	0.00	27.68	100	Fe-oxyhydroxide. cement
GT126	4	2.58	3.28	0.84	3.14	1.36	0.35	2.18	0.00	17.03	42.13	0.00	0.00	27.11	100	Fe-oxyhydroxide. cement
GT126	5	2.12	2.71	0.63	3.52	1.63	0.39	2.11	0.29	13.16	45.40	0.00	0.70	27.32	100	Fe-oxyhydroxide. cement
GT126	6	2.57	3.08	0.69	3.83	1.41	0.40	3.19	0.18	8.99	48.06	0.00	0.00	27.60	100	Fe-oxyhydroxide. cement
GT126	7	1.47	4.71	0.56	11.33	0.00	1.04	0.76	0.00	47.65	0.59	0.26	0.00	31.64	100	colloform Mn oxyhydroxide.
GT126	8	2.69	8.07	0.86	1.21	0.00	1.23	1.04	0.00	58.13	0.60	0.00	0.00	26.16	100	colloform Mn oxyhydroxide.
GT126	9	1.74	8.13	1.21	0.44	0.00	1.35	0.97	0.00	59.73	0.67	0.00	0.00	25.78	100	colloform Mn oxyhydroxide.
GT126	10	1.64	8.93	1.56	0.46	0.00	1.19	1.22	0.00	58.81	0.00	0.00	0.00	26.21	100	colloform Mn oxyhydroxide.
GT126	11	1.95	8.33	1.32	0.56	0.00	1.25	1.19	0.00	59.40	0.00	0.00	0.00	26.00	100	colloform Mn oxyhydroxide.
GT126	12	2.13	8.53	1.30	0.61	0.00	1.39	1.07	0.00	58.03	0.86	0.00	0.00	26.07	100	colloform Mn oxyhydroxide.
GT126	13	3.36	9.66	2.17	1.25	0.00	0.78	1.11	0.00	53.12	1.24	0.00	0.00	27.31	100	colloform Mn oxyhydroxide.
GT126	14	3.83	8.20	3.37	5.57	0.00	0.96	2.21	0.00	44.40	1.07	0.00	0.00	30.39	100	colloform Mn oxyhydroxide.

		Element (weight % normalised to 100 %)														COMMENTS
SAMPLE	No	Na	Mg	Al	Si	P	K	Ca	V	Mn	Fe	Co	Sr	O (calc)	*Total wt.%	
GT129	1	2.09	1.40	2.41	8.78	2.44	0.99	1.89	0.18	0.00	47.72	0.31	0.00	31.80	100	Fe-oxyhydroxide. cement
GT129	2	3.17	1.57	2.27	7.46	2.49	1.09	4.09	0.00	0.18	46.04	0.54	0.00	31.11	100	Fe-oxyhydroxide. cement
GT129	3	2.84	1.29	2.31	7.59	2.52	1.11	2.14	0.16	2.21	46.25	0.00	0.58	31.00	100	Fe-oxyhydroxide. cement
GT129	4	2.57	1.99	0.14	3.77	2.66	0.34	2.08	0.26	4.41	53.89	0.00	0.00	27.89	100	Fe-oxyhydroxide. cement
GT129	5	3.06	3.69	0.42	2.97	1.67	0.30	1.70	0.00	23.44	35.58	0.00	0.00	27.17	100	colloform Mn oxyhydroxide.
GT129	6	2.87	3.91	0.50	2.61	1.47	0.36	1.66	0.00	26.27	33.49	0.00	0.00	26.86	100	colloform Mn oxyhydroxide.
GT129	7	3.51	3.99	0.40	2.72	1.44	0.28	1.67	0.00	26.97	31.30	0.00	0.86	26.86	100	colloform Mn oxyhydroxide.

3 Stable isotope characteristics

3.1 GENERAL

The results of the stable isotope ($\delta^{13}C$ and $\delta^{18}O$) analyses of the carbonate material from the Croker Carbonate Slab MDAC samples, determined by the 'small carbonate analysis method (Volume 1: Section 2.3), are given in Table 17. The data represent carbonate minerals sampled from distinct parts of each sample that were micro-sampled to try to extract specific carbonate components or generations of carbonate cement. One hundred and fifty micro-drilled samples were taken this way, one hundred and twenty-seven of which yielded sufficient carbonate to be successfully analysed, with twenty-three samples failing because they contained insufficient mass of carbonate.

Three samples of epoxy-resin used in the preparation of the polished blocks, from which the isotope micro-samples were taken, were mixed 50:50 proportions and analysed to check whether there was any contribution from the epoxy-resin to the isotope values. The presence of epoxy-resin resin was found to have only a minimal effect on the isotopic analysis (<0.3‰ lower for $\delta^{13}C$ and <0.2‰ lower for $\delta^{18}O$).

The variation in the $\delta^{13}C$ and $\delta^{18}O$ composition of the carbonate cements and bioclastic carbonate components is summarised in Figure 18. The two main groups of carbonate cement can be differentiated on the basis of their carbon and oxygen stable isotope composition. These correspond closely to the mineralogy of the cement and its temporal position within the sequence of diagenetic mineral precipitation:

- High magnesian calcite cements: with values ranging between -50.1 to -34.2‰ for $\delta^{13}C$ and +1.09 to +4.0‰ for $\delta^{18}O$ (Area A, Figure 18);
- Aragonite cements with values ranging between -54.2 to -37.8‰ for $\delta^{13}C$ and 0.3 to 2.6‰ for $\delta^{18}O$ (Area B, Figure 18)

Area A and Area B (illustrated in Figure 18) define the range of analyses for samples which essentially contain a single generation of carbonate mineral. There are outliers for both groups which are discussed in more detail below.

Dolomitic cements were not differentiated on the basis of the petrological analysis, and therefore not distinguished as part of the isotopic analysis. However, as dolomite was clearly identified in some samples within the XRD, it is probable that some of the micro-sampling of the high magnesian-calcites is likely to include end-member dolomite.

Figure 19 illustrates the stable isotope composition of MDAC samples from the Mid Irish Sea and the Braemar Pockmark Area that were studied previously by Milodowski et al. (2009) and Milodowski and Sloane (2013), respectively. Comparison with the data from the present study shows that the high-magnesium calcites and aragonites from this study, are broadly comparable to the stable isotope compositions encountered in the previous Mid Irish Sea study. There is some overlap with the Braemar Pockmark Area, although these analyses tend to show higher $\delta^{18}O$ values. However, the dolomite cements from the Braemar Pockmark Area are quite distinct from both the Irish Sea studies, having considerably higher $\delta^{13}C$, and slightly higher $\delta^{18}O$ values.

3.2 CARBON ISOTOPE COMPOSITION

The carbon isotopic composition of diagenetic carbonate cements varies significantly depending on the process producing the carbonate/bicarbonate ions in the porewater from the breakdown of organic matter. Negative $\delta^{13}C$ values, typically between 0 to -25‰ (relative to VPDB), are generated by the bacterial reduction of iron, manganese and sulphate (Claypool and Kaplan, 1974; Pisciotto and Mahoney, 1981; Coleman, 1985; Mozley and Burns, 1993;). With deeper burial below the zone of bacterial reduction, carbonates with $\delta^{13}C$ values between -10 and + 15‰$_{VPDB}$

can be precipitated during methanogenesis (Claypool and Kaplan, 1974; Pisciotto and Mahoney, 1981; Coleman, 1985; Mozley and Burns, 1993). This is because methanogenic bacteria produce very ^{12}C-rich methane, leaving porewaters with residual bicarbonate enriched in ^{13}C (Hoeffs, 2009). Carbonates with $\delta^{13}C$ values lower than -25‰ (relative to VPDB) are characteristic of sediments where methane oxidation has produced CO_2 depleted in ^{13}C (Pirrie and Marshall, 1991; Mozley and Burns, 1993).

The majority of the aragonite and magnesian calcite cements (defined by Group A and B in Figure 18) display highly depleted ^{13}C compositions, with $\delta^{13}C_{VPDB}$ values between -34 to -54‰. These values are strongly indicative of carbonate cements precipitated as a result of methane oxidation, and are characteristic of MDAC deposits described previously from other areas (Jensen et al., 1992; Sakai et al., 1992; Bohrmann et al., 1998; Peckmann et al., 2001; Muralidhar et al., 2006; Milodowski et al., 2013). Similarly, depleted carbon isotope data from MDAC hardgrounds sampled in the mid-Irish Sea area are reported by Milodowski et al. (2009) and O'Reilly et al. (2014). They therefore lend strong support to the hypothesis that all of the aragonite- and magnesium calcite-cemented sandstones and siltstones recovered from the Croker Carbonate Slab area in the mid-Irish Sea also represent MDAC. Samples of aragonite and magnesian-calcite cement that gave analyses with lower $\delta^{13}C_{VPDB}$ values, either contained confirmed bioclastic material, or probably included significant bioclastic material.

Six of the micro-samples represent bioclastic material (bryozoan and serpulid encrustations, or bivalve shells). These analysis display $\delta^{13}C_{VPDB}$ values between -2 to +2‰ (Table 17 and Figure 18), typical of normal marine carbonate. Two samples with lower $\delta^{13}C_{VPDB}$ values (-12 to -14 $\delta^{13}C_{VPDB}$), are bioclasts with significant aragonite coatings and hence plot midway between the bioclastic material and the cements (denoted by green 'X' symbols in Figure 18). Other mixed component samples shown in Figure 18 are more cement-dominated, plotting closer to the 'end-member', single-component cement values.

3.3 OXYGEN ISOTOPE COMPOSITION

The temperature at which the carbonate cement precipitated can be estimated from the temperature-dependant equilibrium oxygen isotope fractionation ($\delta^{18}O$) between the carbonate mineral and the water from which it has precipitated, assuming the carbonate is in equilibrium with the water. The calcite-water system is the best understood carbonate mineral system and is most widely used in palaeotemperature studies, and there are a number of published empirical palaeotemperature equations for the equilibrium precipitation of calcite from solution (Leng and Marshall, 2004). Two such equations were used in this study, to estimate the temperature for the formation of the MDAC from the Croker Carbonate Slab, mid-Irish Sea:

Equation 1: Hays and Grossman's (1991) equation based on their revised 'fit' of O'Neil et al.'s (1969) experimental data. This gives very similar results to most other equations.

$$T = 15.7 - 4.36(c\text{-}w) + 0.12(c\text{-}w)^2$$

Equation 2: Leng and Marshall's (2004) expression of Kim and O'Neil's (1997) more recent equation. This gives slightly lower calculated palaeotemperatures than Equation 1 and other published equations.

$$T = 13.8 - 4.58(c\text{-}w) + 0.08\,(c\text{-}w)^2$$

In both cases, T is the temperature (°C), c is $\delta^{18}O$ of calcite relative to the Pee Dee Belemnite (VPDB) international standard, and w is the $\delta^{18}O$ of the water relative to the Standard Mean Ocean Water (SMOW) international standard. The calculations made in this report have assumed the oxygen isotope composition of the seawater on the bed of the mid-Irish Sea to be the same as SMOW (i.e. $\delta^{18}O = 0$‰).

These equations are based on the empirical relationship between temperature, the isotopic composition of calcite, and the composition of the water from which it formed. Aragonite and magnesian calcites precipitated at equilibrium, are generally isotopically higher than pure or low-magnesian calcites. Review of published literature indicates that aragonite $\delta^{18}O$ values are typically around +0.6‰ higher than the equivalent calcite (Leng and Marshall, 2004). The $\delta^{18}O$ values of magnesian calcites typically increase by 0.06‰ per mol% of $MgCO_3$ in solid-solution in the calcite (Tarutani et al., 1969, cited in Leng and Marshall, 2004). These offsets in $\delta^{18}O$ appear to be independent of temperature (cf. Kim and O'Neil, 1997). Dolomite similarly tends to be isotopically higher than calcite precipitated under the same environment. Land (1980: (also cited by Leng and Marshall, 2004)), indicates that $\delta^{18}O$ values for dolomite are generally around +3‰ higher than the equivalent calcite mineralisation, at normal surface temperatures.

The isotopic compositions of carbonate cements that should precipitate in equilibrium with the seawater, at present-day seabed temperatures in the mid-Irish Sea area, was calculated using quadratic solution of Equation 1, for comparison to the MDAC carbonates (taking into account the offset in $\delta^{18}O$ values between that for pure calcite and for aragonite, high-magnesian calcite and dolomite, discussed above). For these calculations, the present-day seabed temperature within the area of study was estimated to be between 10.5 and 11 °C (JNCC, 2003). It should be noted that whilst these calculations have assumed an Irish Sea water isotopic composition equivalent to SMOW (i.e. $\delta^{18}O$ = 0‰), the actual isotopic composition may differ significantly from SMOW as a result of global latitude variations in $\delta^{18}O$ of seawater: higher latitudes typically having lower values that equatorial regions (Schmidt et al., 1999; Rohling, 2013).

Based on these calculations, the $\delta^{18}O$ of the aragonite cements predicted to be in equilibrium with seawater under present-day northern mid-Irish Sea sea-bed temperatures (10.5-11 °C) is estimated to be between 1.7 and 1.8‰ (taking into account that aragonite $\delta^{18}O$ values are typically around +0.6‰ higher than the equivalent calcite). This coincides closely with the bulk of $\delta^{18}O$ values for aragonite cements defined by Group B (Figure 18). However, the actual range of $\delta^{18}O$ values for the Group B is significantly wider (0.3 and 2.6‰ for $\delta^{18}O$). These data suggest the aragonite may have formed within a wider temperature range than current conditions: calculations suggest temperatures between 7.5 and 17 °C (again, taking into account that aragonite $\delta^{18}O$ values are typically around +0.6‰ higher than the equivalent calcite). These data compare are comparable with the aragonite cements from the previous, more limited mid-Irish Sea study by Milodowski et al. (2009). Aragonite cements from the Braemar Pockmark area of the North Sea (Milodowski and Sloane, 2013) overlap in $\delta^{18}O$ values, although their range extends to slightly higher $\delta^{18}O$ values than seen in this study. These data may indicate that the Braemar MDAC cements have precipitated under slightly colder conditions than the Mid Irish Sea samples. Present day seabed temperatures in the Braemar area are estimated to be between 6 and 10 ºC (Knight et al., 1993; Defra, 2010), which are cooler than the Mid Irish Sea temperatures.

The $\delta^{18}O$ of the high-magnesium cements predicted to be in equilibrium with seawater under present-day northern mid-Irish Sea sea-bed temperatures (10.5-11 °C) is estimated to be between 2.5 to 3.5‰$_{VPDB}$. Most of the data defined by Group A (Figure 18) fall within this range of values (Figure 18), suggesting the magnesian calcite cements may largely have precipitated in conditions similar to the present day. A few data points show a wider scatter of lower (more negative) values than those predicted to be in equilibrium with seawater under present-day. These may have been modified by partial recrystallization, and /or subsequent diagenetic processes affecting the sediment.

Petrological evidence from samples where both aragonite and magnesian calcite cements are present, show that the aragonite cements are paragenetically-later than the magnesian calcite. The temperatures predicted from the isotopic data for the aragonite cements suggests precipitation from a much wider temperature range (7.5 and 17 °C) than current seabed temperatures (10.5-11 °C), whereas the bulk of the magnesian calcite cements are within the predicted present-day range. This suggests the interpretation is more complex, and there are probably other factors which need to be considered with regards the aragonite cement. The major controlling variables on oxygen isotope values in marine carbonates are often temperature and the degree of saturation with regards calcium carbonate (Burton and Walter, 1987), and salinity (Hoefs, 2009). However, the situation may be more complex than this. As pointed out by O'Reilly et al. (2014), ^{18}O enrichment in MDAC at gas seeps sites has also been well-documented (e.g. Bohrmann et al., 1998; Aloisi et al., 2000; Chen et al., 2005) and may result from precipitation from ^{18}O waters transported from deep hydrocarbon sources (Milkov et al., 2005). Thus, the temperatures predicted here (and previously by Milodowski et al., 2009) on the basis of $\delta^{18}O$ of the aragonite should be regarded with caution. It is feasible that deep-sourced water, enriched in ^{18}O and carrying methane, could be derived from the underlying Carboniferous (Dinantian and Westphalian) strata. These rocks are known to be the source of methane reservoired in the Sherwood Sandstone Group (Triassic)-hosted gas fields in the East Irish Sea Basin (Stuart and Cowan, 1991).

As expected, samples comprising mixed aragonite and magnesian calcite cements have $\delta^{18}O$ values that overlap within the range of the main clusters (Areas A and B in Figure 18) of analyses for both the aragonite and high magnesian-calcite cements.

Table 17. Stable isotope data ($\delta^{13}C$ and $\delta^{18}O$) from micro-sampled carbonate components

Sample / sub sample	$\delta^{13}C_{VPDB}$ (‰)	CALCITE $\delta^{18}O_{VPDB}$ (‰)	ARAGONITE $\delta^{18}O_{VPDB}$ (‰)	Mineral	Description of sample
GT004-1	-42.60	+2.85		Mg-calcite	Mg calcite +quartz + traces of illitic clay
GT004-2	-43.86	+3.34		Mg-calcite	Mg calcite +quartz
GT004-3	-39.57	+2.87		Mg-calcite	Mg calcite +quartz + illitic clay
GT004-4	-41.53	+2.58		Mg-calcite	Mg calcite +quartz + illitic clay
GT004-5	-42.14	+3.04		Mg-calcite	Mg calcite +quartz + illitic clay+ minor iron oxide
GT005-1	-26.46	+1.13		Mg-calcite	Mixed Mg calcite + significant calcareous bioclasts (foraminifera and mollusc fragments) + quartz
GT005-2	-29.62	+1.51		Mg-calcite	Mixed Mg calcite + significant calcareous bioclasts (foraminifera and mollusc fragments) + quartz
GT005-3	-29.08	+0.36		Mg-calcite	Mixed Mg calcite + significant calcareous bioclasts (foraminifera and mollusc fragments) + quartz
GT005-4	-37.20	+2.24		Mg-calcite	Mg calcite + minor calcitic bioclast + quartz + K-feldspar
GT005-5	-34.18	+2.16		Mg-calcite	Mg calcite + minor calcitic bioclast + quartz
GT007-1	-44.99	+3.46		Mg-calcite	Predominantly Mg calcite + quartz + minor K-feldspar
GT007-2	-45.24	+2.92		Mg-calcite	Predominantly Mg calcite + quartz + illitic clay + K-feldspar
GT007-3	-42.40	+3.15		Mg-calcite	Predominantly Mg calcite + quartz
GT007-4	-39.72	+2.58		Mg-calcite	Predominantly Mg calcite + quartz + with minor K-feldspar and bioclasts
GT007-5	-42.45	+3.05		Mg-calcite	Predominantly Mg calcite + quartz + minor K-feldspar
GT009-1	FAIL	FAIL		Mg-calcite	Mg calcite + quartz + illitic clay. Only a very small quantity of material drilled out and low-calcite matrix.
GT009-2	-39.33	+2.41		Mg-calcite	Mg calcite +quartz + secondary iron oxyhydroxide + illitic clay + minor calcareous bioclasts and K-feldspar
GT009-3	-42.34	+2.15		Mg-calcite	Predominantly Mg calcite + quartz + very minor K-feldspar. Trace bioclasts
GT009-4	-43.93	+3.12		Mg-calcite	Predominantly Mg calcite + quartz + very minor K-feldspar. No obvious bioclasts
GT009-5	-47.32	+3.31		Mg-calcite	Predominantly Mg calcite + quartz
GT012-1	-0.75	+2.19		Calcite	Bryozoan sampled directly from surface of clast (pure calcite)
GT012-2	-39.61		+1.83	Aragonite	Predominantly aragonite + quartz
GT012-3	-43.43	+2.53	+2.69	Mixed	Mixed aragonite + Mg-calcite + quartz
GT012-4	-41.47	+2.28	+2.43	Mixed	Mixed aragonite + Mg-calcite + quartz

Sample / sub sample	$\delta^{13}C_{VPDB}$ (‰)	CALCITE $\delta^{18}O_{VPDB}$ (‰)	ARAGONITE $\delta^{18}O_{VPDB}$ (‰)	Mineral	Description of sample
GT012-5	-39.31		+2.51	Aragonite	Aragonite + minor Mg calcite + quartz + trace bioclasts
GT014-1	-43.94	+2.95		Mg-Calcite	Predominantly Mg calcite + quartz + minor K-feldspar + illitic clay
GT014-2	-40.28	+2.92		Mg-Calcite	Predominantly Mg calcite + quartz + minor K-feldspar
GT014-3	-42.64	+2.98		Mg-Calcite	Predominantly Mg calcite + quartz + minor K-feldspar
GT014-4	-41.45	+3.13		Mg-Calcite	Predominantly Mg calcite with later, coarser lower-Mg-calcite + quartz + minor K-feldspar and illitic clay
GT014-5	-42.91	+3.36		Mg-Calcite	Predominantly Mg calcite with later, coarser lower-Mg-calcite + quartz + minor K-feldspar
GT015-1	-45.88	+1.82		Mg-Calcite	Mg-calcite + minor calcareous bioclasts + quartz + minor K-feldspar
GT015-2	-41.59	-1.92		Mg-Calcite	Mg-calcite + ?minor early coarse calcite or detrital limestone grains + quartz + minor K-feldspar
GT015-3	-43.60	+1.90		Mg-Calcite	Mg-calcite + minor calcareous bioclasts + quartz + minor K-feldspar
GT015-4	-46.86	+2.41		Mg-Calcite	Mg-calcite + quartz + minor K-feldspar
GT015-5	-40.09	+2.54		Mg-Calcite	Mg-calcite + quartz + minor K-feldspar
GT024-1	-41.36	+1.21		Mg-Calcite	Mg calcite + minor calcareous bioclasts + quartz + minor K-feldspar
GT024-2	-40.17	+2.44		Mg-Calcite	Mg calcite + quartz + illitic clay
GT024-3	-44.26	-1.45		Mg-Calcite	Mg calcite + bioclasts + minor early rhombohedral calcite + detrital limestone fragments encrusted in later Mg-calcite
GT024-4	-42.11	+2.92		Mg-Calcite	Mg calcite + quartz + illitic clay + minor K-feldspar
GT025-1	FAIL	FAIL		Mg-Calcite	Mg-calcite + minor to trace aragonite + quartz + occasional detrital limestone clasts. Dense colloform cement containing abundant calcareous inclusions, possibly of bioclastic origin
GT025-2	-33.97	-0.39		Mg-Calcite	Mg-calcite + minor to trace aragonite + quartz. Dense colloform cement containing abundant calcareous inclusions, possibly of bioclastic origin
GT025-3	-32.49	+1.87		Mg-Calcite	Mg-calcite + common detrital limestone + quartz (BSEM photo GT025_aem_001.tif)
GT025-4	-34.45	+1.85		Mg-Calcite	Mg-calcite + common detrital limestone + quartz
GT025-5	-34.48	+1.63		Mg-Calcite	Mg-calcite + common detrital limestone + trace bioclasts + quartz
GT025-6	-0.90	+1.33		Calcite	Serpulid casing from surface of hand sample (no resin)
GT025-7	-12.88		+0.71	Calcite	Serpulid casing from surface of hand sample (no resin) on an aragonite coating
GT039-1	-28.27	+1.51		Mg-Calcite	Mg calcite + abundant calcareous microfossil detritus
GT039-2	FAIL	FAIL		Mg-Calcite	Mg calcite + abundant calcareous microfossil detritus
GT039-3	FAIL	FAIL		Mg-Calcite	Mg calcite + abundant calcareous microfossil detritus
GT039-4	FAIL	FAIL		Mg-Calcite	Mg calcite + abundant calcareous microfossil detritus
GT050-1	-48.68	+2.47		Mg-Calcite	Mg-calcite + illitic clay + quartz
GT050-2	-50.00	+3.32		Mg-Calcite	Mg-calcite + illitic clay + quartz
GT050-3	-50.94	+1.28		Mg-Calcite	Fine grained Mg-calcite with subordinate / minor later lower Mg-calcite + quartz + illite clay (BSEM phot GT050-aem_001)

Sample / sub sample	$\delta^{13}C_{VPDB}$ (‰)	CALCITE $\delta^{18}O_{VPDB}$ (‰)	ARAGONITE $\delta^{18}O_{VPDB}$ (‰)	Mineral	Description of sample
GT050-4	-49.31	+3.65		Mg-Calcite	Predominantly very fine grained Mg-calcite with illitic clay + quartz
GT050-5	-50.01	+3.59		Mg-Calcite	Predominantly very fine grained Mg-calcite with illitic clay + quartz
GT055-1	-41.50	+3.07		Mg-Calcite	Mg-calcite + quartz and other detrital silicates
GT055-2	-36.66	+1.36		Mg-Calcite	Mg calcite + significant fine grained calcareous microfossil detritus + quartz
GT055-3	-35.90	+2.48		Mg-Calcite	Mg calcite + significant fine grained calcareous microfossil detritus + quartz
GT055-4	-40.67	+2.56		Mg-Calcite	Mg-calcite + quartz and other detrital silicates
GT055-5	-39.36	+2.64		Mg-Calcite	Mg-calcite + quartz and other detrital silicates
GT066-1	-49.99		+1.89	Aragonite	Aragonite + detrital quartz and other detrital silicates
GT066-2	FAIL	FAIL		Aragonite	Aragonite (minor) + clay matrix + detrital quartz and other detrital silicates
GT066-3	-50.36		+2.16	Aragonite	Aragonite + detrital quartz and other detrital silicates
GT066-4	-45.32		+1.75	Aragonite	Aragonite + detrital quartz and other detrital silicates
GT066-5	-52.66		+1.04	Aragonite	Aragonite + detrital quartz and other detrital silicates
GT066-6	-41.23		+1.29	Aragonite	Aragonite + detrital quartz and other detrital silicates
GT071-1	FAIL	FAIL		Mg-Calcite	Mg calcite + contains calcareous microfossil detritus + detrital quartz and other detrital silicates: weakly cemented area
GT071-2	-30.76	+2.45		Mg-Calcite	calcareous microfossil detritus+ detrital quartz and other detrital silicates: only weakly cemented area
GT071-3	-28.00	+1.34		Mg-Calcite	Mg calcite + abundant microfossil detritus + quartz and other detrital silicates
GT071-4	-28.29	+0.95		Mg-Calcite	Mg calcite + abundant microfossil detritus + quartz and other detrital silicates
GT071-5	-27.23	+0.74		Mg-Calcite	Mg calcite + abundant microfossil detritus + quartz and other detrital silicates
GT076-1	-37.25	+3.02		Mg-Calcite	Mg-calcite (micritic) + quartz and other detrital silicates
GT076-2	-39.28	-2.78		Mg-Calcite	Recrystallized Mg-calcite micrite, with minor late low-Mg calcite overgrowth + quartz and other detrital silicates (BSEM photos GT076_aem_001 and CG076_aem_002)
GT076-3	-40.27	+2.20	+2.36	Mixed	Mixed aragonite + Mg calcite (micritic to micro-idiomorphic) + quartz and other detrital silicates
GT076-4	-39.54	+3.34		Mg-Calcite	Mg calcite (micritic to micro-idiomorphic) + quartz and other detrital silicates
GT076-5	-31.81	+2.18	+2.34	Mixed	Mixed aragonite + Mg calcite (micritic to micro-idiomorphic) + bioclastic detritus + quartz and other detrital silicates
GT104-1	-14.18	+1.11		Mg-calcite	Bivalve shell with authigenic aragonite coating
GT104-2	-33.01		+1.63	Aragonite	Aragonite dense fibrous cement + quartz
GT104-3	-47.16		+0.30	Aragonite	Aragonite dense fibrous cement + quartz
GT104-4	-34.26		+0.43	Aragonite	Aragonite fibrous cement + quartz
GT104-5	-30.60		-1.81	Aragonite	Aragonite fibrous cement + quartz
GT106-1	+1.39	+1.16		Calcite	Calcite shell
GT106-2	-1.46	+0.86		Calcite	Calcite shell

Sample / sub sample	$\delta^{13}C_{VPDB}$ (‰)	CALCITE $\delta^{18}O_{VPDB}$ (‰)	ARAGONITE $\delta^{18}O_{VPDB}$ (‰)	Mineral	Description of sample
GT106-3	-52.44		+1.78	Aragonite	Aragonite fibrous fill lining cavity
GT106-4	-54.02		+1.52	Aragonite	Aragonite fibrous fill lining cavity
GT106-5	-47.76		+1.78	Aragonite	Aragonite fibrous fill lining cavity
GT106-6	FAIL	FAIL		Mixed	Dense aragonite cement + enclosing and replacing Mg-calcite micritic + quartz
GT106-7	-47.92		+1.67	Aragonite	Fibrous aragonite cement crust
GT106-8	-35.49	+2.22	+2.38	Mixed	Dense aragonite cement + enclosing and replacing Mg-calcite micritic + quartz
GT108-1	-31.04	+0.81		Mg-calcite	Dense Mg-calcite cement, partially recrystallised or altered and replaced by later micro-sparry calcite.
GT108-2	-41.33	+2.87		Mg-calcite	Mg-calcite micrite + quartz and other detrital minerals
GT108-3	-42.90	+3.36		Mg-calcite	Mg-calcite micrite + quartz and other detrital minerals
GT108-4	-40.53	+2.77		Mg-calcite	Mg-calcite micrite + quartz and other detrital minerals, trace bioclasts
GT108-5	-39.61	+2.79		Mg-calcite	Mg-calcite micrite + quartz and other detrital minerals, trace bioclasts
GT110-1	-45.20		+1.86	Aragonite	Fine aragonite cement + detrital quartz and other detrital silicates.
GT110-2	-44.32		+1.62	Aragonite	Fine aragonite cement + detrital quartz and other detrital silicates.
GT110-3	-49.26		+2.20	Aragonite	Fine aragonite cement + detrital quartz and other detrital silicates.
GT110-4	-48.34		+2.08	Aragonite	Fine aragonite cement with vuggy coarse acicular aragonite in patches + detrital quartz and other detrital silicates.
GT112-1	+0.16	+0.93		Calcite	Bryozoan encrustation, principally low-Mg calcite with some secondary Mg calcite cement
GT112-2	FAIL	FAIL		Calcite	Very thin serpulid encrustation – mainly clay matrix with very little calcite
GT112-3	FAIL	FAIL		Mg-calcite	Mg-calcite micritic cement + quartz + other detrital silicates. Low calcite content. Minor bioclastic detritus.
GT112-3	FAIL	FAIL		Mg-calcite	Mg-calcite micritic cement + quartz + other detrital silicates. Low calcite content. Minor bioclastic detritus
GT112-5	-37.61			Mg-calcite	Mg-calcite micritic cement + quartz + other detrital silicates. High calcite content. Minor bioclastic detritus
GT116-1	-42.80		+0.37	Aragonite	Principally fibrous aragonite cement with minor detrital quartz and other detrital silicates
GT116-2	-40.98		+0.77	Aragonite	Principally fibrous aragonite cement with minor detrital quartz and other detrital silicates
GT116-3	FAIL	FAIL		Mixed	Bivalve shell with authigenic fibrous / acicular aragonite overgrowths. Very thin in section, possibly mainly epoxy resin
GT116-4	-37.81		+1.67	Aragonite	Predominantly aragonite with minor Mg-calcite micritic cement + detrital; quartz and other detrital silicates. Bulk matrix
GT116-5	FAIL	FAIL		Mixed	Predominantly aragonite with minor Mg-calcite micritic cement + detrital; quartz and other detrital silicates. Bulk matrix – very small sample.
GT117-1	-45.49	+2.96		Mg-Calcite	Bulk cement. Very small sample recovered
GT117-2	-45.15	+3.50		Mg-Calcite	Bulk cement. Very small sample recovered

Sample / sub sample	$\delta^{13}C_{VPDB}$ (‰)	CALCITE $\delta^{18}O_{VPDB}$ (‰)	ARAGONITE $\delta^{18}O_{VPDB}$ (‰)	Mineral	Description of sample
GT117-3	-44.95	+3.01		Mg-Calcite	Bulk cement with detrital quartz and other detrital silicates
GT117-4	-47.78	+3.20		Mg-Calcite	Bulk cement with detrital quartz and other detrital silicates
GT117-5	-47.53	+3.04		Mg-Calcite	Bulk cement with detrital quartz and other detrital silicates
GT120-1	FAIL	FAIL		Calcite	Bivalve shell. Very thin shell, and very limited material drilled out.
GT120-2	FAIL	FAIL		Calcite	Bivalve shell. Very thin shell, and very limited material drilled out.
GT120-3	FAIL	FAIL		Aragonite	Aragonite + detrital quartz and other detrital silicates. Only very thin aragonite coatings and very porous pore-filling fibrous aragonite. Only very limited aragonite present.
GT120-4	-46.30		+1.47	Aragonite	Fibrous aragonite cement nucleating around bivalve shell. Dense aragonite cement, virtually all aragonite.
GT120-5	-47.15		+1.53	Aragonite	Aragonite + detrital quartz and /k-feldspar. Bulk matrix sample of pore-filling fibrous aragonite cement. No other carbonate present.
GT121-1	-30.31		+1.83	Aragonite	Mixed fibrous aragonite pore-filling cement + abundant bioclastic detritus (foraminifera fragments, bivalve fragments) + detrital quartz.
GT121-2	FAIL	FAIL		Calcite	Detrital calcite-cemented sandstone or sandy limestone clasts
GT121-3	-26.04		+0.93	Aragonite	Mixed fibrous aragonite pore-filling cement + abundant bioclastic detritus (foraminiferal fragment, bivalve fragments) + detrital quartz.
GT121-4	-38.89		+1.99	Aragonite	Predominantly fibrous aragonite cement + detrital quarts and other detrital silicates.
GT121-5	-38.48		+1.47	Aragonite	Predominantly pore-filling aragonite cement + detrital quartz and other detrital silicates. No obvious bioclastic contamination or magnesium calcite.
GT123-1	-40.01	+2.79		Mg-calcite	Predominantly Mg calcite micrite + detrital quartz and other detrital silicates. Well-cemented by Mg-calcite
GT123-2	-41.74	+3.67		Mg-calcite	Predominantly Mg calcite micrite + detrital quartz and other detrital silicates. Well-cemented by Mg-calcite.
GT123-3	-44.90	-0.01		Mg-calcite	Mg calcite micrite + detrital quartz and other detrital silicates. Well-cemented by Mg-calcite. Possibly partially recrystallised or partially replaced by coarser micro-spar
GT123-4	-42.66	+1.08		Mg-calcite	Mg calcite micrite + detrital quartz and other detrital silicates. Very porous area with very little carbonate cement content. Possibly partially recrystallised or partially replaced by coarser micro-spar but relationship unclear
GT123-5	FAIL	FAIL		Mg-calcite	Mg calcite micrite + detrital quartz and other detrital silicates. Very porous area with very little carbonate cement content. Possibly partially recrystallised or partially replaced by coarser micro-spar
GT126-1	-46.22	+3.42		Mg-calcite	Mg calcite micrite + detrital quartz and other detrital silicates. Weakly cemented.

Sample / sub sample	$\delta^{13}C_{VPDB}$ (‰)	CALCITE $\delta^{18}O_{VPDB}$ (‰)	ARAGONITE $\delta^{18}O_{VPDB}$ (‰)	Mineral	Description of sample
GT126-2	-43.83	+3.66		Mg-calcite	Mg calcite micrite + detrital quartz and other detrital silicates. Well cemented
GT126-3	-49.24	+4.76		Mg-calcite	Mg calcite micrite + detrital quartz and other detrital silicates. Well cemented
GT126-4	FAIL	FAIL		Mg-calcite	Predominantly /Mg calcite + detrital quartz + other detrital silicates. Very small sample only – mainly epoxy resin.
GT129-1	-44.21	+3.84		Mg-calcite	Mg calcite micrite dominated + detrital quartz and other detrital silicates. Well cemented.
GT129-2	-44.27	+3.99		Mg-calcite	Mg calcite micrite dominated + detrital quartz and other detrital silicates. Well cemented.
GT129-3	-42.79	+3.42		Mg-calcite	Mg calcite micrite dominated + detrital quartz and other detrital silicates. Well cemented
GT129-4	-38.91	+2.88		Mg-calcite	Mg calcite micrite + detrital quartz and other detrital silicates. Very porous area, may possibly have some Mg calcite micro-spar (unclear)
GT129-5	-41.48	+2.24		Mg-calcite	Mg calcite micrite + detrital quartz and other detrital silicates. Very porous area, may have some Mg calcite micro-spar (unclear)
GT141-1	-48.27		+2.55	Aragonite	Late, coarse, fibrous aragonite crust lining burrow cavity
GT141-2	-48.39		+2.23	Aragonite	Late, coarse, fibrous aragonite crust lining burrow cavity
GT141-3	-50.05		+1.22	Aragonite	Micritic to fibrous aragonite at base of late, aragonite crust may include micritic aragonite pellets.
GT141-4	-47.66		-0.80	Aragonite	Bulk matrix fibrous aragonite cement + detrital quartz and other detrital silicates.
GT141-5	-50.77		+2.31	Aragonite	Bulk matrix fibrous aragonite cement + detrital quartz and other detrital silicates.
GT143-1	-49.79		+1.86	Aragonite	Predominantly dense porous fibrous aragonite + possibly includes minor micritic Mg calcite minor detrital quartz and other detrital silicates.
GT143-2	-47.45		+2.35	Aragonite	Predominantly porous fibrous aragonite + possibly includes minor micritic Mg calcite minor detrital quartz and other detrital silicates. Well cemented area.
GT143-3	FAIL	FAIL		Aragonite	Predominantly porous fibrous aragonite + possibly includes minor micritic Mg calcite minor detrital quartz and other detrital silicates. Very little carbonate present.
GT143-4	-47.83		+2.60	Aragonite	Predominantly dense porous fibrous aragonite + possibly includes minor micritic Mg calcite minor detrital quartz and other detrital silicates.
GT143-5	FAIL	FAIL		Aragonite	Predominantly porous fibrous aragonite + possibly includes minor micritic Mg calcite minor detrital quartz and other detrital silicates. Well cemented area.
GT150-1	+1.02	+1.45		Calcite	Bryozoan sampled directly from surface of clast (pure calcite)
GT150-2	FAIL	FAIL			very minor bioclasts. Rock clast – not MDAC cemented sediment
GT150-3	FAIL	FAIL			Rock clast – not MDAC cemented sediment

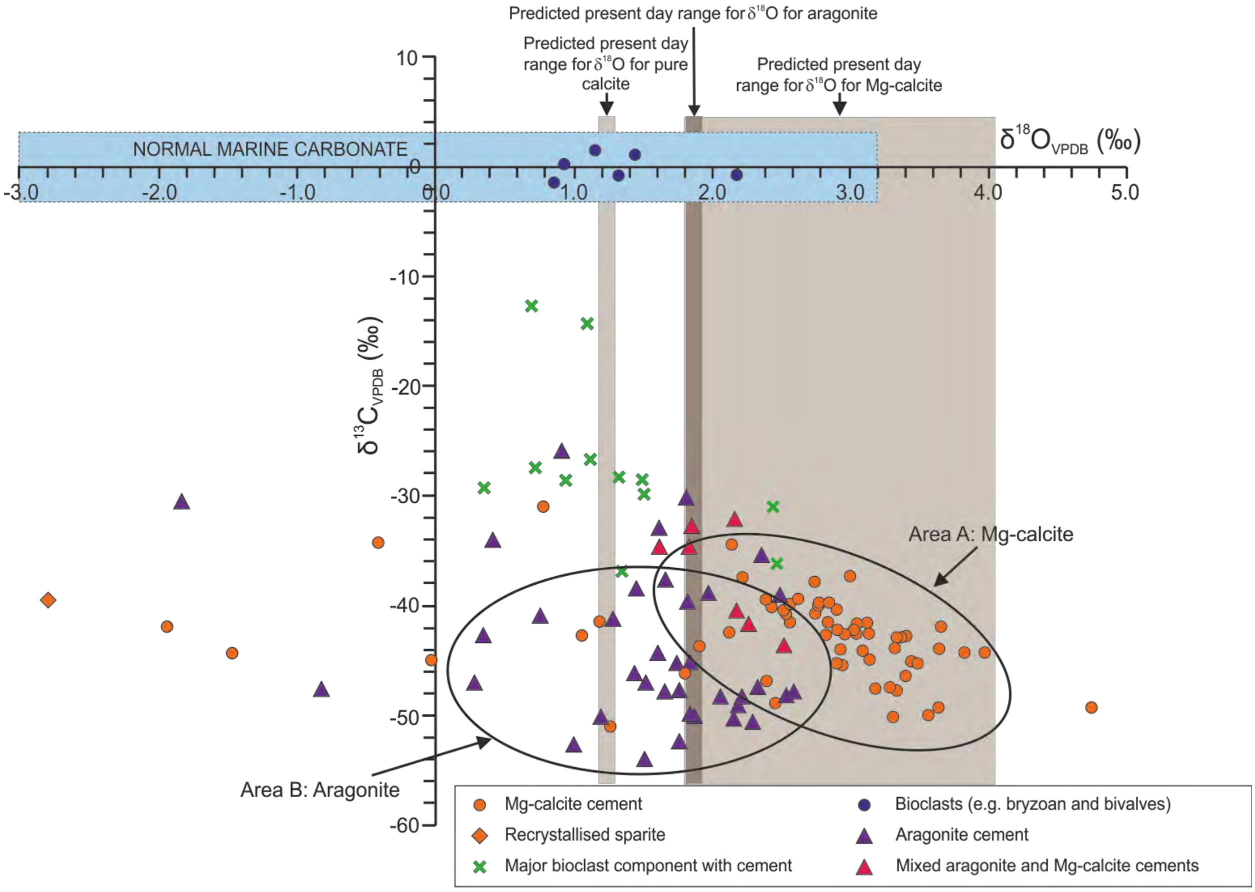

Figure 18. Cross-plot of $\delta^{13}C$ and $\delta^{18}O$ illustrating the variation in stable isotopic composition for the MDAC samples, together with the maximum predicted present day ranges for the $\delta^{18}O$ values for aragonite and magnesian calcite of similar chemistry, assuming equilibrium with seawater under present-day Mid Irish Sea sea-bed temperatures. The main clusters (Areas A and B) for magnesian calcite and aragonite analyses are also shown.

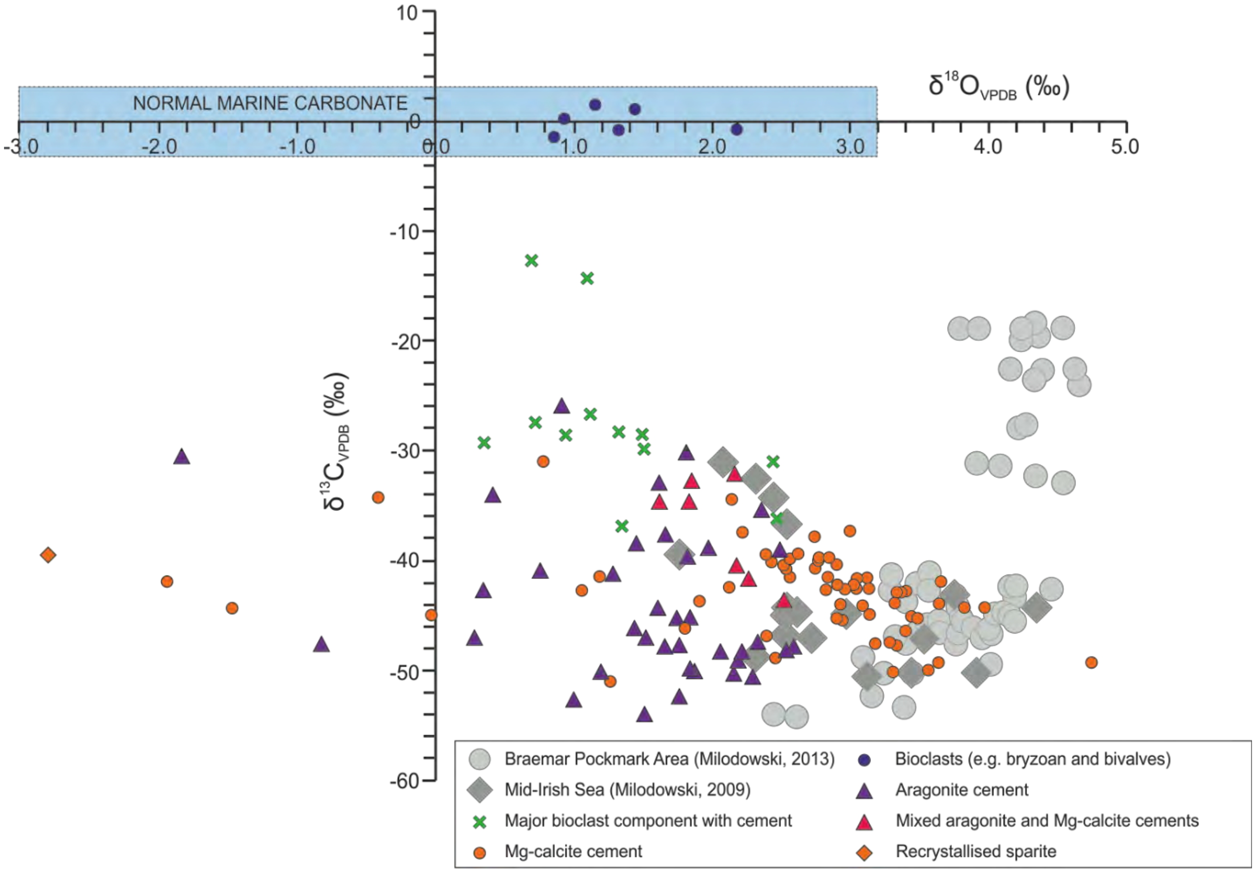

Figure 19. Cross-plot of $\delta^{13}C$ and $\delta^{18}O$ illustrating the variation in stable isotopic composition for the MDAC samples, together with data from previous studies in the Mid Irish Sea and Braemar Pockmark Area (Milodowski et al., 2009, and Milodowski and Sloane, 2013).

There are a number of 'outliers' within the data set with negative $\delta^{18}O$ values which should be viewed with caution. Examination of the residual pit from the micro-drilling for the most extreme data point (-2.78‰VPDB $\delta^{18}O$) confirmed that this material has been affected by recrystallization processes, and the cement analysed was a microsparite. The other negative $\delta^{18}O$ data points did not show evidence for recrystallisation, but may possibly have been affected by other influences, including contamination by detrital limestone clasts.

4 Summary and conclusions

Thirty samples of carbonate-cemented sediment recovered from the seabed in the Croker Carbonate Slabs area of the Mid Irish Sea have been characterised mineralogically and petrographically. The $\delta^{13}C$ and $\delta^{18}O$ compositions of their component carbonate cements have also been analysed to evaluate the origin of the carbonate cement. Twenty-nine of these samples are carbonate-cemented and contain high magnesian-calcite, aragonite, or a combination of both cements. One sample, GT150, appears to be a collection of random rock clasts (including igneous and other rock fragments). The clast used for XRD did contain carbonate cement, and provided the highest dolomite content (24.4%) of any of the samples. A second clast from the same group, prepared as a polished thin section for petrographic analysis, proved to be a metasedimentary rock clast encrusted by bryozoans and serpulid worm tubes.

4.1 TYPES OF CARBONATED-CEMENTED SEDIMENT

The carbonate-cemented sediments can be categorised into two principal end-member lithologies; aragonite-dominated or high-magnesium calcite dominated cements.

4.1.1 Aragonite-dominated cements

This is exemplified by samples such GT012, GT110, GT116 and GT120, which are sandy sediments cemented by aragonite cements comprising:

1. Isopachous grain-coating aragonite fringes coating detrital grains;
2. Precipitation of ‘clots’, or framboidal, microbotryoidal aggregates of micritic or microcrystalline aragonite. These may coalesce to form a locally dense micritic ‘crystal mush’ matrix. Some of this micritic precipitate may be reworked and incorporated within, and redeposited as, sand-grade faecal pellets;
3. Coarse acicular aragonite overgrowths on molluscan shell fragments.

The aragonite is strontium-rich with up to 2 mole% $SrCO_3$ in solid-solution. In samples where both aragonite and magnesian calcite cement are present (e.g. GT012, GT014, GT106), the aragonite cement can be demonstrated to have formed later than the magnesian calcite cements, forming isopachous coatings on pre-existing micrite (e.g. GT106), or early-stage acicular needles nucleating on the micrite (e.g. GT014).

4.1.2 High-magnesium calcite-dominated cements

This is exemplified by samples such as GT004, GT005, GT007 and GT112. These samples display:

1. Early globular, spheroidal aggregates of very fine grained high-magnesium calcite coating detrital grains
2. Precipitation of ‘clots’, or spheroidal aggregates of micritic or microcrystalline high-magnesian calcite. These micrite aggregates may coalesce to form a locally dense micritic matrix. Some of this micritic precipitate may be reworked and incorporated within, and redeposited as, sand-grade faecal pellets.
3. Well-developed microcellular fabrics, comprising aggregates of magnesian calcite microcrystals typically less than 1 μm in size that have nucleated around, or encrust, a central micro-cavity about 1-2 μm in diameter. These structures very closely resemble fossilised and mineralised bacterial cells described from experimental studies and other environments in the literature (cf. Martill and Wilby, 1994; Wilby and Whyte, 1995). Denser areas of cementation have formed as these microcellular structures coalesce and become more compacted.

The magnesian calcites typically have a composition ranging from about 11-48 mole % $MgCO_3$ in solid-solution, which is within the range of compositions observed from other MDAC deposits.

Petrographic observations also show that some of the micritic carbonate sediments were being reworked by benthic marine organisms, prior to lithification and then redeposited as sand-grade faecal pellets composed of micrite. The petrographic evidence suggests that these micritic sediments were produced by, and associated with, abundant bacteria, which probably provided the base of a food chain for larger, higher-order fauna prior to sediment lithification.

4.1.3 Dolomite-dominated cements

Although XRD analysis indicates the presence of dolomite, particularly in samples GT024, GT108 and GT123, dolomite cements could not be definitively identified petrographically. Dolomite can occur as a high-calcium dolomite, which contains up to 10 mole% excess $CaCO_3$ relative to ideal stoichiometric dolomite, as observed in previous studies (Milodowski et al, 2009 and Milodowski and Sloane, 2013). This may indicate that the dolomite is relatively poorly ordered and/or metastable, and may have precipitated rapidly (Vahrenkamp and Swart, 1994) possibly forming via a 'protodolomite' precursor (cf. Deer et al., 1992).

4.2 ORIGIN OF THE CARBONATE-CEMENTS

All of the aragonite and magnesium calcite cements display highly depleted ^{13}C composition, with $\delta^{13}C$ values generally between -34 to -54‰. This is consistent with a diagenetic origin in which carbonate precipitation is related to methane oxidation, and is characteristic of MDAC deposits described previously from other areas (Jensen et al., 1992; Sakai et al., 1992; Bohrmann et al., 1998; Peckmann et al., 2001; Muralidhar et al., 2006; Milodowski et al., 2009, 2013). Therefore, this provides strong evidence that the aragonite- and magnesian calcite-cemented sandstones and siltstones recovered from the Croker Carbonate Slabs in the Mid-Irish Sea represent MDAC.

The observed $\delta^{18}O$ signature of the aragonite-cemented MDAC materials carbonate cements display a broad range from (+0.3 and +2.6‰ for $\delta^{18}O$ for aragonite-dominated carbonate), However, within this range the majority of aragonite cements have a $\delta^{18}O$ close to that predicted to be in equilibrium with present-day sea-bed temperature in the Croker Carbonate Slab area of the mid-Irish Sea (10.5-11 °C). The palaeotemperatures calculated from the $\delta^{18}O$ signature for the aragonite cements range from 5.2 to 14.4 °C. However, the calculated temperatures should be regarded with caution because ^{18}O enrichment in MDAC at gas seeps sites has also been well-documented (cf. Bohrmann et al., 1998; Aloisi et al., 2000; Chen et al., 2005). Anomalous $\delta^{18}O$ values may result from precipitation of carbonate cement from ^{18}O waters that are derived from deep hydrocarbon sources. It is feasible that porewater, enriched in ^{18}O and methane could be derived from the underlying Carboniferous strata, which are the source of methane reservoired in the Irish Sea gas fields.

In contrast to the aragonite MDAC cements, the high-magnesian calcite MDAC cements have oxygen isotope compositions that broadly correlate to the predicted values for magnesium calcite precipitating in equilibrium with seawater at the present-day seabed (i.e. $\delta^{18}O$ is predicted to be between 1.7 to 4.1‰ for high magnesian-calcite).

The more complex MDAC samples represented by samples such as GT012, GT014, GT106, in which magnesian calcite cemented MDAC is superceded by aragonite–cemented MDAC indicates that in the area where these samples formed, there have been at least two distinct phases of MDAC formation: (i) an earlier phase in conditions similar to the present day, when high-magnesian calcite was precipitated, and; (ii) a later phase of MDAC formation when aragonite was precipitated.

The early micritic magnesian calcite cements and the micritic aragonite cements are both often associated with early diagenetic pyrite. The pyrite may be finely-disseminated microcrystals or may form framboidal aggregates, and is intergrown or included within these carbonate cements. Pyrite formation would originally have occurred under anoxic porewater conditions, during sulphate and iron-reduction, and clearly shows that these MDAC cements formed under reducing porewater conditions. This indicates that the formation of bicarbonate in the porewaters, leading to the subsequent precipitation of authigenic carbonate, has occurred via anoxic oxidation of methane (AOM). Sample GT141 preserves particularly interesting sedimentary and diagenetic fabrics with regard to understanding the origin of these carbonate-cemented sediments. In this sample, the early micritic high magnesian-calcite has developed as 'pendant cements' or 'bearded grains'. This geopetal fabric is normally characteristic of cements formed in the subaerial or vadose zone sediments (e.g. Tucker, 2001). However, given the geographic position of these marine sediments in the mid-Irish Sea they cannot have been subjected to this type of hydrogeological condition. A more plausible explanation is that this micrite cement fabric formed in 'gas-filled' porosity rather than water-saturated porosity. Under such conditions, cement fabrics similar to those found in vadose-zone environments might be expected to develop as a result of precipitation from porewater films draining under gravity through the unsaturated gas-filled porosity. Later, coarser acicular aragonite fringes, which have nucleated on the earlier micrite films do not develop this geopetal fabric. Therefore, the aragonite cement is considered to have precipitated within a water-saturated sediment rather than in gas-filled porosity, and most probably represents mineralisation after the loss of accumulated gas from the sediment. The presence of synsedimentary soft-sediment disturbance in GT141, with the development of 'flame-like' or 'flare-like' structures is also consistent with disturbance produced by gas-release from the underlying sediment. This, together with the formation geopetal 'bearded grain' micrite structures characteristic of cementation in unsaturated sediment, provides strong evidence for gas accumulation and the sediment porosity at this site being gas-filled during the precipitation of the early micritic high magnesian calcite.

4.3 IN-SITU OR REWORKED ORIGINS

These samples do not show the high degree of abrasion with discrete erosional surfaces noted in some of the samples from the Braemar Pockmark Area. Many samples display distinct surface 'crusts' or coatings that may indicate a 'way-up' orientation of the sample (e.g.GT104, GT106, GT110), and have evidence of heavy bioturbation and / or boring by marine organisms (e.g. GT014, GT015). They also bear evidence of post-lithification colonisation by encrusting bryozoan, or calcareous serpulid worm tubes. These features suggest that some samples may have been retrieved in-situ. However, other samples, most notably GT150, are more likely to have been detrital clasts eroded from their original source. In the case of GT150, this appears include metasedimentary rocks that may be glacially-derived from Lower Palaeozoic metamorphic terrain around the margins of the Irish Sea (e.g. North Wales, NW England or SW Scotland).

Many clasts have weathered, oxidised surfaces stained and coated by secondary iron (and less commonly, manganese) oxyhydroxides (e.g. GT004, GT0025, GT055). Some samples have developed locally significant iron oxyhydroxide-rich cements, and colloform manganese oxyhydroxide precipitates and crusts (GT025, GT104, GT117, GT126 and GT129) These may have precipitated directly from overlying seawater under oxidising conditions. Some of the iron oxyhydroxide has formed from the oxidation of early diagenetic pyrite that originally co-precipitated in close association with the MDAC carbonate minerals. Oxidation of this early diagenetic pyrite and the precipitation of iron and manganese oxyhydroxide, may indicate that these carbonate-cemented sediments were subsequently exhumed by erosion and exposed to weathering by oxic seawater of the sea-bed. However, this is not necessarily the case, and it should be noted that ferromanganese crusts can form in close association with methane seeps, as has been described from the Gulf of Cadiz (Merinero et al., 2008).

4.4 DISTRIBUTION OF DIFFERENT CARBONATE MINERALS

The spatial distribution of the major or dominant carbonate mineral cements present in the samples studied from the Croker Carbonate Slabs is summarised in Figure 20. This appears to show a broad variation in MDAC mineralogy across the area. Although bioclastic (shell fragments) may make some contribution to the total amount of aragonite detected by XRD, aragonite cement appears to be the dominant authigenic carbonate, or a significant component, in MDAC samples from the northeast to east of the area (Figure 20). In contrast, aragonite is either absent or present only in trace amounts in the central and western area of the Croker Carbonate Slabs, where magnesian calcite is the principal authigenic carbonate. At the southern end of the study area, the MDAC is dominated by magnesian calcite but minor aragonite is also present. Dolomite is recorded by XRD as a major carbonate component in MDAC samples from the north and west, within the area dominated by magnesian calcite (Figure 20).

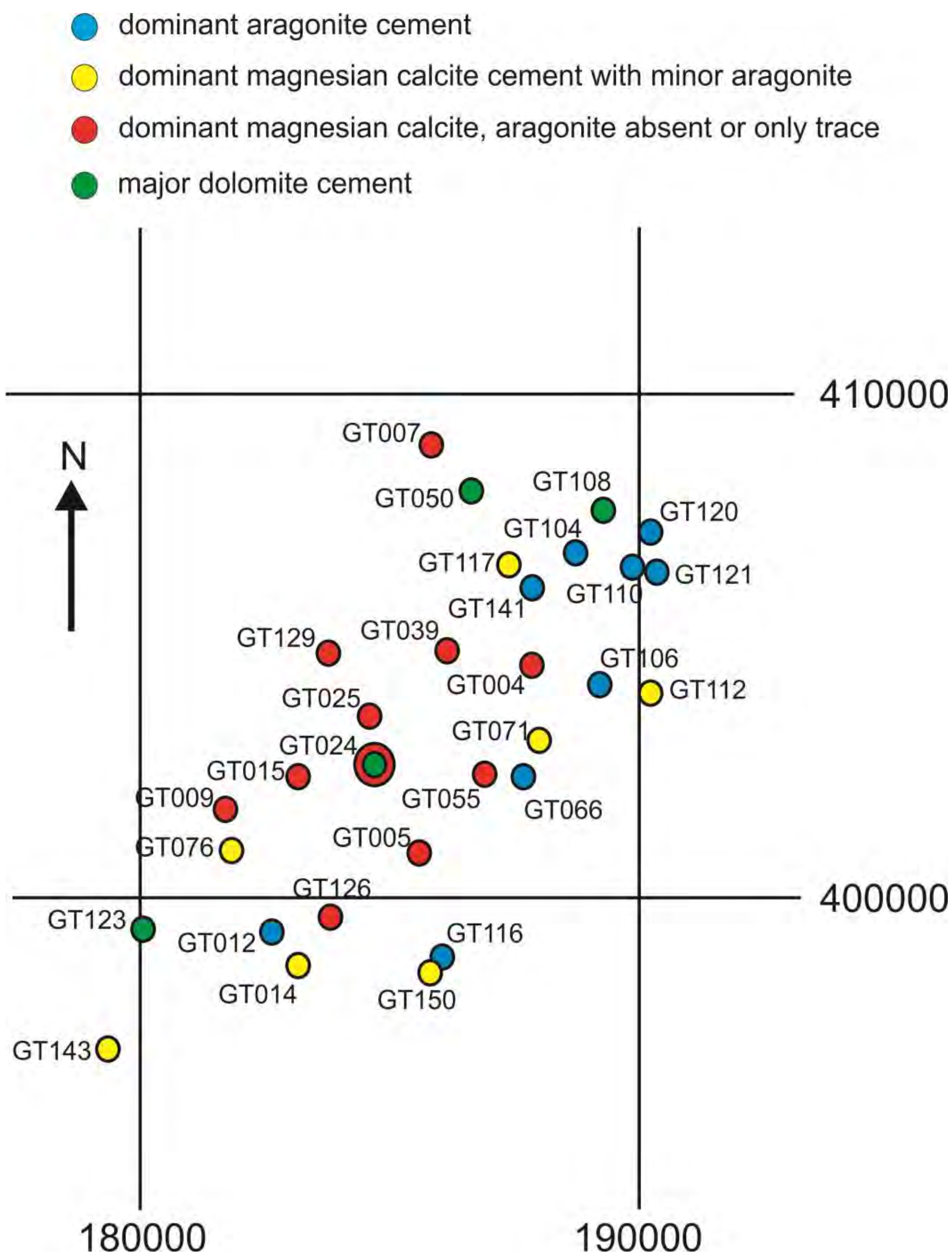

Figure 20. Distribution of dominant carbonate mineral cements within MDAC samples from the Croker Carbonate Slabs area. Data based on whole-rock XRD analyses.

In all the samples studied, the paragenetic relationships show that aragonite precipitation is later than magnesian calcite. The magnesian calcite principally occurs as a fine-grained micritic precipitate, whereas the aragonite tends to occurs as coarser crystalline cement lining or filling, cleaner (and presumably more permeable) intergranular porosity or as discrete crusts. The magnesian calcite and aragonite distribution pattern may indicate a change in MDAC formation across the area over time. The temporal relationships between aragonite and magnesian calcite suggest that early MDAC formation associated with magnesian calcite precipitation may have started in the west. However, later MDAC formation associated with aragonite formation may have been focused towards the northeast and eastern side of the Croker Carbonate Slabs.

Glossary

Anhedral	Crystal morphology with no obvious crystal shape or faces. Synonymous with xenomorphic.
BGS	British Geological Survey.
BSEM	Backscattered electron microscopy.
Cefas	Centre for Environment, Fisheries and Aquiculture Science.
ESEM	Environmental scanning electron microscope.
Euhedral	Crystal morphology with well-developed crystal shape and good planar faces. Synonymous with *idiomorphic*.
Idiomorphic	Crystal morphology with well-developed crystal shape and good planar faces. Synonymous with *euhedra*l.
JNCC	Joint Nature Conservancy Council.
EDXA	Energy-dispersive X-ray spectroscopy.
ESEM	Environmental scanning electron microscope microscopy.
ED-EPMA	Quantitative energy-dispersive electron probe microanalysis (i.e. quantitative EDXA).
MDAC	Methane-Derived Authigenic Carbonate.
SAC	Special Area of Conservation.
cSAC	Candidate Special Area of Conservation.
SCI	Site of Community Importance.
SEM	Scanning electron microscope / microscopy.
Subidiomorphic	Crystal morphology with some well-developed crystal shape and some crystal faces. Synonymous with *subhedral*.
Subhedral	Crystal morphology with some well-developed crystal shape and some crystal faces. Synonymous with *subidiomorphic.*
Xenomorphic	Crystal morphology with no obvious crystal shape or faces. Synonymous with anhedral.
XRD	X-ray diffraction.

References

British Geological Survey holds most of the references listed below, and copies may be obtained via the library service subject to copyright legislation (contact libuser@bgs.ac.uk for details). The library catalogue is available at: https://envirolib.apps.nerc.ac.uk/olibcgi.

ALTHOFF, P.L. 1977. Structural refinements of dolomite and a magnesian calcite and implications for dolomite formation in the marine environment. *American Mineralogist*, **62**, pages 772-783.

ALOISI, G., PIERRE, C., ROUCHY, J.-P., FOUCHER, J.-P., AND WOODSIDE, J. 2000. MEDINAUT Scientific Party 2000. Methane-related authigenic carbonates of Eastern Mediterranean Sea mud volcanoes and their possible relation to gas hydrate destabilisation. *Earth and Planetary Science Letters*, **184**, 321-338.

BERNER, R.A. 1969. The synthesis of framboidal pyrite. *Economic Geology,* **64**, 383-384.

BERNER, R.A. 1980. *Early Diagenesis: A Theoretical Approach*. Princeton University Press, Princeton, New Jersey, USA, 241pp.

BOHRMANN, G., GREINERT, J., SUESS, E. AND TORRES, M. 1998. Authigenic carbonates from the Cascadia subduction zone and their relation to gas hydrate stability. *Geology*, **26**, 647-650.

CALVERT, S.E. AND PRICE, N.B. 1970. Composition of Manganese Nodules and Manganese Carbonates from Loch Fyne, Scotland. *Contr. Mineral. And Petrol*. **29**, 215-233.

CALVERT, S.E. AND PRICE, N.B. 1977. Geochemical variation in ferromanganese nodules and associated sediments from the pacific ocean. *Marine Chemistry*. **5**, 43-74.

CHEND.F., HUANG, Y.Y., YUAN, X.L., AND CATHLES III, L.M. 2005. Seep carbonates and preserved methane oxidizing archaea and sulphate reducing bacteria fossils suggest recent gas venting on the seafloor in the Northeastern South China Sea. *Marine and Petroleum Geology*, **22**, 613-621.

CHESTER, R. AND JICKELLS, T. (2012). Chapter 15.3 'Hydrogenous' components: halmyrolysates and precipitates. In: *Marine Geochemistry*, 3rd edition. Wiley-Blackwell. Chichester.

CLAYPOOL, G.E. AND KAPLAN, I.R. 1974. The origin and distribution of methane in marine sediments. In: KAPLAN, I.R. (editor) *Natural Gases in Marine Sediments*, Plenum Press, New York, 99-140.

COLEMAN,M.L. 1985. Geochemistry of diagenetic non-silicate minerals: kinetic considerations. In: EGLINTON, G., CURTIS, C.D. MCKENZIE, D.P. AND MURCHISON, D.G. (editors). *Geochemistry of Buried Sediments*. The Royal Society, London, 39-54

CRAIG, H. 1957. Isotopic standards for carbon and oxygen & correction factors for mass spectrometric analysis. *Geochimica et Cosmochimica Acta*, 12, 133-149.

CROKER , P.F., KOZACHENKO, M. AND WHEELER, A.J. 2005. Gas-related seabed structures in the Western Irish Sea (IRL-SEA6). *Technical Report of the Petroleum Affairs Division of Ireland, produced for Strategic Environmental Assessment – SEA6*

DEER, W.A., HOWIE, R.A. AND ZUSSMAN, J. 1962a. *Rock Forming Minerals. Volume 5: Non-Silicates*. Longmans, London.

DEER, W.A., HOWIE, R.A. AND ZUSSMAN, J. 1992b. *An Introduction to the Rock Forming Minerals (2nd edition)*. Pearson Education Limited, Harlow, London.

DEFRA. 2010. Charting *Progress 2: An assessment of the state of UK seas. Feeder Report: Ocean Processes*. UK Marine Monitoring and Assessment Strategy (UKMMAS) Community, Defra, United Kingdom. http://chartingprogress.defra.gov.uk.

GLASBY, G.P. 2006. Manganese: Predominant role of nodules and crusts. In: SCHULZ, H.D. AND ZABEL, M. (editors) *Marine Geochemistry*, 2nd ed. Springer, Germany.

GOLDSTEIN, J.I., NEWBURY, D.E., ECHLIN, P., JOY, D.C., FIORI, C. AND LIFSHIN, E. 1981. *Scanning Electron Microscopy and X-Ray Microanalysis*. Plenum Press, New York.

HAYS, P.D. AND GROSSMAN, E.L. 1991. Oxygen isotopes in meteoric calcite cements as indicators of continental paleoclimate. *Geology*, **19**, 441-444.

HOEFS, J. 2009. Stable Isotope Geochemistry. 6th edition. Springer. Berlin.

HOVLAND, M. AND TALBOT, M.R. 1987. Hydrocarbon seeps in northern marine waters; their occurrence and effects. *Journal of Sedimentary Research*, **57**.

JENSEN, P., AAGAARD, I., BURKE JR., R.A., DANDO, P.R., JØGENSEN, N.O., KUIJPERS, A., LAIER, T., O'HARA, S.C.M. AND SCHMALJOHANN, R. 1992. 'Bubbling reefs' in the Kattegat: submarine landscapes of carbonate-cemented rocks support a diverse ecosystem at methane seeps. *Marine Ecology Progress Series*, **83**, 103-112.

JNCC. 2003. *Irish Sea Pilot*. Joint Nature Conservation Committee (JNCC). http://www.jncc.gov.uk/pdf/irish_finalreport(maps).pdf

JNCC, 2012. Offshore Special Area of Conservation: Croker Carbonate Slabs. SAC Selection Assessment Document V5.0. http://jncc.defra.gov.uk/pdf/CrokerCarbonateSlabs_SACSAD_v_5_0.pdf

JUDD, A.G. 2005. The distribution and extent of methane-derived authigenic carbonate. *DTI Strategic Environmental Assessment, Area 6 (SEA6)*. United Kingdom Department of Trade and Industry (Dti)

KIM, S.T. AND O'NEIL, J.R., 1997. Equilibrium and non-equilibrium oxygen isotope effects in synthetic carbonates. *Geochimica et Cosmochimica Acta*, 61, 3461–3475.

KIM, S.T. et al 2007. Phosphoric acid fractionation factors for Calcite and Aragonite between 25 and 75 ^{o}C*: Revisited Chemical Geology* 246 (2007) 135-146

KNIGHT, P.J., WILKINSON, M. AND GLORIOSO, P. 1993. Current profile and sea-bed pressure and temperature records from the northern North Sea Challenger cruises 84 and 85: September 1991 – November 1991. *Proudman Oceanic Laboratory Report*, **28 (1993)**, 417pp.

KONHAUSER, K. 2007. *Introduction to Geomicrobiology*. Blackwell Publishing, Oxford, UK, 425pp.

LAND, L.S., 1980. The isotopic and trace element geochemistry of dolomite: the state of the art. In: ZENGER, D.H., ET AL. (Editor.), Concepts and Models of Dolomitisation, Society of Economic *Paleontologists and Mineralogists (SEPM), Special Publication*, **28**, 87–110, Tulsa, Oklahoma.

LENG, M.J. AND MARSHALL, J.D. 2004. Palaeoclimate interpretation of stable isotope data from lake sediment archives. *Quaternary Science Reviews*, **23**, 811-831.

LIESKI, L.E. AND RAYMO, M.E. 2005. A Pliocene-Pleistocene stack of 57 globally distributed benthic δ_{18}O records. *Paleooceanography*, **20**, PA1003, 17pp, .doi:10.1029/2004PA001071

MACHEL, H.G. 1987. Some aspects of diagenetic sulphate-hydrocarbon redox reactions. In: Marshall, J.D. (editor) *Diagenesis of Sedimentary Sequences.* Geological Society of London, Special Publication, **36**, 15-28.

MACKENZIE, F.T., BISCHOFF, W.D., BISHOP, F.C., LOIJENS, /M., SCHOONMAKER, J. AND WOLLAST, R. 1983. Chapter 4. Magnesian calcites: low-temperature occurrence, solubility and solid-solution behaviour. In: REEDER, R.J. (editor). *Carbonates: Mineralogy and Chemistry. Reviews in Mineralogy,* Volume 11, Mineralogical Society of America, Washington D.C. USA, pp. 97-144.

MARTILL, D.M. AND WILBY, P.R. 1994. Lithified prokaryotes associated with fossil soft tissues from the Santana Formation (cretaceous) of Brazil. *Kaupia.* **4**, 71-77.

MCCREA, J., 1950. On the isotopic chemistry of carbonates and palaeo-temperature scale. *Jour. Chem. Physics*, 18, 849-57.

MERINERO, R. LUNAR, R., MARTÍNEZ-FRÍAS, J., SOMOZA, L. AND DÍAZ-DEL-RÍO, V. 2008. Iron oxyhydroxide and sulphide mineralization in hydrocarbon seep-related carbonate submarine chimneys, Gulf of Cadiz (SW Iberian Peninsula). *Marine and Petroleum Geology*, **25**, 706-713.

MILKOV, A.V., CLAYPOOL, G.E., LEE, Y.-J., AND SASSEN, R. 2005. Gas hydrate systems at Hydrate Ridge offshore Oregon inferred from molecular and isotopic properties of hydrate bound and void gases. *Geochimica et Cosmochimica Acta*, **69**, 1007-1026.

MILODOWSKI, A.E. TULLBORG, E.-L., BUIL, B., GÓMEZ, P., TURRERO, M.-J., HASZELDINE, S., ENGLAND, G., GILLESPIE, M.R., TORRES, T., ORTIZ, J.E., ZACHARIÁŠ, SILAR, J., CHVÁTAL, M., STRNAD, L., ŠEBEK, O. BOUCH, J.E., CHENERY, S.R., CHENERY, C., SHEPHERD, T.J. AND MCKERVEY, J.A. 2005. Application of Mineralogical, Petrological and Geochemical tools for Evaluating the Palaeohydrogeological Evolution of the PADAMOT Study Sites. PADAMOT PROJECT - EU FP5 CONTRACT NO. FIKW-CT2001-20129. *PADAMOT Project Technical Report, WP2*. 228pp +digital appendices.

MILODOWSKI, A.E. LACINSKA, A. AND SLOANE, H. 2009. Petrography and stable isotope geochemistry of samples of methane-derived authigenic carbonates (MDAC) from the Mid Irish Sea. *British Geological Survey, Commissioned Report*, **CR/09/051**, 62pp.

MILODOWSKI, A.E. AND SLOANE, H. 2013. Petrography and stable isotope geochemistry of samples of methane-derived authigenic carbonates (MDAC) from the Braemar Pockmark Area, North Sea. *British Geological Survey, Commissioned Report*, **CR/13/078**, 112pp.

MOZLEY, P. AND BURNS, S.J. 1993. Oxygen and carbon isotope comparison of marine carbonate concretions: an overview. *Journal of Sedimentary Petrology*, **63**, 73-83.

MURALIDHAR, K., MAZUMDAR, A., KARISIDDAIAH, S.M., BOROLE, D.V. AND RAO, B.R. 2006. evidences of methane-derived authigenic carbonates from the sediments of the Krishna-Godavari Basin, eastern continental margin of India. *Current Science*, **91**, 318-323.

O'REILLY, S.S., HRYNIEWICZ, K., LITTLE, C.T.S., MONTEYS, X., SZPAK, M.T., MURPHY, B.T., JORDAN, S.F., ALLEN, C.C.R. AND KELLEHER, B.P. 2014. Shallow water methane-derived authigenic carbonate mounds at the Codling Fault Zone, western Irish Sea. *Marine Geology*, **357**, 139-150.

PECKMANN, J., REIMER, A., LUTH, U., HANSEN, B.T., HEINICKE, C., HOEFS, J. AND REITNER, J. 2001. Methane-derived carbonates and authigenic pyrite from the northwestern Black Sea. *Marine Geology*, **177**, 129-150.

PIRRIE, D AND MARSHALL, J.D. 1991. Field relationships and stable isotope geochemistry of concretions from James Ross Island, Antarctica. *Sedimentary Geology*, **71**, 137-150.

PISCIOTTO, K.A AND MAHONEY, J.J. 1981. Isotopic survey of diagenetic carbonates Deep Sea Drilling Project Leg 63. *Initial Reports of the Deep Sea Drilling Programme (DSDP)*, **63**, 595-609.

REEDER, R.J. 1983. Chapter 1. Crystal chemistry of the rhombohedral carbonates. In: REEDER, J.J. (editor), *Carbonates: Mineralogy and Chemistry*, Reviews in Mineralogy, **11**, Mineralogical Society of America, Washington D.C. USA,. pp. 1-47.RICKARD, D.T. 1970. The origin of framboids. *Lithos,* 3, 269-293. 96

RICKARD, D.T. 1975. Kinetics and mechanism of pyrite formation at low temperatures. American Journal of Science, 274, 636-652.

ROHLING E.J. 2013. Oxygen Isotope Composition of Seawater. In: ELIAS, S.A. (editor) *The Encyclopedia of Quaternary Science*, vol. 2, pp. 915-922. Elsevier, Amsterdam.

ROSENBAUM J., and SHEPPARD S.M.F. 1986. An Isotopic study of siderites, dolomites and ankerites at high temperatures *Geochimica et Cosmochimica Acta*, **50**, 1147-1150

SAKAI, H., GAMO, T., OGAWA, Y. AND BOULEGUE, J. 1992. Stable isotope ratios and origins of the carbonates associated with cold seepage at the eastern Nankai Trough: fluids in convergent margins. *Earth and Planetary Science Letters*, **3-4**, 391-404.

SEARL, A. 1994. Discontinuous solid-solution in Ca-rich dolomites: the evidence and implications of dolomite petrographic and geochemical data. *Special Publication of the International Association of Sedimentologists*, **21**, 361-376.

SCHMIDT, V. AND MCDONALD, D.A. 1979. Texture recognition of secondary porosity in sandstones. *In*: SCHOLLE, P.A. AND SCHLUGER, P.R. (editors). *Aspects of Diagenesis*. Society of Economic Paleontologists and Mineralogists Special Publication, **26**, 209-225.

SCHMIDT, G.A., BIGG, G.R. AND ROHLING, E.J. 1999. *Global Seawater Oxygen-18 Database*. http://data.giss.nasa.gov/o18data/.

SCHRAG, D.P., ADKINS, J.F., MCINTYRE, K., ALEXANDER, J.L., HODELL, D.A., CHARLES, C.D. AND MCMANUS, J.F. 2002. The oxygen isotopic composition of seawater during the Last Glacial Maximum. *Quaternary Science Reviews*, **21**, 331–342.

SHARMA, T. AND CLAYTON, R.N. (1965). Quoted in: Friedman I. and O'Neil J .R. 1977. Compilation of stable isotope fractionation factors of geochemical interest. Fleischer (Ed), *Data of Geochemistry, 6th Ed*. United States Geological Survey, Professional Paper 440-KK.SKINNER, H.C.W. 1963. Precipitation of calcian dolomites and magnesian calcites in the southeast of South Australia. *American Journal of Science*, **261**, 449-472.

STUART, I.A. AND COWAN, G. 1991. The South Morecambe Field, Blocks 110/2a, 110/3a, 110/8a, UK East Irish Sea. *Geological Society of London, Memoir*, **14**, 527-541.

SWEENEY, R.E. AND KAPLAN, I.R. 1973. Pyrite framboid formation: laboratory synthesis and marine sediments. *Economic Geology*, **68**, 618-634.

TARUTANI, T., CLAYTON, R.N., AND MAYEDA, T. 1969. The effect of polymorphism and magnesium substitution on oxygen isotope fractionation between calcium carbonate and water. *Geochimica et Cosmochimica Acta*, **33**, 987–996.

TUCKER, M.E., 2001. *Sedimentary Petrology: an introduction to the origin of sedimentary rocks*, 3rd ed. Blackwell, UK.

VAHRENKAMP, V.C AND SWART, P.K., 2001.Late Cenozoic dolomites of the Bahamas: metastable analogues for the genesis of ancient platform dolomites. *Special Publication of the International Association of Sedimentologists,* **21**, 133-153.

VERNON, R.H.., 2004. *A practical guide to Rock Microstructure*, 1st ed. Cambridge University Press, UK.

WHORMERSLEY, P., WILSON, C., LIMPENNY, D. AND LESLIE, A. 2008. Understanding the marine environment – seabed habitat investigations of Submarine structures in the mid-Irish Sea and Solan Bank Area of Search (AoS) – cruise report. JNCC Contract No: F90-01-1200. *CEFAS Cruise Report* **CEND 11/08**, 120pp. JNCC CONTRACT NO: F90-01-1200.

WILBY P.R., AND WHYTE, M.A. 1995. Phosphatized soft tissue in bivalves from the Portland Roach of Dorset (Upper Jurassic) *Geological Magazine***, 132,** 117-120.

British Geological Survey
NATURAL ENVIRONMENT RESEARCH COUNCIL

British Geological Survey
Environmental Science Centre
Keyworth
Nottingham
United Kingdom
NG12 5GG

Tel +44 (0)115 936 3143
Email enquiries@bgs.ac.uk

REPORT APPROVAL FORM

Report title and authors
Mineralogy, petrography and stable isotope study of methane-derived authigenic carbonates (MDAC) from the Croker Carbonate Slab, CEND 23/25 Survey. Part 1 and Part 2
L.P. Field, A.E. Milodowski, D.Wagner, H. Sloane, M.J.Leng and A.L Marriott

Client name and address	
Cefas – Lowestoft Laboratory Pakefield Road Lowestoft Suffolk NR33 0HT United Kingdom	Version control **Final v1.0**
	BGS Report No. **CR/16/164**
	Client contract **Cefas. PO 20035669**
	Ref. BGS project code **NEE5903R**
	Classification **Commercial-in-confidence**

Version	Status	Prepared by	Checked by	Approved by	Date
1.0	Final	L.P.Field	[signature]	Michael Allen	6/12/16

BGS/RAFv3.0; Jan 2013